12-2023

Dynamics Modeling of Molten Salt Reactors

Visura Umesh Pathirana
vpathira@vols.utk.edu

To the Graduate Council:

I am submitting herewith a dissertation written by Visura Umesh Pathirana entitled "Dynamics Modeling of Molten Salt Reactors." I have examined the final electronic copy of this dissertation for form and content and recommend that it be accepted in partial fulfillment of the requirements for the degree of Doctor of Philosophy, with a major in Nuclear Engineering.

Ivan Maldonado, Major Professor

We have read this dissertation and recommend its acceptance:

Ivan Maldonado, Ondrej Chvala, Lawrence Heilbronn, Shayan Shahbazi

Accepted for the Council:

Dixie L. Thompson

Vice Provost and Dean of the Graduate School

(Original signatures are on file with official student records.)

Dynamics Modeling of Molten Salt Reactors

A Dissertation Presented for the

Doctor of Philosophy

Degree

The University of Tennessee, Knoxville

Visura Umesh Pathirana

December 2023

Acknowledgements

This research and development at the University of Tennessee is funded by a grant from Oak Ridge National Laboratory (subcontract 4000159472). Partial support for this work comes from the United States Department of Energy award DE-NE0008793.

This work would not have been possible without the support of my committee members, Dr. Ivan Maldonado, Dr. Ondřej Chvála, Dr. Lawrence Heilbronn and Dr. Shayan Shahbazi. I thank and express gratitude to all the committee members. I would like to especially thank Dr. Ondřej Chvála for hiring me as a graduate student and getting me into the field of system dynamic modeling. I also would like to thank my family, colleagues, and friends for their tremendous support. I could not have done this without everyone of you.

The sole meaning of life is to serve humanity.

-Leo Tolstoy-

A mind all logic is like a knife all blade. It makes the hand bleed that uses it.

-Rabindranath Tagore-

Abstract

The abundance of energy is a necessity for the prosperity of humanity. The rise in energy demand has created energy shortages and issues related to energy security. Nuclear energy can produce vast amounts of reliable energy without many of the negative externalities associated with other competing energy sources, such as coal and natural gas. As a result, public interest in nuclear power has increased in the past decade, and many new types of nuclear reactors have been proposed. These nuclear reactor designs feature many passive technologies that can operate without external influence. Reactors that feature advanced passive safety features are classified as Generation IV advanced reactors. Molten Salt Reactors (MSRs) are a type of advanced reactor that uses molten alkali halide salts as both the coolant and the fuel matrix. MSRs remain as understudied systems with complex dynamic behaviors. Non-linear dynamic simulations allow modeling complex systems such as MSRs. Non-linear modeling as such presented here can be used to understand the unique dynamic behaviors of MSRs. The modeling methodology is implemented in Modelica, an open-source dynamic modeling environment, and is publicly available. Modeling capabilities include 1D thermal hydraulic coupled neutronics, dynamic decay heat production, fission product inventory tracking, and a collection of support utilities. The modeling toolkit Scalable Modular Molten Reactor Model (SMD-MSR) is specifically geared toward modeling thermal spectrum MSRs. Its modular implementation allows the substitution of various physics modules to capture the specific functional requirements of a specific MSR system. The

publication includes three dynamic models of MSR systems of varying complexity. They include Molten Salt Reactor Experiment (MSRE), Molten Salt Demonstration Reactor (MSDR) and Molten Salt Research Reactor (MSRR). The modeling of each system is discussed, and several transients, including both normal and non-normal transients, are performed to demonstrate the SMD-MSR toolkit's modeling capabilities.

Table of Contents

List of Tables

List of Figures

List of Acronyms

ANS American Nuclear Society

ACU Abilene Christian University

AP Advanced Passive

AEC Atomic Energy Commission

ANP Aircraft Nuclear Propulsion

API Application Programming Interface

ARE Aircraft Reactor Experiment

BOC Beginning of the Cycle

BRE Boiling Reactor Experiment

BWR Boiling Water Reactor

CANDU Canada Deuterium Uranium

CFR Code of Federal Regulations

DHRS Decay Heat Removal System

DNP Delayed Neutron Precursor

EOC End of the Cycle

FLiBe LiF-BeF_2 (67-33 mole %)

FP Fission Product

FWHM Full Width Half Max

GUI Graphical User Interface

GDC General Design Criteria

HALEU High Assay Low Enriched Uranium

HRE-1 Homogenous Reactor Experiment No. 1

HRE-2 Homogenous Reactor Experiment No. 2

HRE-3 Homogenous Reactor Experiment No. 3

HYPO High Power Reactor

ISHR Intermediate-Scale Homogenous Reactor

LAPRE Los Alamos Power Reactor Experiment

LEU Low Enriched Uranium

LMTD Log Mean Temperature Differance

LOPO Low Power Reactor

LWR Light Water Reactor

MATLAB MATrix LABoratory

MOC Middle of the Cycle

mPKE modified Point Kinetics Equation

MSBR Molten Salt Breeder Reactor

MSDR Molten Salt Demonstration Reactor

MSR Molten Salt Reactor

MSRE Molten Salt Reactor Experiment

MSRR Molten Salt Research Reactor

NRC Nuclear Regulatory Commission

NTU Number of Transfer Units

ODE Ordinary Differential Equation

OMEdit Open Modelica Connection Editor

ORNL Oak Ridge National Laboratory

OTSG Once Through Steam Generator

PHX Primary Heat Exchanger

PKE Point Kinetics Equation

PWR Pressurized Water Reactor

QA Quality Assuarance

SG Steam Generator

SHX Secondary Heat Exchanger

SMD-MSR Scalable Modular Molten Reactor Model

SSC System, Sub-system and Component

SUPO Super Power Reactor

SMR Small Modular Reactor

TestIO Test Input-Ouput

UHX Ultimate Heat Exchanger

ZPA Zero-Power Approximation

Chapter 1

Introduction

1.1 Dissertation Goals

The dissertation goals can be summarized under two main objectives. The first objective of the dissertation is to develop a Molten Salt Reactor (MSR) dynamic modeling tool that is openly available. The second objective is to investigate the dynamic behavior of several MSRs.

Goals of the MSR dynamic modeling tool:

- Make the modeling toolkit openly available
- Does not require proprietary programs to use the toolkit
- Toolkit must be simple and adaptive
- Achieve fast simulation times
- Allow creation of reconfigurable models
- Ability to simulate normal and off-normal transients
- Ability to simulate depletion-dependent transients

Goals of investigating dynamic behavior of MSRs:

- Demonstrate modeling features of modeling toolkit
- Identify unique dynamic characteristics of MSRs
- Model normal and off-normal transients of Molten Salt Reactor Experiment (MSRE)
- Model normal and off-normal transients of Molten Salt Demonstration Reactor (MSDR)
- Model normal and off-normal transients of Molten Salt Research Reactor (MSRR)

1.2 Overview

Energy is essential for all aspects of modern life, and access to energy greatly affects the quality of life. It is well established that per capita energy consumption is highly correlated with various quality of life indicators up to a threshold [1]. With the expansion of the global population and the increase in per capita income, the demand for energy is increasing. To meet the increasing demand, energy is derived from both renewable and non-renewable energy sources. Since the 1970s, most of the world's energy demand has been met using non-renewable sources such as coal, oil, and natural gas [2]. The energy produced using sources such as nuclear, biofuels, hydro, solar, and wind has grown in the last three decades but represents only 22.2 % of the world's energy supply in 2020. Each of these energy sources has unique advantages and disadvantages. For example, fossil fuels produce greenhouse gases, but they can be easily converted into usable forms of energy. The selection of a suitable energy source for a specific application is based on advantages and disadvantages. One of the key defining factors in the selection of the energy source is the cost per usable energy produced. However, this criterion alone should not be a decisive factor.

The cost per usable energy produced does not always include negative external costs associated with the use of the energy source considered. There are several proposed policies to address this issue, such as the carbon tax. However, these solutions are not currently widely implemented. Some countries have established national policies to phase out energy sources with negative externalities, such as coal. Eliminating energy sources such as coal is necessary to effectively address global challenges such as climate change. However, countries with growing economies cannot afford to use alternative energy sources due to their high initial capital investments. In growing economies, the per capita income is increasing, which in turn increases the per capita energy consumption. Countries, where policies have been implemented to reduce greenhouse gas emissions, face other challenges. The selection of energy sources is a difficult task with laborious considerations. Appropriate considerations must be taken to ensure that eliminating one energy source does not create consequences such as energy insecurity. Each energy source has its limitations; hence, suitable energy sources must be carefully selected to replace polluting energy sources. Coal is mainly used to produce base load electricity; therefore, replacing coal requires an energy source that is capable of producing electricity without interruptions throughout the day. Many European countries have chosen to use energy sources such as solar and wind, but this has failed because solar and wind are incapable of producing base load electricity. Nuclear power would be an excellent option to replace coal; however, the initial capital cost and negative social stigma have discouraged the construction of new nuclear power plants. Global concerns such as global warming and climate change are widely debated and speculated. Unlike global warming and climate change, energy security issues are apparent to most of the world population.

Fossil fuels are a scarce resource that is not evenly distributed throughout the world. This creates monopolies in the energy market and creates supply disturbances due to conflicts. Additionally, fossil fuels must be transported from mining sites to locations where they are refined and then finally consumed. This creates a complex

supply chain that is prone to breakdowns. For example, the natural gas pipeline that supplies natural gas to the European continent from Africa is routed through many countries. Any political or civil disturbance in countries which the pipeline line is routed through can have severe consequences for the natural gas supply in Europe. In light of concerns about energy security, advanced nuclear reactors with passive safety features have gained popularity in some countries. Current nuclear power reactors are used to generate base load electricity, with few exceptions that provide district heating. Unlike current commercial nuclear reactors, advanced reactors can be used for many other applications, which are discussed in Sections 1.2.1 and 1.2.2.

The passive safety features of advanced reactors theoretically reduce the probability of catastrophic failures by design. In 2001, the Gen IV International Forum was established to share further developments of advanced reactors. The Gen IV Forum announced six reactor concepts that show significant technological merits to be used as advanced reactors. MSRs are one of the selected reactor concepts. Unlike traditional Light Water Reactors (LWRs), MSRs use molten salt mixtures as both fuel matrix and heat transport media. Molten salt mixtures are chemically stable and can be heated up to $\approx 1200\,^{\circ}\mathrm{C}$ without turning into vapor. Therefore, MSRs can be operated at high temperatures near atmospheric pressures, eliminating catastrophic explosions that can eject highly radioactive material into the atmosphere. A detailed discussion of MSRs is presented in Section 1.3

1.2.1 Contemporary Nuclear Reactors

Currently, there are 436 operable nuclear power reactors around the world. Another 59 reactors are under construction and 321 are proposed. Among operable reactors, 301 are Pressurized Water Reactors (PWRs) 46 are Canada Deuterium Uranium (CANDU) reactors and 41 are Boiling Water Reactors (BWRs) [3]. It is clear that most popular reactor designs use water as either the moderator or the coolant. The use of water limits the applications of these power plants to electricity production

and low-temperature thermal applications such as district heating. Nuclear power contributes to 20 % of the U.S. electrical grid [4]. Water boils at 100 °C at standard pressure. Commercial power reactors such as PWRs operate in the range of 300 to 400 °C. In order to operate at these temperatures, the reactors are maintained at higher pressures $\approx 1200\,psi$. These high operational pressures pose many technical challenges and require multiple layers of reinforced containment. The circulation in these reactors is maintained using pumps and is not designed to utilize passive circulation when the pumps are inoperable. Nuclear fuel produces decay heat even when the reactor is shut down; therefore, forced circulation is required to ensure that the fuel remains at a safe temperature. If the cooling of nuclear fuel is disrupted, the temperature of the nuclear fuel can reach its melting temperature and cause core damage. Furthermore, at temperatures above 1600 °C water reacts with core structural metals such as fuel cladding, producing explosive mixtures of hydrogen and oxygen. There are few LWR designs that use passive technologies as an additional safety measure to provide core cooling in total plant blackout events, such as the Westinghouse Advanced Passive (AP) series PWRs. There, cooling water is stored above the containment vessel and can be fed to the reactor core by gravity without any external power.

1.2.2 Future Prospects of Nuclear Energy

Most of the commercial power reactors that operate currently cannot produce high temperatures due to their pressure boundary limitations, and therefore application is limited to the production of electricity. The recorded energy consumption of the United States is 97.3 Quads in 2021. Of the total energy consumption, only 36.6 Quads accounts for the electricity consumption which is 37.6 % [5]. Therefore, the contribution of nuclear energy to total energy consumption is 8.36 %. The energy supply of each source and the consumption of each sector are shown in Figure 1.1.

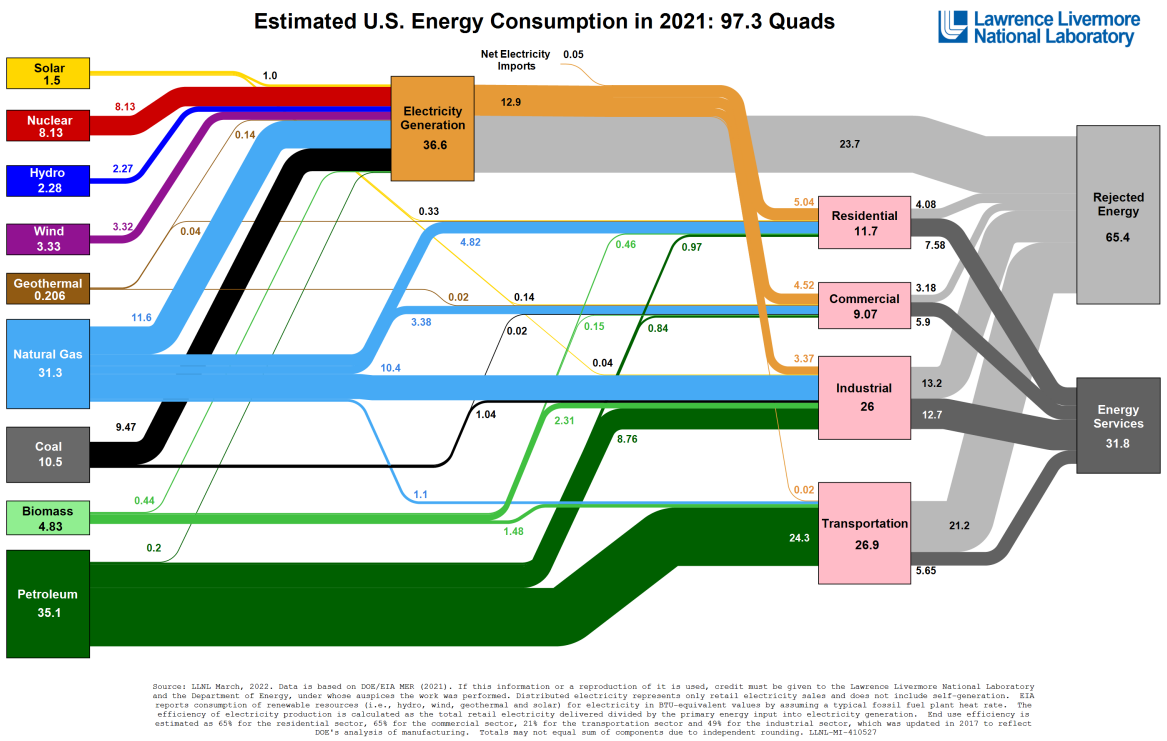

Figure 1.1: Energy consumption of United States in 2021 [5]

Upon a close examination of Figure 1.1, it is clear that the current market of electricity in which nuclear power competes is saturated with many other energy sources. Advanced reactors have the ability to produce high temperatures and, therefore, can be used for process heat applications. With advanced reactors, nuclear energy can be tapped into industrial applications where high-temperature process heat is required. This will greatly increase the available markets for nuclear power and its utilization. With renewed interest in nuclear energy, both the public and private sectors are investing large sums of money in the research and development of advanced reactors.

The initial capital cost of a current nuclear power plant is in the range of $1,200-$5,000 per kilowatt of capacity and competing energy sources, such as natural gas, only cost in the range of $400-$1200 per kilowatt of capacity [6]. Although the capital cost of nuclear energy is significantly higher than other competing energy sources, the fuel cost is low, making them lucrative long-term investments. However, due to regulatory and financial constraints, only a handful of nuclear power plants have been built in the United States in the last two decades. As a possible rectification, the nuclear industry is adopting Small Modular Reactor (SMR) technology. Since SMRs are modular designs, the reactor system can be built in a controlled environment and then transported to the power plant site. Using SMR technology, construction times can be greatly reduced. The use of a modular system allows the expansion of the plant capacity and reduces the design licensing cost of each unit.

1.3 Molten Salt Reactors

MSRs are a type of advanced Gen IV reactors that use eutectic mixtures of alkali and alkali earth metal halides as both the coolant and the fuel matrix. MSRs can be considered as a class of fluid-fueled reactors. However, there are some MSR designs where the fuel salt does not circulate but is filled into fuel rod-shaped vessels and

is kept within the reactor core. Circulating MSRs are designed with multiple loops of eutectic salts where heat is transferred from one loop to the other through heat exchangers. Molten halide salts are chemically stable and have a high affinity for holding most of the Fission Products (FPs) so that they are localized only to the fuel salt itself. Less reactive elements, such as nodal metals and gasses, can nucleate out of the molten salt mixtures. Nucleated elements can be captured in specialized systems. MSRs can operate in thermal, epithermal, and fast spectrums, making the overall reactor concept versatile and can be adapted for various applications. MSR's history can be rooted in the development efforts of fluid-fueled reactors. Therefore, in Section 1.3.1 the history of fluid-fueled reactor research is briefed, and then the development of MSRs is summarized. A rigorous history of fluid-fueled reactors and their development can be found in [7]. In Section 1.3.2 the proposed MSR commercial power reactors are presented and in Section 1.3.3 design and licensing challenges are discussed.

1.3.1 History

Fluid-fueled reactors predate the Manhattan Project and are one of the earliest attempted systems to achieve self-sustaining nuclear fission chain reactions. In December 1940, French physicists Hans Halban and Lew Kowarski conducted a series of experiments in the Cavendish Laboratory of Cambridge University. In these experiments, varying amounts of natural U_3O_8 powder were mixed with heavy water in an aluminum sphere immersed in heavy mineral oil that acted as a neutron reflector. From the experiments, Halban and Kowarski calculated that the multiplication factor of the system is 1.18 when the atomic ratio of deuterium to uranium is 380 to 1. These experiments are the first recorded of using homogeneous fluidized systems to achieve criticality. The results of these experiments were not published at the time due to the ongoing World War II. U_3O_8 is not soluble in water; therefore, it would have formed a suspension without mechanical agitation. From the work of Halban and Kowarski,

it was concluded that it is impossible to create critical systems with natural U_3O_8 and light water. Due to the scarcity of heavy water at the time, homogeneous reactor studies were purely academic.

In December 1942, experiments led by Enrico Fermi achieved criticality in the Chicago Pile, marking the first achievement of the Manhattan Project. By early 1943, the United States and Canada produced large amounts of heavy water. In March 1943, Harold Urey, a pioneer in isolating deuterium and a member of the Committee on Uranium, conferred with Enrico Fermi to review the prospects of fluidized homogeneous reactors. They discussed the multiplication factor attained by Halban and Kowarski during experiments conducted at the Cavendish Laboratory. The theoretic multiplication factor in a slurry reactor with U_3O_8 and heavy water was determined to be lower than previously calculated by Halban and Kowarski. As a result of insufficient cross-sectional data for deuterium, it was difficult to predict the volume of heavy water required to build a homogeneous slurry reactor. Attention was paid to heterogeneous designs in which a mixture of U_3O_8 and heavy water would be pumped through a lattice of tubes submerged in heavy water that would act as a moderator. Eugene Wigner estimated that the uranium concentration in the slurry should be 2.5 to $3\,\mathrm{g/cm^3}$. This concentration was achievable only through pure UF_6, which had a uranium density of $2.48\,\mathrm{g/cm^3}$. It was considered to construct a pile with UF_6; however, it was concluded that the operation of such a pile would pose many technical challenges since UF_6 is extremely corrosive. In July 1943, experiments performed by Alexander Langsdorf showed that the absorption cross-section of deuterium was much lower than previously known. The requirement of high-uranium density slurries was not a priority. The University of Chicago Metallurgical Laboratory proposed three types of slurry reactors at the end of 1943. All three designs used mixtures of uranium with heavy water. The first design was homogeneous and the second and third designs were heterogeneous with light water and heavy water cooling. However, these designs were considered alternatives in the

case where Hanford piles do not perform their mission. With the successful operation of Hanford reactors, interest in slurry reactors as production reactors at the University of Chicago Metallurgical Laboratory declined.

Several other national laboratories worked on fluid-fueled reactors in 1943. Efforts at Los Alamos Laboratory designed, built, and operated several reactors fueled with uranyl sulfate. Interestingly, unlike many sulfate compounds, uranyl sulfate is water-soluble. Under the leadership of Donald William Kerst, Los Alamos designed "power boiler", a homogeneous reactor that utilized a solution of uranyl sulfate. During the design phase "power boiler" was expected to be a high-power reactor using enriched uranium. However, this design was altered in favor of Robert Frederick Christy's Low Power Reactor (LOPO) design. In 1944, the LOPO reactor was built and experiments were conducted. With the experience of LOPO, extensive design alterations were made to build the High Power Reactor (HYPO) reactor. The HYPO reactor used a solution of uranyl nitrate. Initially, it was thought that uranyl nitrate was less soluble than uranyl sulfate. However, later this assumption was proven to be inaccurate. In 1949, HYPO was extensively modified to create Super Power Reactor (SUPO) as a safe experimental tool. The SUPO was equipped with a gas recombination system that is capable of reacting hydrogen and oxygen that were released from the reactor by radiolysis to form water. In 1955, after extensive experimentation and lessons learned from SUPO, two experimental power reactors Los Alamos Power Reactor Experiment (LAPRE)-1 and LAPRE-2 were designed. LAPRE reactors used enriched uranium oxide in concentrated phosphoric acid. The LAPRE-1 reached criticality in 1956 and operated at 20kW$_t$ for about 5 hours. Corrosion in gold-plated cooling coils caused radioactive FPs to be leaked into the steam side. The experiment was shut down and LAPRE-1 was dismantled.

After enriched uranium became available, the idea of developing a homogenous reactor became more appealing due to reduced D_2O requirement and the possibility of building a reactor using ordinary water. Clinton Laboratories, now Oak Ridge

National Laboratory (ORNL) began researching enriched-uranium reactors, and various reports were released by the Chemistry Division. In 1944, Coryell and Turkevich proposed constructing a homogeneous reactor that used a salt solution in ordinary water as fuel. In their proposal, they discussed several advantages to such a reactor, including the preparation of radioactive tracers and radioactive sources, as well as further research and studies on radiation and radioactive elements. In addition to the Chemistry Department, the physicists were also interested in the proposal, as they saw it as an opportunity to study and potentially establish a ^{233}U-thorium breeding cycle.

Work on the reactor continued through 1945; however, there were a few basic problems with the reactor that the scientists were unable to solve, including bubbles forming in the homogeneous solution, caused by water decomposing into hydrogen and oxygen. These bubbles caused difficulties in controlling the operating level of the reactor, and the nuclear physics calculations performed showed that there was a potential for the reactor to go out of control because of the bubbles. The scientists were unable to build a tank capable of handling the elevated temperature and pressure required to minimize bubbling, and they were not familiar with handling radioactive materials in a high-pressure environment. Some other problems with the reactor included corrosion, solution stability, and external holdup of fissionable material. Due to the multiple unsolved problems with the homogeneous reactor, the scientists decided to return to the heterogeneous reactor proposed at the Metallurgical Laboratory in the hopes that further research with this reactor would help solve the problems of the homogeneous reactor.

In 1949, Alvin Weinberg, the research director at ORNL proposed a re-evaluation of homogeneous reactors. The re-evaluation concluded that a homogenous, experimental reactor should be constructed. A homogenous reactor committee was established, led by C.E. Winters, and a preliminary homogenous reactor design was developed. The construction of Homogenous Reactor Experiment No. 1 (HRE-1)

began in 1950 and was completed in 1952. After a period of non-nuclear testing, HRE-1 reached criticality 3 months after completion and continued to run for 2 years, being dismantled after a successful demonstration of the stability of a homogeneous reactor. During the operation of HRE-1, designs were drafted for a Boiling Reactor Experiment (BRE) and Intermediate-Scale Homogenous Reactor (ISHR), but this work was abandoned once the development of Homogenous Reactor Experiment No. 2 (HRE-2) was decided to be the best course of action. HRE-2 was developed to demonstrate the ability of a homogeneous reactor to continuously operate a nuclear power plant. The construction of HRE-2, at the site of HRE-1 was completed in 1956 and reached criticality in 1957 and full power operation in 1958. During operation at full power, a crack in the core tank allowed fuel to leak into the D_2O blanket, but operations were resumed after considering the nuclear behavior of a reactor with fuel in both the core and the blanket. While HRE-2, was in operation, ORNL began development of an experimental thorium breeder reactor, Homogenous Reactor Experiment No. 3 (HRE-3).

During this time, industrial interest in homogeneous reactors began to grow. Westinghouse and Pennsylvania Power and Light Company conducted a joint study, through Atomic Energy Commission (AEC), to determine the economic practicality of aqueous, homogeneous reactor power plants. The results of their study indicated that these plants have excellent long-term possibilities for competitive power production, but further development would be required to determine any certainty about the feasibility of these plants. Following this study, the two companies created the Pennsylvania Advanced Reactor Project in 1955 with a proposal to build a power station financed with private funds. The same proposal was later modified and resubmitted as a part of the Power Demonstration Reactor Program. Despite this proposal, a second group, Foster Wheeler and Worthington Corporations proposed building a homogeneous reactor in coordination with the government. The AEC initially accepted their proposal in 1956 and Congress appropriated funds for the

construction of the reactor, but in 1958 the AEC announced that the plans had been canceled due to a significant increase in the proposed cost of the plant. The Pennsylvania Power and Light Company and Westinghouse Electric Corporation's second proposal was then determined as an acceptable proposal for negotiation by the AEC. This second proposal called for the construction of a power plant that would be operated by the Pennsylvania Power and Light Company, but AEC would cover the cost of research and development. However, the proposal was recalled following a review by the Joint Congressional Committee on Atomic Energy.

It is clear that fluid-fueled reactor development has been a focus during early nuclear reactor research. With the advancement of nuclear reactors after the Manhattan Project, the United States Army Air Forces was interested in building a nuclear-powered aircraft. It was evident that a nuclear-powered aircraft would have an unlimited range compared to a conventional aircraft. This interest was increased in the 1950s when the United States Navy commissioned several nuclear-powered vessels under the direction of Admiral Hyman G. Rickover. It should be recalled that during this period of time, there were no long-range ballistic missiles. Therefore, the idea of a nuclear-powered aircraft with unlimited range would have been very interesting. Aircraft propulsion requires machines that can rotate a blade at very high speeds or a heat source that can heat an air stream to a very high temperature. The latter was chosen, and the Aircraft Nuclear Propulsion (ANP) project was started in 1950 and Aircraft Reactor Experiment (ARE) was built in 1954 at ORNL [8, 9]. The ARE was a beryllium oxide moderated thermal spectrum 2.5 MW_t system and used a mixture of NaF-ZrF_4-UF_4 (53.09-40.73-6.18 mole %) as fuel [10]. The ARE used highly enriched uranium with 93.4% enrichment so that the system can be compact. The ARE was operated for 96 MW hr and reached temperatures up to 860 °C. The ARE was a successful experiment and was able to demonstrate the technical capabilities of MSRs. However, the ANP program was subsequently scrapped due to feasibility concerns and the development of intercontinental ballistic missiles.

The MSR developments continued at ORNL under the guidance of then ORNL director Alvin Weinberg. With the experience of the ANP program ORNL designed and built MSRE in the 1960s. The MSRE is a graphite-moderated, thermal spectrum 8 MW_t system that used LiF-BeF_2 (67-33 mole %) (FLiBe). The MSRE featured a two-loop design in which fuel salt is circulated between the reactor and the heat exchanger which makes up the primary loop and the secondary loop which transports heat from the heat exchanger to a radiator [11]. MSRE was fueled with several compositions of fuels made up of LiF-BeF_2-ZrF_4-UF_4. Furthermore, ^{233}U was also used as fuel for several experiments to demonstrate the capability of MSRs as breeder-burners with U-Th fuel cycles. During the program, many new technologies were developed, including the development of the Hastelloy-N alloy and remote maintenance [12]. To this day, the MSRE remains the only MSR that has been operated for a significant time with archived design and experimental data. During the operation of the MSRE two other MSRs were designed. They are the MSDR and Molten Salt Breeder Reactor (MSBR). The MSDR was intended as a graphite-moderated FLiBe based Low Enriched Uranium (LEU), 750 MW_t power reactor. The system was designed with a Rankin cycle power conversion cycle and was designed to produce 250 MW_e. The MSBR was intended as the next phase of MSRs and was designed as a two-fluid system to demonstrate a U-Th cycle and breed ^{233}U in the blanket. However, both of these systems never progressed beyond the initial design phase. The MSR program was canceled in the 1970s.

1.3.2 Proposed Designs

There are several MSR designs in development. They all have unique features based on the primary mission they are designed to perform. MSRs can be categorized according to several criteria such as neutron spectra, choice of fuel, scale, and primary boundary configuration. Based on these criteria, some popular proposed MSR designs are categorized in Table 1.1.

Table 1.1: MSR concepts and their classifications

Company	**Concept**	**Spectra**	**Fuel**	**Scale**	**Config.**
Copenhagen Atomics	Burner-Breeder	Thermal	Pu-Th	100MW$_t$	Loop
ThorCon Power	TMSR	Thermal	U-Th	557MW$_t$	Loop
Flibe Energy	LFTR	Thermal	U-Th	595MW$_t$	Loop
Terrestrial Energy	IMSR	Thermal	LEU	440MW$_t$	Integral
TerraPower	MSFR	Fast	U	N/A	Integral

Some of the companies mentioned in Table 1.1 have already started licensing activities with the Nuclear Regulatory Commission (NRC). Copenhagen Atomics is a reactor company based in Copenhagen, Denmark. Their burner-breeder reactor is a 100 MW_t, heavy water moderated loop type system. The reactor is a modular design, built in the form of a 40ft shipping container to allow easy transportation. Their burner-breeder reactors are designed to burn plutonium extracted from spent nuclear fuel of LWRs and breed thorium in the process. The use of heavy water enables the burner-breeder concept. They plan to deploy multiple units of burner-breeder reactors per power plant to produce variable amounts of cumulative capacity based on customer requirements.

ThorCon has proposed their TMSR concept. TMSR is planned as a 557 MW_t graphite moderated reactor that uses a uranium-thorium cycle. The TMSR is a loop-type system built in modules. ThorCon power plant is designed in a barge that can be relocated and utilizes ship-building techniques to streamline its production process. Each barge houses two TMSR modules and is equipped with a power conversion system.

Flibe Energy is developing a two-fluid breeder burner reactor named LFTR. The LFTR has a blanket of thorium surrounding a uranium burning core similar to the MSBR design. It is a loop-type system where fuel salt flows from the reactor to the heat exchanger through excore piping.

Terrestrial is a Canadian reactor company that develops an integral MSR named IMSR. Terrestrial plans to use LEU and graphite moderator for its design. IMSR modules can produce 440MW_t. Their design does not feature piping between the reactor core and the heat exchanger, therefore, the heat exchanger is integrated into the reactor vessel itself.

TerraPower is developing their MSFR system. The MSFR is a fast reactor and uses highly enriched chloride fuel. The final capacity of the reactor is not yet publicly known. The MSFR is another integral MSR.

1.3.3 Design Challenges and Licensing

All advanced reactors pose design challenges, but MSRs have a unique set of design and licensing challenges that have not yet been addressed. One of the main technical challenges is to understand the chemistry and physical properties of the molten salt and its interaction with other reactor materials. As a MSR operates FPs get produced in the fuel salt, which in turn changes the chemistry and physical properties of the fuel salt. The lack of data and uncertainties of the said changes makes it difficult to understand and accurately predict the separation and migration of FP from the fuel salt. In reactor licensing, the reactor developer must demonstrate that the reactor does not pose an additional radiological risk to the public. Due to the distributed nature of the FP inventory in MSRs, it requires some rigorous evaluations of the source terms. All General Design Criteria (GDC) stated in Appendix A of 10 Code of Federal Regulations (CFR) Part 50 are applicable to MSRs and it is clearly stated that GDC are applicable to non LWRs. However, the application of some of the criteria is slightly different. Therefore, the NRC is implementing a licensing framework specifically geared toward advanced reactors under 10 CFR 53. The American Nuclear Society (ANS) 20.2 working group was established to implement the standard of design for MSRs. Furthermore, the safeguards present of MSR resents a unique set of challenges as there are no discrete fuel assemblies or rods. Currently, work is being done at national laboratories and universities to develop turnkey technologies to address these issues and challenges.

1.4 Thesis Synopsis

In this research, a publicly available MSR dynamic modeling toolkit named Scalable Modular Molten Reactor Model (SMD-MSR) is developed. The developed toolkit contains reactor physics and thermal hydraulics models that are reconfigurable to model a range of MSR System, Sub-system and Components (SSCs). The modeling

approach was inspired by the theoretical dynamic and stability analysis of MSRE performed at ORNL during the design and operations of the MSRE in the 1960s. The modeling methodology developed by ORNL is greatly improved with many additional physics models and is implemented in MATrix LABoratory (MATLAB) Simulink and then in Modelica. Modelica implementation of the modeling methodology greatly improved its usability and open distributivity. The modeling methodology is detailed in Chapter 2 and then the models created using the toolkit are detailed in Chapter 3. A validation against available MSRE results is given in Chapter 4. Various normal and off-normal transients were performed to understand MSR dynamic behavior and to showcase the capabilities of SMD-MSR. The transients performed, and their implications are discussed in Chapter 5. Lastly, conclusions and suggestions for future work are presented in Chapter 6.

1.5 Author Contribution

The work presented in this dissertation developed an open-source MSR dynamic modeling framework and includes work published in several separate journal articles [13, 14, 15, 16, 17] and three ANS transactions [18, 19, 20]. All versions of the SMD-MSR toolkit are freely available on GitHub [21]. This work is important in developing multiphysics modeling methods for MSRs which in turn can be useful to develop and establish envelops for MSR safety criteria, design, and licensing requirements. Following are the author's direct contributions to the modeling methodology,

- Dynamic decay heat model
- Simulation of normal and off-normal transients
- Depletion-dependent and multi-parameter sensitivity study
- Implementation of modeling approach in Modelica

Chapter 2

Methodology

This chapter discusses the entire modeling approach of the SMD-MSR. First, dynamic modeling in MATLAB Simulink and Modelica is discussed briefly since the development of the SMD-MSR roots to replication of MSRE stability analysis performed by ORNL in MATLAB Simulink. SMD-MSR is then reimplemented in Modelica to increase availability and utilize the unique functionality of Modelica. The background of modeling is detailed in Sections 2.1, 2.2, and 2.3.

The methodology is organized in two separate sections for the sake of clarity. Section 2.4 describes the underlying general physics modules and functionalities of the modeling toolkit and is intended to function as the general theoretical manual. Each subsection of Section 2.4 discusses special considerations and modifications made to the general theory used in other nuclear engineering applications such as in LWR analysis. Section 2.5 details general component models that can be created using individual physics modules. It is intended as the user manual for the SMD-MSR. These generic components can be customized by adding or removing physics modules to fit the modeling scope. Additionally, these component models can be used as a guide to create application-specific components as needed.

2.1 Dynamic System Modeling in Simulink

Simulink is a multi-domain graphical programming environment designed for dynamic simulations by MathWorks Inc. with MATLAB [22]. MATLAB Simulink is a proprietary software package. Simulink allows the user to represent a dynamic system with blocks that manipulate signals. The use of signal-based representation and the dependence on input signals fed to blocks to produce output signals make Simulink a causal approach to modeling. Units are not assigned to signals; therefore, it is the user's responsibility to route signals and keep track of units of quantities that are being used. Simulink is equipped with several fixed and variable time step solvers that allow efficient solving of systems of Ordinary Differential Equations (ODEs). Solvers in Simulink allow for solving of both stiff and non-stiff systems. MATLAB Simulink is user-friendly and intuitive for a novice system modeler. Simulink's usability is enhanced by many other proprietary support applications of MATLAB.

2.2 Dynamic System Modeling in Modelica

Modelica is an open-source decalative object-oriented programming language designed by the Modelica Association for dynamic system modeling [23]. It uses an acausal approach, unlike Simulink. Although Modelica's language is open source, it requires a compiler to compile and simulate models. There are several Modelica compilers, both proprietary and open source. Dymola and SimulationX are some of the proprietary Modelica compilers. Open Modelica Connection Editor (OMEdit) is an open-source compiler developed by the Open Modelica Consortium. Due to the acausual representation, Modelica compilers rearrange systems ODEs to optimize the method of solving. Like Simulink, Modelica also has a Graphical User Interface (GUI) that allows for graphical interactions with models such as model creation and parameter editing. Proprietary Modelica compiler packages have additional functionalities in

comparison to their open-source counterparts, such as Application Programming Interfaces (APIs) to interact with other programs.

2.3 SMD-MSR

SMD-MSR is a low-fidelity dynamic modeling toolkit specifically developed to model MSRs. The toolkit features easy-to-use generic models of key components of a MSR. The component models are designed to be easily modified by the user to model any MSR topology. SMD-MSR is intended as a first-order engineering estimation tool. Using low-fidelity models can help understand the functional and safety requirements of an individual SSC. Models created with the toolkit can be run on a personal computer. A simulation of 10,000 s can be simulated under 1 min.

The modeling approach is inspired by the MSRE stability analysis performed by ORNL [24]. The modeling approach was then later implemented in MATLAB Simulink and validation was performed against available MSRE experiment data [25]. The validated modeling approach was improved by adding dynamically producing decay heat, component scaling, modular architecture, and depletion dependency [13, 14]. Later, the improved modeling approach was implemented in Modelica using OMEdit compiler to increase availability [15]. A detailed comparison between the Simulink and Modelica versions of the model is presented in Section 4.2. SMD-MSR is a great teaching and research tool that can be used to improve awareness of the unique dynamic behaviors and operational procedures of MSRs.

2.4 Modeling Approach

In this section, the modeling approach is described in detail. This is intended as the theory manual for the SMD-MSR toolkit. Some of the sections have been previously published; therefore, appropriate disclaimers are added with citations. The modeling

approach is based on conservation equations. Conservation of heat and species are explicitly considered in the current publishing iteration. Section 2.4.1 discusses the implementation of individual nodes. Transport is an important consideration for the dynamic modeling of MSRs. Section 2.4.2 details the transport modeling strategy. Point Kinetics Equations (PKEs) are a simple but powerful method to represent nuclear kinetics and dynamics. Section 2.4.3 is dedicated to describing the special considerations required to model point kinetics in MSRs as well as PKE implementation in the modeling approach. Decay heat is an important aspect when evaluating nuclear reactor safety. It is responsible for about 7% of the heat produced in an operating nuclear reactor. Traditional methods of decay heat calculations require tracking of the FP inventory. The presented method does not require such complicated mechanisms and uses a simplified approach. Section 2.4.4 is dedicated to analyzing the simplified decay heat precursor method and describing how it is integrated into the model. Section 2.4.5 details a simple utility included in the model to calculate and visualize the flux profiles of a bare homogeneous reactor with analytical solutions of one group diffusion equation. Temperature reactivity feedbacks are essential to control a nuclear reactor and are discussed in Section 2.4.6. FPs with high absorption cross-sections affect the dynamics of a reactor. Modeling said FPs in a MSR requires special treatments. Section 2.4.7 describes modifications done to the general FP poison representation. Section 2.4.8 details the effects of depletion in a typical thermal spectrum MSR in depth. This section discusses neutronics as well as variations in the physical properties of fuel salt as a MSR operates. Section 2.4.9 summarizes the modes of heat generation terms in the modeling approach. Sections 2.4.10, 2.4.11, and 2.4.12 are dedicated to the presentation of partial heat transfer models in the model. These sections include the implementation of conduction, convection, and radiation heat transfer modes throughout the modeling approach. Sections 2.4.13, 2.4.14, and 2.4.15 describe special instances of heat transfer. These instances are general Mann's model, fuel channel, and heat exchanger

clusters. Mixing nodes are another special instance in the modeling approach and are presented in Section 2.4.16. Subsections 2.4.17, 2.4.18, and 2.4.19 document the supporting functionalities of the model.

2.4.1 Nodalization

SMD-MSR utilizes a nodal approach with constant volume. Individual nodes make up the simplest units where conservation principles are applied. Multiple nodes are clustered and connected using various connectors to create node clusters that are capable of representing components. Components with node clusters can be connected to create systems and subsystems. Individual nodes do not contain any fixed geometric restrictions and are represented as arbitrary geometries where geometry is characterized by specified node volume and its interfacial surface areas. The use of constant volumes simplifies the implementation of nodalization. However, the said simplification limits implementations of physical treatments such as thermal expansions through changing node volume. It is possible to implement a nodal scheme where the volume of the node is dynamic. Dynamic nodal volumes significantly reduce the computational efficiency of the overall model and can lead to singularity errors during extreme scenarios where the node volume reaches zero. It was found that the use of constant volumes and the accounting for individual species is the best practice for the purposes of dynamic modeling of MSRs.

All nodes function through the conservation of volume and heat energy. Although momentum conservation is required to properly treat pressure drops and model flow behaviors, it is not implemented in this iteration of SMD-MSR since the simulation tool is geared toward generalized first-order engineering design work. Modeling of pressure drop and flow characteristics would require design-specific details that might be lacking during the initial design phase. Conservation of volume and heat energy is achieved through the resolution of the inflow, outflow, production, and removal

rates. The heat energy balance for a node with an arbitrary geometry is shown in Figure 2.1.

Using Figure 2.1 as a guide, an energy balance equation can be written as follows to calculate the internal heat energy within a node,

$$Q_{internal} = Q_{in} - Q_{out} + Q_{generation} - Q_{removal} \tag{2.1}$$

where $Q_{internal}$ is the total internal heat energy, Q_{in} is the sum of heat energy flow in, Q_{out} is the sum of heat energy flow out, $Q_{generation}$ is the sum of heat energy generated within the node due to mechanisms such as fission and decay, and $Q_{removal}$ is heat energy removed by user prescribed functions.

Heat energy can enter or leave a node through mechanisms such as flow, conduction, convection, and radiation. Heat energy can be generated within a node due to fission heat or decay heat, while heat energy can be removed by a user-defined removal to simulate an energy-removing device or a component. Each term is discussed in detail in Sections 2.4.9, 2.4.10, 2.4.11, and 2.4.12.

2.4.2 Transport

Transport is an important consideration for the dynamic modeling of MSRs. MSRs experience fuel and coolant salt circulation due to forced convection and free convection. Forced convection is achieved using pumps, while free convection is the result of temperature gradients within the system. Since momentum conservation is not explicitly accounted for in SMD-MSR, bulk transport is calculated by normalizing the specified flow rate. Normalization is done for the flow rate to simply form a flow rate-dependent non-dimensional variable. The flow fraction is a unitless variable dependent on time that has a maximum value of one and a minimum value of zero. The flow fraction, FF, can be derived as Equations 2.2 or 2.3.

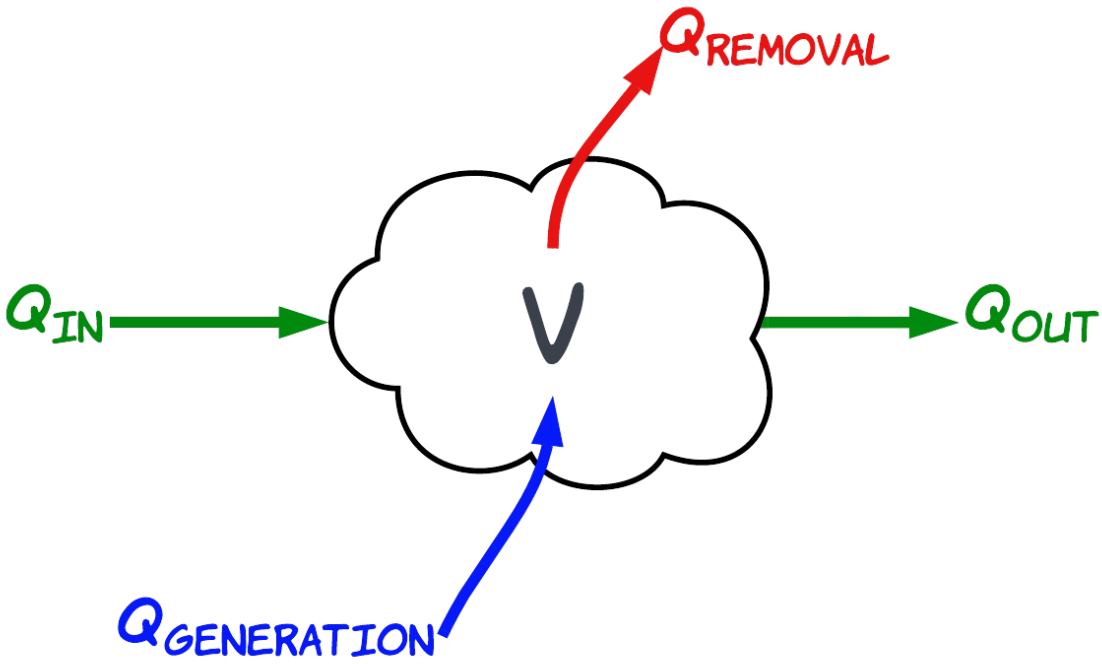

Figure 2.1: Depiction of energy conservation within a node.

$$FF(t) = \frac{\dot{V}(t)}{\dot{V}_{nominal}} \tag{2.2}$$

$$FF(t) = \frac{\dot{m}(t)}{\dot{m}_{nominal}} \tag{2.3}$$

Here, $\dot{V}(t)$ and $\dot{m}(t)$ are time-dependent volumetric and mass flow rates, respectively. Terms $\dot{V}_{nominal}$ and $\dot{m}_{nominal}$ are nominal volumetric and nominal mass flow rates of the specific loop. Although both definitions shown in Equations 2.2 and 2.3 are valid and equal during constant densities, they should not be used interchangeably. SMD-MSR specifically uses the volumetric expression of FF shown to accommodate temperature-dependent thermophysical properties.

The transport of bulk fluid in components such as pipes is implemented using transport delays in Modelica language. The Modelica language allows variable time delays which are utilized to deploy variable flow rates. The delay time, which is also known as the resident time, τ. The resident time τ of a channel with a uniform cross-section, such as a pipe, can be expressed as Equations 2.4 or 2.5.

$$\tau(t) = \frac{L}{v(t)} \tag{2.4}$$

$$\tau(t) = \frac{V}{\dot{V}(t)} \tag{2.5}$$

In Equation 2.4, L is the length of the channel and $v(t)$ is the velocity of the fluid. In Equation 2.5, V is the volume of the channel and $\dot{V}(t)$ is the volumetric flow of the fluid. Equation 2.5 can also be written in terms of component mass m and mass flow rate $\dot{m}(t)$ according to Equation 2.6.

$$\tau(t) = \frac{m}{\dot{m}(t)} \tag{2.6}$$

From the above definitions, it is clear that the resident time τ is closely related to the flow fraction FF discussed previously. Therefore, in the implementation of resident times, the flow fraction is explicitly used to calculate the variable time delay and can be defined as Equation 2.7.

$$\tau(FF) = \frac{\tau_{nominal}}{FF(t)} \tag{2.7}$$

In Equation 2.7, $\tau(FF)$ is a variable delay expressed as a function of FF, $\tau_{nominal}$ is the resident time of the fluid at the nominal flow rate, and $FF(t)$ is the time-dependent flow fraction defined in Equations 2.4 and 2.5.

2.4.3 Point Kinetics

Disclosure - This section was originally published in an ANS Winter 2021 Transaction [18]. Subsequently, the text was modified and published as part of a journal article [16]. The text here is slightly modified to fit this publication.

The PKEs feature a system of time-dependent differential equations that encompass the power contribution of delayed neutrons emitted by FPs [26]. However, the traditional PKEs often used in modern reactor kinetics and dynamic analysis are derived for stationary fuel (i.e., such as LWR fuel). In the MSR designs under consideration, the primary salt simultaneously serves as both the fuel and the coolant and is pumped into and from the core vessel. Fuel salt circulation entails a special treatment of neutron flux, precursor drift, and decay in the PKEs.

Exact PKEs are derived by factorizing diffusion or transport equations into a purely time-dependent neutron population function, and space- and energy-dependent shape functions. PKEs are approximate equations derived by factorization of the Boltzmann equation by projecting the static adjoint [26]. However, due to the flowing nature of the fuel used in MSRs, flux cannot be completely factorized and perturbed

[27]. Therefore, point reactor kinetics cannot reconstruct some features associated with circulating fuel reactors [28]. As an alternative method, the approximated PKEs are modified to obtain a version of the PKEs, called modified Point Kinetics Equations (mPKEs), which accommodates the fuel salt flow and variable circulation rates [29, 30]. Due to the simplicity and flexibility of mPKEs, this method is generally used in MSR Dynamic Modeling [31]. This study aims to evaluate the influence of fuel circulation speed and delayed neutron precursor distribution on system reactivity. For simplicity, a Zero-Power Approximation (ZPA) is assumed, such that the temperature-induced reactivity feedbacks are taken to be zero.

Reactor kinetics is paramount to nuclear reactor design and safe operation. Neutrons are categorized as either prompt or delayed, according to the time at which they are generated relative to that of a fission reaction. Prompt neutrons are created within $\approx 10^{-14}$ s from fission, and initially possess an initial kinetic energy larger than its delayed counterparts, emanating from FP decays or (γ,n) reactions. The majority of delayed neutron production is assumed to occur through the former mechanism (FP decay). Relatively short-lived radioactive FPs yield (primarily through beta decay) excited daughter nuclei that stabilize by releasing neutrons (i.e., delayed neutron precursors).

Establishing a comprehensive inventory of fuel salt species at any moment within the time frame of reactor operation is not only computationally expensive but also unnecessary and tedious. Therefore, the delayed neutron precursors are grouped according to the time it takes to subsequently produce neutrons and calculated through experimental means [32].

PKEs establish the relationship between delayed neutrons and the neutron population in a given time. The PKEs compute the fractional neutron population density at a time, t, from a subsequent event. Expressions based on the Delayed Neutron Precursor (DNP) concentrations evaluate the contemporary precursor concentration from a previous fission event through the rates of production and decay.

PKEs are widely used in reactor kinetics and dynamics due to their simplicity. As such, MSR kinetics and dynamics analysis use PKEs. However, fuel recirculation implies a special mathematical treatment. Since DNPs travel with the flow of the fuel, the circulation removes neutron precursors from the core that decay within the external loop and thus do not contribute to the fission chain reaction. Therefore, the inflow of the aforementioned (previously described as the "outflow") fuel salt mass is less concentrated in DNPs and the wasted DNPs are modeled by a loss term. The fraction of precursors that return to the core region re-enters after some time, which is represented by an additional gain term.

The fuel circulation rate is susceptible to change due to events such as pump trips. As such, it is ideal to treat both precursor loss and gain as functions of the circulation rate. With the additional terms mentioned above, the PKEs are modified to account for the delayed neutron precursor drift, giving Equations 2.8 and 2.9 as:

$$\frac{\partial n(t)}{\partial t} = \frac{\rho(t) - \beta}{\Lambda} n(t) + \sum_{i=1}^{6} \lambda_i C_i + S(t) \tag{2.8}$$

$$\frac{\partial C_i}{\partial t} = \frac{\beta_i}{\Lambda} n(t) - \lambda_i C_i(t) - \frac{C_i(t)}{\tau_c} + \frac{C_i(t - \tau_l) e^{-\lambda_i \tau_l}}{\tau_c} \tag{2.9}$$

where n represents the fractional neutron population, i is the ith delayed precursor group, β is total delayed neutron fraction (that is, $\sum_{i=1}^{6} \beta_i$), Λ is the neutron generation time, S the external neutron source*, λ is the decay constant for a given DNP group, C is the concentration of DNPs, τ is the fuel residence times within the core (subscript c) and loop (subscript l), and the resultant reactivity of the system, $\rho(t)$, is given by:

$$\rho(t) = \rho_{external} + \rho_{feedbacks} + \rho_0, \tag{2.10}$$

$\rho(t)$ is comprised of external reactivity insertion (such as by a control rod movement), $\rho_{external}$, temperature induced reactivity feedbacks (equal to zero in ZPA), $\rho_{feedbacks}$,

*External neutron source is used for reactor startup [33].

and the compensation reactivity, ρ_0, for the reactivity lost due to fuel circulation, which is specific to circulating fuel reactors. Circulation of fuel salt around the primary loop removes DNPs from the active core, reducing its reactivity by ρ_0. Thus, to maintain the criticality of a circulating core, a positive compensatory reactivity insertion, equal to ρ_0, is required. This reactivity impact of fuel circulation during steady-state operation is obtained by setting time derivatives in the Equations 2.8 and 2.9 to zero and solving for ρ as:

$$\rho_0 = \beta - \sum_{i=1}^{6} \frac{\beta_i}{1 + \frac{1}{\lambda_i \tau_c}[1 - e^{-\lambda_i \tau_l}]} \tag{2.11}$$

Although Equation 2.8 is not altered by fuel circulation, the two rightmost terms in Equation 2.9 distinguish this set of coupled equations from the original PKEs, hence being deemed the mPKEs. The third and fourth terms of Equation 2.9 describe DNP drift from the core region and the subsequent reentry of surviving DNPs, respectively. The conventional PKEs are recovered from the mPKEs by considering the static fuel limit (i.e. $v = 0$) that forces both resident times τ to go to infinity. In the case of infinite circulation velocity, the DNPs are evenly spread throughout the primary loop.

Table 2.1 and Figure 2.2 show the relation between fuel circulation speed, v, and ρ_0 during steady state operation of an MSRE-like system. The nominal flow rate of MSRE is 0.2 m/s with corresponding core and loop transit times of 8.463 and 16.73 seconds, respectively.

The results given in Table 2.1 and Figure 2.2 demonstrate that the fuel flow rate profoundly affects ρ_0. The circulation velocity increases with ρ_0 until it reaches an asymptote. When the circulation velocity, v, is infinitely fast, the DNPs are uniformly distributed in the system, and the delayed neutron fraction born in the core region is proportional to the ratio of the volume of in-core salt out of the entire system volume; therefore the delayed neutron fraction is reduced to the fraction of fuel salt in-core, which can be expressed as $\tau_c/(\tau_c + \tau_l)$.

Table 2.1: Effects of Flow Velocity on Resident Times and ρ_0 in MSRE ($\beta = 0.0066$)

$v\,[ms^{-1}]$	τ_C	τ_L	ρ_0 [pcm]
0	$\lim_{v\to 0}\tau_C$	$\lim_{v\to 0}\tau_L$	0.000
0.1	16.93	33.46	186.4
0.2	8.463	16.73	246.5
0.5	3.385	6.692	322.8
10	0.1692	0.3346	429.6
∞	$\lim_{v\to\infty}\tau_C$	$\lim_{v\to\infty}\tau_L$	440.0

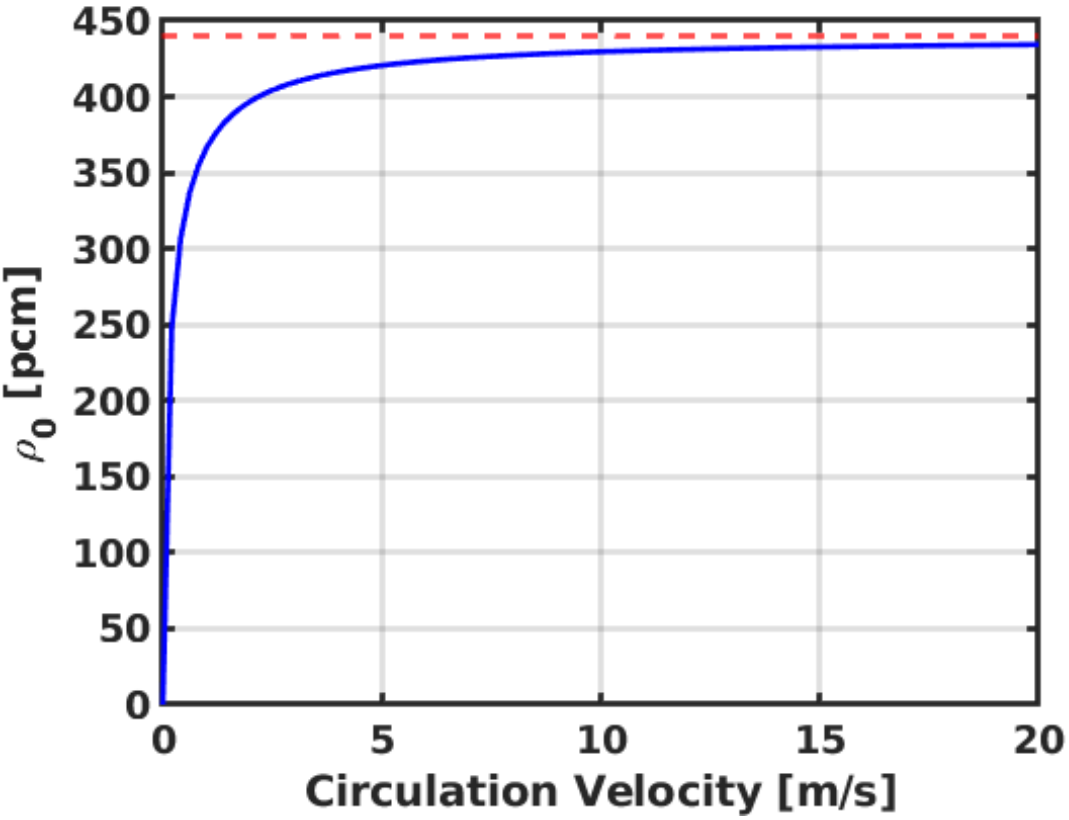

Figure 2.2: Reactivity lost due to circulation ρ_0 dependence on fuel circulation velocity v [16]

A concern that is specific to MSRs is that regarding the margin of reactivity between critical and super-prompt critical, usually expressed as 1 dollar, 1\$=β, and is modified by the circulation reactivity. This can be seen in Equation 2.8 term $(\rho(t)-\beta)$. As long as the term remains negative, the core is subcritical on prompt neutrons alone. However, with the influence of fuel circulation, the term becomes: $(\rho(t) + \rho_0 - \beta)$. This reduces the margin to super-prompt criticality by ρ_0. In conclusion, the dollar units of reactivity are dependent on the circulation speed such that $1\$ = (\beta - \rho_0)$, or, substituting in Equation 2.11, the dollar worth of reactivity can be expressed as:

$$1\$ = \sum_{i=1}^{6} \frac{\beta_i}{1 + \frac{1}{\lambda_i \tau_c}[1 - e^{-\lambda_i \tau_l}]}. \tag{2.12}$$

The dollar worth of reactivity as a function of circulation speed must be considered during the operation of MSRs.

It should be noted that in many MSR designs, such as LEU converters, the delayed neutron fraction β will evolve with burnup similar to that of LWRs. The amount of ^{239}Pu breeding contributes to fission, so β will correspondingly decrease due to β_{Pu239} being approximately a third of the value of β_{U235}.

An additional concern arises as a result of changes in circulation velocity. During standard operation and start-up, molten salts in the primary loop must flow at a nominal rate. This includes reactor start-up, where the core is kept subcritical via external negative reactivity insertion, insufficient fissile material, and/or higher core temperature. If the primary circulation pump trips, the flow will decrease to a final finite speed set by natural convection, and the quantity of heat transferred out of the primary fluid via parasitic heat loss, and heat removed by the decay heat removal system. However, the minimum convective flow speed will occur at low power. As the circulation rate is reduced, the more time the fuel salt spends in the external loop, which allows an increased number of DNPs to decay outside the core, thus increasing the reactor power.

Modified point kinetics is a simple, yet versatile approach to model spatially independent MSR neutronics over time. The delayed neutron precursor drift changes with flow velocity, which governs the delayed neutron fraction lost in transit. The deficit of delayed neutrons in MSRs fundamentally depends on the prompt neutrons to achieve and maintain criticality. The prompt dependence of neutrons gives rise to adverse effects regarding reactivity insertions during loss of fuel flow transients and effects compounded by depletion and poisonous FPs.

2.4.4 Decay Heat

Disclosure - This section was originally published as part of a journal article [13]. The text here is slightly modified to fit this publication.

Understanding decay heat production and removal is imperative to understand reactor transients as well as accident scenarios. Decay heat is especially important for MSRs to keep their fuel salt in the molten state for a period of time after shutdown. MSR temperature reactivity feedbacks are significant due to the large difference between their operating temperature and the liquidus temperature of the fuel salt, typically in the range of 200 to 300 K. Because of this, decay heat plays a significant role in delayed effects in transients.

Decay heat management is the main focus of reactor licensing. This focus emphasizes the need to maintain temperature at safe levels. In the case of MSRs, there may be a need not only to remove heat to prevent the volatilization of the salt component or structural material degradation but also to maintain a high enough temperature to maintain the state of the molten fuel. Therefore, a proper understanding of decay heat production and removal becomes a safety concern.

MSRs must worry about the freezing of the primary circuit. This can be addressed by heating elements surrounding the primary circuit. However, these heating elements are active components. Passive safety features are more desirable.

Unlike fission power, which is proportional to neutron population, decay heat is driven by FP inventory which depends on past fissions. Accounting for the production of decay heat with sufficient accuracy requires tracking the power history of the system. Prior modeling approaches ignored this dependency and simply added the decay heat into the fission heat without discernment. A decay heat model based on precursors is presented in this section.

Decay heat production is implemented using a lumped decay heat precursor model, analogous to the delayed neutron precursors in the point kinetics model. DNPs undergo decay and emit neutrons, decay heat precursors undergo decay, and release decay heat in various forms. The point kinetics model does not consider the decay of one neutron precursor group to another. Likewise, decays from one decay heat precursor group to another are not considered in the lumped decay heat precursor model.

Each group of decay heat precursors is described by a relative decay heat yield and a decay constant. The relative decay heat yield represents the amount of decay heat produced by each decay heat precursor group. This relation is represented by Equation 2.13,

$$dP_d/dt = \sum_{i=1}^{N} \left[n(t)/n_0 \ \delta_i - \lambda_i P_{d,i}(t) \right], \tag{2.13}$$

where N is the number of decay heat precursor groups (for this paper, 3); $n(t)/n_0$ is the relative neutron population; δ_i is the relative decay heat yield of the i^{th} group; and λ_i is the decay constant of the i^{th} group. Note that the neutron population is normalized for easy implementation in the modified point-kinetics model. As a result, the production of decay heat P_d is expressed as a dimensionless fraction $P_d = P_{decay}\,[\mathrm{MW}]\,/P_{nominal}\,[\mathrm{MW}]$.

This generic approach allows for great flexibility and can be implemented with various established decay heat standards, as well as with any preferred number of decay heat precursor groups.

Currently, there are no established decay heat standards for MSRs. Burn-up calculations can be used to generate an estimated decay heat curve for a specific reactor design, fuel salt composition, and processing approach. For demonstration of the methodology, the ANS94 standard [34] was used for the decay heat curve, and three decay heat precursor groups were used to fit this curve. The values of the parameters in Equation 2.13 are obtained with two assumptions.

The first assumption is that when the reactor is shut down, the decay heat precursors are no longer produced and only decay. Therefore, Equation 2.13 can be represented as Equation 2.14,

$$P_d^{shutdown}(t) = \sum_{i=1}^{N} P_{d,i}(0)\ e^{-\lambda_i t}, \tag{2.14}$$

where $P_{d,i}(0)$ is the power contribution from the group i immediately after shutdown and $P_d^{shutdown}$ is the decay heat production after shutdown. The second assumption is that the decay heat precursor groups are at equilibrium during steady-state full-power operation. In other words, the production of decay heat precursor groups is equal to their decay.

Using the first assumption, a summation of exponentials can easily be fit to a chosen decay heat standard, establishing the decay constants, λ_i, as well as the decay heat contribution, $P_{d,i}(0)$, of the exponential decay functions for the initial condition in the model. Specifically, in the three-group example and the ANS94 standard, the following Equation 2.15 is found by a parameter fit;

$$P_d^{shutdown}(t) = 0.0252\, e^{-0.0946\, t} + 0.0199\, e^{-0.00442\, t} + 0.0228\, e^{-8.61e{-}5\, t}. \tag{2.15}$$

Using the second assumption, the production parameters in the values of Equation 2.13, δ are calculated. Specific values of δ_i and λ_i obtained in the three-group model using the ANS94 standard [34] are shown in Table 2.2. This methodology can be used to characterize any design-specific decay heat curve.

The model presented assumes that the fuel salt is homogeneous. Consequently, the decay heat was deposited in all fuel salt nodes proportional to the node mass as an energy generation term and discussed in Subsection 2.4.9.

2.4.5 Flux Profiles

Flux profiles are essential for the design of nuclear reactors. During steady-state operations of a nuclear reactor, it is desirable to maintain a constant power profile throughout the reactor. Accurate predictions of flux profiles involve detailed calculations using mechanisms such as Monte Carlo. The flux profiles are required to understand the power distribution of a reactor. However, during the initial design phase of a reactor system, the information necessary to perform a detailed Monte Carlo calculation might not be available. As a first approximation, flux profiles can be approximated using methods such as solving diffusion equations for mono-energetic neutrons. The flowing nature of fuel in MSRs makes using diffusion approximation challenging for several reasons. The said challenges stem from fuel flow-dependent phenomena that cause drift of DNP with the flow and variations in the radial flow speed in the core. Most of the proposed thermal spectrum MSRs are designed with a core geometry close to a cylinder. In the modeling approach, it was assumed that the core of the reactor is a cylinder, and the mentioned flow-dependent phenomena are neglected to simply resolve the problem.

The modeling approach does not calculate the flux profile for internal use. However, a simple utility is included to calculate the flux profile through analytical solutions for diffusion approximation for a finite cylinder. The analytical solution for a finite cylinder can be obtained by considering individual 2-D geometries of a finite

Table 2.2: Parameters calculated for each decay precursor group

Group	δ Heat yield$[s^{-1}]$	λ Decay const.$[s^{-1}]$	$P_{d,i}(0)$ Initial cond.
1	0.0024	0.09453	0.02522
2	8.7763e-05	0.004420	0.01986
3	1.9596e-06	8.6098e-05	0.02276

cylinder, a circle, and a rectangle with the radius of the circle as the width. Therefore, normalized flux can be written as a function of r being the radial variable of radius R of the circle and z being the axial variable of height Z of the rectangle as,

$$\frac{\phi(r,z)}{\phi_0} = R(r)Z(z) \tag{2.16}$$

$$\frac{\phi(r,z)}{\phi_0} = J_0\left(\frac{2.405r}{\tilde{R}}\right)cos\left(\frac{\pi z}{\tilde{Z}}\right) \tag{2.17}$$

$$\tilde{R} = R + d \tag{2.18}$$

$$\tilde{Z} = Z + 2d \tag{2.19}$$

Where J_0 is the zero-order Bessel function, R is the radius, Z is the height, and d is the extrapolated length.

2.4.6 Temperature Reactivity Feedback

Disclosure - This section was originally published as part of a journal article [16]. The text here is slightly modified to fit this publication.

Understanding temperature reactivity feedback is essential for the safe operation of nuclear reactors since temperature reactivity feedback plays an important role in reactor kinetics and dynamics. The NRC requires all commercial power reactors designed and built in the United States to have prompt temperature feedback that is capable of compensating for rapid increases in reactivity [35]. Temperature reactivity feedback is an inherent property of materials and stems from mechanisms such as the Doppler effect and thermal expansion. The reactivity feedback response of Doppler broadening of resonance is immediate, unlike thermal expansion, which depends on the rate of thermal propagation within the material. SMD-MSR modeling approach

uses temperature feedback coefficients that encapsulate the feedback effects of both Doppler and thermal expansion. The temperature feedback coefficients used can be calculated using a neutron transport code such as SERPENT, MCNP, or SCALE. The temperature feedbacks of the individual fuel and graphite nodes are calculated using Equations 2.20 and 2.21.

$$\rho_{fb,F} = I_F \alpha_F (T_F(t) - T_{F,0}) \tag{2.20}$$

$$\rho_{fb,G} = I_G \alpha_G (T_G(t) - T_{G,0}) \tag{2.21}$$

Here, $\rho_{fb,F}$ and $\rho_{fb,G}$ are the temperature feedback of the fuel and graphite, respectively, and the subscripts F indicate the fuel while G indicates the graphite. I is the temperature importance of the node. α is the temperature feedback coefficient. $T(t)$ is the temperature of the node, while T_0 is the reference temperature of the node in the steady state of full reactor power. The total temperature feedback of the reactor, ρ_{fb} can be calculated by summing all individual temperature feedback as shown in Equation 2.22.

$$\rho_{fb} = \sum \rho_{fb,F} + \sum \rho_{fb,G} \tag{2.22}$$

2.4.7 Reactivity Effects from Fission Products

Disclosure - This section was originally published as part of a journal article [16]. The text here is slightly modified to fit this publication.

FP poisons have immediate and delayed effects on the reactor behavior. ^{135}Xe and ^{149}Sm are two of the most important FPs because of their large thermal neutron absorption cross-sections. Therefore, in the presented method, only ^{135}Xe and ^{149}Sm are explicitly modeled. It is difficult to accurately calculate the contribution of reactivity from each FP without a detailed neutronics calculation coupling. As an

alternative method, the reactivity feedback of ^{135}Xe and ^{149}Sm is calculated using the change of concentrations from the steady state concentration at full reactor power. Concentrations of ^{135}Xe and ^{149}Sm are calculated using modified Bateman equations to emulate MSR specific phenomena. The Bateman equation takes a form similar to Equation 2.23.

$$\frac{\partial C(t)}{\partial t} = \dot{R}_{production} - \dot{R}_{remove} \tag{2.23}$$

Here, $C(t)$ is the concentration, $\dot{R}_{production}$ and $\dot{R}_{remove}$ are the production and removal rates, respectively. FP poisons can be produced from direct fission and subsequent decay of a parent. Removal pathways include decay, neutron absorption, and migration out of the fuel salt. In MSRs, only the fuel salt that resides in the core region experiences a considerable neutron flux when operational. Therefore, a non-dimensional quantity that explicitly expresses the fraction of fuel salt volume residing in the core out of the total fuel salt inventory is introduced to production because of fission and loss because of absorption terms. The volume fraction can be expressed as $V_{(F,c)}/V_{(F,t)}$. Alternatively, the same quantity can also be denoted as a ratio of resident times as $\tau_c/(\tau_c + \tau_l)$ where τ_c is the core resident time and τ_l is the loop resident time. The concept of resident times and resident time modeling is explicitly discussed in Section 2.4.2.

The isotope ^{135}Xe is produced by fission or by subsequent beta decay of ^{135}I. The routes of production of ^{135} Xe are the same in solid- and liquid-fueled reactors. However, since ^{135}Xe is a noble gas, it is less likely to form chemical bonds and remain in the liquid fuel. This leads ^{135}Xe to nucleate into gas bubbles that can leave the liquid fuel and accumulate in free spaces or be removed by degassing methods such as sparging. The modeling of individual mechanisms of degassing methods is a complex topic that is beyond the scope of the presented study. For our purposes, the removal of ^{135}Xe through degassing is represented with a constant removal rate. With these

considerations, balanced equations for ^{135}Xe and its parent nuclides ^{135}Te and ^{135}I are shown in Equations 2.24, 2.25 and 2.26.

Unlike ^{135}Xe, ^{149}Sm is stable and soluble in fuel salt. As a result, the decay and degassing loss terms, which are necessary to characterize the concentration of ^{135}Xe, are not necessary to determine the concentration of ^{149}Sm. The nuclide ^{149}Sm is a direct FP [36] and is also produced as a result of the subsequent beta decay of ^{149}Pm. A system of equations for the accounting of ^{149}Pm and ^{149}Sm is set up as shown in Equations 2.27 and 2.28.

$$\frac{\partial N_{Te}(t)}{\partial t} = \gamma_{Te}\Sigma_F\phi(t)\frac{V_{(F,c)}}{V_{(F,t)}} - \lambda_{Te}N_{Te}(t) \tag{2.24}$$

$$\frac{\partial N_{I}(t)}{\partial t} = \gamma_{I}\Sigma_F\phi(t)\frac{V_{(F,c)}}{V_{(F,t)}} + \lambda_{Te}N_{Te}(t) - \lambda_{I}N_{I}(t) \tag{2.25}$$

$$\frac{\partial N_{Xe}(t)}{\partial t} = \gamma_{Xe}\Sigma_F\phi(t)\frac{V_{(F,c)}}{V_{(F,t)}} + \lambda_{I}N_{I}(t) - \lambda_{Xe}N_{Xe}(t) - \sigma_a^{Xe}\phi(t)N_{Xe}(t)\frac{V_{(F,c)}}{V_{(F,t)}} - \lambda_{gas}N_{Xe}(t) \tag{2.26}$$

$$\frac{\partial N_{Pm}}{\partial t} = \gamma_{Pm}\Sigma_F\phi(t)\frac{V_{(F,c)}}{V_{(F,t)}} - \lambda_{Pm}N_{Pm}(t) \tag{2.27}$$

$$\frac{\partial N_{Sm}}{\partial t} = \gamma_{Sm}\Sigma_F\phi(t)\frac{V_{(F,c)}}{V_{(F,t)}} + \lambda_{Pm}N_{Pm}(t) - \sigma_a^{Sm}\phi(t)N_{Sm}(t)\frac{V_{(F,c)}}{V_{(F,t)}} \tag{2.28}$$

Where, $N(t)$ is the number density $[\#atom\,cm^{-3}]$, γ is the fission yield, λ is the decay constant $[s^{-1}]$ and σ_a is the microscopic adoption cross-section $[cm^{-2}]$ of each isotope which is indicated by subscripts and superscripts Te, I, Xe, Pm and Sm. Σ_F is the macroscopic cross-section of the fuel $[cm^{-1}]$, ϕ is the average neutron flux of the core at full reactor power $[n\,cm^{-2}\,s^{-1}]$, $V_{(f,c)}/V_{(f,t)}$ is the ratio between the

fuel volumes in-core and ex-core, and λ_{gas} is the removal constant associated with degassing $[s^{-1}]$.

The modeling approach does not explicitly calculate the average neutron flux ϕ. Therefore, ϕ is calculated using the normalized neutron population shown in Section 2.4.3 as Equation 2.29.

$$\phi(t) = \phi_0 \frac{n(t)}{n_0} \tag{2.29}$$

Here, ϕ_0 is the average neutron flux across the core during full reactor power, and $n(t)/n_0$ is the normalized neutron population at t time.

In a steady state, the negative reactivity of poisons must be balanced [37]. Therefore, our modeling approach linearizes the reactivity effect of FP poison based on the steady-state absorption rate. As a result, when the FP poison concentration increases above the steady state value, the modeling approach treats the excess concentration as a negative reactivity insertion, and vice versa.

The magnitude of reactivity insertion is based on the amount of the neutron population that is absorbed by the FP poison in a steady state. The reactivity compensated is the population of neutrons absorbed by the FP at steady state divided by the neutron population that would have been absorbed into the fuel; similar to the calculation of the thermal utilization factor. The equation for the steady state reactivity of ^{135}Xe is given by Equation 2.30. [26, p.332] [38]

$$\rho_{Xe,0} = -\frac{\Sigma_{Xe(0)}}{\Sigma_{a,Fuel}} \tag{2.30}$$

Here, $\Sigma_{Xe(0)}$ is the macroscopic absorption cross-section of FP (in this case, ^{135}Xe) and $\Sigma_{a,Fuel}$ is the total macroscopic absorption cross-section of the fuel. Therefore, $\rho_{Xe,0}$ is represented as the ratio between the probability of neutron absorption in xenon and the probability of neutron absorption in fuel. The reactivity $\rho_{Xe,0}$ is where

we linearize the reactivity from the presence of ^{135}Xe. The reactivity at any given time t from ^{135}Xe is expressed by Equation 2.31.

$$\rho_{Xe}(t) = \rho_{Xe,0}\left(\frac{N_{Xe}(t)}{N_{Xe(t=0)}} - 1\right) \tag{2.31}$$

In Equations 2.30 and 2.31, we show the reactivity impact of ^{135}Xe. These equations are also applicable to other highly absorptive FP nuclides, specifically the ^{149}Sm.

2.4.8 Depletion Dependence

Disclosure - This section was originally published as part of a journal article [14]. The text here is slightly modified to fit this publication.

Nuclear fuel depletion affects core kinetics and dynamics by several means. Specifically, two phenomena related to the evolution of kinetic parameters are of interest: the evolution of the delayed neutron precursor terms and that of the effective neutron removal term.

A typical fresh fuel is LEU. As the fuel depletes, plutonium isotopes breed in and contribute to fissions. The delayed neutron fraction of the fission ^{239}Pu is only about a third of the delayed neutron fraction of the fission ^{235}U. Consequently, there is a reduction in the effective delayed neutron fraction β as such fuel depletes. With depletion also comes the production of FPs. Many of these isotopes are neutron absorbers. This will cause a neutron spectrum absorption hardening and reduce the neutron generation time Λ. Regardless of the details of the fuel cycle, unless the system is an equilibrium isobreeder with a time-independent depletion matrix, the delayed neutron fraction and the neutron spectrum will evolve with burnup.

The MSDR model uses mPKEs 2.8,2.9 coupled with linear temperature feedbacks, Equations 2.20 and 2.21 to model neutronics. Both parameters β and Λ drive the mPKEs. Second, changes in fuel absorption will also affect the core dynamic

temperature-reactivity feedbacks of fuel, α_f and graphite, α_g in Equations 2.20 and 2.21.

Discussion of the burnup evolution of the feedback coefficients is more complicated, design dependent, and beyond the scope of this discussion. It should be noted that each reactor concept must ensure that the coefficients remain sufficiently negative throughout the fuel cycle.

Similarly, the thermophysical characteristics of heat-transferring fluids and structural materials change due to changes in chemical composition, radiation damage, and material deposits on heat-transfer surfaces. Specifically, regarding the dynamic model parameters, the density and heat capacity of the fuel salt, as well as the heat transfer coefficients of the primary heat exchanger, are expected to evolve with burnup. Depletion has profound effects on the dynamic nature of the reactor system. The accounting for how these changes affect the dynamic behavior of the system is important during the preliminary engineering stage to ensure that the transient behavior of the proposed reactor system is safe for the entire planned operational period.

It is computationally expensive to accurately deplete the core during a transient, in particular for a system dynamic simulation; it is also unnecessary. The transient duration is very short compared to the depletion timescale. Therefore, the difference in radionuclides present in the fuel salt is small as a consequence of the transient as compared to steady-state depletion. The exemptions are highly absorptive reactivity-relevant isotopes of ^{135}Xe and ^{149}Sm, which are explicitly handled by the dynamic model.

These considerations lead to an effective temporal factorization of the problem into transient time and depletion time, where the parameters dependent on depletion are precalculated prior to transient evaluation. The transient is then executed at a particular time along the fuel cycle, and the depletion-dependent parameters are kept constant during the transient. The presented model uses precalculated neutronics

data to describe the depletion dependence of neutron generation time, DNP group values β_i, DNP group decay constants λ_i, fuel and moderator temperature reactivity feedbacks α_{fuel} and $\alpha_{graphite}$. These parameters can be calculated using neutron transport codes with depletion capability such as SCALE, VERA, or Serpent for the nuclear reactor under investigation. For the scope of this work, depletion data was obtained directly from ORNL [39] for a MSDR model that covers a period of 10 years of continuous operations. The same data set was used in a Modelica-based dynamic modeling environment developed by ORNL, TRANSFORM to model MSDR [40]. These parameters are shown in Figure 2.3. The data set itself can be found in the GitHub repository and contains all depletion-dependent neutronics parameters of importance except for DNP group decay constants. Changes in precursor group decay constants were found to be negligible during the operating cycle of 10 years.

Neutronics data calculated from a transport code are saved as a structured table along with the depletion timeline in a text file. The model uses a MATLAB script that reads the text file with the depletion data and interpolates them. The parameter file then uses these interpolated neutronics data to initialize the model to the user-specified depletion point in order to simulate the desired transient.

The evolution of thermophysical parameters during depletion, such as the heat capacity and conductivity of the fuel salt, the viscosity and density of the fuel salt, and the heat conductivity across heat exchangers and between the fuel salt and the graphite moderator, can be treated in the same manner as in our model. However, the dependence of these parameters on depletion is currently not known, design-dependent, and difficult to establish. Presumably, significant experimental and theoretical research efforts by the respective MSR vendors will be needed to establish these parameter dependencies. Therefore, the presented model does not change these parameters, though extending the model to include them is trivial.

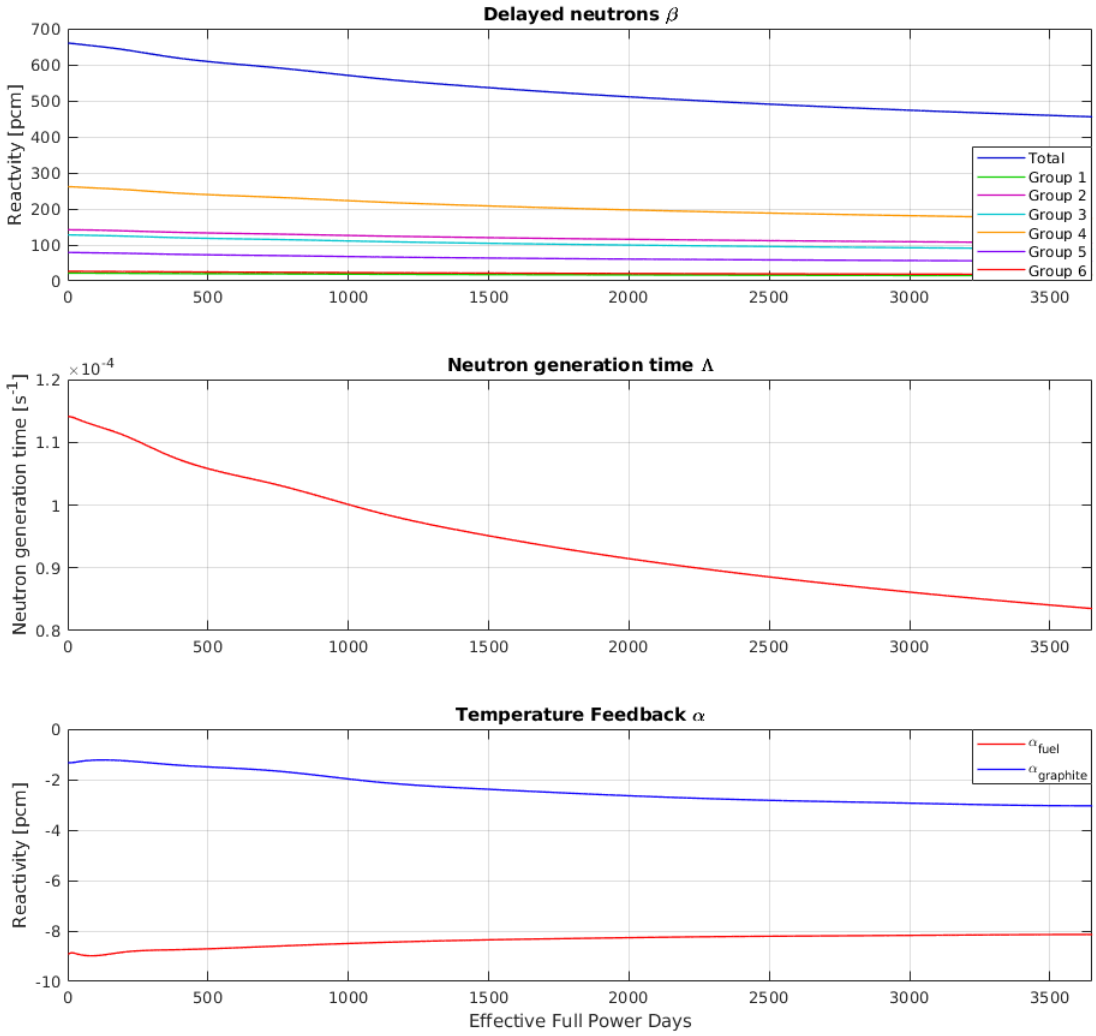

Figure 2.3: Depletion dependency of point kinetics parameters, effective delayed neutron fractions β (top), generation time Λ (middle); and reactivity temperature feedbacks α (bottom) [14]

2.4.9 Heat Generation

The primary purpose of nuclear power reactors is to produce heat energy through nuclear fission, which can be converted into other forms of energy, such as electricity. Nuclear fission reactors produce heat by several different means, such as fission and the decay of FPs. Fission reactions release large amounts of heat, and the exact amount depends on the specific nuclear fission reaction. For example, thermal fission of ^{235}U produces approximately 210 MeV energy. Unlike popular understanding, fission energy is not produced in the form of heat. Fission produces FPs, additional neutrons, and gamma radiation. Most of the energy of fission energy is distributed among the FPs and neutrons in the form of kinetic energy, which is ultimately turned into the heat energy of fuel, moderator, and structural material as a result of particular collisions. The gamma radiation produced also subsequently produces heat in the material due to radiation interactions. Fission heat is directly proportional to the neutron flux, as discussed in Section 2.4.5. Since the flux profile of a nuclear reactor in a steady state is a spatial distribution, fission heat is also spatially distributed. For purposes of modeling in SMD-MSR it was assumed that 93% of the fission heat is produced in the fuel that resides in the core and only 7% is generated in the graphite of the core. The spatial effects of the generation of fission heat and the dependence of the material are captured by a non-dimensional fraction, which is defined in Equation 2.32. The fission heat generated at a considered node is calculated using Equation 2.33.

$$k_{fission} = k_{spacial} k_{material} \tag{2.32}$$

$$\dot{Q}_{fission,gen} = k_{fission} \dot{Q}_{fission} \tag{2.33}$$

Here, $k_{fission}$, $k_{spcaial}$ and $k_{material}$ are non-dimensional fractions that capture the overall fraction of fission heat produced in the node, fraction of fission heat produced

in the designated node based on location and fraction of heat produced based on material. $\dot{Q}_{fission,gen}$ is the fission heat generated at the node considered and $\dot{Q}_{fission}$ is the total fission heat.

Unlike fission heat, decay heat is produced due to the decay of FPs as discussed in Section 2.4.4. In the modeling approach of SMD-MSR it was assumed that the decay heat precursors are evenly distributed throughout the fuel. Therefore, the decay heat generated in a considered fuel node is proportional to the volume of the node and can be written as Equation 2.34.

$$\dot{Q}_{decay,gen} = \dot{Q}'''_{decay} V_{node} \tag{2.34}$$

Here, $\dot{Q}_{decay,gen}$ is the decay heat generated in the fuel node considered. $\dot{Q}'''_{decay}$ is the volumetric generation of decay heat, and V_{node} is the volume of the fuel node.

Calculating volumetric decay heat $\dot{Q}'''_{decay}$ can be done using the decay heat precursor method shown in Section 2.4.4, the nominal reactor power $P_{nominal}$, and the total fuel volume $V_{f,total}$. However, the calculation of the total fission heat $\dot{Q}_{fission}$ requires some additional considerations. When the reactor is at nominal power, the sum of total fission heat $\dot{Q}_{fission}$ and total decay heat $\dot{Q}_{decay}$ must be equal to the nominal power of the reactor. Meanwhile, the normalized neutron population n/n_0 should be equal to 1 when the reactor is at nominal power. It is intuitive that the fission power is directly proportional to the total fission power. However, if we multiply the nominal reactor power by the normalized neutron population n/n_0 to obtain the total fission power $\dot{Q}_{fission}$, the total power would exceed the nominal reactor power by the amount of total decay power. Since the normalized total decay power P_{decay} at nominal reactor power is known from calculations done in Section 2.4.4 we can adjust the proportionality constant between the normalized neutron population n/n_0 and the total fission power $\dot{Q}_{fission}$.

$$\dot{Q}'''_{decay} = \frac{P_{decay}(t) P_{nominal}}{V_{f,total}} \tag{2.35}$$

$$\dot{Q}_{fission} = (1 - P_{decay}) P_{nominal} \left(\frac{n(t)}{n_0} \right) \tag{2.36}$$

Here, $P_{decay}(t)$ is the time-dependent normalized decay heat calculated from the decay heat precursor method, P_{decay} is the normalized decay heat at full reactor power, and $n(t)/n_0$ is time-dependent normalized neutron population.

2.4.10 Conduction Heat Transfer

Conduction is the transfer of heat through matter without discrete movement of particles. It is the dominant mode of heat transfer within solids and occurs as a result of temperature gradients. When there is a temperature gradient in a material, heat is transmitted from high-temperature regions to low-temperature regions by propagating atomic and molecular vibrations. In the modeling approach of SMD-MSR, such conduction between solid nodes is ignored. However, conduction within fluid nodes is considered to expand simulation capabilities where the fluid flow rate is zero. When a fluid stagnates in a confined area, it experiences conduction similar to that of a solid. Since the SMD-MSR nodalization does not consider spatial discretization, the resistive analogue of heat conduction is applied to the fluid nodes instead of Fourier's law. The resistive analogue to conduction assumes that heat conduction behaves similarly to that of Ohm's law which can be written as shown in Equation 2.37.

$$V = IR \tag{2.37}$$

Here, V is the voltage, I is the current, and R is the resistivity. According to Ohm's law, the current I is the flow due to the potential difference of V against resistance R. The same analogy can be applied to conduction considering the

potential difference V as the temperature difference, the current I as the heat flow rate and the resistance R as the thermal resistance. The implementation of conduction in the model can be illustrated as shown in Figure 2.4.

Figure 2.4 shows a node with length L and having a cross-sectional area of A_c and thermal resistivity of R_{TH}. The node experiences a temperature difference (ΔT) that drives heat conduction through the node. Using the previously discussed Ohm's law analog, the heat flow rate due to conduction can be expressed by Equation 2.38.

$$\dot{Q} = \frac{T_{in} - T_{out}}{R_{TH}} \tag{2.38}$$

$$R_{TH} = \frac{L}{A_c k} \tag{2.39}$$

Where $\dot{Q}$ is the heat flow rate, T_{in} and T_{out} are the temperature of the node inlet and outlet and R_{TH} is the thermal resistivity of the node. The thermal resistivity of the node can be calculated according to the Equation 2.39, where k is the conductivity of the fluid in the node.

2.4.11 Convective Heat Transfer

Convection is the primary mechanism by which heat transfer occurs between fluids and solid surfaces. Like conduction, convection is driven by temperature gradients. However, unlike conduction, convection is closely related to fluid behavior. Since the SMD-MSR modeling approach does not consider momentum balances, some characteristics of convection cannot be accurately modeled. The modeling approach is limited to modeling forced convection. Phenomena such as free convection need additional physics modules that are not implemented in the presenting iteration of SMD-MSR. Figure 2.5 shows a representation in which convection occurs between a fluid node and a solid node.

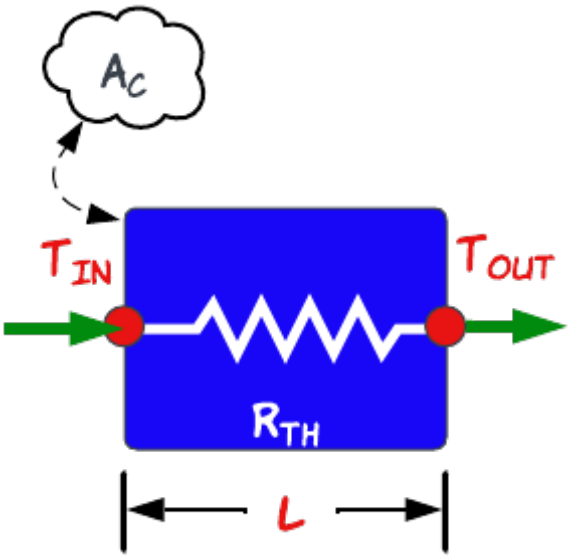

Figure 2.4: Depiction of conduction in a fluid node

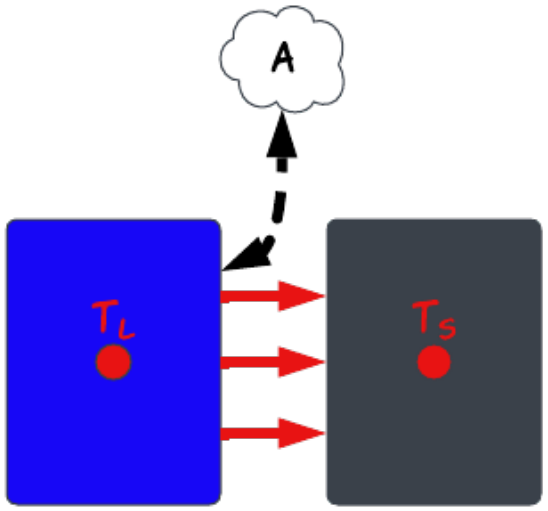

Figure 2.5: Depiction of convection between a fluid node and a solid node

The interface between the fluid node and the solid node has an effective heat transfer area A. The temperature of the fluid node is T_L and the temperature of the solid node is T_S. Using Newton's cooling law, which can be written as shown in Equation 2.40.

$$\dot{Q} = hA(T_L - T_S) \tag{2.40}$$

Here, $\dot{Q}$ is the convection heat transfer rate and h is the heat transfer coefficient. Heat transfer coefficient is a variable dependent on the flow behavior and geometry of the flow channel.

2.4.12 Radiation Heat Transfer

Radiation heat transfer is a mode of heat transfer that transports heat through electromagnetic radiation and does not require a medium. Radiation heat transfer is minimal when the absolute temperature of the object in question is low. However, MSRs operate at temperatures around 900 K where radiation heat transfer is significant. In the modeling approach, a simple radiation heat transfer model is included to approximate radiation heat transfer-related phenomena. Thermal radiation is characterized by the Stefan-Boltzmann law. The law states that the rate of heat transfer from the surface of a black body is proportional to the fourth power of the absolute temperature. Stefan-Boltzmann law can be written as Equation 2.41.

$$\dot{Q} = \sigma A T^4 \tag{2.41}$$

In Equation 2.41, $\dot{Q}$ is the heat transfer rate due to thermal radiation, σ is the Stefan-Boltzmann constant, A is the effective surface area of thermal radiation and T is the absolute temperature of the body.

Although Equation 2.41 is valid for black bodies, materials used in nuclear reactors cannot be considered black bodies. Additionally, the reactor components

are surrounded by other bodies that emit thermal radiation. Figure 2.6 illustrates a node that experiences thermal radiation, which has an absolute temperature of T_N and an effective heat transfer area of A. In the figure, the surrounding is represented by a green circle and has an absolute temperature of T_∞. Taking into account the incoming thermal radiation from the surrounding and surface effects, Equation 2.41 can be modified by adding two additional terms and can be written as Equation 2.42.

$$\dot{Q} = \sigma \epsilon A (T_N^4 - T_\infty^4) \tag{2.42}$$

In Equation 2.42, ϵ is the emissivity, which is a corrective factor that accounts for the surface effects.

2.4.13 Mann's Model of Heat Transfer

Mann's model heat transfer is a nodal heat transfer scheme that is done to simplify heat transfer between a solid surface and a liquid. This method allows one to reduce the number of total nodes required to represent a solid-liquid interface. Reducing the number of nodes in a component reduces the number of variables and equations that must be solved. This method explicitly involves convective heat transfer. The Mann model can be illustrated as shown in Figure 2.7.

Figure 2.7 shows a cluster of three nodes. Two fluid nodes are colored blue with labels $L1$ and $L2$, while the solid node is colored gray with the label S. The combined effective areas of convection heat transfer of the liquid-solid interfaces are A_{L1} and A_{L2}. The fluid with temperature T_{IN} enters the first node from the bottom. When the fluid passes through the first node, its temperature changes to T_{L1} and enters the second fluid node. The fluid exits the second node at temperature T_{L2}. Although both the first and second fluid nodes are in contact with the adjacency solid node, only the first node temperature T_{L1} communicates with the solid node temperature T_S for convective heat transfer. Assume that heat transfer only involves fluid flow

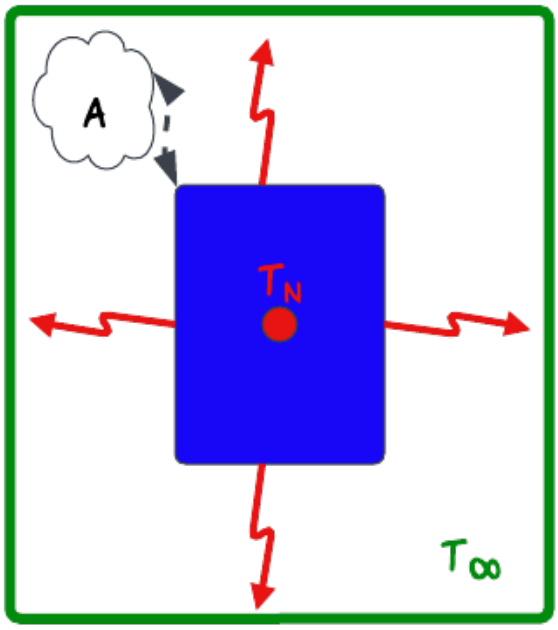

Figure 2.6: Depiction of radiation in a node

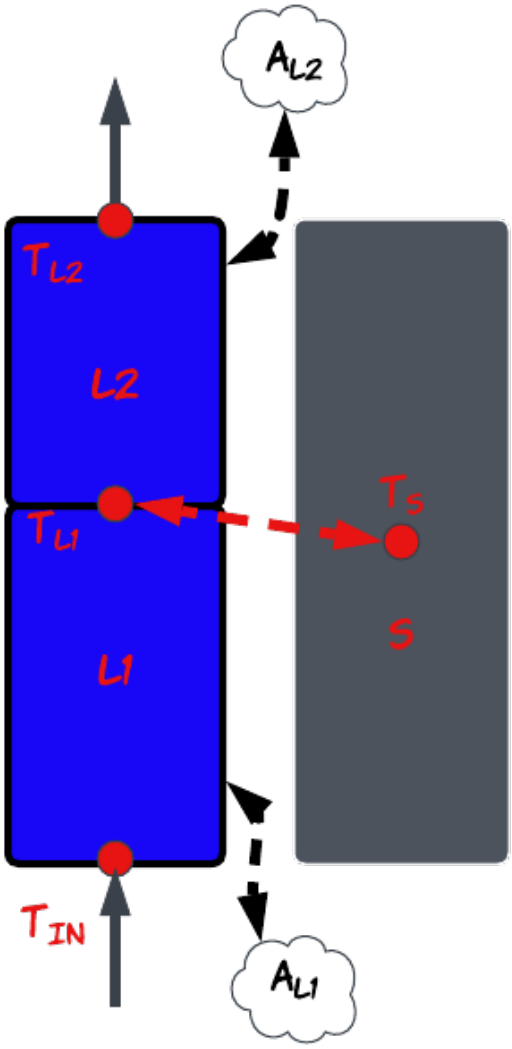

Figure 2.7: Depiction of Mann's Model Heat Transfer

and convection; Equations 2.43, 2.44, and 2.45 can be written to balance the heat in each node.

$$\dot{Q}_{N1} = \dot{Q}_{in,flow,L1} - \dot{Q}_{out,flow,L1} - \dot{Q}_{conv,L1:S} \tag{2.43}$$

$$\dot{Q}_{N2} = \dot{Q}_{in,flow,L2} - \dot{Q}_{out,flow,L2} - \dot{Q}_{conv,L2:S} \tag{2.44}$$

$$\dot{Q}_{S} = \dot{Q}_{conv,L1:S} + \dot{Q}_{conv,L2:S} \tag{2.45}$$

The convective terms of Equations 2.43, 2.44, and 2.45 can be expanded by applying the expansion shown in Sub-Section 2.4.11 and written as Equations 2.46 and 2.47.

$$\dot{Q}_{conv,L1:S} = h_{L1} A_{L1} (T_{L1} - T_S) \tag{2.46}$$

$$\dot{Q}_{conv,L2:S} = h_{L2} A_{L2} (T_{L1} - T_S) \tag{2.47}$$

Here, h_{L1} and h_{L2} are heat transfer coefficients. The Mann's model is suitable to use in situations where the interface solid is highly conductive. In such scenarios, the high conductivity of the solid eliminates the requirement of high fidelity of modeling in the solid side.

In the SMD-MSR implementation, heat transfer coefficients h_{L1}, h_{L2} and the areas A_{L1} and A_{L2} are lumped. The user can choose to separate the terms when appropriate or to increase the number of Mann model clusters axially. Lumping of heat transfer coefficients and heat transfer areas is done by introducing non-dimensional fractions, which determine the ratio between areas of each liquid node. These ratios are introduced to ease the model development process when sufficient design data is unavailable. The total effective area of convection between two liquid nodes and the

solid node can be expressed as $A = A_{L1} + A_{L2}$. Using the non-dimensional fraction corresponding to each liquid node, $kHT1$ and $kHT2$ both areas can be written as Equations 2.48 and 2.49. By this treatment, two heat transfer coefficients can be reduced to one by calculating the average heat transfer coefficient for the considered axial section.

$$A_{L1} = \frac{kHT1}{kHT1 + KHT2} A \tag{2.48}$$

$$A_{L2} = \frac{kHT2}{kHT1 + KHT2} A \tag{2.49}$$

2.4.14 Channel Node Cluster

Channels are modeled using the clusters of nodes of the Mann's model determined in Section 2.4.13. Additional heat transfer physics were introduced and integrated to expand the modeling capabilities and utility. In LWRs the moderator, which doubles as the coolant, flows around the fuel rods. However, in the thermal spectrum MSR the fuel doubles as the heat removal medium flows through the moderator in the channels. The fuel channel geometry in MSRs is design-dependent. Regardless of the design, all molten salt channels require several basic considerations during modeling. Some special design features may require additional considerations, but for the purposes of this discussion, a generic form similar to that used in the MSRE is considered. The fuel channel node cluster used in the modeling approach is illustrated in Figure 2.8.

In Figure 2.8, two fuel nodes $F1$ and $F2$ are illustrated in light blue, and the graphite node G is depicted in gray. Fuel flows through the channel at a rate of $\dot{m}$ and enters the fuel node $F1$ from the bottom with temperature T_{in} and moves upward through two fuel nodes. The fuel nodes $F1$ and $F2$ are at temperatures T_{F1} and T_{F2}, respectively. The temperature of the graphite node G is T_G. The fuel nodes $F1$ and $F2$ have effective convection heat transfer areas $A_{F1:G}$ and $A_{F2:G}$, respectively,

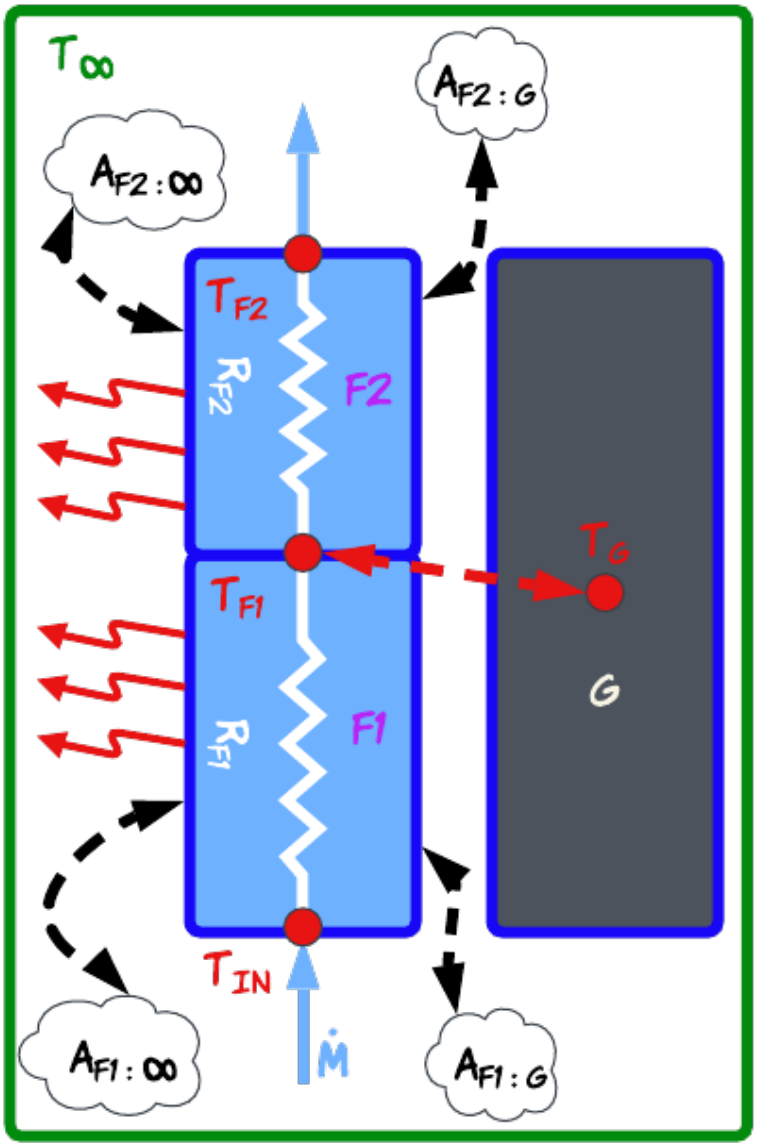

Figure 2.8: Depiction of Channel Node Cluster

between the graphite node. The internal conductive resistances of the fuel nodes are denoted by R_{F1} and R_{F2}. It was assumed that the fuel channel experiences radiation heat transfer. The effective radiative heat transfer areas of the fuel nodes are $A_{F1:\infty}$ and $A_{F2:\infty}$. The ambient temperature is represented by the green oval that has temperature T_∞. Fission heat generation is represented by the blue border at each node, and it was assumed that only the fuel nodes experience decay heat. When considering all heat transfer modes, Equations 2.50, 2.51, and 2.52 can be written to calculate the internal heat of each node.

$$\dot{Q}_{F1} = \dot{Q}_{flow,F1} - \dot{Q}_{cond,F1} - \dot{Q}_{conv,F1} - \dot{Q}_{rad,F1} + \dot{Q}_{gen,F1} \tag{2.50}$$

$$\dot{Q}_{F2} = \dot{Q}_{flow,F2} - \dot{Q}_{cond,F2} - \dot{Q}_{conv,F2} - \dot{Q}_{rad,F2} + \dot{Q}_{gen,F2} \tag{2.51}$$

$$\dot{Q}_{G} = \dot{Q}_{conv,F1} + \dot{Q}_{conv,F2} + \dot{Q}_{gen,G} \tag{2.52}$$

Individual terms in Equations 2.50, 2.51, and 2.52 can be expanded as explained in Sub-Sections 2.4.10, 2.4.11, 2.4.12, and 2.4.13.

2.4.15 Heat Exchanger Node Cluster

The heat exchanger node cluster is an extended version of the channel node cluster. The heat exchanger node cluster is intended to be used in components where two fluids flow on both sides of a solid where heat transport between two fluids is facilitated by the solid divider. Heat exchangers are vital components of any energy conversion system. As such in MSRs, heat exchangers are used to transfer heat between working fluids without mixing them. In MSRs, heat exchangers can be found between each loop. For use in SMD-MSR a simple counter flow heat exchanger cluster with five individual nodes was constructed. The five node cluster is illustrated in Figure 2.9.

Here, two nodes on the left, depicted in light blue, nodes $P1$ and $P2$ make up the shell side where the primary fluid flows at a mass flow rate of $\dot{m}_P$. Two nodes on the right, illustrated in green, $S1$ and $S2$ represent the tube side through which the secondary fluid flows at a mass flow rate of $\dot{m}_S$. The middle node, M in gray, represents the tube wall between the primary fluid and the secondary fluid. The primary fluid enters the shell side at a temperature of $T_{in,P}$ from the bottom, while the secondary fluid enters the tube side from the top at a temperature of $T_{in,S}$. The convection heat transfer interfaces between the shell and the tube are $A_{P1:M}$ and $A_{P2:M}$. The peripheral areas of the shell that transmit radiation heat are $A_{P1:\infty}$ and $A_{P2:\infty}$. The tube metal node M and the secondary fluid inside the tube have convective heat transfer areas $A_{S1,M}$ and $A_{S2,M}$. The nodes $P1$ and $P2$ on the side of the shell have internal thermal resistivity of R_{P1} and R_{P2} while the nodes $S1$ and $S2$ on the tube side have thermal resistances of R_{S1} and R_{S2}, respectively. Furthermore, the fuel salt, which resides in the shell side, produces decay heat. The decay heat generation is discussed in Section 2.4.9. Taking into account all modes of heat transfer and generation, balanced Equations 2.53, 2.54, 2.55, 2.56, and 2.57 can be written.

$$\dot{Q}_{P1} = \dot{Q}_{flow,P1} - \dot{Q}_{cond,P1} - \dot{Q}_{conv,P1} - \dot{Q}_{rad,P1} + \dot{Q}_{gen,P1} \tag{2.53}$$

$$\dot{Q}_{P2} = \dot{Q}_{flow,P2} - \dot{Q}_{cond,P2} - \dot{Q}_{conv,P2} - \dot{Q}_{rad,P2} + \dot{Q}_{gen,P2} \tag{2.54}$$

$$\dot{Q}_{M} = \dot{Q}_{conv,P1} + \dot{Q}_{conv,P2} \tag{2.55}$$

$$\dot{Q}_{S1} = \dot{Q}_{flow,S1} - \dot{Q}_{cond,S1} + \dot{Q}_{conv,S1} \tag{2.56}$$

$$\dot{Q}_{S2} = \dot{Q}_{flow,S2} - \dot{Q}_{cond,S2} + \dot{Q}_{conv,S2} \tag{2.57}$$

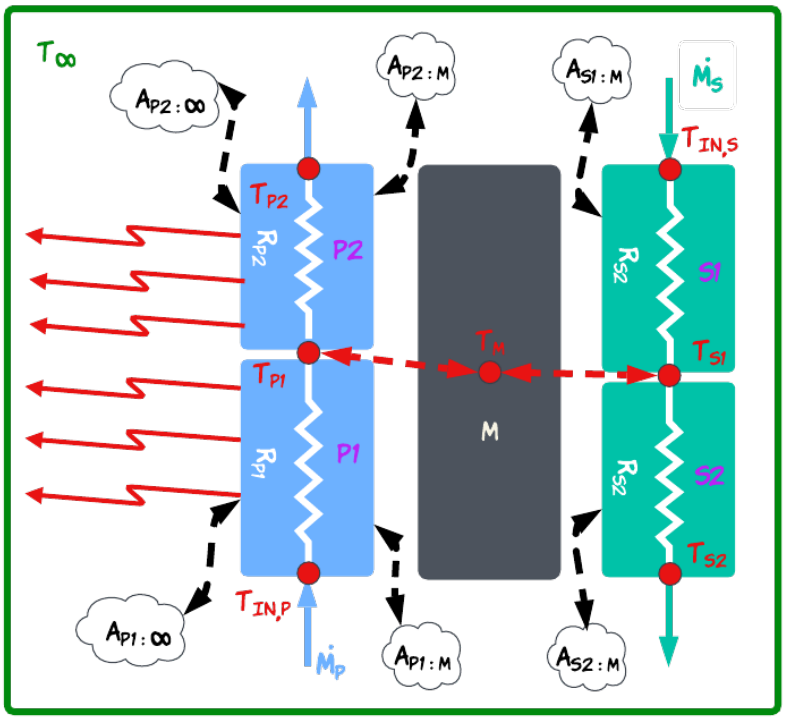

Figure 2.9: Depiction of Heat Exchanger Node Cluster

2.4.16 Mixing Nodes

Mixing nodes are fluid volumes that allow two or more fluid streams to mix in a prescribed volume. The mixing of fluid streams is assumed to be ideal within the mixing node; therefore, there are no temperature gradients. A mixing node with four inlet streams is illustrated in Figure 2.10.

Here, the mixing node is depicted in light blue. Four separate liquid streams with mass flow rates $\dot{m}_1$, $\dot{m}_2$, $\dot{m}_3$ and $\dot{m}_4$ that enter from the bottom of the node with inlet temperatures $T_{in,1}$, $T_{in,2}$, $T_{in,3}$ and $T_{in,4}$, respectively. The mixing node has an internal thermal resistance of R_{MN}. The four fluid streams mix within the mixing node and exit at a mass flow rate of $\dot{m}_{out}$ with a temperature of T_{MN}. The mixing node is exposed to the ambient temperature of T_∞; therefore, it experiences radiation heat transport through the external surface area of $A_{MN:\infty}$. Convection heat transfer between the node and ambient temperature is ignored to remove design dependencies. The heat balance of the mixing node can be expressed as Equation 2.58.

$$\dot{Q}_{MN} = \dot{Q}_{flow} - \dot{Q}_{cond} - \dot{Q}_{rad} + \dot{Q}_{gen} \tag{2.58}$$

In Equation 2.58, $\dot{Q}_{MN}$ is the rate of change in internal energy within the mixing node. The terms $\dot{Q}_{flow}$, $\dot{Q}_{cond}$, and $\dot{Q}_{rad}$ are the rates of change of energy due to flow, conduction, and radiation, respectively. $\dot{Q}_{gen}$ is the rate of energy generation at the node due to phenomena such as decay heat. The rates of the terms of energy change can be explicitly expressed as shown in Sections 2.4.10, 2.4.12, and 2.4.9. Some special treatments are required to terms involving flow and conduction due to the presence of multiple fluid inflow streams. The flow term can be expanded as Equation 2.59 to be expressed in terms of fluid inflow $\dot{Q}_{flow,in}$ and outflow $\dot{Q}_{flow,out}$. The inflow term can be expanded further as shown in Equation 2.60, where $\dot{Q}_{flow,1,in}$, $\dot{Q}_{flow,2,in}$, $\dot{Q}_{flow,3,in}$, and $\dot{Q}_{flow,4,in}$ are the energy rate gains of the mixing node due to the respective fluid flows. If we consider an arbitrarily mixing node, with n flowing fluid inflow, the term

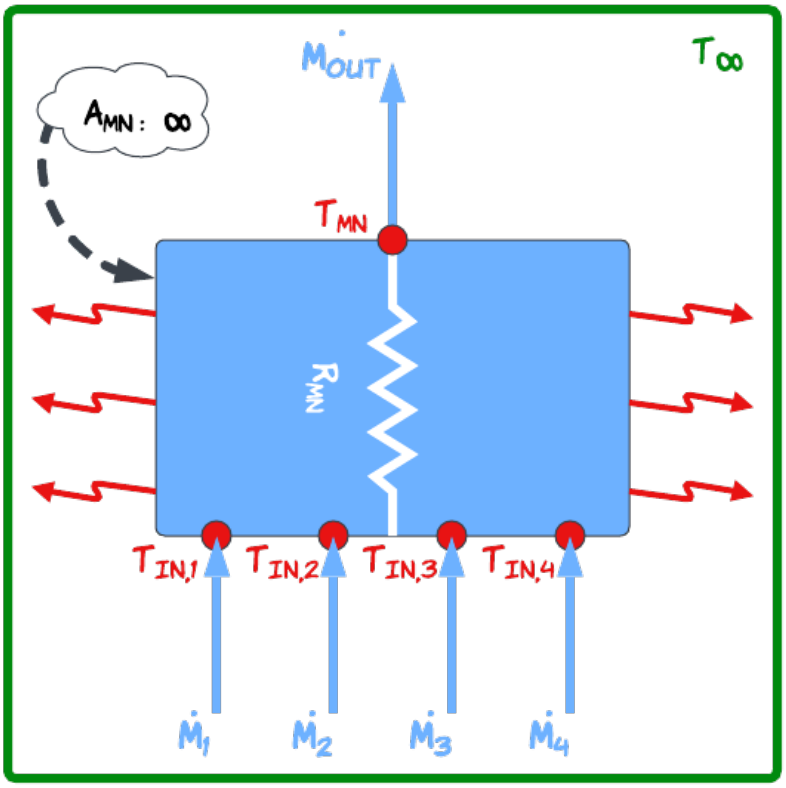

Figure 2.10: Depiction of Mixing Node

$\dot{Q}_{flow,in}$ can be further simplified as in Equation 2.61. Calculating the energy outflow rate is straightforward when the principle of mass conservation is applied. The sum of the mass flow rates of all inputs should be equal to that of the mass flow outlet, as shown in Equation 2.62. To calculate the rate of energy conduct, the average temperature of all inflow streams is calculated and used as the inlet temperature of the node.

$$\dot{Q}_{flow} = \dot{Q}_{flow,in} - \dot{Q}_{flow,out} \tag{2.59}$$

$$\dot{Q}_{flow,in} = \dot{Q}_{flow,1,in} + \dot{Q}_{flow,2,in} + \dot{Q}_{flow,3,in} + \dot{Q}_{flow,4,in} \tag{2.60}$$

$$\dot{Q}_{flow,in} = \sum_{i=1}^{n} \dot{Q}_{flow,i,in} \tag{2.61}$$

$$\dot{m}_{out} = \sum_{i=1}^{n} \dot{m}_{in,i} \tag{2.62}$$

2.4.17 Units

The Modelica language allows the user to define quantities along with their associated units and limits. Models can be checked in the OMEdit before compiling them into a simulation to test the balance of the units of written equations. If there are unit inconsistencies, the compiler prints out warnings and specifies the error. This is useful during model development and integration. Therefore, a unit package is implemented with the SMD-MSR specifying all units used throughout the modeling framework. The unit package also specifies limits and types of quantities. Specified limits include the applicable minimum and maximum values associated with a quantity. The specification of type declares whether the associated quantity is an integer, a real, or a complex number. For example, the quantity length should be expressed as a real number in units of meters and has the smallest physical value of zero. During

model execution, warnings are printed if the variables violate specified quantity limits. Although limit violations do not cause the simulation to fail, these warnings can be used to further investigate and debug the modeling approach.

2.4.18 Ports and Connectors

The SMD-MSR toolkit includes a package of ports and connectors. This package includes all required associated connector types. Modelica language supports potential and flow variables in each connector; however, this feature is not used due to the signal flow-based architecture of the SMD-MSR modeling approach. For clarity, the connector symbols for the inputs and outputs are represented with circles with and without filling, respectively, as shown in Figure 2.11.

2.4.19 QA Toolbox

Disclosure - This section was originally published as part of a journal article [15]. The text here is slightly modified to fit this publication.
Implementation validations of the SMD-MSR Modelica package are performed using the Quality Assuarance (QA) toolbox. The QA toolbox is a sub-package that resides within the main package of SMD-MSR Modelica. The QA toolbox package contains specialized models designed to test functionalities of both physics and component models located within the Nuclear and Heat Transfer packages and has inputs and outputs for construction of test cases for both physics and component models. Test cases can be done at several levels of complexities and with or without certain physics couplings, allowing modeling errors to be isolated and easily identified. These test cases are comprised of toy problems that will have simple analytical or obvious solutions.

The individual physics and component model test cases are summarized in Table 2.3. Basic test cases can verify the proper implementations and functionality of an individual model. The inputs, test conditions, to the model are chosen in a

Figure 2.11: Generalized icon style for input and output ports.

Table 2.3: Basic Test Cases used for Model Verification [15]

Model	**Test Conditions**	**Qualifying Results**
mPKE	$\rho_{fb} = 0$ $f_p = 1$	$n/n_0 = 1$
Decay Heat (ANS94)	$n/n_0 = 1$	$P_{decay} = 0.068$
	$n/n_0 = 0$	P_{decay} fits ANS 94
Temp. Feedback	$T_{in,N} = T_{set,N}$	$\rho_{fb} = 0$
Poison	$n/n_0 = 1$	$\Delta\rho_{poison} = 0$
Fuel Channel	$f_p = 1$ $n/n_0 = 0$ $P_{decay} = 0$ $T_{in} = T_{out}$	All node temps are equal
PHX	$f_p = 1$ $f_s = 1$ $P_{decay} = 0$ $T_{in,p} = T_{out,p}$ $T_{in,s} = T_{out,s}$	All node temps are equal
SHX	$f_p = 1$ $f_s = 1$ $T_{in,p} = T_{out,p}$ $T_{in,s} = T_{out,s}$	All node temps are equal
Radiator	$f_p = 1$ $T_{in} = T_{out}$	All node temps are equal
DHRS	$f_p = 1$ $t_{DHRS} = 0$ $\mathrm{P}_{Decay} = 0$ $\mathrm{T}_{in} = \mathrm{T}_{out}$	$P^{max}_{DHRS} = 0$
Pipe	$f_p = 1$ $P_{Decay} = 0$	$T_{in} = T_{out}$
UHX	$f_p = 1$ $t_{UHX} = 0$	$T_{in} = T_{out}$

manner that provides an obvious solution. For example, the mPKE module is tested with zero feedback ($\rho_{fb} = 0$) and with a nominal primary flow fraction ($f_p = 1$). Regardless of the speed of circulation, the mPKE module should produce a relative neutron population of 1 ($n/n_0 = 1$) as a test result. The dynamic decay heat model is adapted to follow the ANS94 decay heat standard. The decay heat model can be tested in two steps. In the first step, when the relative neutron population is 1 ($n/n_0 = 1$), the output of the decay heat model should be the maximum decay heat fraction during nominal operations, which is 6.8% of nominal power ($P_{decay} = 0.068$). In the second test, the relative neutron population is set to 0 ($n/n_0 = 0$) and the output decay heat should agree with the post-shutdown ANS94 decay heat curve. In the next test case, the temperature feedback model is tested by making the input temperatures equal to the set temperatures of the respective nodes ($T_{in,N} = T_{set,N}$). When the input temperatures of the feedback model are equal to the set temperature points, the temperature feedback should be 0 ($\rho_{fb} = 0$).

The poison model consists of the tracking of the concentration of five isotopic species, ^{135}Te, ^{135}I, ^{135}Xe, ^{149}Pm and ^{149}Sm. For this test case, the initial conditions are calculated for steady-state concentrations at full power operations. Therefore, the model can be tested using the full power relative neutron population ($n/n_0 = 1$). The concentrations should remain in the initial steady state, and therefore the reactivity feedback from a change in poison concentration should be zero ($\Delta\rho_{poison} = 0$).

For the rest of the components included in the list, the fuel channel, Primary Heat Exchanger (PHX), Secondary Heat Exchanger (SHX), radiator, Decay Heat Removal System (DHRS), pipe, and Ultimate Heat Exchanger (UHX), are tested for the continuity of equations by connecting the respective output temperatures of the model to the input temperatures of the model while maintaining nominal flow fractions and no heat depositions. Testing individual component models in this fashion yields equal temperatures across all nodes in the considered model.

Multiple components and physics couplings can be tested using several strategies, such as heat balances. These strategies can be implemented to varying degrees of complexity. The Test Input-Ouput (TestIO) sub-package residing within the QA toolbox can be used to make physics decoupling by set parametric values that resolve to an obvious solution. Figures 2.12 and 2.13 are some basic examples of such test model constructions using defined model blocks. Figure 2.12 is a composite model that tests the implementation and proper functionality of the PHX model beyond the basic tests previously enumerated in Table 2.3. In this test scenario, the fuel salt, FLiBe+UF_4, and the secondary salt, FLiBe, are used as primary and secondary salts, respectively, in PHX. The decay heat deposition was set to 0 MW and both flow fractions were set to nominal ($f_p = f_s = 1$). Constant heat production and constant heat removal blocks are used on both sides of the PHX model to deposit and remove equal amounts of heat. The PHX node temperatures will reach a steady state as the PHX model converges, confirming the proper implementation and functionality of the model.

The same strategy can be used to test a multi-loop system in which multiple heat exchangers and/or components are involved. Using the same principle, a composite test model can be set up for the reactor, as shown in Figure 2.13. Heat is produced in the fuel channel through both dynamic fission and decay heating. The heat deposited in the fuel channel is removed by the constant heat removal block. Coupling the fuel channel heat transfer model with the mPKE model through linear temperature feedback will result in a nominal reactor power equal to that of constant heat removal. Similar to the PHX heat balance test, the fuel channel node temperatures will reach a steady-state value.

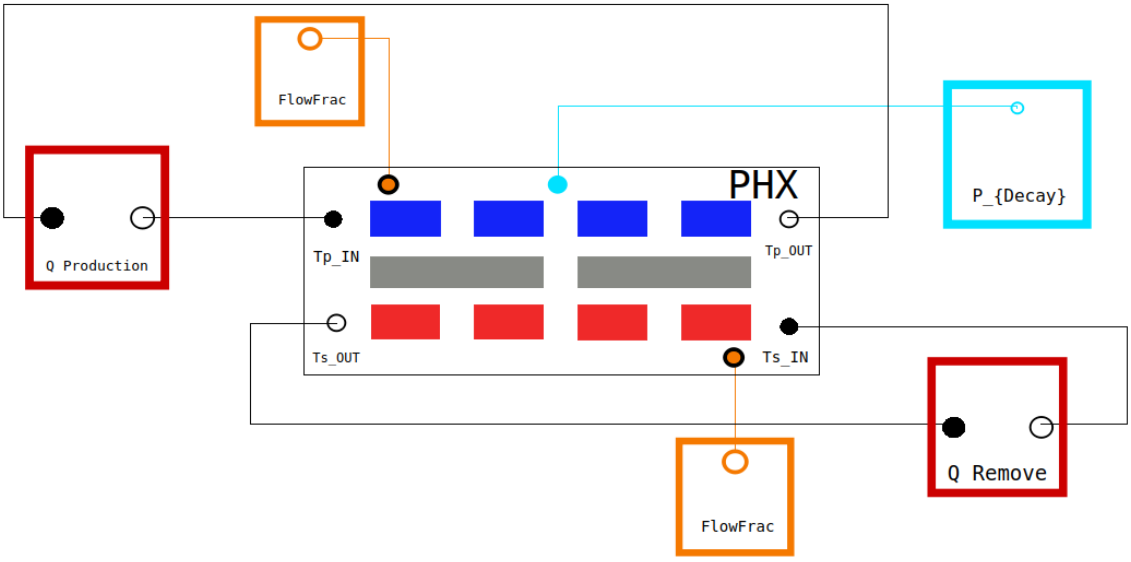

Figure 2.12: PHX Heat Balance Test [15]

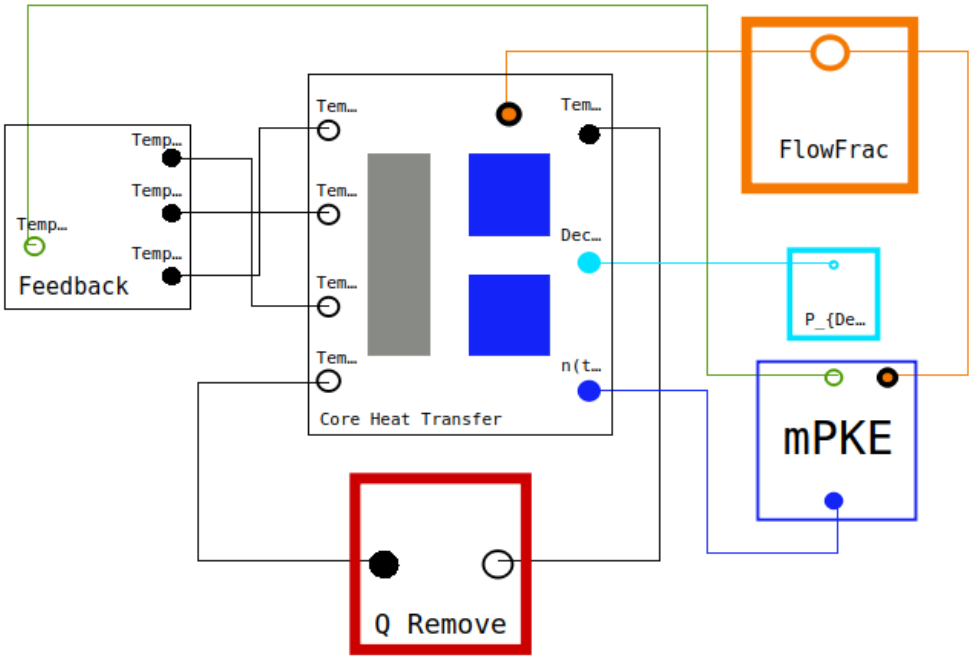

Figure 2.13: Reactor Heat Balance Test [15]

2.5 Component Models

This section aims at documenting commonly used generic component models created with the detailed methodology of Section 2.4. This section presents the component icon, input, and output ports. All input parameters associated with the component are also documented along with a general description of the parameter. Parameter conditions and units are not included in the parameter description, since they are indicated in the model itself and can be seen during model construction using the compiler. Further, there are additional component models in the toolkit that are not documented here. These additional components are created using several generic components to create an application-specific component.

2.5.1 Point Kinetics

Composite model of PKE calculates normalized neutron population n/n_0. The model works for stationary and recirculating fuels. It uses PKEs described in Section 2.4.3 to calculate the normalized neutron population n/n_0. Variable flow rates are allowed and the implementation of variable flow rates is explained in Section 2.4.2. PKE model has a single output and four inputs. The output of the model is the normalized neutron population n/n_0. Four inputs are external reactivity ρ_{ext}, independent neutron source strength S, reactivity feedback ρ_{fb}, and fuel flow fraction FF_f. PKE model icon is shown in Figure 2.14. In the Figure 2.14, the top four solid circles are the input ports. When looking from the left, the input ports are external reactivity ρ_{ext} (black), independent neutron source strength S (magenta), reactivity feedback ρ_{fb} (green) and fuel flow fraction FF_f (green). The bottom hollow circle is the output port of the calculated normalized neutron population n/n_0 (blue). The parameters of the PKE model are listed in Table 2.4.

Figure 2.14: PKE model icon view

Table 2.4: PKE model parameter summary

numGroups	=	number of DNP groups
LAMBDA	=	mean neutron generation time
beta	=	DNP group fractions
lambda	=	DNP group decay constants
nomTauCore	=	nominal fuel resident time incore
nomTauLoop	=	nominal fuel resident time excore
n_0	=	initial nominal neutron population
addRho0	=	add rho_0 for circulation correction switch

2.5.2 Decay Heat

The decay heat model calculates the normalized decay heat $\dot{Q}_{decay}$. The modeling approach of the decay heat model is described in Subsection 2.4.4. The decay heat model has one input and one output. The input is normalized neutron population n/n_0 and the output is normalized decay heat $\dot{Q}_{decay}$. The icon of the decay heat model is shown in Figure 2.15. In the Figure 2.15, the top solid circle is the input port of the normalized neutron population n/n_0 (blue) and the bottom hollow circle is the output port, normalized decay heat $\dot{Q}_{decay}$. Decay heat model parameters are summerized in Table 2.5.

2.5.3 Temperature Feedback

The feedback model calculates the temperature feedback of the individual fuel and graphite nodes and sums them up to produce the total temperature feedback of a region ρ_{fb} as documented in Subsection 2.4.4. The temperature feedback model has three inputs and one output. The inputs are the temperatures of two fuel nodes T_{F1}, T_{F2}, and the temperature of the graphite node T_G in a core region. The single output is the total temperature feedback from the core region ρ_{fb}. The icon of the temperature feedback model is shown in Figure 2.16. In the Figure 2.16, the top solid red circles are the input ports. The input ports when moving from left are the temperature of the fuel node 1 T_{F1}, the temperature of the fuel node 2 T_{F2}, and the temperature of the graphite node T_G. The output port is the hollow green circle at the bottom, the total temperature feedback of the region rho_{fb}. Model parameters of the feedback model are shown in Table 2.6.

2.5.4 Sum Reactivity

The sum reactivity is a block that sums multiple reactivity inputs to produce a single output. The block can handle any number of inputs. OMEdit prompts a pop-up when

Figure 2.15: Decay heat model icon view

Table 2.5: Decay heat model parameter summary

numGroups	=	number of decay heat precursor groups
DHYG	=	decay heat yield per group per fission
DHlamG	=	decay heal precursor group decay constant

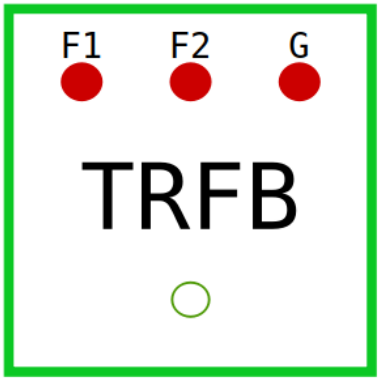

Figure 2.16: Temperature feedback model icon view

Table 2.6: Temperature feedback model parameter summary

aF	=	fuel temperature feedback coefficient
aG	=	graphite temperature feedback coefficient
IF1	=	fuel node 1 importance
IF2	=	fuel node 2 importance
IG	=	graphite node importance
TF1_0	=	fuel node 1 temperature setpoint
TF2_0	=	fuel node 2 temperature setpoint
TG_0	=	graphite node temperature setpoint

wires are connected to the input. The order of inputs in this case is irrelevant, because regardless of the connection order block only produces a single summed output. The sum reactivity block icon is shown in Figure 2.17. The top solid green circle is the input port where all reactivities that need to be summed are connected. The bottom hollow green circle is the summed reactivity output. Sum Reactivity block parameter is listed in Table 2.7.

2.5.5 Power Block

The power block calculates the total fission power $\dot{Q}_{fission}$ and the volume-specific decay heat $\dot{Q}'''_{decay}$ as shown in Section 2.4.9. The power block has two inputs as well as two outputs. Two inputs are for normalized neutron population and normalized decay heat. Figure 2.18 shows the power block icon view. Two solid circles on the top starting from the left are input ports for the normalized neutron population (blue) and normalized decay heat (cyan). Two output plots are at the bottom and are represented by hollow circles. Starting from the left (dark purple), the first hollow circle is the total fission power, while the next one (light purple) is the volume-specific decay power. Power Block parameters are listed in Table 2.8.

2.5.6 Core Region

The core region model is a composite model that is used to represent heat transfer in a single core region of a reactor core. The core region model inherits the partial model described in Section 2.4.14. The core region model icon is shown in Figure 2.19. The model has four inputs and three outputs. From top to bottom, the input ports are fission heat FH (dark purple), volume-specific decay heat DH (light purple), fuel flow fraction FF (orange) and region inlet fuel temperature T_In (red). From top to bottom, the output ports are the fuel node 2 temperature T_FN2, the graphite node temperature T_G, and the fuel node 1 temperature T_FN1. The model parameter of the core region is summarized in Table 2.9.

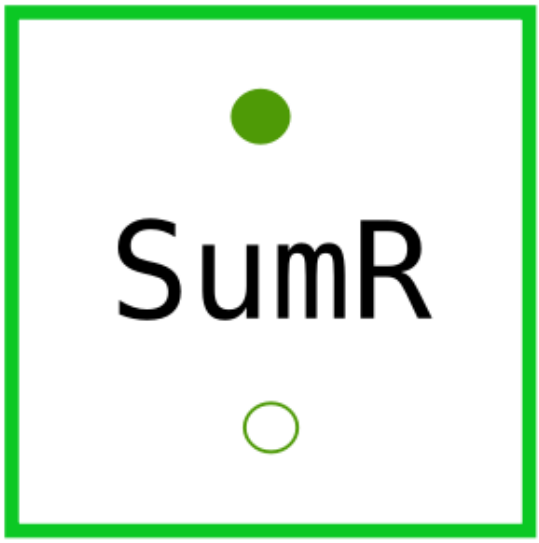

Figure 2.17: Sum reactivity block icon view

Table 2.7: Sum feedback model parameter summary

numInput	=	number of inputs

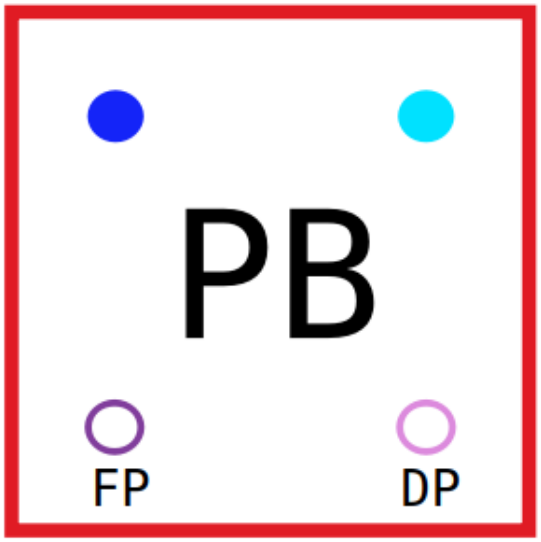

Figure 2.18: Power block icon view

Table 2.8: Power block model parameter summary

P	=	nominal reactor power
TotalFuelVol	=	total fuel volume

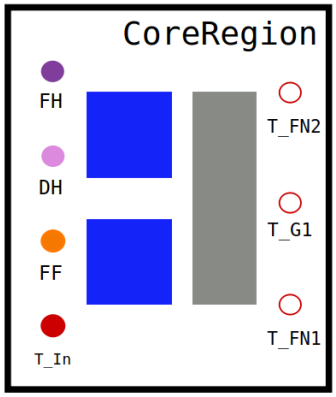

Figure 2.19: Core region model icon view

Table 2.9: Core region model parameter summary

vol_FN1	=	volume of fuel node 1
vol_FN2	=	volume of fuel node 2
vol_GN	=	volume of graphite node
rho_fuel	=	density of fuel
rho_grap	=	density of graphite
cP_fuel	=	heat capacity of fuel
cP_grap	=	heat capacity of graphite
Vdot_fuelNom	=	volumetric flow rate of fuel
kFN1	=	fraction of fission heat deposited in fuel node 1
kFN2	=	fraction of fission heat deposited in fuel node 2
kG	=	fraction of fission heat deposited in graphite
hAnom	=	convection between fuel and graphite
kHT_FN1	=	fraction of convection fuel node 1:graphite
kHT_FN2	=	fraction of convection fuel node 2:graphite
TF1_0	=	fuel node 1 initial temperature
TF2_0	=	fuel node 2 initial temperature
TG_0	=	graphite node initial temperature
regionFlowFrac	=	fuel flow fraction of the region
KF	=	fuel salt conductivity
Ac	=	cross-sectional flow area of fuel salt
LF1	=	length of fuel node 1
LF2	=	length of fuel node 2
OuterRegion	=	outer region switch
ArF1	=	outer surface area of fuel node 1
ArF2	=	outer surface area of fuel node 2
e	=	emissivity
Tinf	=	ambient temperature

2.5.7 Mixing Pot

The mixing pot model is an extension of the mixing node detailed in Section 2.4.16. The model icon is shown in Figure 2.20. The model has three input ports and one outlet port. Three input ports are on the left side of the icon, while the outlet port is located on the right side of the icon. The input ports are volume-specific decay heat DH, input temperatures T_In, and flow fractions FF. The input ports T_In and FF are expandable. Temperatures and their corresponding flow fractions must be connected to the correct input number of the expansion. When a connection is made, OMEdit prompts a dialogue asking for the input number. The parameters of the mixing pot model are summarized in Table 2.10.

2.5.8 Salt to Salt Heat Exchanger

The heat exchanger model is a composite model that uses two units of the partial heat exchanger cluster described in Section 2.4.15. The heat exchanger model is designed to model counterflow heat exchangers. The primary side is assumed to be the shell side where the fuel salt is flowing, while the secondary side is the coolant side with coolant. The primary and secondary sides cannot be used interchangeably in this model because decay heat is deposited only on the primary side and only the primary side is assumed to experience radiation heat transfer. The heat exchanger icon is shown in Figure 2.21. The heat exchanger model has five inputs and two outputs. Three of these inputs are for the primary side, while two are for the secondary side. The inputs of the primary side are the input temperature of the primary side Tp_IN, the primary flow fraction FFp, and the decay heat DH. The inputs on the secondary side consist of the secondary inlet temperature Ts_IN and the secondary flow fraction FFs. Model outputs are for the primary side outlet temperature Tp_OUT and the secondary side outlet temperature Ts_OUT. The heat exchanger model parameters are summarized in Table 2.11.

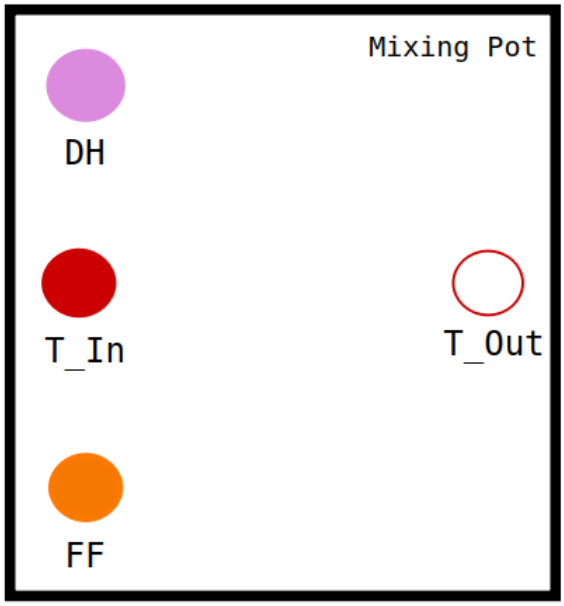

Figure 2.20: Mixing pot model icon view

Table 2.10: Mixing pot model parameter summary

numStreams	=	number of streams connected to inlet
vol	=	volume of mixing pot
vDotNom	=	volumetric flow rate
rho	=	average density of fluid
cP	=	average heat capacity of fluid
K	=	average thermal conductivity of fluid
Ac	=	cross-sectional area of mixing pot
L	=	length of the mixing pot
Ar	=	outer surface area of mixing pot
e	=	emissivity of outer surface
T_0	=	initial temperature of mixing pot
Tinf	=	ambient temperature

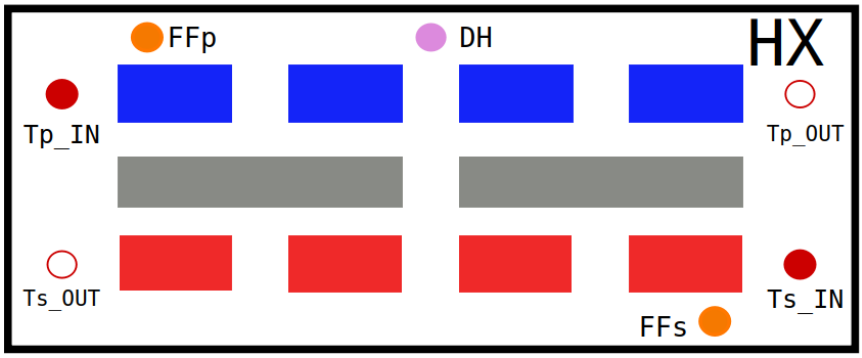

Figure 2.21: Heat exchanger model icon view

Table 2.11: Heat exchanger model parameter summary

vol_P	=	volume of primary side
vol_T	=	volume of metal tubes
vol_S	=	volume of secondary side
rhoP	=	density of primary side
rhoT	=	density of metal tubes
rhoS	=	density of secondary side
cP_P	=	heat capacity of primary side
cP_T	=	heat capacity of metal tubes
cP_S	=	heat capacity of secondary side
VdotPnom	=	nominal volumetric flow rate of primary side
VdorSnom	=	nominal volumetric flow rate of secondary side
hApNom	=	convection of primary side to tube
hAsNom	=	convection of tube to secondary side
TpIn_0	=	initial inlet temperature of primary side
TpOut_0	=	initial outlet temperature of primary side
TsIn_0	=	initial inlet temperature of secondary side
TsOut_0	=	initial outlet temperature of secondary side
Kp	=	conductivity of primary side
Ks	=	conductivity of secondary side
Ac_P	=	cross-sectional flow area of primary side
Ac_S	=	cross-sectional flow area of secondary side
Lp	=	length of primary side
Ls	=	length of secondary side
Ar_P	=	outer surface area of primary side
e	=	emissivity
Tinf	=	ambient temperature

2.5.9 Salt to Air Radiator

The radiator is a composite model where heat is transferred from salt to air. The model is an extension of the partial convection model described in Section 2.4.11. The model does not explicitly account for the tube. Therefore, the model utilizes an overall heat transfer coefficient. The model has two nodes. The primary side is the tube side, while the secondary side is the air side. The radiator model has four inputs and one output. The radiator icon is shown in Figure 2.22. Four inputs are on the top of the icon and are the secondary input temperature $TsIN$, the secondary flow fraction FFs, the primary input temperature $TpIN$, and the primary flow fraction FFp. The primary temperature output is located at the bottom. The secondary inlet temperature $TsIN$ and the secondary flow fraction FFs are designed to accept external functions. The use of external functions allows the user to perform transients driven by the air side perturbations. The radiator model parameters are tabulated in Table 2.12.

2.5.10 Ultimate Heat Exchanger

The UHX is a composite model that removes heat based on an external function. The model has three inputs and one output. The UHX model icon is shown in Figure 2.23. Three inputs are the primary side flow fraction FF, the primary side input temperature, and the input for the power removal function. The primary side outlet temperature is the only output. This model can be used instead of a radiator when sufficient information is not available to design a radiator. Since the heat removal of the model is based on a user-defined function, it provides flexibility to perform transients where the transient is driven by the ultimate heat removal rate of the system. Furthermore, this model can be used during model development in conjunction with the presented QA toolbox in Section 2.4.19 to ensure that individual heat producing components function accurately. The UHX model parameters are summarized in Table 2.13.

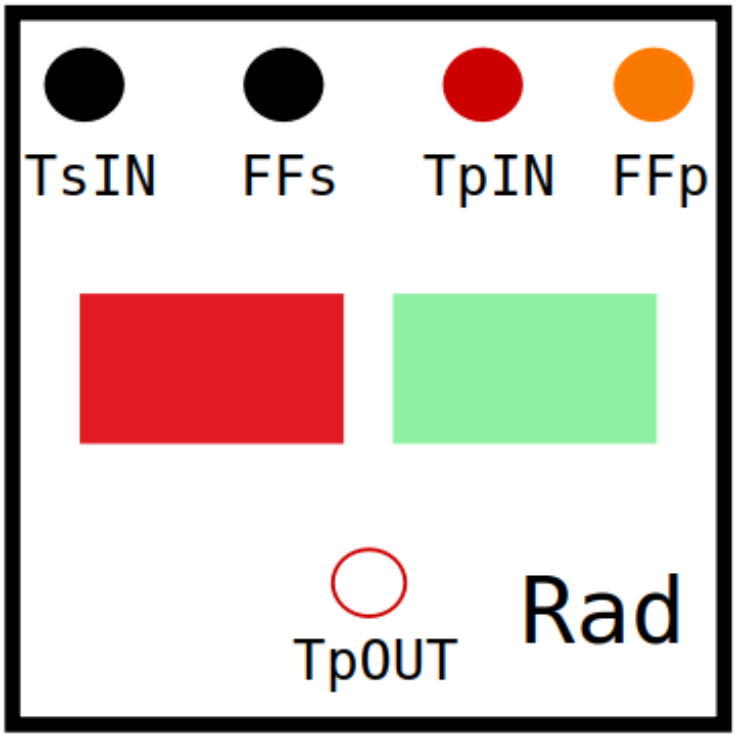

Figure 2.22: Radiator model icon view

Table 2.12: Radiator model parameter summary

vol_P	=	volume of primary side
vol_S	=	volume of secondary side
rhoP	=	density of primary side
rhoT	=	density of metal tubes
cP_P	=	heat capacity of primary side
cP_T	=	heat capacity of metal tubes
VdotPnom	=	nominal volumetric flow rate of primary side
VdorSnom	=	nominal volumetric flow rate of secondary side
hAnom	=	convection from primary side to secondary side
TpIn_0	=	initial inlet temperature of primary side
TpOut_0	=	initial outlet temperature of primary side
TsIn_0	=	initial inlet temperature of secondary side
TsOut_0	=	initial outlet temperature of secondary side

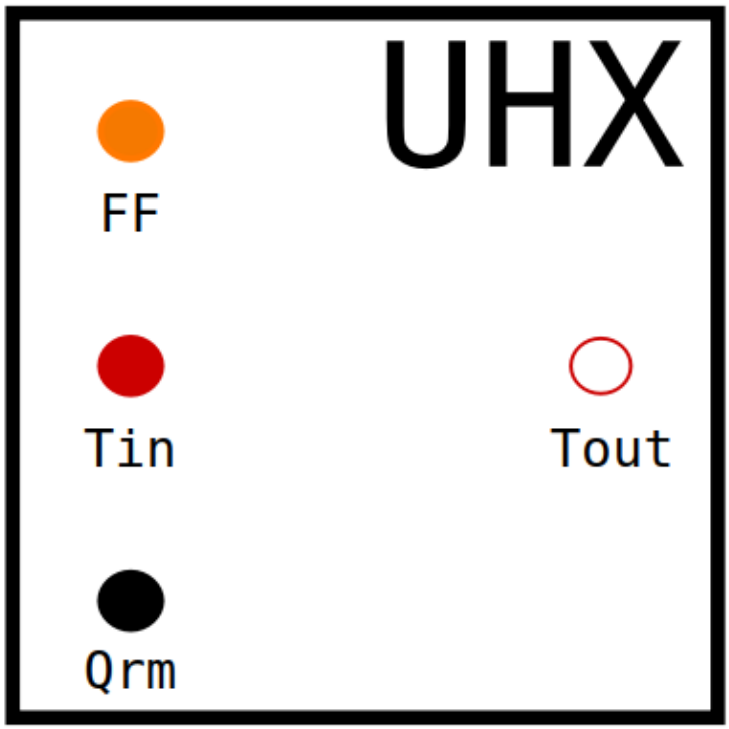

Figure 2.23: Ultimate heat exchanger model icon

Table 2.13: Ultimate heat exchanger model parameter summary

P	=	power to be removed
vol	=	volume of fluid node
rho	=	density of fluid
cP	=	specific heat capacity of fluid
vDotNom	=	nominal volumetric flow rate of fluid

2.5.11 Decay Heat Removal System

The DHRS is a modified heat removal component based on the UHX. Power removal is based on a modified sigmoid function to emulate DHRS heat removal transient. The DHRS model has three inputs and one output. Three outputs are volume-specific decay heat DH, temperature input Tin, and flow fraction FF. The only output is the temperature outlet $Tout$. The DHRS model icon is shown in Figure 2.24. This model is intended to evaluate functional requirements of a functional DHRS. More accurate DHRS can be designed using radiators and heat exchanger components as their heat removal rates are based on the flow rate and temperature of the secondary working fluid. Parameters of the DHRS model are tabulated in Table 2.14.

2.5.12 Pipe

The pipe model is a special model that is made up of a single node that has extensions from conduction and radiation. Accurate representation of a pipe requires many small nodes that are connected. If a pipe is represented by a single node, it cannot accurately capture the transport delay associated with a pipe. As a rectification pipe model has a single node that is accompanied by two transport delays. Only a fraction of the pipe volume is represented by the node to account for changes that would otherwise occur through the pipe, such as decay heat production. This approach to modeling pipes increases the computational efficiency by reducing the number of nodes required. The pipe model icon is shown in Figure 2.25. The pipe model has three inputs and a single output. Three inputs are volume-specific decay heat DH, inlet temperature Tin, and flow fraction FF. The only output is the pipe outlet temperature $Tout$. The parameters associated with the pipe model are listed in Table 2.15.

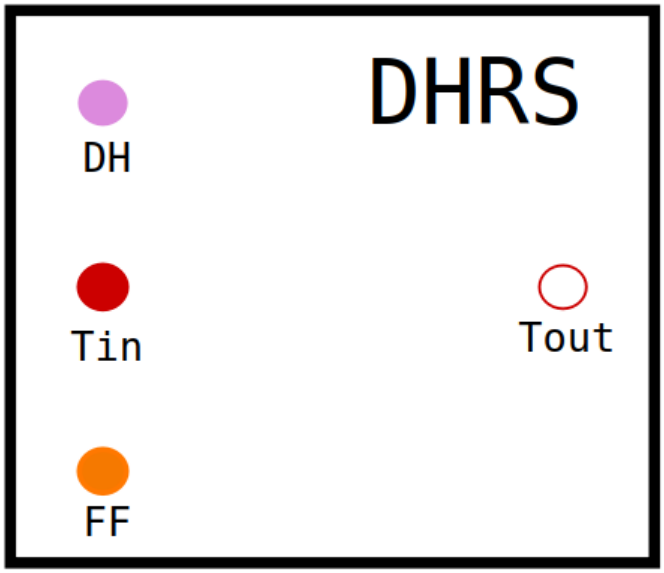

Figure 2.24: Decay heat removal system model icon

Table 2.14: Decay heat removal system model parameter summary

vol	=	volume of DHRS
rho	=	density of fluid
cP	=	specific heat capacity of fluid
vDotNom	=	nominal volumetric flow rate of fluid
DHRS_tK	=	DHRS time constant
DHRS_MaxP_Rm	=	DHRS maximum power removal
DHRS_P_Bleed	=	DHRS power bleed
DHRS_time	=	DHRS initiation time
K	=	conductivity of the fluid
Ac	=	cross-sectional flow area
L	=	length of the pipe
Ar	=	outer surface area
e	=	emissivity
Tinf	=	ambient temperature
T_0	=	initial temperature of DHRS

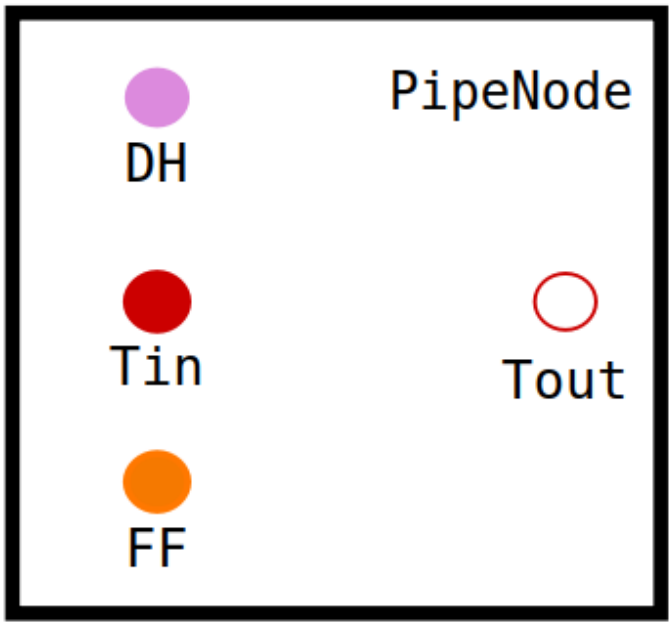

Figure 2.25: Pipe model icon

Table 2.15: Decay heat removal system model parameter summary

vol	=	volume of pipe
volFracNode	=	fraction of pipe volume represented
vDotNom	=	nominal volumetric flow rate
rho	=	density of fluid
cP	=	heat capacity of fluid
K	=	conductivity of fluid
Ac	=	cross-sectional flow area
L	=	length
Ar	=	outer surface area
e	=	outer surface emissivity
T_0	=	initial temperature
Tinf	=	ambient temperature

2.5.13 Pump

The pump model is used to calculate time-dependent flow fractions. The calculated flow fraction is used to simulate transients driven by the pump behavior. The pump model is equipped to simulate pump start-up and trip transients. Pump startup can be done in several ramps; therefore, the model allows for the use of several ramps. However, pump trip occurs due to a failure in the pump, therefore captured by a single exponential decay function. The icon of the pump model is shown in Figure 2.26. The flow fraction FF is the outlet port in the pump model. The parameters of the pump model are tabulated in Table 2.16.

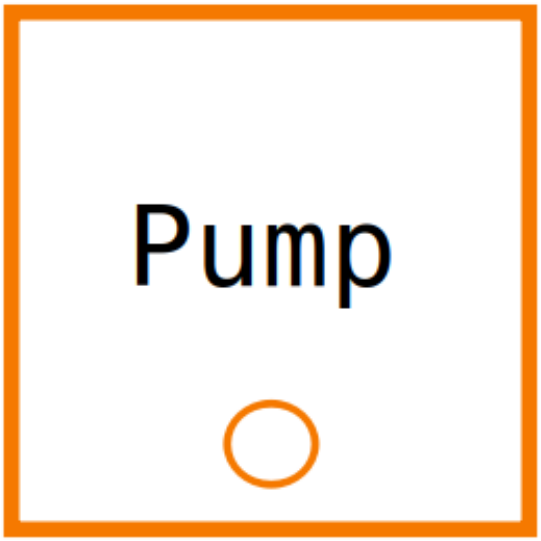

Figure 2.26: Pump model icon

Table 2.16: Pump model parameter summary

numRampUp	=	number of ramp ups
rampUpK	=	ramp up time constant
rampUpTo	=	flow rates to ramp up to
rampUpTime	=	time to initiate ramp up
tripK	=	pump trip time constant
tripTime	=	time to initiate pump trip

Chapter 3

MSR Models

Dynamic modeling of reactor systems can be done in different levels of detail. The level of detail modeling should be determined by the availability of design information and considering the purpose of the dynamic model. If the availability of design information is limited and the objective is to establish functional needs for each individual SSCs it is possible to make appropriate assumptions, such as when choosing flux profiles or heat transfer coefficients. The model can be improved as more information becomes available. Improvements can generally be made by increasing the number of nodes and characterizing the system with supporting calculations such as neutronics and flow. Neutronics calculations can be done to improve flux profiles, temperature feedback coefficients, etc. Flow-related phenomena can be improved by using different heat transfer correlations or by using experimental data. To demonstrate this, several MSR dynamic models are made with the SMD-MSR toolkit. The created models include benchmarking models of MSRE, Section 3.1, a complete paper reactor design of MSDR, Section 3.2, and a system with limited information MSRR, Section 3.3. MSRE models are created with available design information, as well as studies carried out by ORNL during the experiment to understand the dynamics and stability of MSRE. The created MSRE models are used to recreate several experimental transients to provide verification and validation

that are discussed in Chapter 4. The MSDR model is created using available preliminary design calculations and demonstrates the use of a model to simulate dynamic behavior of the system during full cycle operations. The MSRR model is developed to demonstrate that dynamic system models can be performed using limited information and that the created model can be used to explore transient behaviors and establish functional needs of SSCs.

3.1 MSRE Models

Disclosure - This section and the included subsections were originally published as part of a journal article [14]. The text here is slightly modified to fit this publication.

Two competing MSRE models were created using SMD-MSR. These two models are identical except for the core models. Two core models have different number of core regions, hence two levels of fidelity. The simplest of the two is the one-region core model, which features two fuel nodes and one graphite node. The second core model is made up of nine regions. The nine-region core model have 18 fuel nodes and 9 graphite nodes. By increasing number of region in the core, the fideliy is increased. The one-region core model is discussed in Section 3.1.1 and the none-region core model is discussed in the Section 3.1.2.

3.1.1 One-Region Core

For reference, MSRE is modeled using the developed SMD-MSR Modelica package and shown in Figure 3.1. The implementation is an exact replication of the MSRE model published in the SMD-MSR Simulink paper [13]. The nodalization of MSRE is shown in Figure 3.2, the figure is labeled and color coded to improve clarity. Figure 3.1 shows the implementation of MSRE using a prior version of the SMD-MSR toolkit.

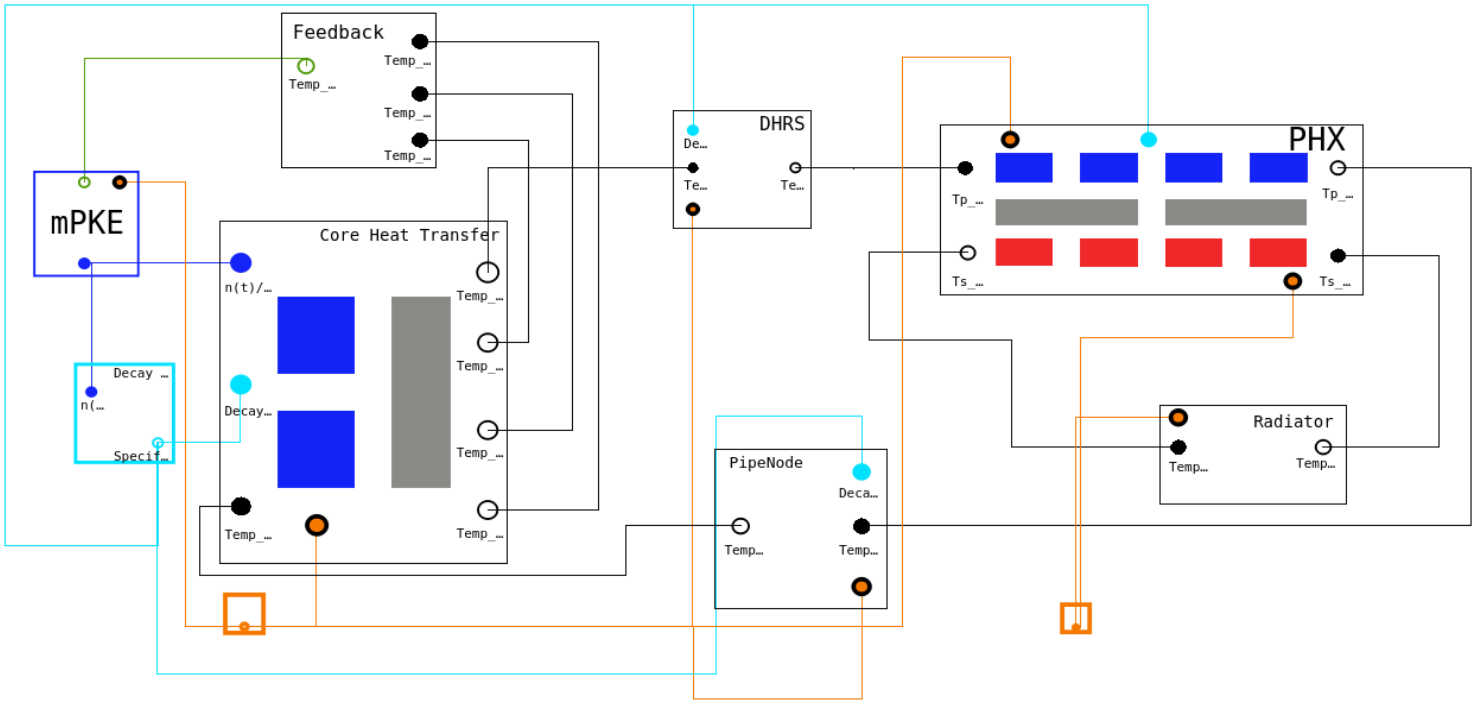

Figure 3.1: MSRE Implementation using SMD-MSR Modelica [15]

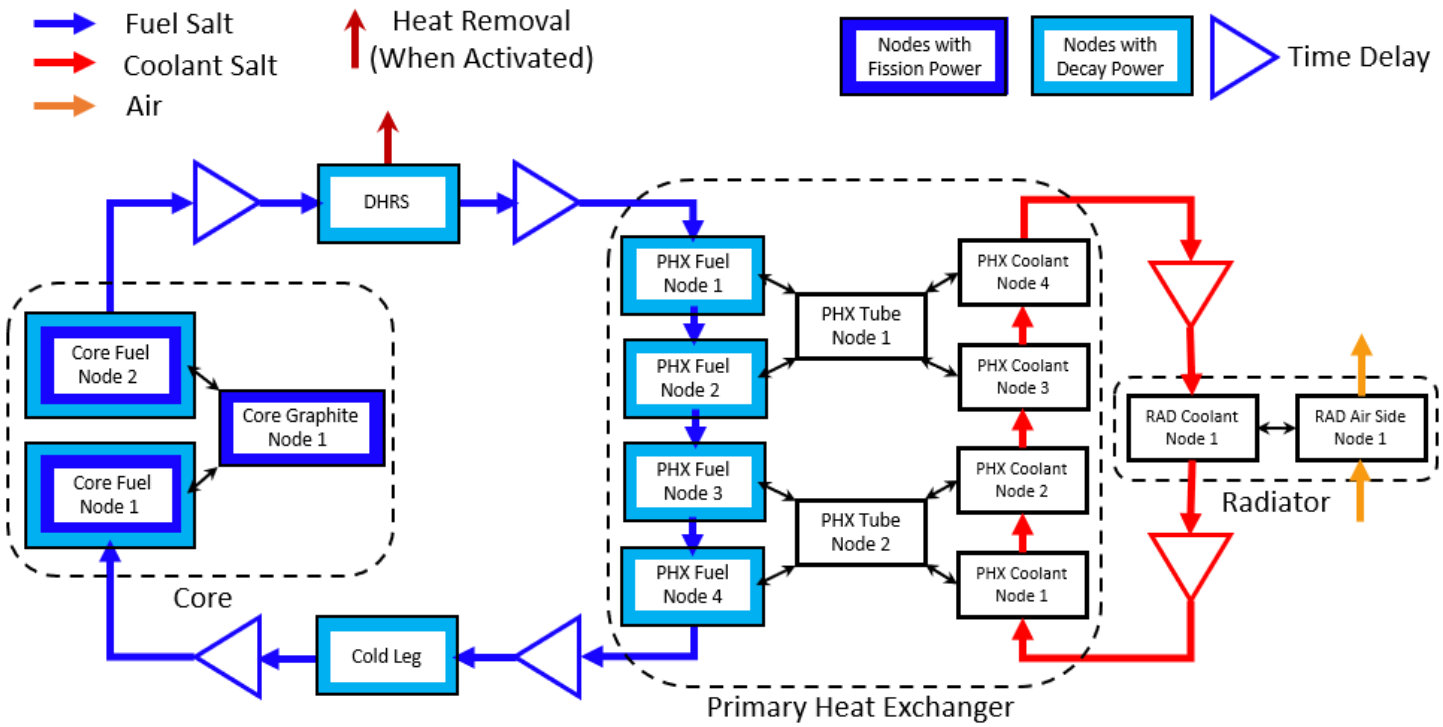

Figure 3.2: MSRE model nodalization [13]

Heat transfer is coupled with neutronics through linear temperature feedback. The neutronics are modeled using the mPKEs, which explicitly accounts for the delayed drift of the neutron precursor [31]. The dynamic decay heat is integrated into the model using the lumped dynamic decay heat approach developed for Simulink SMD-MSR [13]. Since the model assumes that the fluid nodes are homogeneous, dynamic decay heat is deposited in each of the primary loop nodes proportional to the node mass. The counter-flow primary heat exchanger is modeled with two solid nodes representing a tube bundle that exchange heat from the primary side to the secondary side. The primary and secondary fluids residing in the primary heat exchanger are indicated with four fluid nodes on each side.

A DHRS, which is based on a sigmoid function, was placed between the reactor core and the primary heat exchanger. The MSRE did not have a DHRS. However, a DHRS is incorporated into the model to expand the modeling capabilities and to be consistent with the published Simulink model. The normal operating mode has DHRS deactivated. When DHRS is deactivated, it functions as an ideal insulated fuel node with resident time equivalent to 1 s at nominal primary flow rate or node mass equivalent to 162.5 kg. Similarly, a fuel node is placed between the return fuel pipe from the primary heat exchanger to the core that has the same mass as the DHRS node.

Piping paths that are not nodalized are represented within the model as transport delays. Many nodes are required to represent a pipe accurately; however, this comes as a trade-off of computational efficiency. Using transport delays with a single node eliminates the requirement of many small nodes to represent pipes and preserve the accurate system behavior due to fluid transit time in insulated pipes. The secondary loop of the system removes heat from the primary heat exchanger to the atmosphere through a radiator. The radiator is made up of two nodes; one node represents the coolant salt, and the other node represents the air. The MSRE model uses two pump models, one for each loop. Pump models simulate a flow rate transient following a

pump trip using a logarithmic characteristic curve. Due to natural convection, MSRs experience non-zero flow rates even when the pumps are not operating. The flow rate model, a transport calculation based on the heat flow rate, and the calculation of the heat transfer coefficient are detailed in previous publications [13, 16].

3.1.2 Nine-Region Core

To demonstrate more advanced features of the SMD-MSR Modelica package, a MSRE model with a core model of nine regions was developed. The modeling approach is similar to the original nine-region dynamic model created by ORNL for stability analysis MSRE [24]. The nine-region model MSRE uses all the same component models of the one-region model presented in Sections 3.1.1, which is shown in Figure 3.1, except for the reactor core model. The reactor core features four radial regions. It is assumed that no heat transfer occurs between the radial regions. The regional arrangement and nodalization of the core model of nine regions are illustrated in Figure 3.3.

The fuel mass of the core is distributed in a ratio of 2.34%, 13.68%, 31.56%, and 52.42%, respectively, from the first radial region to the fourth radial region. The first radial region (R1) represents the central fuel channels of the core. In the MSRE, the control rods were located in the center of the core. This causes the dip in the radial thermal neutron flux seen in Figure 3.4. Furthermore, the presence of control rods reduces the volume available for fuel, which is reflected in the ratio of fuel mass. Therefore, a single region is used to reconstruct the entire first radial region. The second radial regions (R2, R3, and R4) experience the highest radial thermal neutron flux, which can be verified from Figure 3.4. Therefore, the second radial region is represented by three axial regions. The neutron flux in the third radial region (R5, R6, and R7) is similar to that of the first radial region according to Figure 3.4. However, the third radial region is made up of 13.5× more fuel than the first radial region. Therefore, the third radial region is represented by three axial regions. The

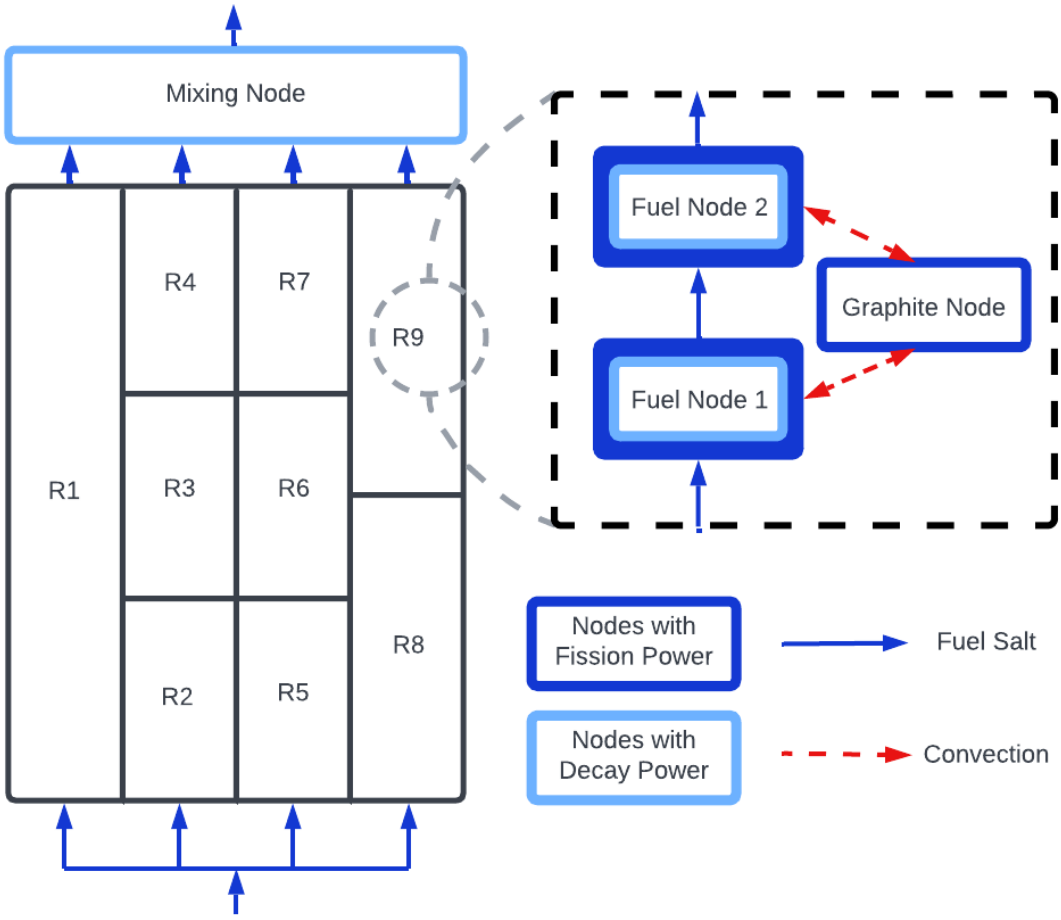

Figure 3.3: Nodalization of the reactor core in the nine-region MSRE model [15]

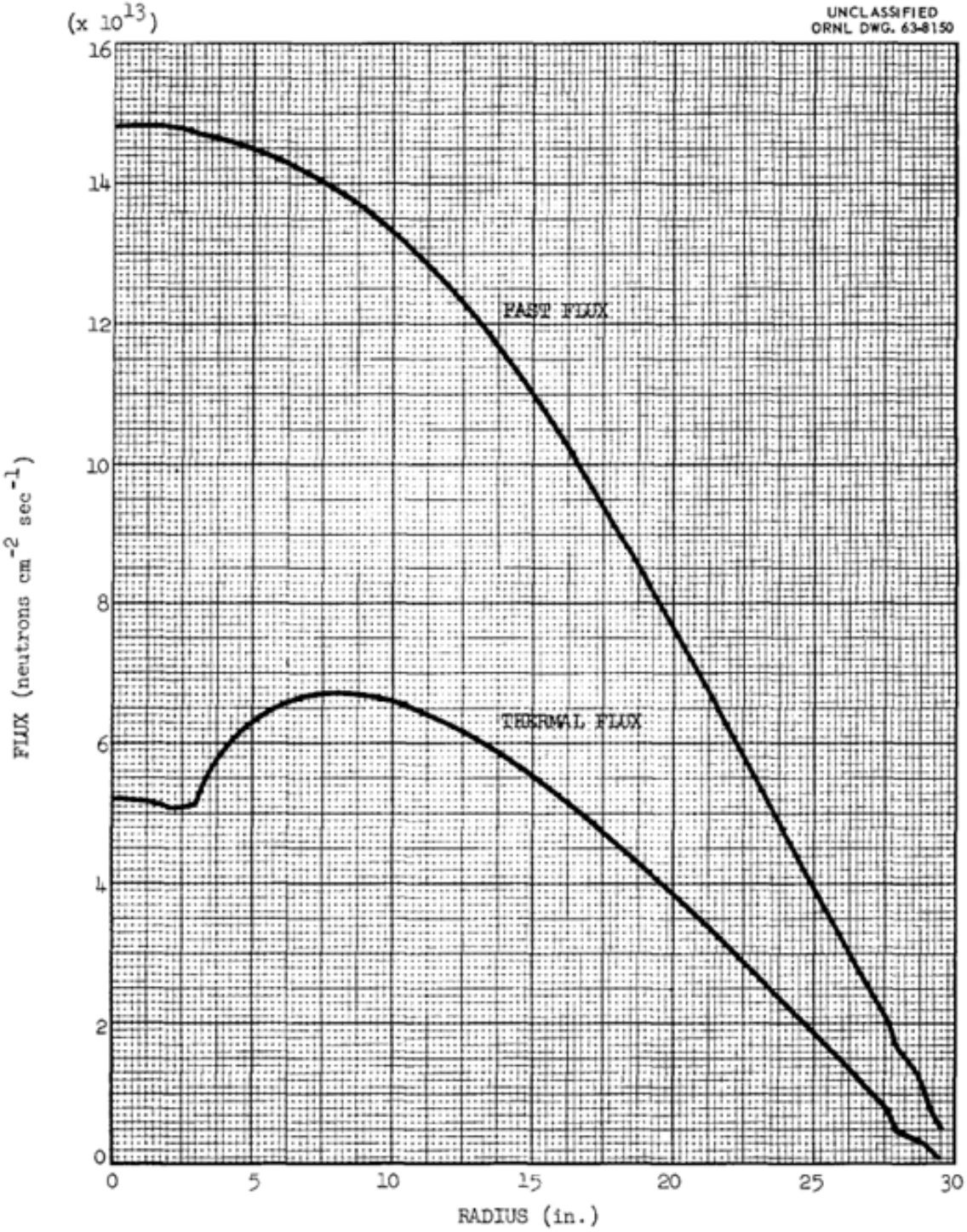

Figure 3.4: MSRE Two group, radial flux distribution[41]

fourth radial region (R8 and R9) has two axial regions. The neutron flux at the fourth radial region is the lowest, but it has the highest fuel mass of all four radial regions. Consequently, it was chosen to represent the last radial region with two axial regions (R8 and R9).

The heat transfer and temperature feedback of each core region are calculated using the same component blocks used in the one-region model presented in Section 3.1.1. The nine-region core model contains 18 fuel nodes and 9 graphite nodes. The lower plenum and reactor downcomer are not explicitly modeled. The fuel flow from the input of the core fuel is distributed to each radial region. The fuel salt flows through each radial fuel region and exits the upper plenum. The upper plenum is represented by a single fuel node, where the fuel entering from each radial region is ideally mixed. It was assumed that no fission occurs in the mixing node; therefore, only decay heat is deposited.

Temperature feedback from each region is calculated using a weight factor corresponding to each node's importance. The total feedback calculated from each region is routed to the reactivity summing block. The reactivity summing block has a pre-allocated number of inputs and produces a single output with resultant feedback. The feedback is subsequently fed into the mPKE module that calculates the nominal neutron population. As shown in the one-region model in Section 3.1.1, the nominal neutron population is used to calculate dynamic decay heat and fission power in each node appropriately. Fractions of fission power generated in each node and importance functions can be calculated from depletion codes such as SERPENT. The masses of the nodes, the fractions of fission power produced, the weight factors of the feedback for each individual node, and the flow rates through each radial region are tabulated in stability analysis MSRE and a previous publication [24, 42].

3.2 MSDR Model

Disclosure - This section and the included subsections were originally published as part of a journal article [14]. The text here is slightly modified to fit this publication.

The model presented in this study is an improved version of the [43] model with several new additions. The model uses the mPKE approach described in [30] coupled with the heat transfer modeling described in [44]. Improvements made to the current model include increased modularity, reworked flow fractions, reworked heat transfer coefficient calculations, reworked variable time delays, and changes to the general arrangement of the model. These improvements are inspired by and similar to the implementations done in [13]. New additions include dynamic decay heat production and removal and a novel depletion accounting module.

3.2.1 Updates to decay heat removal system

Dynamic decay heat production and removal allow a simulation of a wide range of off-normal transients, where the decay heat plays an important role in terms of delayed effects. Implementing the production and removal of dynamic decay heat, together with power scaling, is described in detail in [13]. The DHRS implementation was slightly changed in the presented model from the version included in [13]. The DHRS block in the previous implementation contained a MATLAB function block in the Simulink model itself. Due to adverse effects on computational efficiency introduced by the MATLAB function blocks in Simulink, the new implementation solely uses the Simulink built-in functions even though the fundamental logic remains unchanged. In an effort to further improve usability and efficiency of the model, Simulink variable and enable subsystems are introduced to the UHX block. One option of the variable subsystem allows one to use the full Steam Generator (SG) model, while the other allows for a simplified constant power removal block.

In the previous iteration of the model presented in [43], the SG did not support a complete trip function due to limitations of its implementation. The SG implementation defines three regions according to the state of feed water; subcooled, saturated boiling, and super heated. These three regions are defined by a total of six mass nodes, two for each state of the fluid. These nodes are dynamic, allowing the mass of the node to shrink or grow, simulating the change in vertical length of each fluid region. However, if the SG is tripped by cutting the feed water off, the simulation will fail since the entire secondary side of the SG becomes steam, thus forcing saturated boiling and subcooled regions to have zero node masses. As a correction to this issue, a Simulink enable function is utilized. When the SG is tripped, Simulink completely disables the SG and reroutes the primary hot leg of the SG directly to its cold leg through a transport delay that is equivalent to the delay of the primary side of the SG (Once Through Steam Generator (OTSG) Mode 2 shown in Figure 3.5).

The MSDR power plant consists of three independent intermediate heat removal loops between the core and the SG, as shown in Figure 3.5. Only one loop is shown in detail. Loops 2 and 3 are identical to loop 1. Each intermediate loop is equipped with two PHXs and two SHXs. Each loop has its own primary, secondary and tertiary pumps for fuel salt, FLiBe coolant salt, and HITEC solar salt, respectively. Pumps are not shown in the model schematics. The MSDR has three hot legs, one for each loop. Each hot leg is split into two PHXs. The PHX outlets are then mixed in a mixing node before returning to the reactor cold legs. Fuel salt flows returning from all three loops are mixed together inside a mixing node before they are fed into the reactor core. The DHRS is connected with the mixing node located in the lower mixing plenum, unlike in the previous SMD-MSR model because the volume of pipes from reactor hot legs to each loop was not sufficient to add an additional node dedicated for DHRS without compromising the simulation performance. Decay heat is deposited in all the fuel nodes, proportional to the mass of the individual nodes.

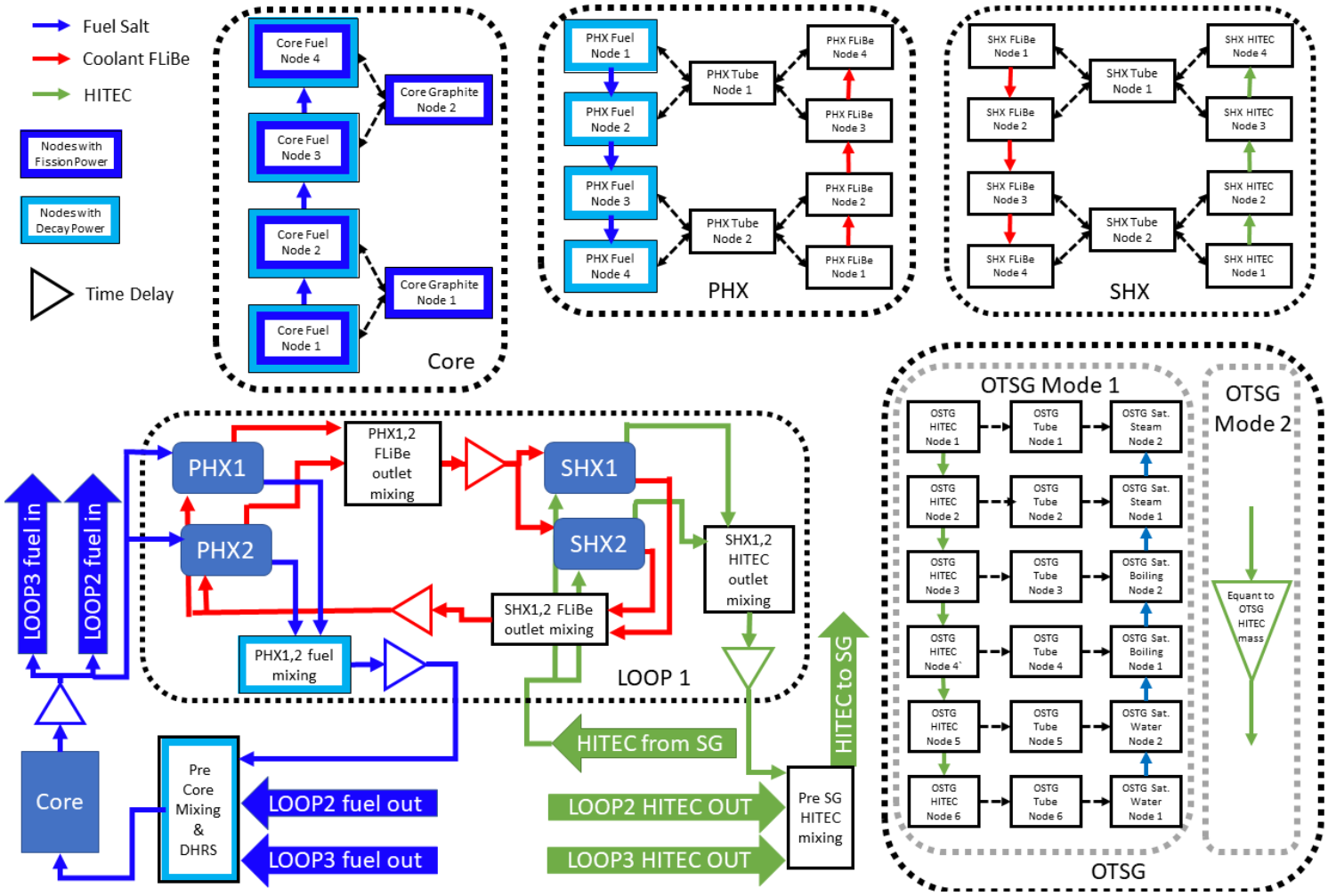

Figure 3.5: Nodal scheme used for MSDR implementation. [14]

The nodalization of the SG is not shown in Figure 3.5 as it is identical to the implementation described in detail in the previous article [43].

FLiBe secondary coolant salt flows between two PHXs and two SHXs in each loop. These flows are combined and mixed in mixing plenums at respective outlets before feeding into the corresponding inlets. HITEC salt from the SG is equally divided into six parallel lines and fed into six SHXs, two per loop. HITEC salt flowing from each SHX in all three loops is combined in a dedicated mixing node before transporting to SG. All mixing plenums are assigned fluid resident times of 1 s.

Although this model is significantly more complex than some of the previously published MSRE-like Simulink models [42, 13], it runs fast on a personal computer. A simulation of a 15,0000 s long transient takes about 15 minutes of wall time on a modern laptop (i.e., 15 seconds are simulated during one real-time second). Due to the speed improvements mentioned above, this model runs at about the same speed as the previous model [43], despite its additional features related to decay heat and increased complexity.

3.2.2 Balance of plant

The previously published model [43] contains a complete balance of the Rankine cycle of the plant. In this iteration, the balance of the plant beyond the steam generator is removed to improve computational efficiency. It was shown in that study that the frequency characteristics important for the system dynamic behavior are essentially bound by the response of the steam generator alone and unaffected by the rest of the balance of plant.

3.3 MSRR Model

The MSRR is a 1 MW_t research reactor that is being built at Abilene Christian University (ACU), in Abilene, Texas. The reactor is a two-loop-type, graphite-moderated, thermal spectrum design, similar to MSRE. MSRR will use molten fluoride fuel salt in its primary and secondary circuits. It uses High Assay Low Enriched Uranium (HALEU) for fuel and 316H stainless steel for structural components, including the primary loop. At the time of writing, ACU has submitted an application to obtain construction permits from the NRC. ACU plans to use the facility as to gather experimental MSR data to understand reactor kinetics and dynamics, fuel salt behaviors, structural material corrosion, fission product migrations, and other effects that impact MSR operation and licensing.

The MSRR feature is two separate molten salt loops. The primary loop that contains the fuel salt consists of the reactor vessel, the reactor access vessel, the primary pump, and the shell side of the heat exchanger in this order. There is a drain tank located between the heat exchanger and the reactor vessel where fuel salt can be drained. The fuel drain tank is connected to two fuel storage tanks. The secondary loop, which contains coolant salt, is made up of the side of the heat exchanger tube, the secondary pump, the surge tank of the secondary loop, and the radiator. The secondary side also has a drain tank located between the radiator and the tube side of the primary heat exchanger. The primary loop of the system is located within a steel reactor enclosure that is placed in a concrete trench. Additional concrete shielding surrounds the reactor enclosure on its sides and on the top. Secondary coolant pipes leading to the side of the primary heat exchanger pass through the concrete shield and carry the heat to an adjacent cell in the trench, where the heat is rejected via a salt to air radiator. The complete layout of the MSRR system is shown in Figure 3.6. Since MSRR is still in the design stages, the final design details are not yet available. However, preliminary design information can be found in the licensing documents filed with NRC [45]. The available information is sufficient to calculate and construct

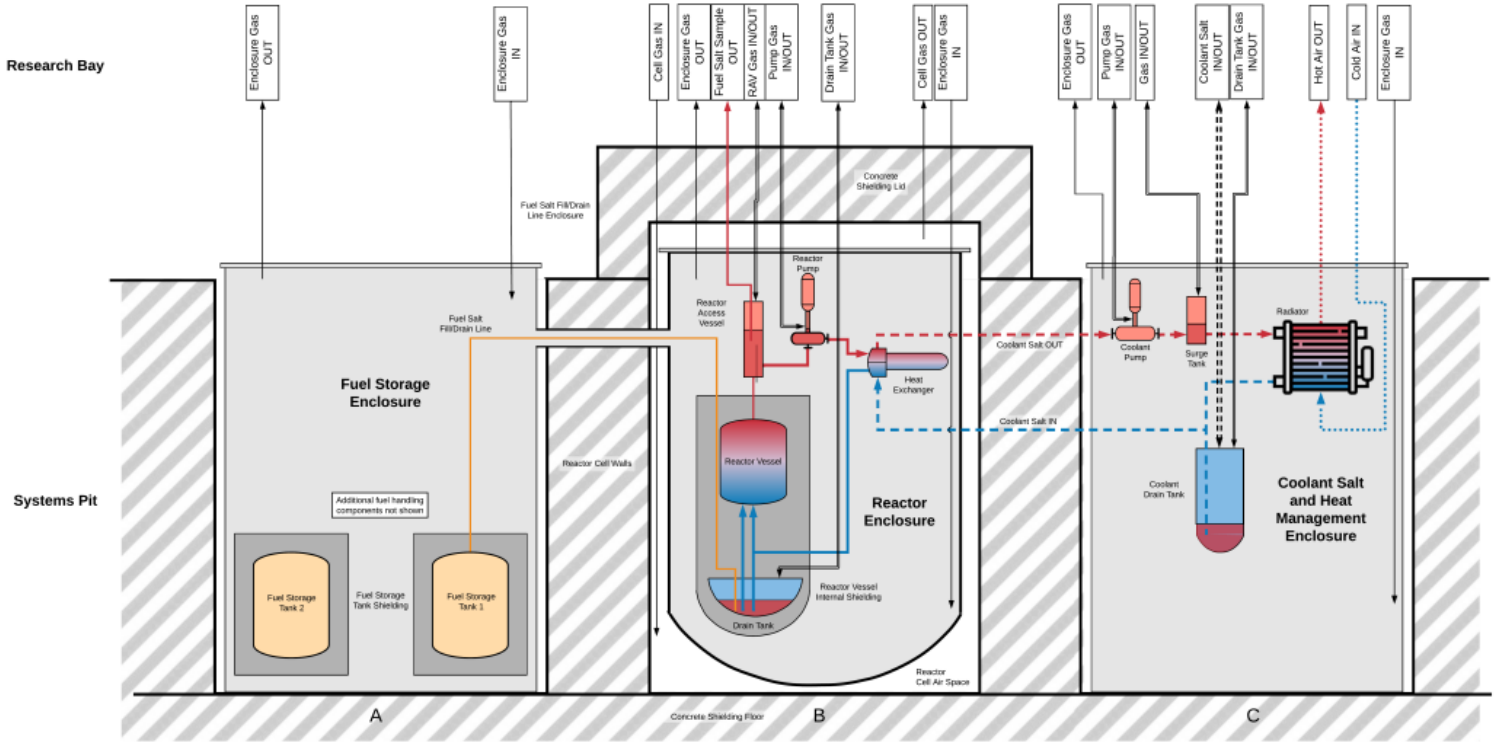

Figure 3.6: MSRR system layout [45]

a dynamic model that is capable of producing some insight into the MSRR dynamic behavior. Data extracted from the preliminary safety analysis report for dynamic modeling are tabulated in Tables 3.1, 3.2, and 3.3.

Upon careful examination of Tables 3.1, 3.2, and 3.3, it is clear that most of the data required to perform a detailed system dynamic analysis of the MSRR is not yet openly available. Therefore, a simple dynamic model is created using available information to emulate the MSRR topology. The system consists of two separate loops that are integrated with a heat exchanger. The primary loop was simplified by assuming that it is composed of the reactor vessel, reactor access vessel, and shell side of the heat exchanger. All the components are connected with piping that fuel salt flows through. Here, the decay heat is produced and deposited. The secondary loop is represented by the tube side of the heat exchanger and the radiator. The heat exchanger and the radiator are connected with pipes as appropriate. The simplified flow diagram of the MSRR model is shown in Figure 3.7.

The design of the primary loop specifies that the total volume of fuel salt in the primary loop is 500 L and that the reactor vessel itself is 400 L making the combined volume of the reactor access vessel, the shell side of the heat exchanger and all the primary piping 100 L. Using this information along with the fuel salt flow rate, the total resident time of the system can be calculated. The calculated resident time of the entire primary loop is 43.5031 s, which corresponds to a reactor vessel resident time of 34.8025 s and 8.7006 s for the rest of the loop. Although the volume of the reactor vessel is available, the core volume is not specified.

The cross section of the MSRR reactor vessel is depicted in the preliminary safety analysis report and a cropped portion is shown in Figure 3.8. In Figure 3.8 the areas where fuel salt flows are shown in orange, control rods in yellow, and graphite in blue. The gray boundary is the wall of the vessel. It is clear that the gap between the graphite and the reactor vessel as well as the graphite and control rods has layers

Table 3.1: MSRR System Design Data Obtained from [45]

System	Parameter	Nominal Value
Reactor Design	Thermal power	1 MW
	Fuel salt	FLiBe+HALEU
	Primary loop volume	500 L
	Reactor fuel volume	400 L
	Core graphite volume	1758 L
	Maximum height of graphite core	151.68 cm
	Graphite density	1.8 g/cc
	Fuel salt inlet temperature	550 °C
	Fuel salt outlet temperature	590 °C
	Average fuel salt temperature	570 °C
	Fuel channel diameter	3.016 cm
	Fuel salt flow rate	23.9 kg/s
Heat Exchanger Design	Coolant salt	FLiBe
	Coolant salt inlet temperature	500 °C
	Coolant salt outlet temperature	508 °C
	Coolant salt mass flow rate	53.4 kg/s
Radiator	Air inlet temperature	37 °C
	Air outlet temperature	121 °C
	Air mass flow rate	11.7 kg/s
Piping and Others	Material	Stainless steel 316H

Table 3.2: Temperature Feedback Coefficients Obtained from [45]

Method	Coefficent	Value
MCNP	Fuel	- 6.46 pcm/K
	Graphite	-5.39 pcm/K
SCALE	Fuel	-6.26 pcm/K
	Graphite	-5.16 pcm/K

Table 3.3: Reactivity Loss due to DNP Flow Obtained from [45]

Flow (% nominal)	Reactivity loss ($)
100	0.1020
50	0.0751
20	0.0452
10	0.0277
1	0.0032

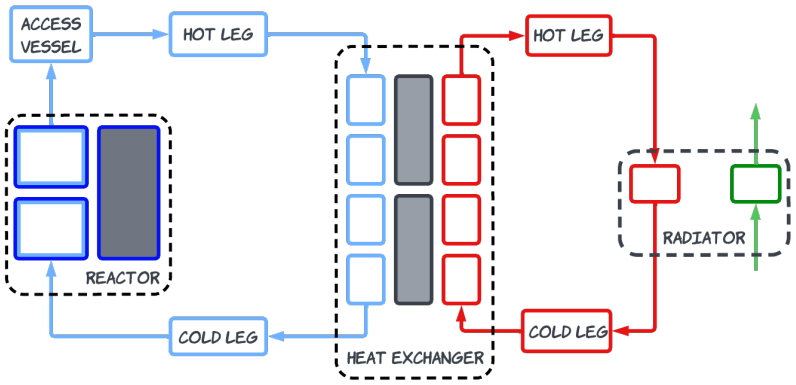

Figure 3.7: Simplified flow diagram of MSRR model

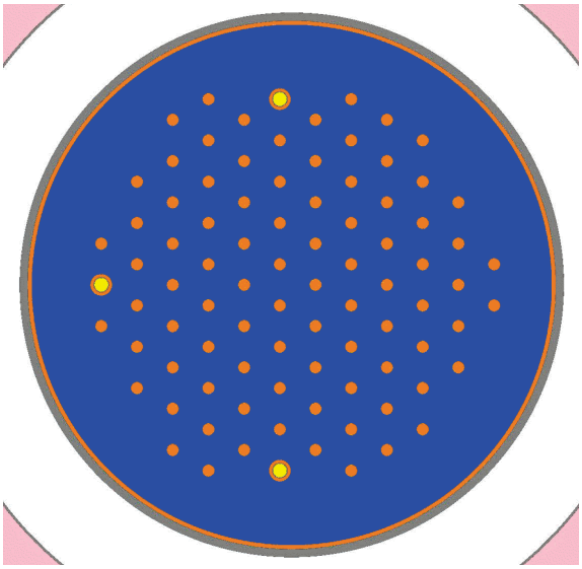

Figure 3.8: Cross-sectional view of MSRR reactor vessel [45]

of fuel salt. This is a typical design choice for MSRs intended to cool and maintain the structural material of the vessel and control rods within a safe temperature.

According to the Figure 3.8 there are 87 circular fuel channels and 3 control rods in the core. When the total volume of the fuel channels was calculated using the given circular channel radius and assuming that the number of channels is 90 and the channel length is equal to that of the maximum height of the graphite core, it was evident that only ≈24% of the fuel volume of the vessel resides in the fuel channels. Since there is no adequate information regarding the volumes of annular space between the core and vessel, the lower and upper plenums, it was chosen to represent the entire reactor vessel with a single region. To approximate the design of MSRR the following calculations are performed. For the purposes of the MSRR model presented here, the physical properties of the fuel and coolant salts were obtained from MSRE salt properties [46].

Since the actual operational fuel inlet and outlet temperatures of the reactor fuel are not known, a heat balance was performed to calculate the increase in temperature in the reactor (ΔT_f) assuming that all the thermal energy generated within the fuel salt resides in the core. An approximate energy balance can be done to calculate the temperature change ΔT_f; using reactor thermal power $P_t = 1\,\mathrm{MW}_t$, fuel salt mass flow rate $\dot{m}_f = 23.9\,\mathrm{kg/s}$ and fuel salt specific heat capacity $Cp_f = 2009.66\,\mathrm{J/kg\ K}$ as,

$$P_t = \dot{m}_f Cp_f \Delta T_f \tag{3.1}$$

From this approximate calculation, it was found that ΔT_f across the reactor at $1\,\mathrm{MW}_t$ is $20.82\,\mathrm{K}$. To preserve the average temperature of the reactor, $T_{reactor,avg}$ at $570\,^{\circ}\mathrm{C}$, reactor inlet $T_{reactor,in}$ and outlet $T_{reactor,out}$ temperatures were calculated as,

$$T_{reactor,in} = T_{reactor,avg} - \frac{\Delta T_f}{2} \tag{3.2}$$

$$T_{reactor,out} = T_{reactor,avg} + \frac{\Delta T_f}{2} \tag{3.3}$$

The calculated reactor fuel salt input, $T_{reactor,in}$ and outlet, $T_{reactor,out}$ temperatures are 559.6 °C and 580.4 °C respectively. Once reactor operational temperatures are established, attention can be paid to flow analysis in the reactor to calculate heat transfer coefficients. Using the average temperature and the choice of an appropriate temperature-based density function, the average density of the fuel salt can be calculated. The average density $\rho_{f,avg}$ of fuel salt is calculated as,

$$rho_f(T_{f,avg}) = 2553.3 - 0.562(T_{f,avg} + 273.15) \tag{3.4}$$

The average density of fuel salt $\rho_f(T_{f,avg})$ is 2079.4 kg/m^3. Using the average density of the fuel salt and the mass flow rate $\dot{m}_f$, the volumetric flow rate of the fuel $\dot{V}_f$ in the primary loop can be calculated as,

$$\dot{V}_f = \frac{\dot{m}_f}{rho_f(T_{f,avg})} \tag{3.5}$$

The volumetric flow rate of the fuel salt $\dot{V}_f$ is 0.0115 m^3/s. Once the volumetric flow rate of the fuel salt $\dot{V}_f$ is available, it can be used to calculate the fuel resident times τ of the fuel in the reactor and the rest of the loop. In this model, the entire reactor is assumed to be the reactor core. With the said assumption, the core volume of MSRR is 0.4 m^3 and the ex-core volume (loop volume) is 0.1 m^3. The fuel resident time of the core τ_c and the fuel resident time of the loop τ_l can be calculated for each volume V using,

$$\tau = \frac{V}{\dot{V}} \tag{3.6}$$

The calculated resident time of the core fuel τ_c is 34.8 s and the resident time of the loop fuel τ_l is 8.7 s. Armed with resident times of the primary system, the

reactivity loss due to DNP drift discussed in Section 2.4.3 can be calculated using Equation 2.11 for variations in fuel flow rate. Variations can be expressed as a fraction of the nominal flow rates and resident times can be calculated based on the fractional flow rate as shown in Section 2.4.2. The loss of reactivity in MSRR due to flow is provided in the preliminary report and tabulated in Table 3.3. The loss of reactivity due to flow is calculated for the presenting model for comparison. DNP group data of the MSRE [41] is used for the calculation. The results of the calculation are depicted in Figure 3.9 along with provided MSRR data.

Upon close inspection of Figure 3.9 it is clear that the calculated reaction loss values are generally in agreement with the MSRR data obtained from the preliminary safety analysis. The divisions seen can be attributed to DNP group data. MSRR uses HALEU while MSRE used fuels with less enrichment. As discussed previously, since the design data required to model the core accurately are unavailable, several assumptions are made to calculate the heat transfer coefficient between fuel salt and graphite. First, it was assumed that all the fuel flows through the circular fuel channels as seen in Figure 3.8. Second, it was assumed that the volumetric flow across the core $\dot{V}_{f,reactor}$ is evenly distributed among the 90 fuel channels previously counted. With these two assumptions, the volumetric flow rate in an individual channel $\dot{V}_{f,channel}$ can be calculated.

$$\dot{V}_{f,channel} = \frac{\dot{V}_{f,reactor}}{\#channels} \tag{3.7}$$

The volumetric flow rate of the fuel in a single fuel channel $\dot{V}_{f,channel}$ is 1.28E-4 m^3/s. Once the volumetric flow rate is available in a single fuel channel, the fuel velocity $v_{f,channel}$ can be calculated using the cross-sectional flow area of the channel $Ac_{channel}$ as,

$$v_{f,channel} = \frac{\dot{V}_{f,channel}}{Ac_{channel}} \tag{3.8}$$

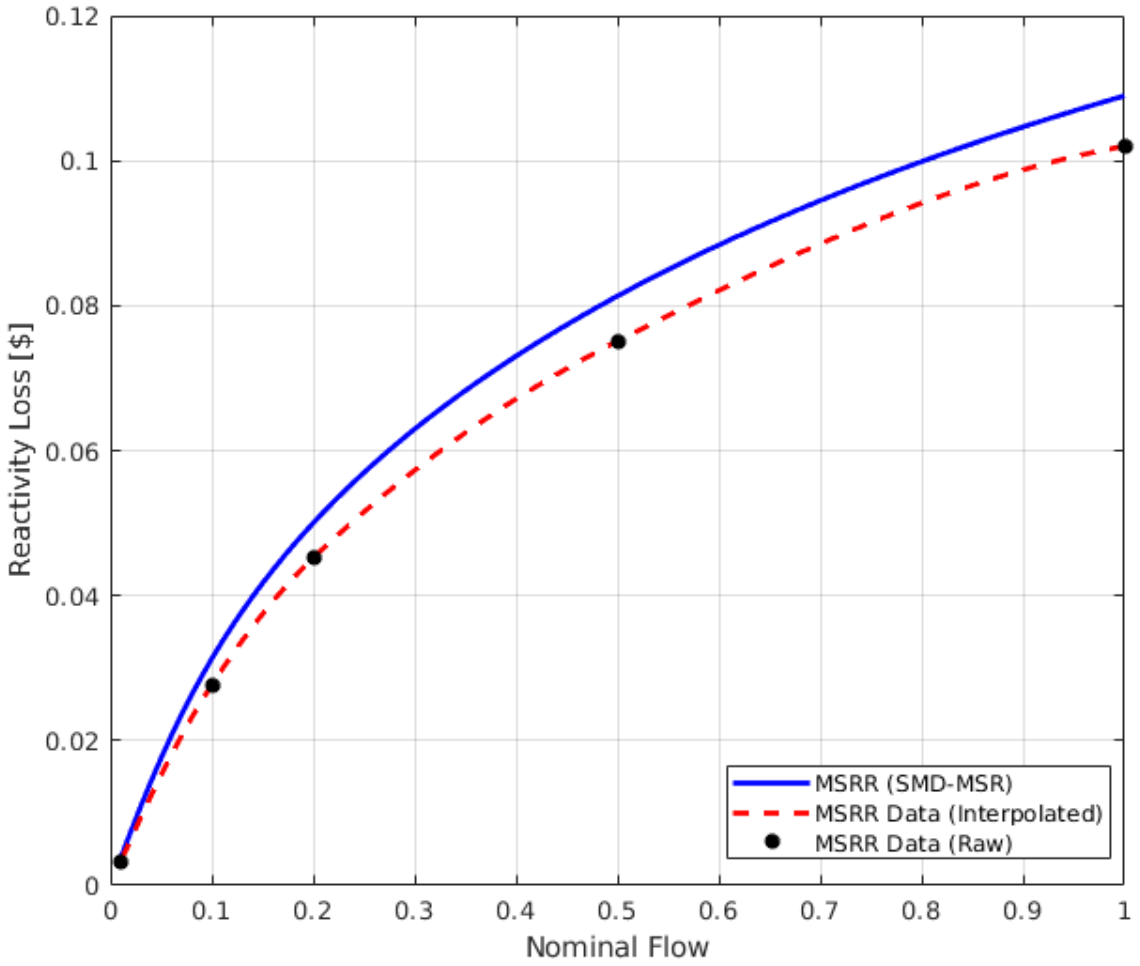

Figure 3.9: Reactivity loss due to fuel flow in MSRR

The fuel velocity $v_{f,channel}$ across a single channel is 0.179 m/s. Using the fuel velocity $v_{f,channel}$, the average density ρ_f, the diameter of the channel $D_{channel}$, the dynamic viscosity μ_f, the heat capacity Cp_f and the conductivity k_f, the Reynolds number Re_D and the Prandtl number Pr_f can be calculated. The dynamic viscosity of the fuel can be calculated using MSRE salt physical properties [46].

$$\mu_f(T_{f,avg}) = 8.4E-5 \; exp\left(\frac{4340}{T_{f,avg}+273.15}\right) \tag{3.9}$$

The calculated dynamic viscosity μ_f is 0.0144 Pa s. The thermal conductivity of the fuel salt k_f is 1.0 W/m K. The Reynolds number Re_D and the Prandtl number Pr_f can be calculated as,

$$Re_D = \frac{\rho_f v_{f,channel} D_{channel}}{\mu_f} \tag{3.10}$$

$$Pr_f = \frac{Cp_f \mu_f}{k_f} \tag{3.11}$$

The calculated Reynolds number Re_D and Prandtl number Pr_f are 776.0 and 29.03 respectively. Due to the low Reynolds number, the fuel flow within the fuel channel is laminar. Although laminar flow is undesirable in nuclear reactors, in this scenario, the laminar flow may transition to turbulent flow due to wall heating. A proper Nusselt correlation is required to calculate the heat transfer coefficient with the calculated Reynolds and Prandtl numbers. To calculate the Nusselt number Nu_D, a version of the Seider-Tate formulation that is modified for laminar flow was used [47].

$$Nu_D = 1.89(Re_D Pr_f (D/L))^{0.33}(\mu_f/\mu_s)^{0.14} \tag{3.12}$$

Here, L is the channel length and μ_s is the fuel viscosity at the interface. It was assumed that there is no variation in the viscosity of the fuel since the calculation

was made for bulk average temperature of fuel; therefore (μ_f/μ_s) =1. The Nusselt number Nu_D is 14.17. The average heat transfer coefficient $\tilde{h}$ can be calculated using the Nusselt number Nu_D, the thermal conductivity of the fuel salt k_f and the diameter of the fuel channel $D_{channel}$ as,

$$\tilde{h} = \frac{Nu_D k_f}{D_{channel}} \tag{3.13}$$

The calculated average heat transfer coefficient $\tilde{h}$ is 469.8 $\mathrm{W/m^2\,K}$. The implementation of the core region model uses the product of the average heat transfer coefficient $\tilde{h}$ and the total heat transfer interface area to form the nominal convection parameter $hAnom$, which can be calculated as

$$hAnom = \tilde{h}(\pi D_{channel})\#channels \tag{3.14}$$

The nominal convection parameter $hAnom$ is equal to 0.0249 MW/K. The flow-dependent convective parameter $hA(FF)$ can be calculated by performing the same calculation by changing the fuel flow rate. Once the flow-dependent convective parameter $hA(FF)$ is calculated for a flow fraction FF in the range of 0.01 to 1; a curve fitting can be performed to create a flow-dependent convective parameter function to be added to the model. For the MSRR model, core region flow dependent convective parameter is expressed as,

$$hA(FF) = 0.02492FF^{0.33} \tag{3.15}$$

The flow-dependent convective parameter $hA(FF)$ calculated using the iterative method and the curve fit of the above equation is shown in Figure 3.10. This step is not required but is recommended to allow the model to perform variable-flow simulations. The fitting of the curve of the calculated convective parameter hA is done to avoid computationally intensive lookup tables. The use of this method greatly reduces simulation execution time.

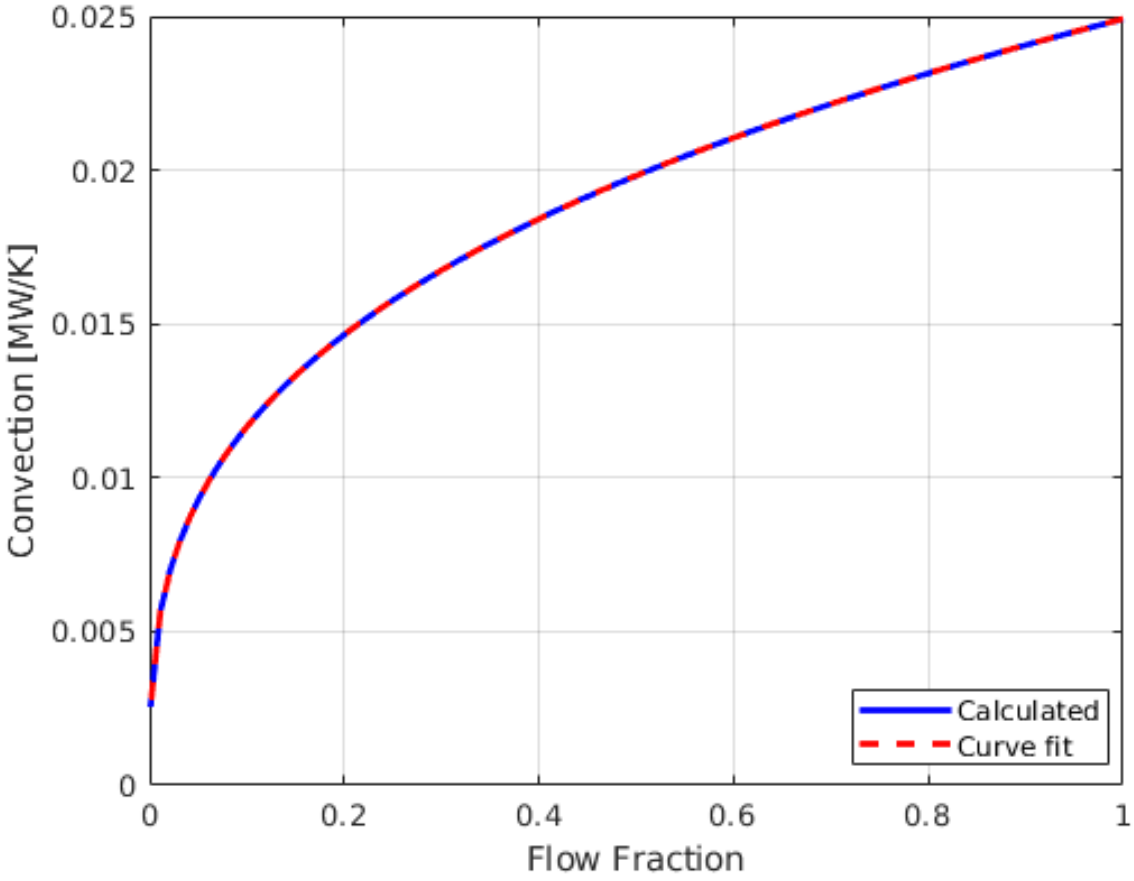

Figure 3.10: Flow-dependent convection of MSRR core model

The preliminary safety report of MSRR does not contain design details for the salt-to-salt heat exchanger. Therefore, it was chosen to perform an analysis for a shell and tube counterflow heat exchanger that would facilitate the removal of the reactor power and maintain the prescribed boundary temperature values. The tube bank is assumed to be U-tubes making it two passes, and the shell is a single pass. The MSRR safety report reports expected pressure losses in each loop; however, this information is not taken into account because the modeling methodology is not able to model pressure loss. The design process of a heat exchanger is complex, and there are more considerations involved than the calculations presented below. Heat exchanger design calculations are made iteratively using methods such as the Bell-Delaware or Kern methods [48, 49]. It should be noted that it is preferable to use the Number of Transfer Units (NTU) approach to design heat exchangers [50]. The heat exchanger tube bank was assumed to be made up of 200 seamless stainless-steel tubes with outer diameter D_o 0.25 in and thickness t 0.02 in. The tubes are arranged in a triangular lattice with a pitch of 0.3125 in ($1.25 \times D_o$). The design of the heat exchanger can begin by calculating Log Mean Temperature Difference (LMTD). The LMTD for a counterflow heat exchanger ΔT_{lm} can be written as,

$$\Delta T_{lm} = \frac{(T_{f,in} - T_{c,out}) - (T_{f,out} - T_{c,in})}{ln((T_{f,in} - T_{c,out})/(T_{f,out} - T_{c,in}))} \tag{3.16}$$

Here, $T_{f,in}$ and $T_{f,out}$ are the fuel inlet and outlet temperatures on the shell side, while $T_{c,in}$ and $T_{c,out}$ are the inlet and outlet temperatures on the tube side of the heat exchanger. It was assumed that the fuel inlet temperature $T_{f,in}$ of the heat exchanger is equal to the reactor outlet temperature $T_{reactor,out}$, while the heat exchanger outlet temperature $T_{f,out}$ is equal to the reactor inlet temperature $T_{reactor,in}$. The tube side inlet temperature of the heat exchanger $T_{c,in}$ is 500 °C and the outlet temperature $T_{c,out}$ is 508 °C. The LMTD of the heat exchanger ΔT_{lm} is 65.9 °C. Using ΔT_{lm}, the overall heat convection of the heat exchanger UA_{hx} can be calculated as,

$$\dot{Q} = UA_{hx}\Delta T_{lm} \tag{3.17}$$

Using the full power of 1 MW as $\dot{Q}$, the calculated overall heat conduction of the heat exchanger UA_{hx} is 1.52E+04 W/K. It is required to calculate the area of heat transfer to calculate tube length. The area can be calculated by calculating the overall heat transfer coefficient U_{hx}. The overall heat transfer coefficient U_{hx} can be expressed as the sum of individual heat transfer coefficients. The tube is assumed to be highly conductive and thin; therefore, there is no significant thermal resistance across the tube wall. With said assumption, the overall heat transfer coefficient U_{hx} can be written using its individual components, the heat transfer coefficient between the fuel and the outer wall of the tube h_o and the heat transfer coefficient between the inner wall of the tube and the coolant h_i as,

$$U_{hx} = \frac{1}{(1/h_o) + (1/h_i)} \tag{3.18}$$

It is clear that in order to calculate the overall heat transfer coefficient U_{hx}, the inner and outer heat transfer coefficients of the tube must be calculated. Heat transfer coefficients can be calculated for nominal flow rates, as shown previously. The physical properties of the fuel salt previously used are used again since the average temperature of the fuel $T_{f,avg}$ remains the same. The physical properties of the coolant salt at the average temperature of the coolant salt $T_{c,avg}$ can be calculated using correlations of MSRE salt properties [46]. The average temperature of the coolant salt $T_{c,avg}$ is 504 °C. The specific heat capacity of the coolant salt Cp_c is 2390.0 J/kgK while the thermal conductivity k_c is 1.1 W/mK.

$$\rho_c(T_{c,avg}) = 2146.3 - 0.488(T_{c,avg} + 273.15) \tag{3.19}$$

$$\mu_c(T_{c,avg}) = 1.16E-4\ exp\left(\frac{3755}{T_{c,avg} + 273.15}\right) \tag{3.20}$$

The density of the coolant salt at the average temperature of the coolant salt $\rho_c(T_{c,avg})$ is 1767.1 kg/m^3 while the dynamic viscosity at the average temperature of the coolant salt $\mu_c T_{c,avg}$ is 0.0146 Pa s. The volumetric flow rates of the fuel salt and the coolant salts can be calculated using the respective mass flow rates and densities as shown during the reactor core analysis. The volumetric flow rate of the fuel is $\dot{V}_f$ is 0.0115 m^3/s and the volumetric flow rate of the coolant salt is $\dot{V}_c$ is 0.0302 m^3/s. It was chosen to select the number of tubes to ensure the coolant flow within the heat exchanger tube bundle, turbulent with Reynolds number Re_D greater than 3000. When the number of tubes is 200, the Reynolds number of coolant salt inside the tubes is calculated using Equation 3.10. The calculated Reynolds number is 4378.1. The Prandtl number for the coolant salt can be calculated using Equation 3.11 and the calculated value is 31.6. The Reynolds number is higher than 3000. The Gnielinski Equation 3.21 was chosen to calculate the Nusselts number [50].

$$Nu_D = \frac{(f/8)(Re_D - 1000)Pr}{1 + 12.7(f/8)^{1/2}(Pr^{2/3} - 1)} \tag{3.21}$$

The Gnielinski Equation 3.21 requires the Darcy friction factor f to calculate the Nusselts number. The Drarcy friction factor was calculated using the Colebrook-White equation.

$$\frac{1}{\sqrt{f}} = -2log\left(\frac{\epsilon}{3.7D_h} + \frac{2.51}{Re\sqrt{f}}\right) \tag{3.22}$$

Here, ϵ is the absolute roughness of the pipe. The roughness of the pipe surfaces depends on how it is manufactured and what surface treatments are performed. For our purposes, it was assumed that the absolute roughness ϵ is 1E-6 m. For the calculated Reynolds number Re_D of coolant salt in the tubes and the assumed roughness ϵ, Drarcy's friction factor f is 0.039. Using the Darcy friction factor along with Re_D and Pr of the coolant salt, the Nusselt's number Nu_D was calculated with Equation 3.21. The Nusselt's number Nu_D is 1.7621. The calculated Nusselt's

number is used to calculate the heat transfer coefficient $\tilde{h}$ between the inner tube wall and the coolant salt using Equation 3.13. The calculated heat transfer coefficient $\tilde{h}$ is 363.4 $\mathrm{W/m^2K}$.

Once the heat transfer calculation on the tube side is completed, attention was paid to the shell side. The inner diameter of the heat exchanger shell was assumed to be equal to the diameter of the tube bundle. The diameters of the tube bundle can be obtained from tabulated data [51]. Data do not exist for 0.25 in outer diameter tubes, therefore the following equation is used to estimate the diameter of the tube bundle D_b,

$$D_b = \left(\frac{N_t}{K}\right)^{(1/n)} \tag{3.23}$$

Here, N_t is the number of tubes, K and n are constants that are tabulated according to the design. For a triangular pitch of 1.25× outer tube diameter, with 2 passes, K and n are 0.249 and 2.207 respectively. The calculated diameter of the tube bundle is 0.1315 m. It was assumed that the diameter of the bundle is the inner diameter of the shell. Tube bundles of heat exchangers are held together by baffles. The baffles are also designed to mix and redirect flow on the shell side. However, in this calculation baffle designs are not considered; therefore, the length of the tube bundle will be an overestimation compared to an actual heat exchanger. The hydraulic diameter of the shell needs to be calculated because even though the shell resembles a pipe, the bundle of tubes creates an obstruction to the flow of the fluid. Hydraulic can be calculated as,

$$D_h = \frac{4Ac}{P} \tag{3.24}$$

Here, Ac is the total flow area that is 0.00725 $\mathrm{m^2}$ and P is the total wetted perimeter equal to 4.40 m. The hydraulic diameter of the shell D_h is 0.00659 m. Using the calculated hydraulic diameter, the Reynolds number can be calculated

with flow velocity and dynamic viscosity using Equation 3.10. The flow velocity on the shell side can be calculated using the volumetric flow rate and the flow area on the shell side. The flow velocity on the shell side $v_{f,shell}$ is 1.5853 m/s. The Reynolds number Re_{Dh} calculated is 1503.0. The Prandtl number Pr_f of the fuel salt is equal to the value calculated previously, since the average temperature of the heat exchanger is equal to that of the reactor. The Prandtl number Pr_f is 29.0. The Nusselt's number Nu_{Dh} for the shell side was calculated using the modified Seider-Tate formulation previously shown in Equation 3.12. The calculated Nusselt's number Nu_{Dh} is 12.24. The average heat transfer coefficient $\tilde{h}$ between the fuel in the shell and the tube is calculated using Equation 3.13. The average heat transfer coefficient $\tilde{h}$ between the fuel in the shell and the tube is 1858.3 $\mathrm{W/m^2K}$. The overall heat transfer coefficient of the heat exchanger U_{hx} calculated using individual heat transfer coefficients previously calculated as shown in Equation 3.18. The overall heat transfer coefficient of the heat exchanger U_{hx} is 303.96 $\mathrm{W/m^2K}$. At the beginning of the calculation of the heat exchanger design, the overall heat convection requirement UA_{hx} was calculated. Using the overall requirement for heat convection UA_{hx} and the calculated overall heat transfer coefficient U_{hx}, the required tube bundle surface area A_{hx} can be calculated as,

$$A_{hx} = \frac{UA_{hx}}{U_{hx}} \tag{3.25}$$

The total surface area required for the tube bundle is 49.95 m^2. Using this surface area and the total perimeter of all tubes, the required tube length L_{tube} can be calculated as,

$$L_{tube} = \frac{A_{hx}}{N_t P_t} \tag{3.26}$$

Here, N_t is the number of tubes in the tube bundle which is 200 and P_t is the outer perimeter (circumference) of a single tube. The required length of the tube

bundle is 12.518 m. With the calculated length and cross-sectional area of the tube, the coolant volume of the tube bundle was calculated. The coolant volume of the tube bundle is 0.056 m^3. The volume of tube metal is 0.023 m^3. The length of the shell is assumed to be half of the tube bundle, since tubes are U-tubes. The volume of the shell side of the heat exchanger is 0.045 m^3.

Once volumes are calculated using the outer surface area and inner surface areas, heat transfer rates can be calculated for the respective sides. Heat convection on the shell side $hAnom_p$ is 0.077965 MW/K and heat convection on the tube side $hAnom_s$ is 0.018150 MW/K. Flow fraction-based convections $hA(FF)$ can be calculated using the same approach as described in fuel channel heat transfer calculation. However, it is clear that this approach cannot be applied to the tube side since the numerator term of the Gnielinski Equation 3.21 becomes negative when the Reynolds number is less than 1000. Therefore, assuming that the heat transfer coefficient changes linearly with the flow fraction, a simple function was implemented. While this approximation is not accurate, it can be used for first-order models. The flow fraction FF dependent convection equations are,

$$hA_p(FF) = 0.07797FF^{0.33} \tag{3.27}$$

$$hA_s(FF) = (1 - 0.01)hAnom_s\ FF + 0.01hAnom_s \tag{3.28}$$

The preliminary safety report of MSRR does not provide any details about the reactor access vessel. Therefore, it was assumed that the reactor access vessel has a fuel volume of 0.04 m^3. The total volume of fuel residing in the pipes can be calculated by subtracting the total volume of fuel residing in the core, shell side of the heat exchanger and the assumed access vessel volume from the total fuel volume in the primary loop. The total fuel volume in the pipe is 0.0146 m^3. There are three main pipe sections in the primary loop. They are the pipe connecting the reactor

vessel to the access vessel, the pipe connecting the access vessel to the shell side of the heat exchanger, and the return pipe of fuel from the heat exchanger shell side to the reactor vessel. It was assumed that all pipes lengths are in ratio of 1:2:3, respectively. Using the assumed ratio, individual pipe volumes were calculated.

The MSRR uses a radiator to remove heat from the reactor system, as shown in Figure 3.7. The radiator is a cross-flow design. Like the heat exchanger, the information on the design of the radiator is not provided in the preliminary safety analysis. The heat transfer coefficients of the cross-flow tube banks can be calculated with several approaches, as shown in [50]. The current radiator model of SMD-MSR is not capable of modeling a radiator with two separate heat transfer coefficients because the tube metal is not represented. Instead, the model uses an overall heat convection value. Cross-flow tube banks require a correction factor to use LMTD. Therefore, the overall convection hA was calculated using average temperatures of both the primary and secondary sides using Newton's cooling law.

$$\dot{Q} = hA_{rad}(T_{salt,avg}T_{air,avg}) \tag{3.29}$$

Here $\dot{Q}$ is the thermal power of the reactor, hA_{rad} is the overall heat convection of the radiator, $T_{salt,avg}$ is the average temperature of the coolant salt in the radiator and $T_{air,avg}$ is the average temperature of the air in the radiator. The calculated overall heat convection of the radiator hA_{rad} is 0.0024 MW/K. The volume of the tube coolant and the volume of air on the air side are required to represent the radiator. Since calculating this information is tedious and provides less significance to final transient results, the MSRE radiator was scaled down using the cube-square law to find volumes on each side. Each pipe connecting the radiator and the heat exchanger tube side was assumed to have $0.01\,m^3$. Furthermore, the radiator model can be completely replaced with the UHX model and an alternative model of MSRR was created with the UHX to represent the radiator. Many of the trivial calculations are not detailed in this section. However, the developed MSRR model is included

in the repository [21] and it is recommended to read through the input files of the model.

3.4 Transient Simulation Strategy

This section describes the transient simulation strategy used in this work. Normal and off-normal transients are the result of event sequance. Therefore, event trees and initiating events are discussed in Section 3.4.1. Then normal and off-normal transients are discussed in Sections 3.4.2 and 3.4.3, respectively. Being able to understand depletion and parameter uncertainty of transients is important and the method of performing such an analysis is discussed in Section 3.4.4. Finally, a possible MSR start-up sequence is detailed in Section 3.4.5.

3.4.1 Event Trees

Event trees are a visual representation of the propagation of events. When analyzing complex systems such as MSRs, event trees can be utilized to predict the propagation of hypothetical or present state of the system. The visual representation of event trees makes them an excellent communication method. Anyone with sufficient understanding of the represented system will be able to comprehend the sequence of events that took place to arrive at the postulated or current status of the system. Any transient can be categorized into normal and off-normal transients. Classification is based on the anticipation of the outcome and type of reactor. For example, reactor pulses are routinely performed in research reactors such as TRIGA to demonstrate the effects of negative feedback, but a commercial power reactor would yield disastrous results. In this work, transients initiated by the reactor operator are considered normal transients, whereas transients initiated by external or unintended internal events are considered off-normal transients. Based on this distinction, off-normal transient initiating events can be classified as shown in Figure 3.11.

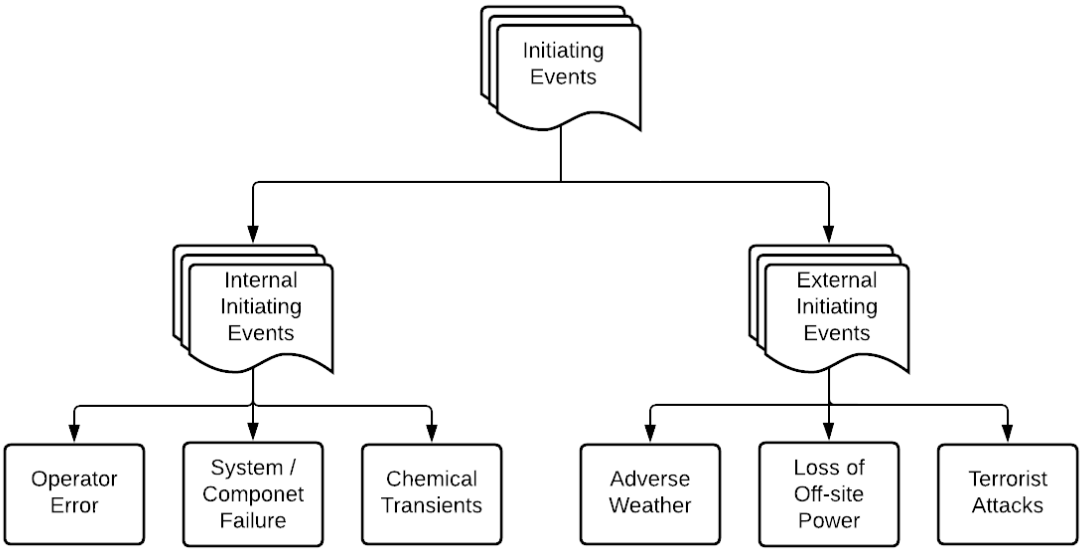

Figure 3.11: Initiating event classification

3.4.2 Normal Transients

Normal transients are transients that are performed regularly; therefore, outcomes are already understood. There is always the possibility that a routine transient triggers an off-normal transient due to SSC malfunctioning. However, these types of events are studied under off-normal transients for the scope of presenting work. The normal transients discussed in Section 5 are intended to help reader in understanding MSR dyanmic behavior through familiar transients and to characterize the considered systems to understand their unique dynamics.

3.4.3 Off-normal Transients

Off-normal transients are initiated by external or unintended internal events and therefore can result in unseen event sequences. In reactor licensing, the NRC regulator mainly pays attention towards radiological impact on the surrounding population and the environment. However, from a reactor developer and a utility point of view, monetary loss and damage to reputation alone is a worthy enough consideration even if the accident does not produce a concerning radiological event. The licensing approach of NRC specifically considers the hypothetical maximum accident. The maximum hypothetical accident involves an event sequence in which the reactor containment was compromised resulting in a significant radiological release. The SMD-MSR toolkit is not designed to analyze such scenarios and has no capability of tracking a large inventory of isotopes or model dispersion. However, SMD-MSR can be used to model the intermediary event sequence between the external initiating event and SSCs failure. This capability is demonstrated with off-normal transients performed and detailed in Chapter 5. MSR hypothetical maximum accidents in MSRs are vastly different from what can be seen in LWR due to the absence of a high-pressure boundary. For example, a hypothetical accident sequence for MSRR is shown in Figure 3.12. Here, the transient is initiated by losing off-site power. If the power on site does not fail, the event sequence will end.

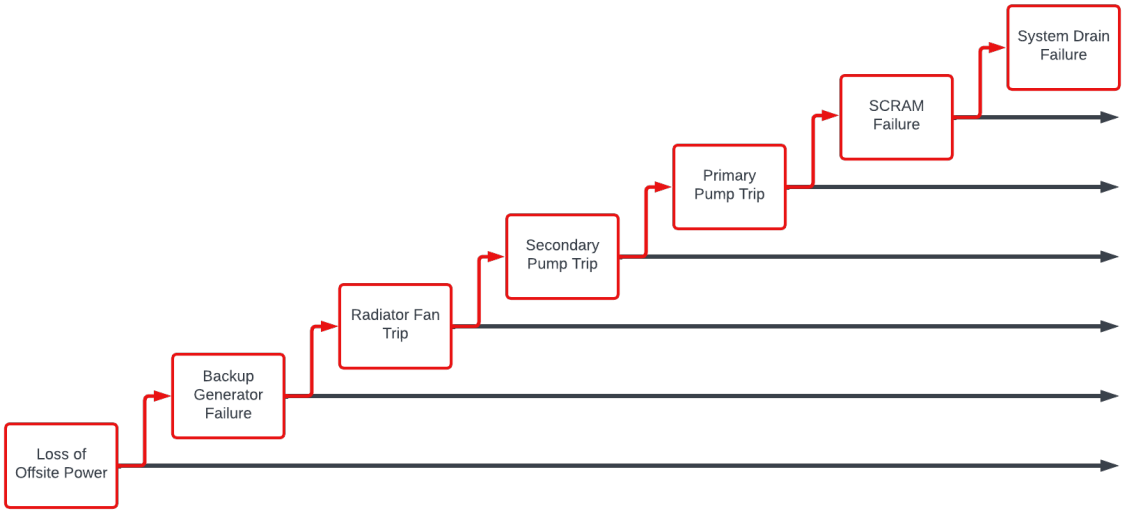

Figure 3.12: MSRR accident progression

If we assume that the on-site backup generators also fail, then all high-voltage electrical components such as radiator fan, primary, and secondary pumps will fail, effectively eliminating forced circulation and ultimate cooling of the system. During an event of this magnitude, the reactor would be SCRAMed and the primary system would be drained without operator intervention. However, if we assume that both of these passive safety layers fail, the result will be a MSR at it maximum accident the SMD-MSR can model.

3.4.4 Depletion and Parameter Sensitivity Simulations

Nuclear fission produces many FP that change both the nuclear properties and the thermophysical properties of fuel salts. The effects of depletion were discussed in Section 2.4.8. The SMD-MSR toolkit is unable to calculate neutronic parameters dependent on depletion. Therefore, fuel depletion calculations are done using external programs such as SERPENT or SCALE. Due to the simplicity and execution speed of the modeling approach in SMD-MSR, it can be used to perform a postulated transient by changing depletion-dependent data to evaluate system behavior changes throughout the considered fuel cycle. Fuel depletion calculations can produce depletion dependent neutronics data. These data can be organized into a text file or a CSV file as a time series. Once a time series of neutronic parameters is created, it can be used to initialize the dynamic model at the desired depletion point. Initialization can be performed manually; however, it is recommended to use a Python script as is included in the SMD-MSR toolkit. Modelica's standard library does include lookup tables that allow preloading of text and CSV files. These lookup tables can also be used if no full life-cycle evaluation is performed.

Since MSRs are understudied systems, it is necessary to understand the effects of parameter uncertainty on reactor performances. Understanding the acceptable uncertainties associated with the nuclear and physical parameters can help reactor developers and regulators determine an acceptable safety envelope for a specific MSR

design. Parameters such as the thermophysical properties of MSR materials are not yet measured to a sufficient degree of accuracy. Measuring these parameters is challenging since it is difficult to produce radiation effects in surrogate materials, as materials would experience in a MSR. Ionizing radiation is capable of greatly affecting both the molecular and lattice structure of materials. Parameter sensitivity studies can be conducted by implementing sensitivity coefficients in model parameters. The deployed sensitivity coefficients can be altered during the initialization of the dynamic model, as done for depletion studies. Multiple depletion dependent and parameter sensitivity analysis are conducted in this study. These transients and their results are discussed in Chapter 5. All the supporting scripts to perform the said analysis are included in the repository of SMD-MSR, [52].

3.4.5 Reactor Start Up

Reactor start-ups are complex operations that require close attention. When considering LWRs, there are two types of reactor start-ups based on the reactor temperature at which the start-up operation is started. The first is known as a cold start-up, where the reactor start-up begins from room temperature. Cold start-ups are generally done when a fresh core is brought to criticality or after a lengthy refueling operation. If the fuel in the core has never undergone fission, there will be no fission products to undergo decay and produce decay heat. Similarly, if the refueling operation was long, the fission products would have decayed enough so that the decay heat produced by the long-lived fission products is low, allowing the system to cool to room temperature. Cold start-ups require an external neutron source. The second type of start-up is hot start-up. This is a scenario where the reactor is brought back online when the reactor is nearly at operational temperature. Hot start-ups may be performed after a reactor SCRAM followed by an external event that does not damage the plant, a short maintenance event, or a short refueling that requires the reactor to be shut down. Hot start-ups do not require external neutron

sources since the fuel produces neutrons through mechanisms such as spontaneous fission or through nuclear reactions that occur as a result of decay of fission products. During cold start-ups, since the fuel and moderator are at a much lower temperature than that of the operational temperature, the reactor feedbacks alone cannot control the reactor, making the start-up procedure tedious. In the case of PWRs, burnable poisons are in the form of boric acid, which is added to the reactor coolant water to provide a reactivity buffer. Cold start-ups require longer time periods than hot start-ups because it requires more time and close attention to heat up the system to operational temperatures.

Similarly to LWRs, MSRs can have cold and hot start-up operations based on the power history of the core. In MSRs, the use of external neutron sources during the start-up procedures is similar to that of LWRs. Unlike in LWRs, it is not possible to heat the primary loop of MSRs using fission heat during a cold start because the eutectic salt mixtures used are solids at room temperature. Therefore, fuel and coolant salts are heated to operational temperature through external means prior to introduction into the system. The initial heating and melting of the fuel and coolant salt can be carried out in external storage tanks that can double as drain tanks. The reactor system itself requires heating to the same temperature as the molten salt prior to the introduction of fuel and coolant salts. The system can be heated by means of electric heaters that are wrapped around components such as pipes and heat exchangers, or directly heated by heating the interior of the containment using hot air or thermal radiation. This initial heating of the reactor components is important to avoid structural failures due to sudden heating of the structural matrix from the introduction of molten salt into a cold reactor system. Once the reactor system, fuel, and coolant salts are at operational temperature, the molten salts can be pumped to their respective loops to resume start-up operations.

For the purposes of this transient, it is assumed that the entire system is continuously heated to maintain the average core temperature throughout the system,

and therefore there are no temperature gradients throughout the system. Because there are no temperature gradients, there is no natural convection driven by buoyancy, which makes the effective bulk flow rate zero when forced convection is absent. The fuel salt and the coolant salt remain static in their respective loops. At this stage of the start-up, the control rods are fully inserted, and the reactor is in a stable static subcritical state. An external neutron source is introduced to the reactor core to initiate fission reactions in the fuel salt, and the neutron population is allowed to stabilize. Once the neutron population is stabilized, the source multiplication method can be done by withdrawing control rods step by step to find the static criticality. The effective multiplication factor k_{eff} of the core with the external source can be found by Equation 3.30.

$$k_{eff} = 1 - \frac{l\,S}{n_{\infty}} \tag{3.30}$$

Where l is the prompt neutron lifetime, S is the source strength in neutrons per second, and n_{∞} is the steady-state neutron population of the core. When the initial effective multiplication factor, $k_{eff,1}$, is known, the desired multiplication factor to be reached, $k_{eff,2}$, can be used to calculate the target steady-state neutron population $n_{\infty,2}$. Then the current steady-state neutron population $n_{\infty,1}$ and the target steady-state neutron population $n_{\infty,2}$ can be used to calculate the required reactivity ρ_2 to reach the target multiplication factor $k_{eff,2}$ from the current reactivity ρ_1 according to Equation 3.31.

$$\rho_2 = \rho_1 \frac{n_{\infty,1}}{n_{\infty,2}} \tag{3.31}$$

In practice, only a half of the predicted required reactivity, ρ_2, is inserted into the reactor. This is done as an operational safety measure because Equations 3.30 and 3.31 are extrapolations performed for a non-linear function.

Chapter 4

Benchmark

This chapter is dedicated to validate SMD-MSR against MSRE step insertion transients. Furthermore, a detailed benchmark is carried out comparing the implementations of SMD-MSR in MATLAB Simulink and Modelica. This chapter features previously published material; therefore, appropriate disclosures are included with citations.

4.1 Validation Against MSRE Data

Disclosure - This section was originally published as part of a journal article [15]. The text here is modified to fit this publication.

SMD-MSR toolkit is validated against the available MSRE results. During the design and operations of MSRE several experiments were carried out, and the results were archived. These experiments include some bench and mock-up experiments. Bench and mock-up experiments were performed during the development and design phase of key reactor components, such as the reactor and the main fuel pump. During operations of MSRE reactivity related experiments were conducted to understand MSR dynamics and varify develop MSR analysis tools.

Two step insertion transients were performed to validate SMD-MSR against MSRE experiment results. The experiment was carried out by inserting the 19.6 pcm step reactivity into the MSRE fueled with ^{233}U. The system was brought to a steady state at 5 MW before performing the experiment [53]. To perform transients and replicate experimental results, both the one-region and nine-region MSRE models implemented in SMD-MSR were initially brought to steady state at the full power of 8 MW. At 2000 s of the simulation time the power was reduced to 5 MW. The simulation was continued for a simulation time of 3500 s without any disturbance to reach a new steady state at 5 MW of the reactor power. At 5500 s of simulation time, 19.6 pcm reactivity was added as a step insertion. The power results of both simulations were extracted and the deviation of power (ΔP) during the transient was plotted along with the experimental results in Figure 4.1.

Upon close inspection of Figure 4.1 it is clear that both the one- and nine-region models create results comparable to the experiment. The error between the experimental and simulation results is not calculated because the experimental results contain a significant amount of noise. The results of the one-region model reach a higher peak power than those of the experimental results and the nine-region model. However, the one-region model produces a Full Width Half Max (FWHM) that is closer to the experimental results. The nine-region model produces a peak power identical to that recorded in the experiment, even though FWHM is significantly underestimated. Both models can be greatly improved by using temperature-dependent physical properties.

4.2 Simulink Vs Modelica Versions

Disclosure - This section and the included subsections were originally published as part of a journal article [15]. The text here is slightly modified to fit this publication.

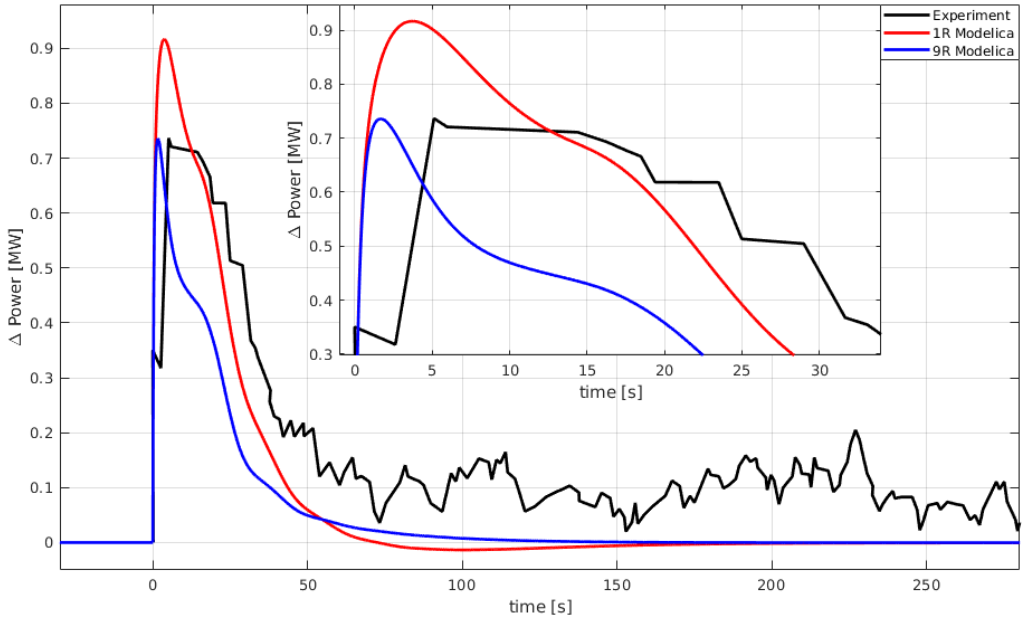

Figure 4.1: 19.6 pcm step insertion benchmark on ^{233}U fueled 5 MW MSRE [15]

A code-to-code benchmark was conducted for two criteria: simulation run times and Modelica model error based on Simulink model. The benchmark was performed using default solvers of each modeling environment on the same computer. The solver parameters are summarized in Table 4.1 and computer specifications are summarized in Table 4.2.

Simulation run time is an important consideration when selecting a modeling environment. Faster simulation run times allow the user to perform a large number of transients while making slight perturbations to selected parameters and compare results with higher computational efficiency. The advantage of faster simulation run times is more evident for high-fidelity dynamic models or for simulations with longer simulation times (simulation time $> 10,000$ s). The development of understudied reactor systems such as MSRs demands rapid simulation capabilities to recognize unique design benefits. For the purposes of this study, the simulation execution time is measured by running the models of one-region MSRE in both simulation environments 100 times for a simulation time of 10,000 s on an identical server computer. All simulation runs were performed by allowing the solvers to converge for the first 2, 000 s of the simulation time. Then, for the next 8,000 s of simulation time, a sinusoidal reactivity insertion was performed with an amplitude of 10 pcm at a frequency of one radian ($\omega = 1$). The simulation execution time was measured using the built-in "time" command of the Linux operating system. To generate individual processes, the Python subprocess package is utilized, and the simulations were executed one by one on a single CPU. The obtained simulation run times are discussed in the Section 4.2.1.

To evaluate the deviation of the simulation results of the Modelica implementation for MSRE is calculated based on the MATLAB-Simulink version of MSRE. The error calculation is performed as follows (Equation 4.1):

$$ME_x = \frac{MR_x - SR_x}{SR_x} \tag{4.1}$$

Table 4.1: Solver Settings [15]

Solver Attribute	MATLAB Simulink	Modelica
Solver Type	Variable time step	Variable time step
Solver Name	ODE45	dassl
Maximum timestep	1E-2	1E-2
Tolerance	1E-6	1E-6

Table 4.2: Computer Specifications [15]

	Specification
Processor	2 × Intel(R) Xeon(R) CPU E5-2660 v3 @ 2.60GHz
RAM	94GB
Operating system	Ubuntu 20.04 LTS

Where ME_x is the Modelica error, MR_x is the Modelica result, and SR_x is the Simulink result of the parameter considered x.

The simulation results from the Simulink and Modelica models have different time vector lengths. To calculate the absolute errors of the simulation results, both time vectors were interpolated to obtain vectors with equal lengths and increments. Once all interested simulation results were interpolated, the absolute error of each parameter was calculated using the Equation 4.1. When the absolute errors were calculated, it was observed that large deviations are present during rapid changes of parameters during instances such as transient initiation. Upon further inspection, it was evident that these large deviations are caused by singular points. These deviations were eliminated to make the absolute error plots legible.

4.2.1 Simulation Run Times

The simulation run-time benchmark was performed as described in Section 4.2 for a MSRE model in both modeling environments. Simulation run times from the Simulink and Modelica MSRE implementation are captured in Figure 4.2. Upon inspection of Figure 4.2 it is clear that the MSRE model built in SMD-MSR Modelica runs faster than the MSRE model executed in Simulink. The mean simulation run time for Simulink was clocked at 19.00 minutes while the SMD-MSR Modelica variant clocked in at 13.17 s.

4.2.2 Step Reactivity Insertion at Full Power

The step insertion benchmark was performed by inserting 100 pcm (equivalent to \$0.241) of reactivity at a simulation time of 2,000 s. A constant power removal block was used as the UHX in the secondary FLiBe loop to remove heat from the system. Simulink and Modelica-based simulations were initialized using ^{235}U parameters that were used to validate the MSRE Simulink model [42]. The reactor parameters such as nominal power, core temperatures, and temperature reactivity feedbacks of both

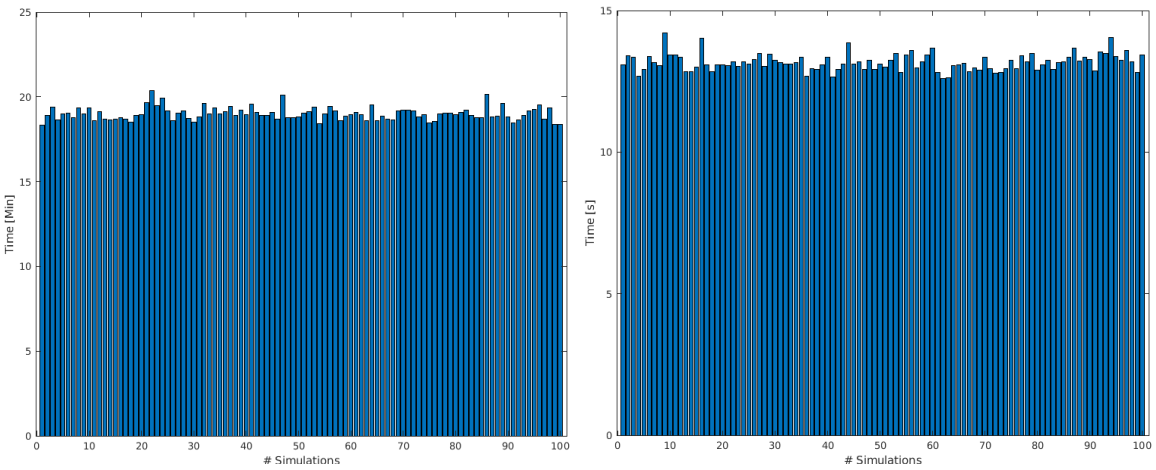

Figure 4.2: (left): SMD-MSR Simulink simulation run times (in minutes), (right): SMD-MSR Modelica simulation run times (in seconds) [15]

models were extracted and plotted in Figures 4.3, 4.4, and 4.5. The first 2000 s of the simulation is offset so that the captured results show the step insertion time at the zero time stamp in all three figures. Plots were started from -100 s to capture steady-state values of both simulations, leading to the external reactivity perturbation. In each figure, the Simulink model results are captured in solid red, whereas the Modelica model results are portrayed in blue dashed lines. The absolute error of the Modelica model for each parameter is calculated as previously shown in Equation 4.1. These error results are plotted along with the respective parameter on the right y-axis in solid green.

The reactor power and its constituents are shown in Figure 4.3; the total nominal reactor power, the nominal fission power and the nominal decay power are shown in the first, second and third panels, respectively. The leading 100 s of results shows that both simulations have reached steady state at 100% power. At full power, 93.2% of the power comes from fission, while 6.8% is produced from the decay of FPs. The nominal fission power shows an immediate increase at the 0 s mark due to the insertion of the 100 pcm step, where it gradually increases, reaching a maximum value of 1.58× nominal power. The decrease in fission power occurs by two different mechanisms as the fuel salt circulates through the primary loop. Circulation removes some of the delayed neutron precursors produced from the core region. Some of these precursors decay outside the core region during transit. The decrease in power initially after the peak occurs at a slower rate as circulation brings fuel salt that was outside the core when the power excursion occurs. This power behavior is unique to circulating fuel reactors and is reflected through longer transient times compared to solid fuel reactors, which last in orders of 100 s magnitude for sub prompt critical reactivity insertions. However, the increase in normalized decay power is more gradual and takes approximately 25 s to reach its maximum. The effects of the fission power are reflected in the decay power, since the concentration of FPs is proportional to the rate of the fission reaction. The combined effect of fission power and decay power can

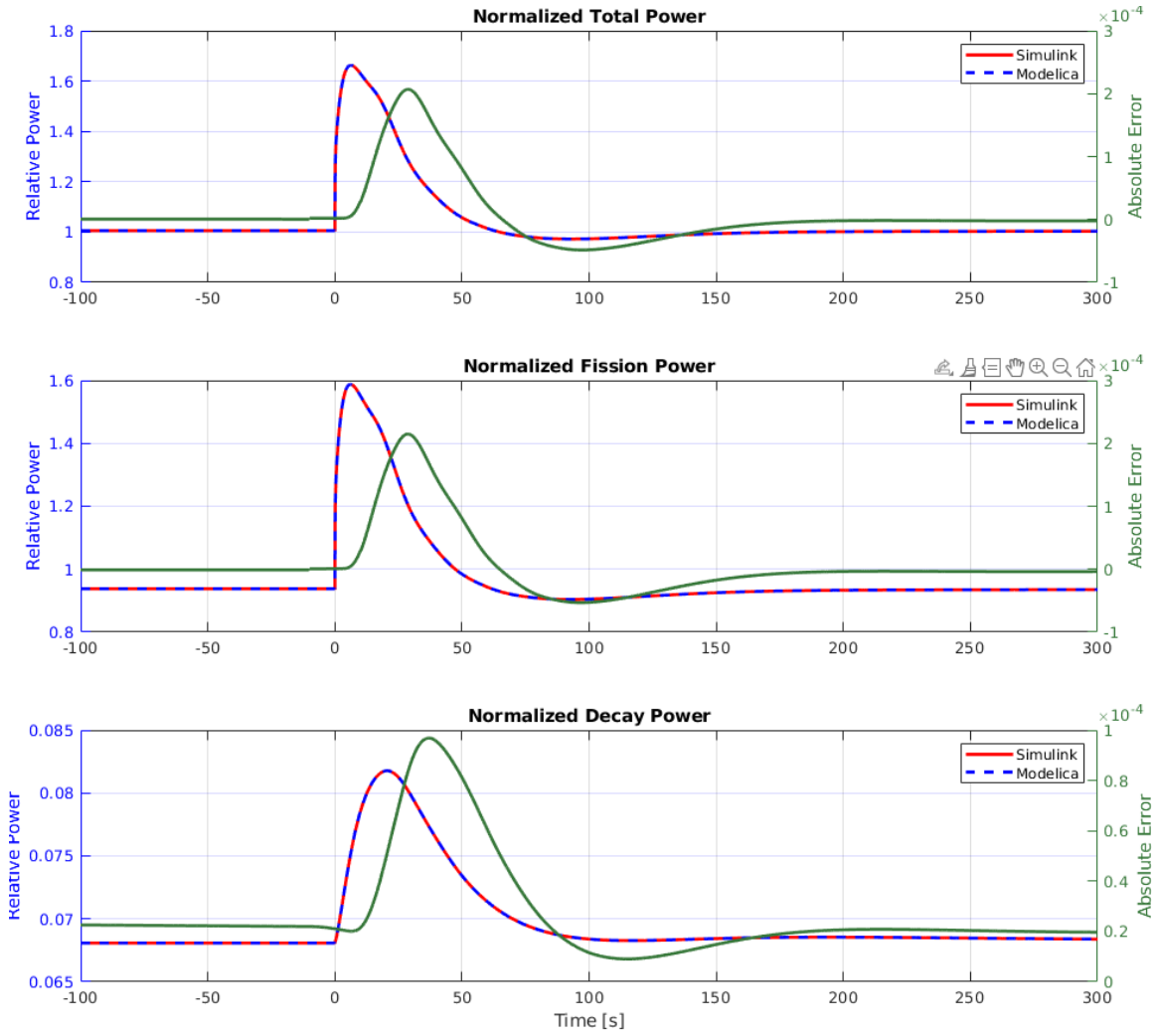

Figure 4.3: Power Results for 100 pcm Step Insertion [15]

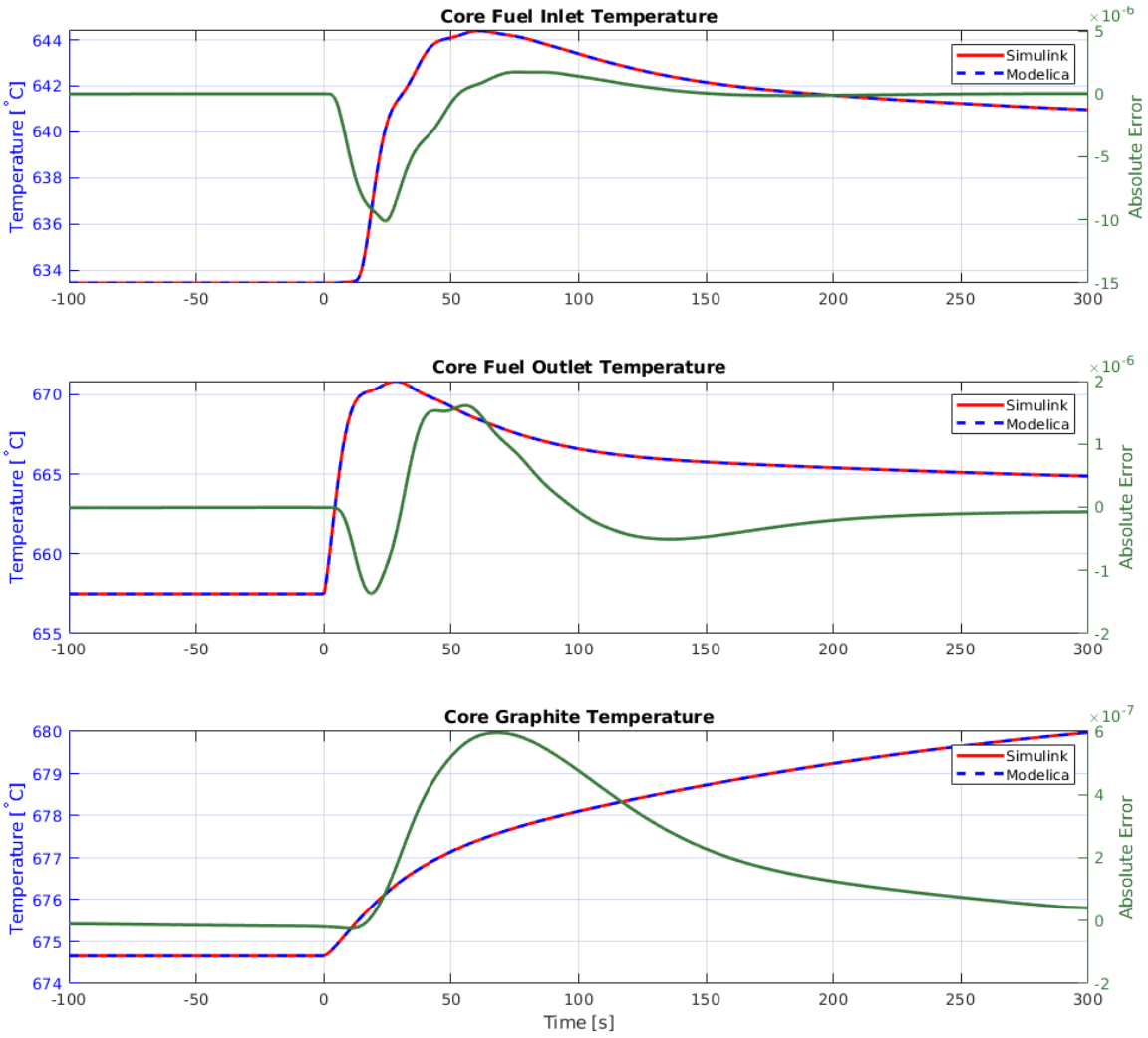

Figure 4.4: Temperature Results for 100 pcm Step Insertion [15]

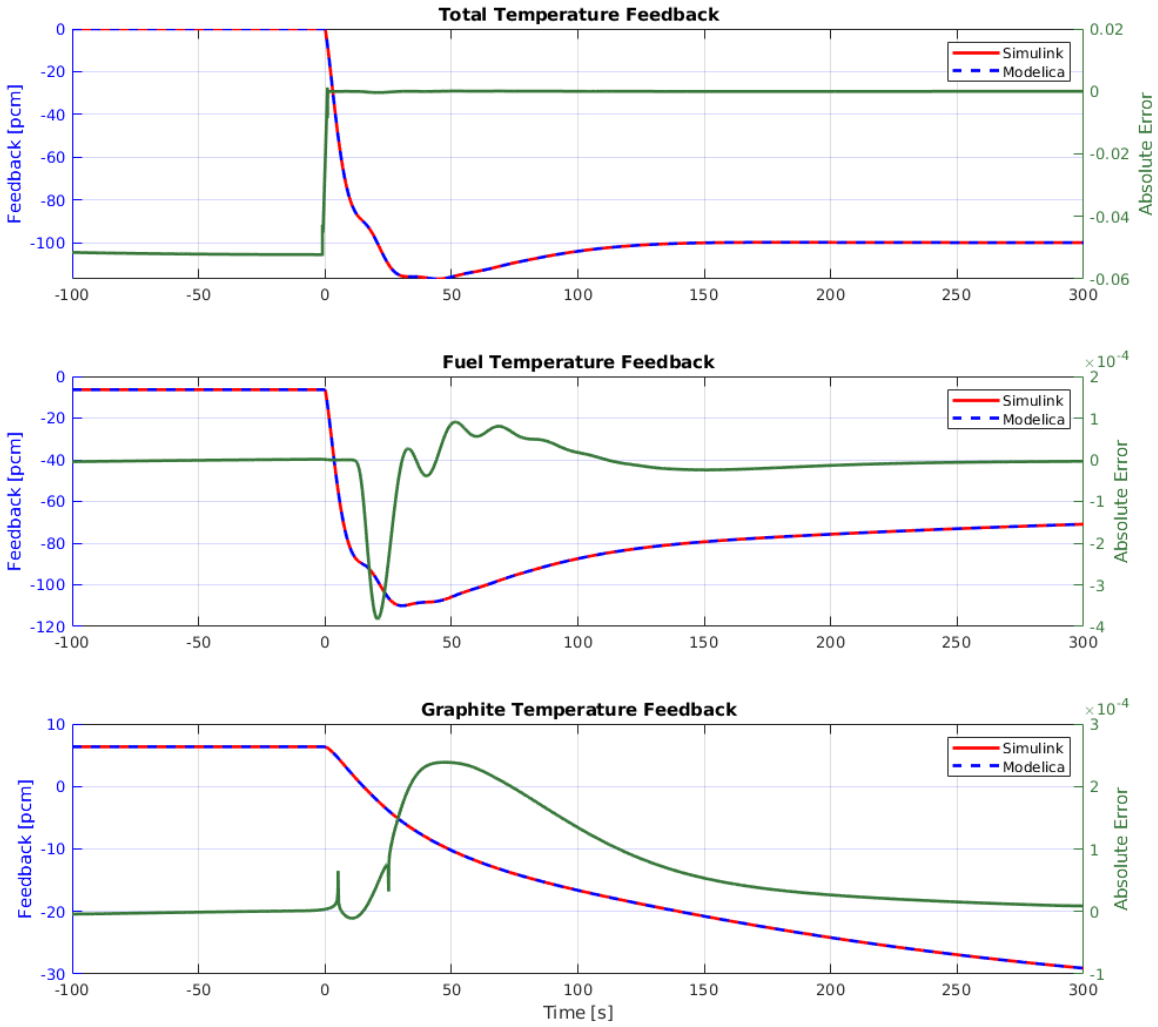

Figure 4.5: Temperature Feedback Results for 100 pcm Step Insertion [15]

be seen in the first panel, total nominal power. Upon close inspection of each power graph, it is clear that both Simulink and Modelica based models are in agreement, as both plots overlap and follow the same trend. Both simulations reach the same new steady state of 100% power following the transient. All absolute errors are in the magnitudes of $\times 10^{-4}$, which is negligible. The three power panels show that the error is subject to change during the transient. Normalized total and fission power do not show an error during the leading steady state to the transient state, unlike decay power, which has an absolute error of 2×10^{-4}.

Reactor temperatures are captured in Figure 4.4. The core outlet, core inlet, and graphite temperature are plotted in order from first to third panel. The first panel shows that the core fuel outlet temperature increases almost instantly while the core fuel inlet temperature shown in the second panel has a delay equivalent to the loop transit time of MSRE, 16.7 s, before the temperature increases. This is the expected behavior of an MSR since the fuel salt residing in the loop side is not subjected to immediate fission heat, as discussed previously. Both core fuel inlet and outlet temperatures reach their new steady state rapidly, while the temperature of graphite increases gradually and reaches its steady state beyond the captured time frame. Similarly to the power results shown in Figure 4.3; temperature results are in agreement. The absolute errors of the temperature results are lower than those of the power results. The absolute errors of the temperature results are in the magnitudes of $\times 10^{-6}$ for the temperature of the input and exit of the core fuel, while the error in the graphite temperature results is of the order of $\times 10^{-7}$. The temperature feedback and its constituents are depicted in Figure 4.5. The first panel shows the total temperature feedback, while the second and third panels show temperature-induced feedback from fuel and graphite, respectively. Temperature feedbacks are induced as a result of a temperature deviation from reactor temperature set points. At steady state, which can be seen from -100 s to 0 s, it is clear that the total temperature feedback is zero and stable. The increase in reactor temperatures seen in Figure 4.5 is reflected

in temperature-induced reactivity feedbacks. Since the core temperatures of both models are in agreement, the temperature feedbacks are also in agreement. Upon inspection of absolute errors, it is evident that the total temperature feedback error is significant during the initial steady state proceeding the transient. Due to the near-zero feedback values at steady state, a small deviation reflects a larger absolute error. Following the insertion of the 100 pcm step, the total temperature feedback compensates for the added external reactivity. Thus, the resultant reactivity is large enough to reduce the absolute error. It is clear that the absolute error of the fuel and graphite temperature feedbacks is in the range of $\times 10^{-4}$. The graphite error shows two extreme points in the simulation time range of 0 to 50 s.s. These extreme points are caused by the large changes in fuel temperature during the transient.

4.2.3 Off-Normal Transient

Both Simulink and Modelica models and their utilities can be used for a variety of simulations; to demonstrate this, several off-normal transients were performed to evaluate the performance of each model. For brevity, only one off-normal transient is presented here, but all transients performed, with input files, are included in the GitHub repository [21]. The transient presented simulates a worst-case scenario with simultaneous UHX trip, primary and secondary pump trips, DHRS open at nominal 8% power, and reactor SCRAM using external reactivity $\sim$ 1400, pcm for a ^{235} U-fueled MSRE. As in the transients shown above, perturbations were introduced at 2,000 s and run for 8,000 s ($\approx$ 2.22 h) of simulation time in both models. The simulation result time is offset by 2,000 s, so that simultaneous perturbations are made at the 0 s time stamp. The simulation results for key reactor parameters are shown in Figures 4.6, 4.7, and 4.8.

The nominal power is shown in Figure 4.6. From all three panels, it is clear that both simulations reached the full-power steady state leading up to the 0 s timestamp. The total nominal power (shown in the first panel) immediately decreases

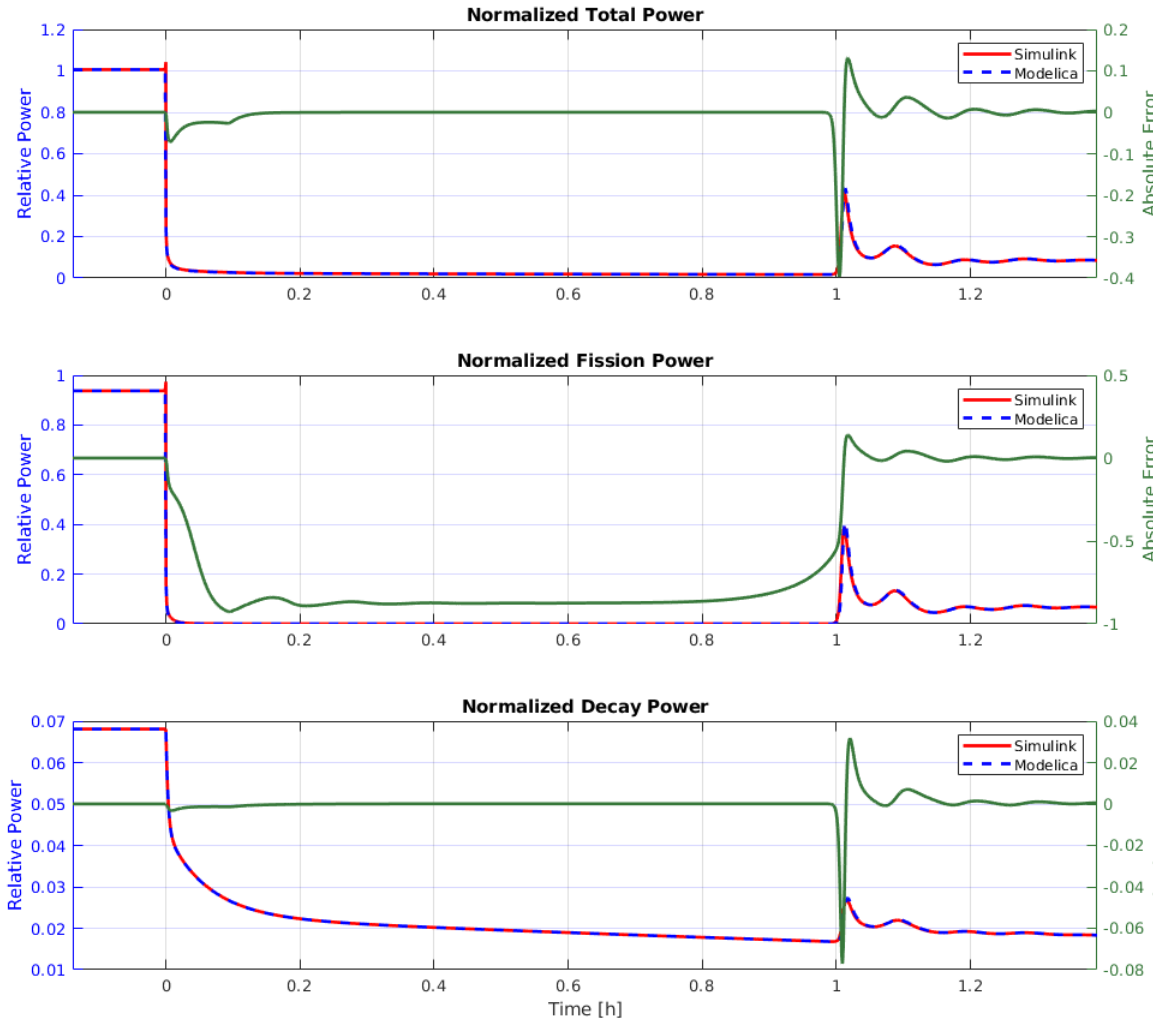

Figure 4.6: Power Results for simultaneous UHX, primary and secondary pumps trip, DHRS open (8%) SCRAM (-1400 pcm) [15]

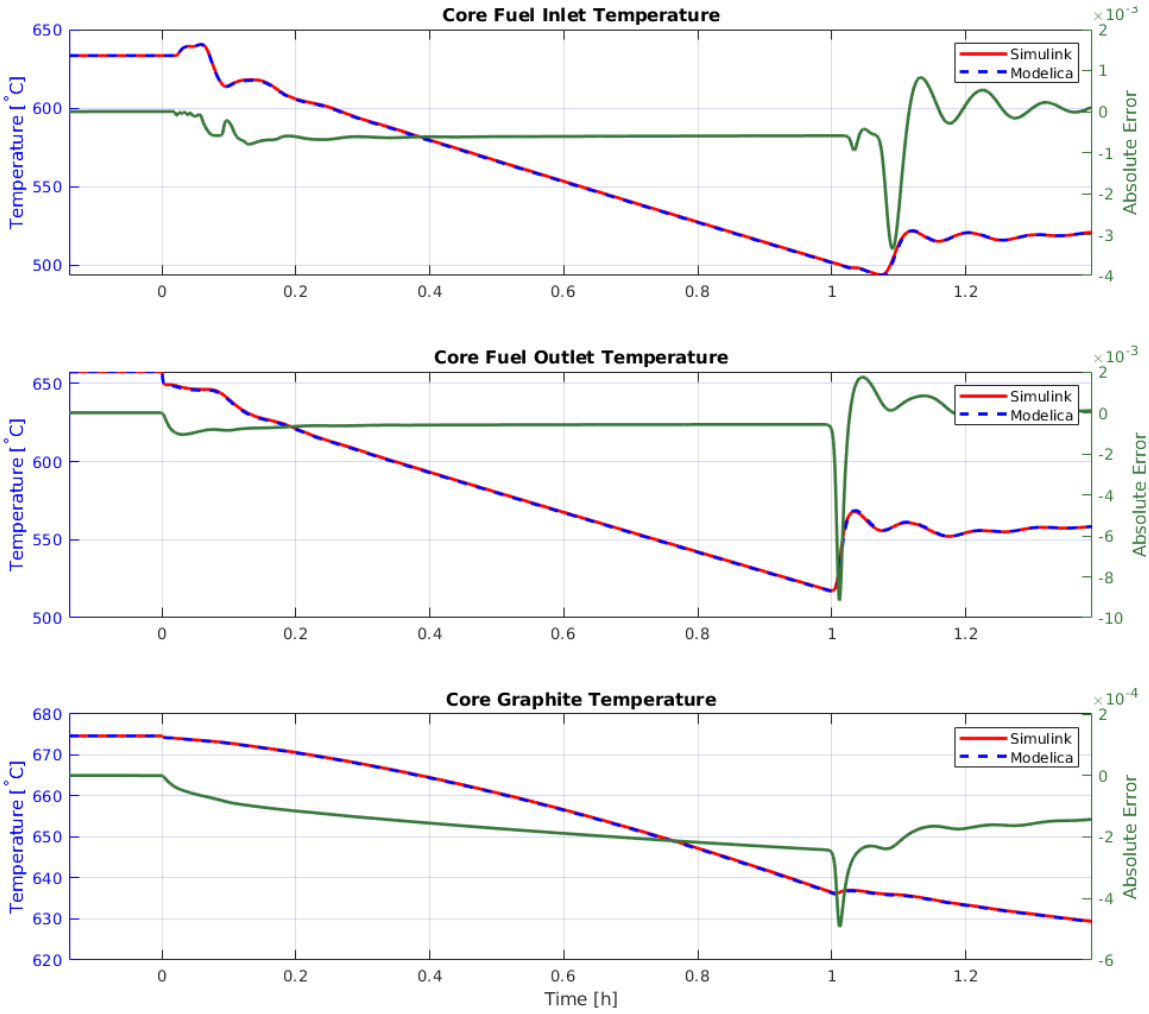

Figure 4.7: Temperature Results for simultaneous UHX, primary and secondary pumps trip, DHRS open (8%) SCRAM (-1400 pcm) [15]

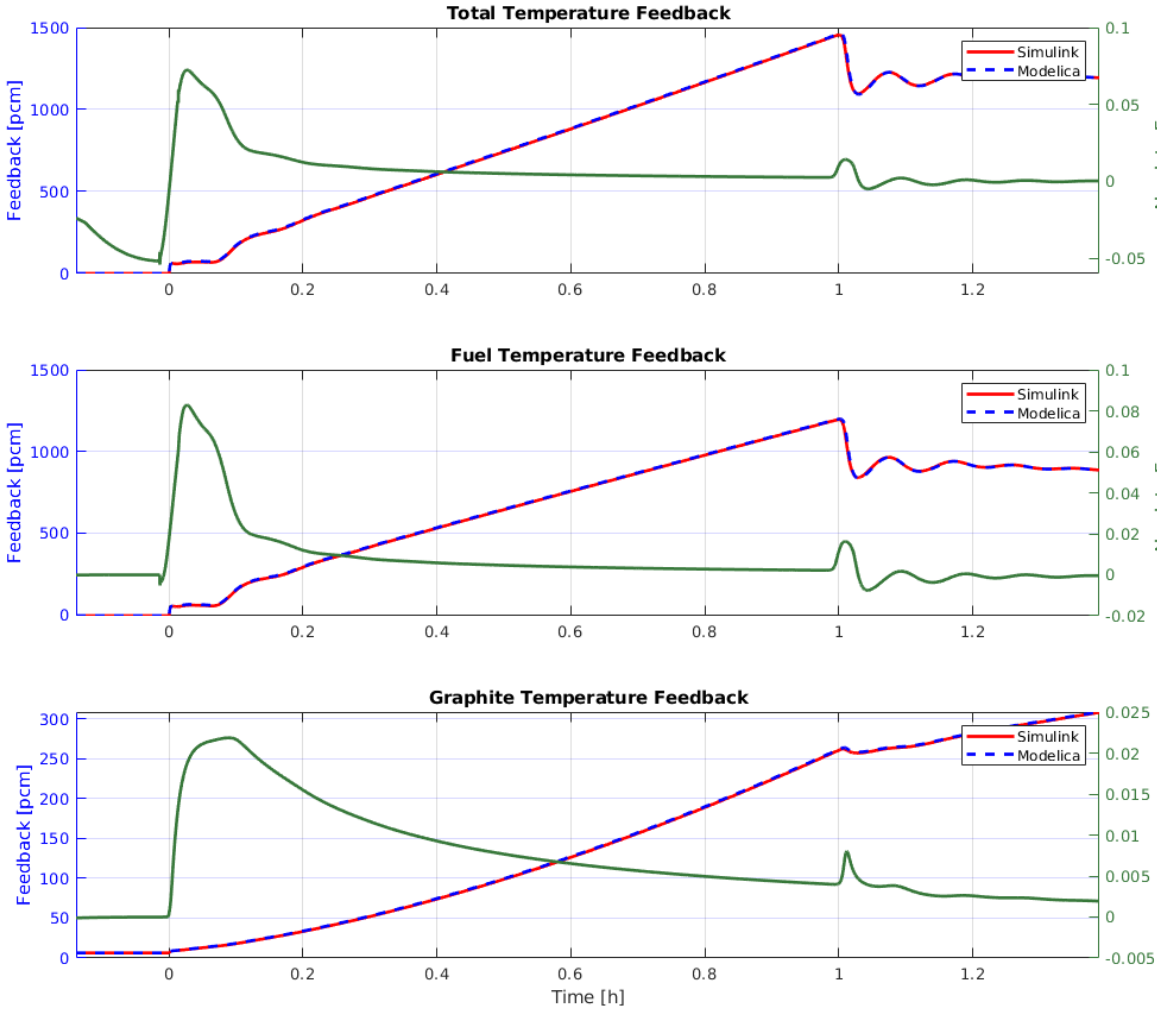

Figure 4.8: Temperature Feedback for simultaneous UHX, primary and secondary pumps trip, DHRS open (8%) SCRAM (-1400 pcm) [15]

when perturbations are introduced. The second panel (nominal fission power) shows that the reactor becomes subcritical. The nominal decay power gradually reduces, confirming the sub-critical state of the reactor. The reactor remains subcritical for 1 h since the introduction of perturbations into the system. When considering the right y-axis of all three power panels, it is clear that the absolute errors are large during the transient. The normalized total and fission power shows the largest deviation. The deviation stems from normalized fission power, which almost falls to zero during the transient. Since the normalized fission power falls to zero, even small results deviations are pronounced when the absolute error is calculated. Note that the highest error is recorded in the instance where re-criticality occurs. During steady states preceding and proceeding to transient states, absolute errors remain near zero.

The core temperatures are shown in Figure 4.7, illustrating the core outlet and inlet temperatures, respectively. It is clear that the temperatures are in a steady state, leading to 0 s. The core outlet temperature decreases rapidly at the start of the transient and then decelerates, while the core inlet temperature increases, reaching a maximum before declining. When the UHX is tripped, the only path for the system to reject heat is the DHRS. Since DHRS is located in the primary loop, heat flows from the secondary loop to the primary loop; increasing the core inlet temperature. Core graphite is cooling to reach equilibrium with core fuel average temperature, and it is reflected in the third panel of Figure 4.7. As a consequence of core fuel and graphite cooling, the total temperature feedback increases. Total temperature feedback and its constituents are shown in Figure 4.8. Since -1400 pcm external reactivity is used to SCRAM the reactor, the core remains sub-critical until the core cools down sufficiently to provide 1,400 pcm of total temperature feedback. At the 1 h mark, it is clear that total temperature feedback exceeds 1,400 pcm. The system achieves re-criticality approximately at the 1 h mark, which is reflected in the total and fission nominal power plots of Figure 4.6. A closer look at total nominal power reveals that total nominal power reaches a new steady state at 8% which corresponds

to a power removal rate of DHRS. Core temperatures and temperature-induced feedback also reaches a new steady state beyond the captured results time. When absolute errors of temperature are examined in Figure 4.7, it is clear errors fall within the range of $\times 10^{-4}$ to $\times 10^{-3}$. As seen in the power results, the largest deviations of temperature errors occur at the recriticality event. From examining Figures 4.6, 4.7, and 4.8, it is clear that both MATLAB Simulink and Modelica produce nearly identical results.

4.2.4 Nine-Region Model Comparisons

Two 100 pcm step insertion transients were performed for a reactor with the topology of ^{235}U fueled MSRE to compare nine-region core model results of SMD-MSR Modelica and a Simulink implementation published in [42]. Both models were inspired by stability analysis of MSRE conducted by ORNL and uses same parameters presented in the MSRE report [24]. Both nine-region models are similar in modeling approach and implementation except for a few differences. The nine-region Simulink model does not model dynamic decay heat explicitly and uses pure time delays to represent transport delays of fluid in pipes. The Modelica, nine-region MSRE model is equipped to simulate dynamic decay heat and utilizes variable time delays with two mass nodes in primary loop piping allowing deposition of decay heat. Having variable time delays accommodate Modelica model to perform transients with flow rate changes. Both models use the Mann's model heat transfer approach and modified point kinetics. Additionally, models share similar approaches of UHX for heat removal from the system. The Modelica version's heat exchanger is slightly different because it allows fuel to deposit decay heat in the primary side. Since the Simulink nine-region model does not simulate dynamic decay heat, two simulations were conducted with and without dynamic decay heat using the Modelica nine-region model. All transients were performed by bringing both models to steady state at full power for 2000 s of simulation time. Then a 100 pcm of reactivity is inserted as a step at

2000 s of simulation time. Important reactor parameters were exported and plotted. Figures 4.9 and 4.10 capture simulation results of Simulink model and compare against Modelica model with and without decay heat respectively.

From the first panels of Figures 4.9 and 4.10 it is clear that the normalized total power behaves identically in the Simulink model and in both Modelica models with and without dynamic decay heat. The reactor power response is similar to that observed with the one-region MSRE model as previously shown in Figure 4.3. However, the maximum nominal power reached by the nine-region models is ≈ 1.48 of the nominal power. Differences between reactor responses in one-region and nine-region models are explicitly discussed in Sections 5.1.4 and 5.1.5. Absolute errors of normalized power are on the order of $\times 10^{-4}$. Examination of the core inlet fuel temperatures in the second panels of Figures 4.9 and 4.10 reveals that the Modelica model with decay heat reaches 3 K higher temperatures than the Simulink and Modelica models without decay heat. The Modelica model with decay heat produces decay heat outside of the core in components such as ex-core piping and the primary side of the heat exchanger. The absolute errors of inlet temperatures of the Modelica model with decay heat are of the order of $\times 10^{-3}$, while the absolute error of the Modelica model without decay heat is in the range of $\times 10^{-4}$. According to the third panels of both figures, it is clear that all the core fuel outlet temperatures are in agreement. The absolute errors of the Modelica model with and without decay heat are in the $\times 10^{-4}$ range. The total temperature feedback depicted in the fourth panels of the two figures shows that the absolute error during the transient becomes ≈ 0. The large error window is a result of ≈ 0 pcm temperature feedback during the leading steady state.

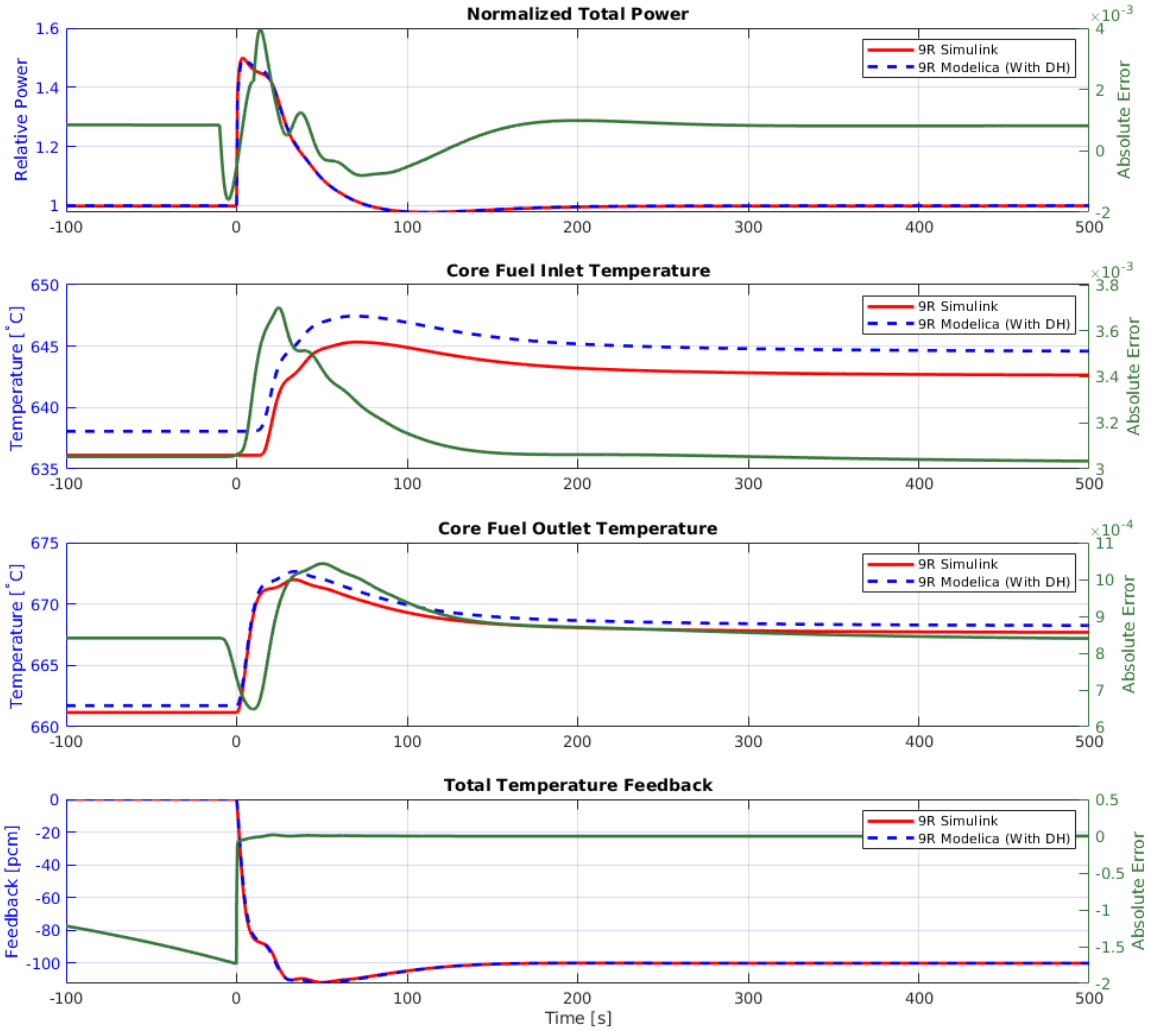

Figure 4.9: 100 pcm step reactivity insertion for Nine-Region MSRE [15]

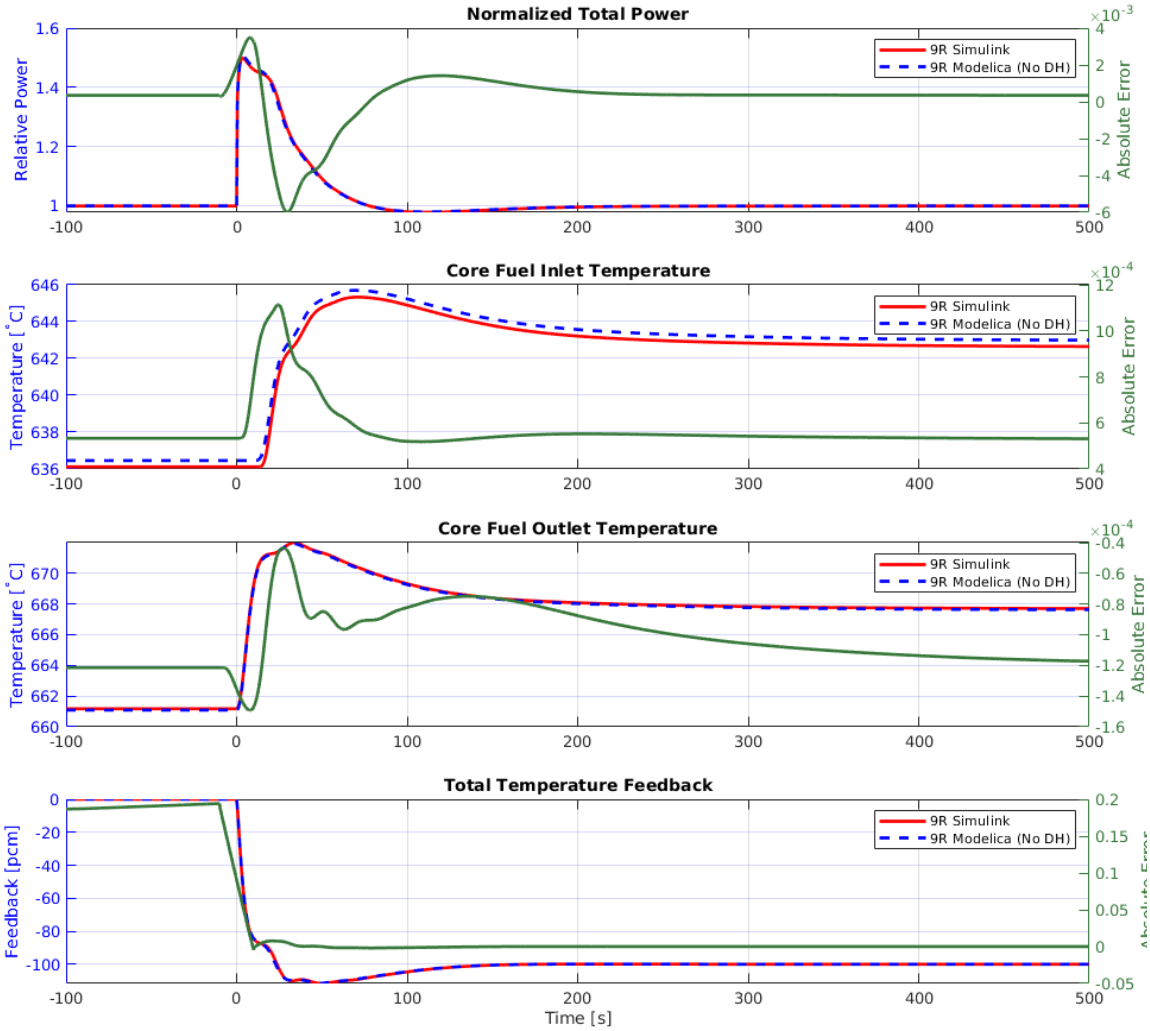

Figure 4.10: 100 pcm step reactivity insertion for Nine-Region MSRE without Decay Heat [15]

Chapter 5

Results and Discussion

This chapter is dedicated to present transients perfomed using developed models. Transients include normal and non-normal transients to gain insight into the system dynamic behavior of MSRs. Some of the results presented were previously published; therefore, appropriate disclosure statements with citations are included as appropriate. The transient behaviors observed and their implications to operations and safety of MSR are discussed within individual subsections for clarity.

5.1 MSRE Transients

Disclosure - This section and the included subsections were originally published as parts of two separate journal articles [13, 15]. The specific citation is mentioned at the beginning of each section. of The text here is slightly modified to fit this publication.

The presented model allows simulation of the dynamic behavior of the MSR system during a large variety of transients. This includes reactivity insertions, load following, loss of ultimate heat sink, pump trips for both primary and secondary loops, accidental opening of DHRS, cold slug insertions, etc. The user can use these simulations to develop and fine-tune the functional requirements of each component.

Previously published studies [42] and [43] demonstrated some of these capabilities. The current study focuses mainly on new features, namely, dynamic decay heat production and removal.

The frequency analysis of the SMD-MSR model is performed with MSRE parameters. The results compare favorably with the MSRE experimental data and with the previous MSRE model [42]. Since demonstration of the new features is the main focus of this study, the plots are not included in the manuscript, but can be found online at [52]. The GitHub repository [52] also contains plots for several other benchmark transients that compare the previous MSRE model [42] and the experimental data from MSRE.

For brevity, only several transients are chosen to demonstrate the new features. Input files for additional interesting transients are included in the GitHub repository [52]. The first scenario focuses on the functionality of the decay heat removal system, showing the system behavior when the ultimate heat sink is lost and DHRS opens, without any control rod action. The second scenario is similar to the first scenario but with control rod insertion. These scenarios are compared to each other. The third case simulates a scenario of a cold slug formation by an accidental DHRS opening. The fourth transient demonstrates simultaneous loss of flow in both loops, loss of the ultimate sink, insertion of the control rod, and action of DHRS. Further, more comparisons are made between one region and nine regions MSRE models. Lastly, a multi-parameter sensitivity analysis is conducted to demonstrate the capability.

The ability to simulate the production and removal of dynamic decay heat in the SMD-MSR model allows it to capture recriticality transients which have not been described by previously published MSR dynamic models [42, 30, 54, 43]. Three transients that are initiated by the loss of the ultimate heat exchanger are presented to demonstrate the impacts of decay heat removal rates, fuel salt flow rates, and control rod actions on recriticality.

5.1.1 Blocking Ultimate Heat Sink with and without Control Rods

Disclosure - This section was originally published as part of a journal article [13]. The text here is slightly modified to fit this publication.

Two simulations were performed to investigate the impact of decay heat on core temperature and the time to recriticality. These simulations model a 8 MW_{th} reactor with MSRE parameters for the fuel salt ^{235} U. In both cases, the ultimate heat exchanger was tripped and DHRS opened simultaneously. The maximum removal of DHRS power was 10% of the nominal power, and the removal of parasitic power was 0.5%. In the first case, no control rod action takes place. In the second case, the control rods are inserted at the time of the transient. This is modeled by insertion of a negative reactivity step of -2800 pcm, which corresponds to half the value of MSRE control rod [11], when the ultimate heat sink is blocked.

The simulation results are shown in Figures 5.1 and 5.2. In each figure, the top panel shows the total power and its individual contributions from fission and decay. The medium panel shows the core inlet, outlet, and graphite temperatures. The bottom panel shows the temperature-reactivity feedbacks of fuel, graphite, and total.

In the first case, as shown in Figure 5.1, the fuel temperature first increases and the resulting negative temperature feedback pushes the reactor to sub-criticality. As the DHRS opens and starts to remove heat, the fuel salt temperature decreases, thus alleviating the negative feedbacks. This phenomenon causes the system to enter into a dampening oscillatory behavior which eventually levels out at 10% of nominal power. It should be noted that the power level reaches a new steady state at 10% power because the maximum power removal of DHRS is set to 10%.

In the second case, shown in Figure 5.2, the reactor becomes subcritical immediately as the rods drop. The reactor remains subcritical for a longer period of time than in the previous case. This is due to the negative reactivity of -2800 pcm that needs to be compensated for by temperature feedbacks. As in the

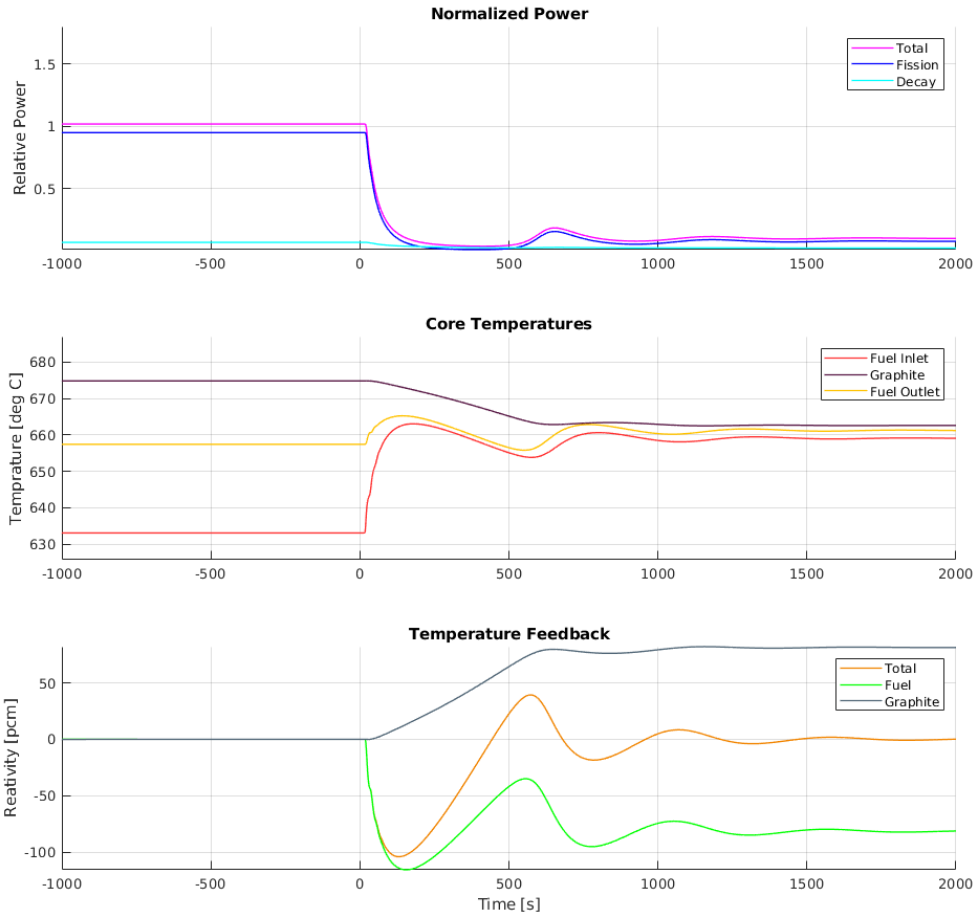

Figure 5.1: Ultimate heat sink tripped and DHRS opened. [13]

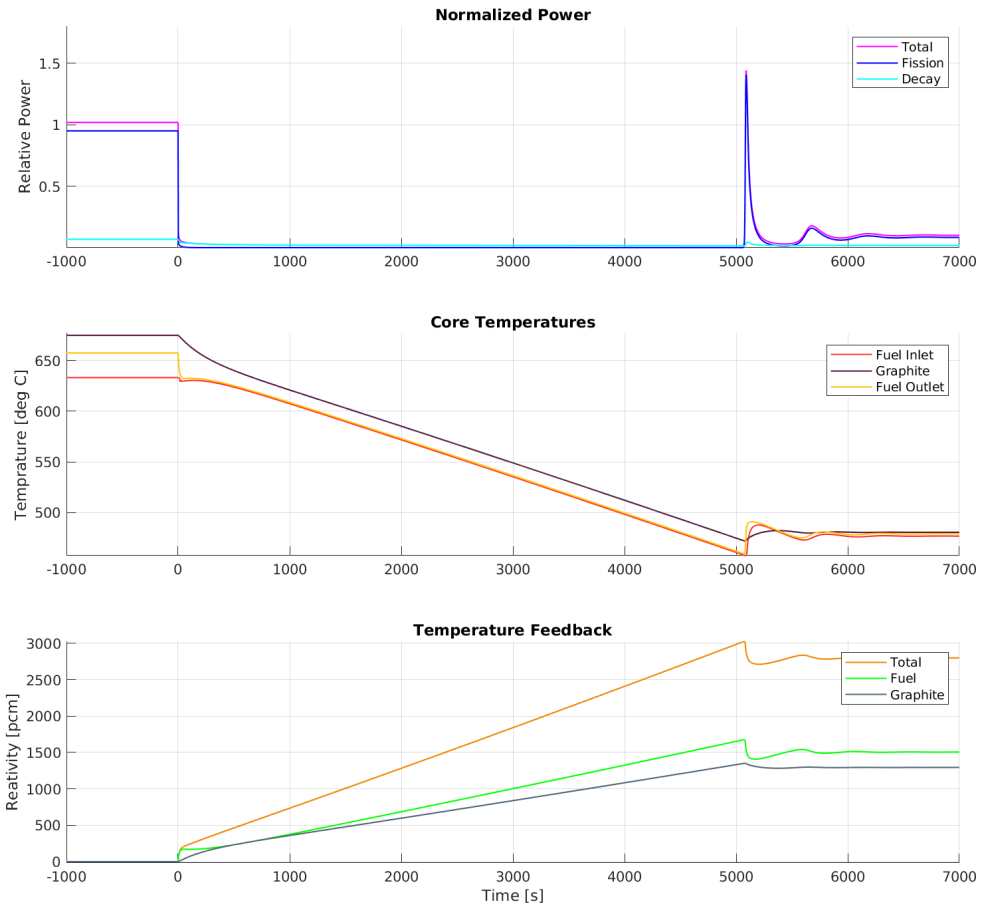

Figure 5.2: Ultimate heat sink trip, DHRS opened, and $-2800\,\mathrm{pcm}$ reactivity insertion [13]

first scenario, the system cools, causing the reactor to become critical again and enters a damping oscillatory state before reaching a new equilibrium power level at 10% of nominal power. However, in this case, the recriticality occurs at a much lower salt temperature because of the large external negative reactivity insertion. Fuel salt temperatures show that the reactor becomes re-critical below the melting point of the salt, indicating that the salt would freeze. The MSRE was equipped with electrical heating elements in its pipes to prevent freezing. This example illustrates how the presented model can be useful in designing reactor reactivity control elements.

5.1.2 Over-cooling due to Failed DHRS

Disclosure - This section was originally published as part of a journal article [13]. The text here is slightly modified to fit this publication.

A simulation is devised to explore the effects of a cold slug formation through over-cooling of circulating fuel salt by a failed DHRS. The simulation is performed for an MSRE-like reactor that uses ^{235} U that operates at 8 MW_{th} power. The reactor was operated for 2000 s to equilibrate the decay heat precursors. At this point, the heat is suddenly removed at a rate of 9.5 MW by DHRS failure to drop the temperature of the DHRS node outlet by 30 K for a period of 8.46 s, producing a cold slug equivalent in volume to the core salt inventory. The simulation results are shown in Figure 5.3. The first panel shows total power, fission power, and decay power. The second panel shows temperatures of interest in the primary loop, DHRS node outlet, core inlet, core outlet, and core graphite temperatures. The third panel shows the total temperature reactivity feedback and its constituents.

The results shown in Figure 5.3 show that the DHRS outlet temperature rapidly drops from 642 °C to 612 °C when over-cooling is initiated by the failed DHRS. The change in the temperature of the core input does not correspond to a drop of 30 K. This discrepancy is due to the lower removal rates at the PHX with lower primary salt temperatures. As the cold slug enters the reactor, the power increases rapidly

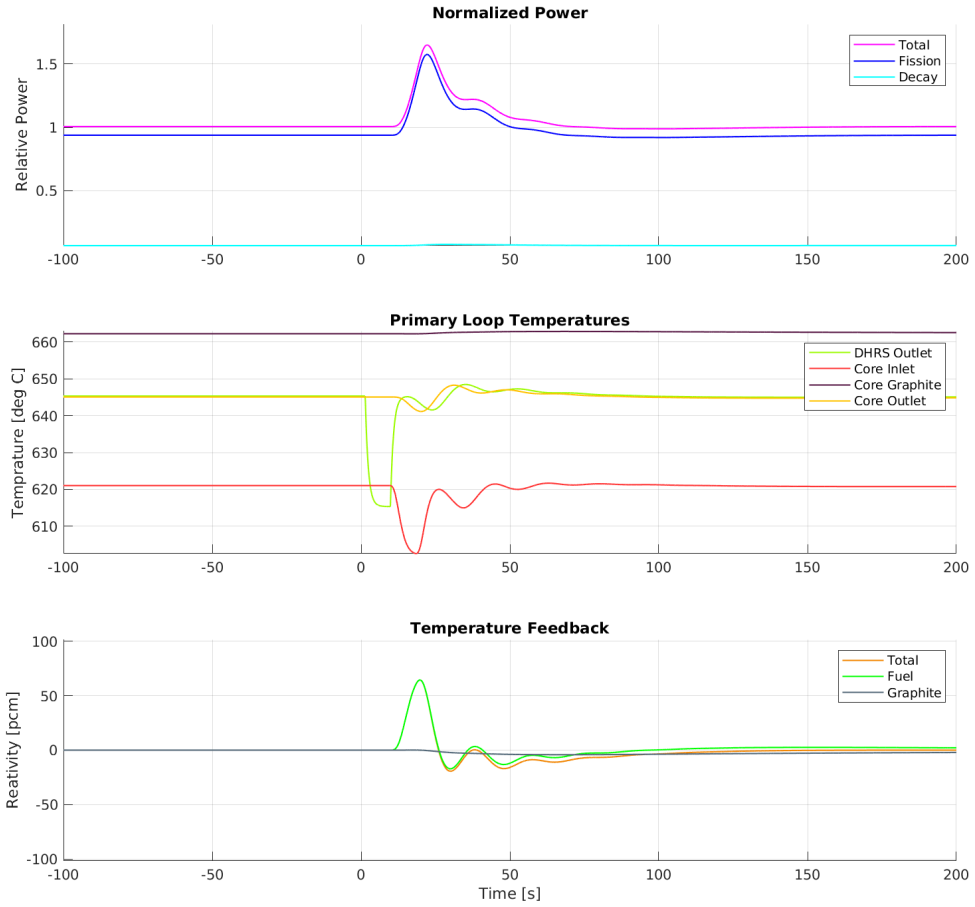

Figure 5.3: Failed DHRS over-cools DHRS node to produce a cold slug dropping 30 K at DHRS outlet for a period of 8.46 s, equivalent to the core transit time [13]

and peaks to about 160% of the nominal power, then rapidly decreases, reaching a plateau for a few seconds before decreasing again. The results indicate that the system temperatures remain well within the safety bounds.

5.1.3 Full Capability Demonstration of the Model

Disclosure - This section was originally published as part of a journal article [13]. The text here is slightly modified to fit this publication.

To demonstrate all the capabilities of the model, an accident scenario is formulated and simulated for a 500 MW_{th} generic molten salt reactor with MSRE topology and MSRE FLiBe ^{235}U fuel. The formulated accident is initiated by tripping the ultimate heat exchanger, primary, and secondary pumps, along with insertion of the control rod and activation of the DHRS simultaneously. However, the model allows the user to define any initiating time for each process individually with delays between them. In this scenario, the insertion of the control rod is represented by a negative reactivity of -1400 pcm. The maximum power removal of DHRS was set at 4% and the minimum parasitic power removal of DHRS was set at 0.1%. The pump trip results in an exponential decrease of loop flow rates, down to the free convection flow rate, which was set to 5% of the nominal flow rate in both the primary and secondary loops.

The results of this scenario are shown in Figure 5.4. The temperature graph shows that graphite is cooled at a much slower rate than fuel. This is due to the loss of forced fuel flow, resulting in a lower heat transfer coefficient between graphite and fuel. The fuel salt cools until the total temperature feedback compensates for the added external reactivity. The re-criticality event shows a much less drastic oscillatory behavior due to slow response of the graphite temperature feedback. This simulation shows how a design issue can be quickly identified with the presented toolbox.

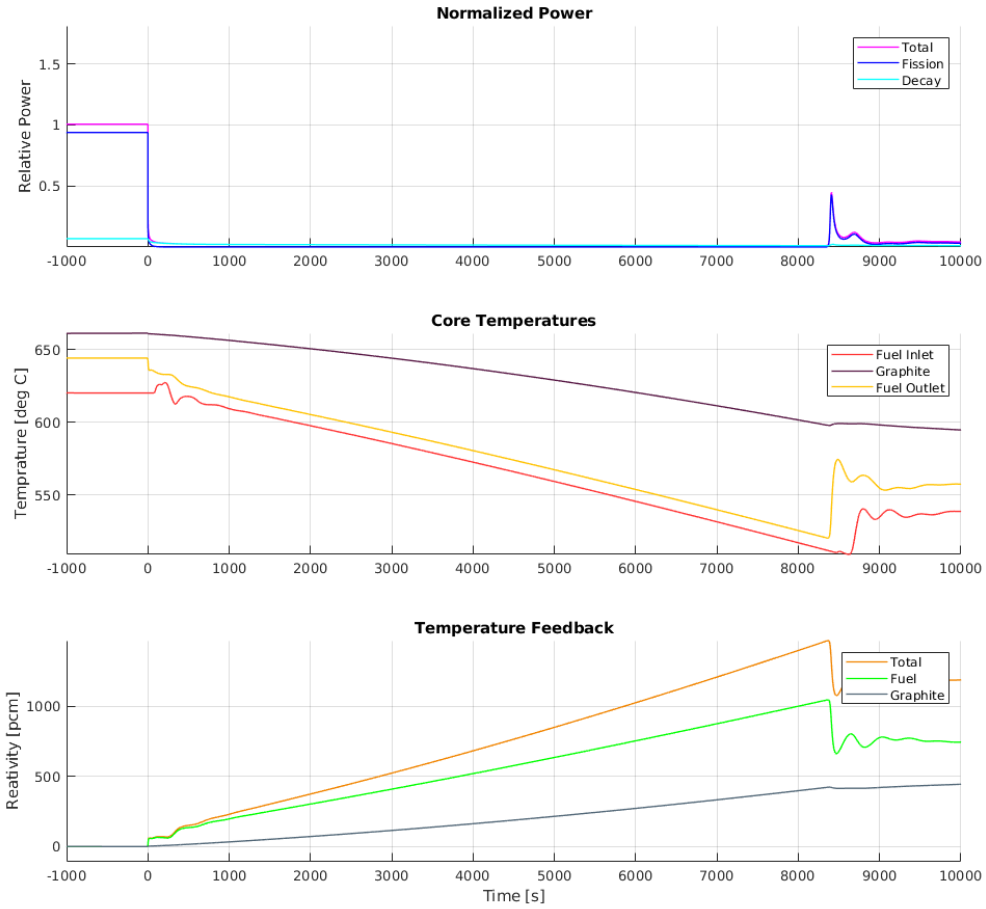

Figure 5.4: Ultimate heat exchanger, primary pump, secondary pump failure resulting SCRAM and DHRS turn on [13]

5.1.4 One-Region vs Nine-Region; Step Reactivity Insertions

Disclosure - This section was originally published as part of a journal article [15]. The text here is slightly modified to fit this publication.

A total of six 10 pcm step insertion transients were performed at three power levels, 1 MW_t, 5 MW_t, and 8 MW_t for ^{233} U and ^{235} U fueled MSRE to compare the core model of one region to the core model of nine regions. 10 pcm corresponds to 9 and 4 cents of reactivity for ^{233}U and ^{235}U fueled MSRE respectively. Both one-region and nine-region models share the same component models and physics modules except for the reactor core model. The construction of a nine-region core model is explicitly discussed in Section 3.1.2. The six transients were performed following 2000 s of the simulation time, allowing the solvers to converge and reach the nominal power 100%. At 2000 s the power was reduced to the desired power level by limiting the power rejection through the UHX. The system was allowed to reach a new steady state at the desired power by allowing another 3000 s of simulation time. The 10 pcm step insertion was added at 5000 s of the simulation time. The power results from all transients were extracted and the deviation of the reactor thermal power is plotted in Figures 5.5 and 5.6. The first, second, and third panels of both figures show delta power results at 1 MW_t, 5 MW_t, and 8 MW_t, respectively. One-region MSRE results using solid red lines, while results from the nine-region model are colored dashed blue.

Upon inspection of Figures 5.5 and 5.6, it is clear that the results of the nine-region model show that the maximum deviation of power (ΔP) is less than predicted in the one-region model. This pattern is consistent throughout all three power levels. In the one-region core model, the fission heat is deposited into both fuel nodes equally, while the graphite node receives 7% and both fuel nodes have equal importance for feedback contribution. Unlike the one-region core model, the nine-region core model does not deposit the same amount of fission heat to the fuel nodes in each region nor does it have the same importance for feedback. Both fuel and graphite nodes in the nine-region core model are weighed on the basis of the neutron flux profile.

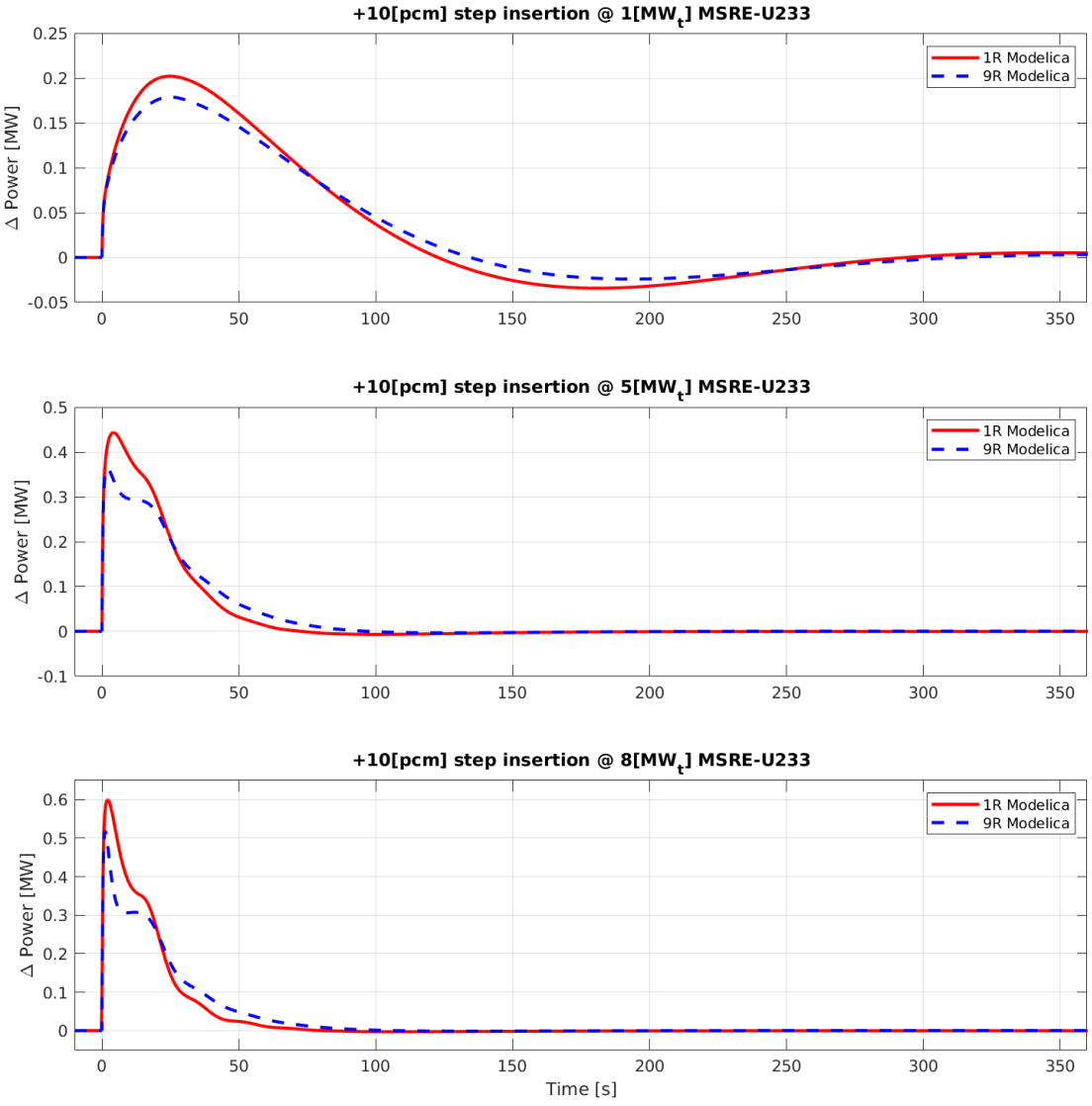

Figure 5.5: 10 pcm step reactivity insertion for ^{233}U Fueled MSRE at 1MW_t, 5MW_t and 8MW_t [15]

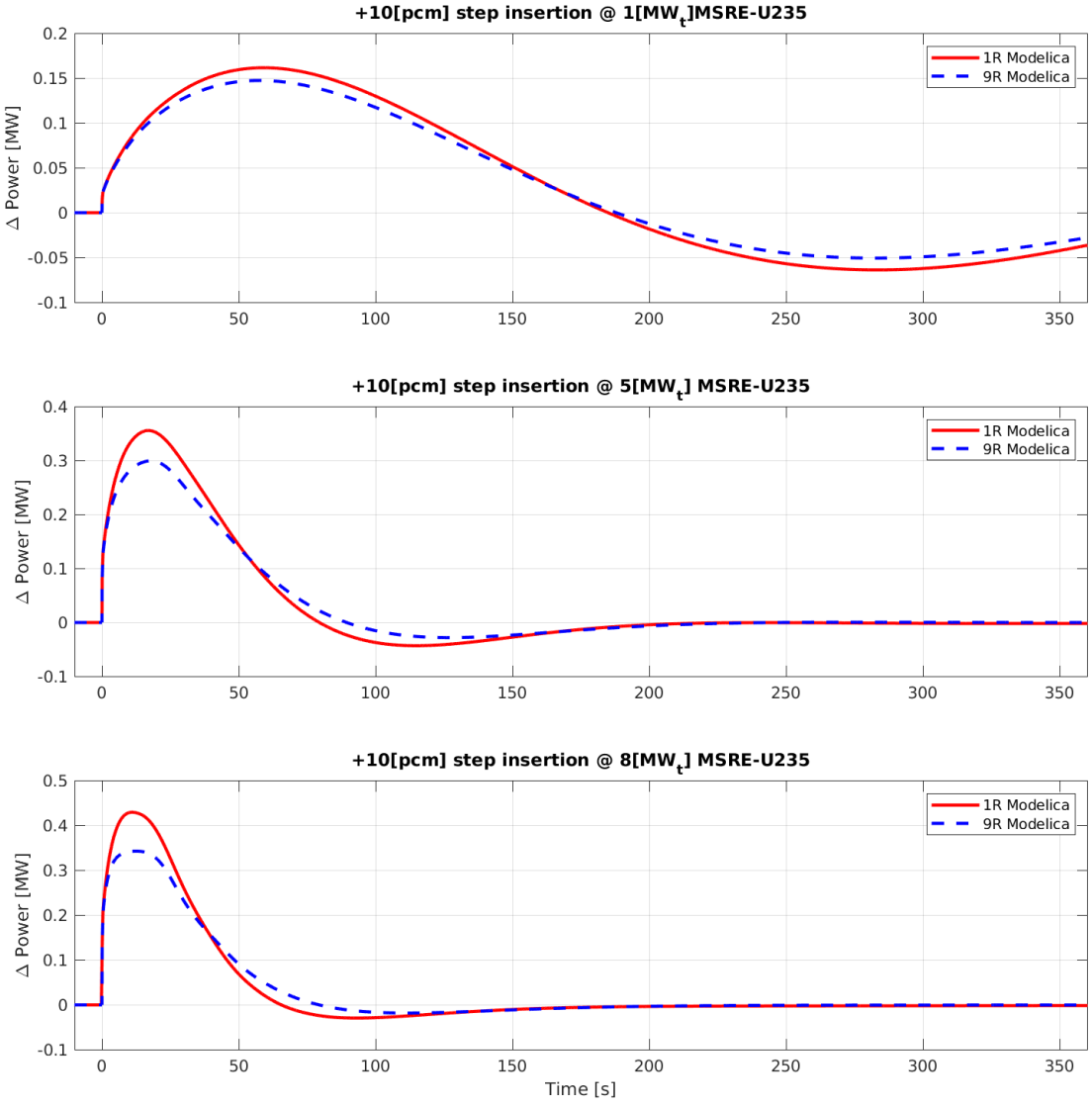

Figure 5.6: 10 pcm step reactivity insertion for ^{235}U Fueled MSRE at 1 MW_t, 5 MW_t and 8 MW_t [15]

Fuel salt entering fuel channels travels up while heating up. Fuel salt is heated through fission heat, decay heat, and convective heat transfer from graphite. Since there are more regions in the nine-region core, heat transfer and feedback resolutions are higher than those of one-region core, lowering the maximum power than that predicted in one-region model. The second and third panels of Figure 5.5 show that both models produce a clear decrease in the rate of power reduction following the maximum power. This phenomenon is observed only in circulating fluid-fueled reactors. The phenomena can be explained in two processes. The first process involves delayed neutron precursors. Fuel circulation causes a fraction of delayed neutron precursors to drift out of the core. Delayed neutron precursors with short half-lives decay outside the core region and do not contribute to fission. However, some of the long-lived precursors re-enter the core region and contribute to delayed neutron terms. The second process involves fuel temperatures and fuel temperature feedback. With the initial power excursion, only fuel that resides in the core experiences heating. Entrance of cooler salt remaining ex-core reduces the core average temperature, undermining fuel temperature feedback. This effect can be clearly seen on close inspection of the core fuel inlet and outlet temperatures of similar step transients shown in Figures 4.4, 4.9, and 4.10. The second phenomenon has profound effects when external reactivity insertion results in a large power deposition and causes a plateau following the initial power excursion as seen in the second and third panels of the Figure 5.5. Power plateaus are more profound in nine-region results than in one-region results, which can be attributed to higher resolution of temperature feedbacks and core heat transfer. The second and third panels of Figure 5.6 show that this described power plateau is not present. This is because the external reactivity insertion is only 4 cents. Overall, it should be noted that all step transients last from 100 s to 350 s window, which is longer than the transient time that will be observed in a solid-fueled reactor.

5.1.5 One-Region vs Nine-Region; Off-Normal Transient

Disclosure - This section was originally published as part of a journal article [15]. The text here is slightly modified to fit this publication.

The off-normal transient performed in Section 4.2.3 for the one-region model was performed with the nine-region model to compare the results. Simulation of the presented off-normal transient follows the same procedure as discussed previously with one-region model simulation and is subjected to the same conditions. The indicator reactor parameters are extracted and captured in Figure 5.7. The results of the one region model are plotted with solid red lines, while the results of the nine regions are plotted in dashed blue lines.

The first panel of Figure 5.7 shows the total nominal power. It is clear that the one-region model takes longer than the nine-region model to achieve recriticality. When panels two and three are considered, it is evident that the nine-region model cools down much faster than that of the one-region model. This is the result of a higher fidelity of heat transfer in the nine-region core model. The four radial regions of the nine-region model experience different flow rates. Radial regions with a high number of fuel channels, such as radial regions 2 and 3, counting from the left of the Figure 3.3, account for more fuel and graphite. These two radial regions experience higher flow rates even when the entire primary system is subject to a free convection flow rate of 0.05% of the nominal flow fraction. Therefore, the nine-region core model cools much faster, by removing heat from graphite. During the re-criticality event, the one-region model power peaks at a higher level and experiences more osculations before reaching the new steady state than that of the nine-region model. The lower power of the recriticality excursion in the nine-region is due to the high fidelity of the temperature feedbacks, as discussed in Section 5.1.4. The nominal total power of both models stabilized at 8%. The fourth panel of Figure 5.7 shows that both models come to the same positive feedback before becoming re-critical. The feedback levels off at 1400 pcm compensating for the added external negative feedback. However,

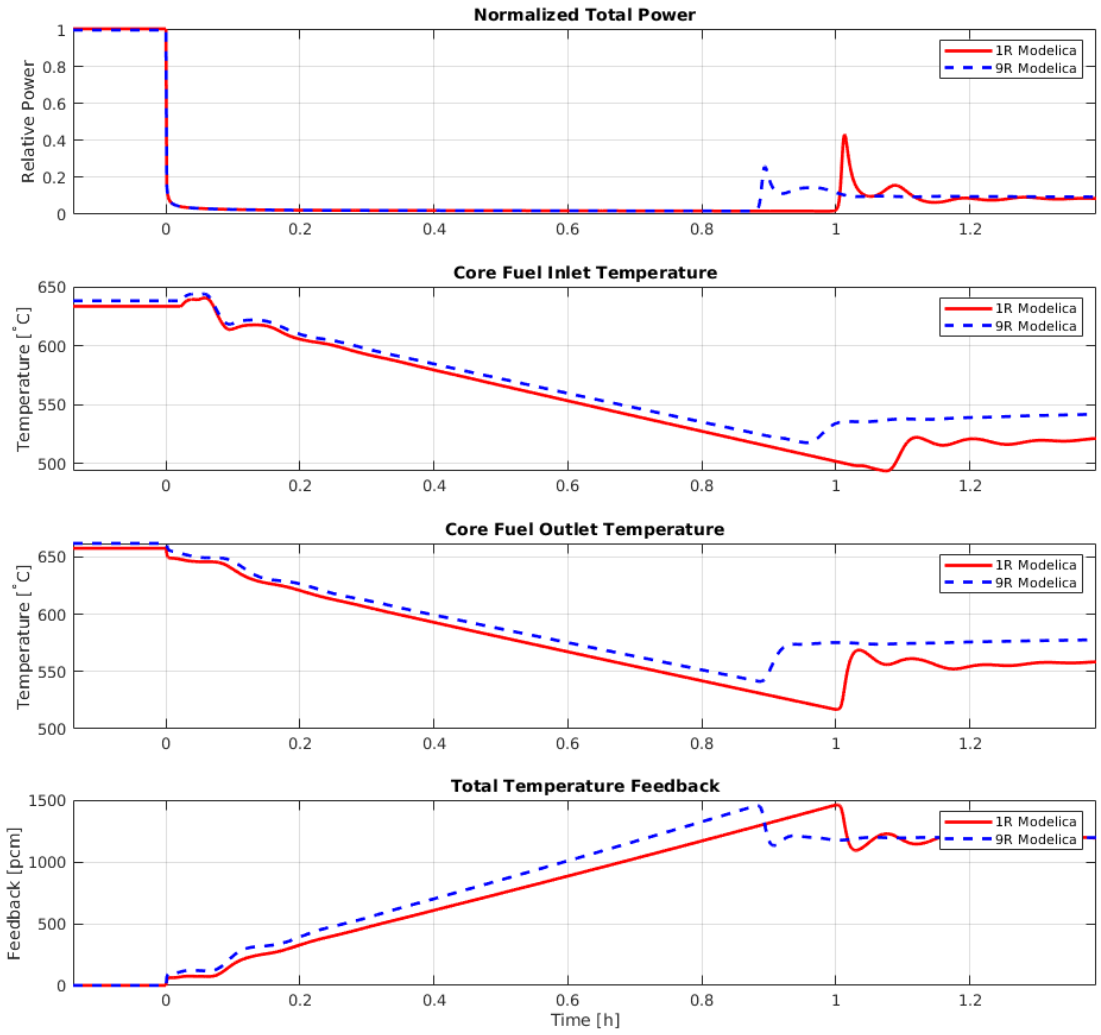

Figure 5.7: Simultaneous UHX, primary and secondary pumps trip, DHRS open (8%) SCRAM (-1400 pcm) [15]

both models reach the same core inlet and outlet temperatures when reaching steady state, and the core average temperature of the nine-region model remains $\approx 5\,\mathrm{K}$ higher than the one-region model.

Recriticality phenomena are not unique to MSRs. It is undesirable in the context of LWR operations and design. However, this phenomenon can be exploited to maintain the fuel in a molten state of an MSR. If fuel salt solidifies within the system, it can lead to hot spots and large temperature gradients across components, posing threats to structural integrity. Recriticality allows the plant operator to perform a system assessment to decide if the fuel salt should be drained and stored for an outage. The time to re-criticality and vital reactor parameters can be maintained within the safety envelope through controlling the heat removal rates and the external negative reactivity. Maintaining the reactor at a low power and temperature preceding re-criticality can be considered as a system failsafe.

5.1.6 Multi-parameter Sensitivity Study

Disclosure - This section was originally published as part of a journal article [15]. The text here is slightly modified to fit this publication.

Parametric sensitivity studies can be utilized to identify parameters that are important for reactor safety. Several parametric sensitivity studies were performed with the Simulink versions of the modeling approach and were published [25, 14, 17]. All mentioned studies were limited to perturbing one parameter at a time due to the long simulation execution times of Simulink implementations. SMD-MSR Modelica is an excellent framework for conducting sensitivity analysis due to its fast execution times. To demonstrate the expanded usability of the SMD-MSR Modelica, a multivariate sensitivity analysis was performed to identify the effects of the heat capacity of the fuel, the heat transfer coefficient between the fuel and the graphite in the core, and the heat transfer coefficient between the fuel and the tubes in the PHX for step insertion previously shown 100 pcm in Section 4.2.2. The aforementioned

physical parameters were randomly perturbed simultaneously between 30% and 200% of their nominal value. A total of 1000 simulations were conducted and parameters important for reactor safety were extracted. The data extracted included maximum values of nominal power, core inlet, graphite, and core outlet temperatures. The correlation coefficients between the extracted data and the perturbation values of the physical parameters were calculated. The calculated correlation coefficients are depicted in Figure 5.8.

Figure 5.8 shows that there is a high positive correlation between fuel heat capacity and maximum nominal power and maximum core inlet temperature while there is a strong negative correlation between maximum core outlet temperature. The correlation between fuel heat capacity and maximum power is 1. When the fuel heat capacity is high, more heat is required to increase the temperature. Therefore, nominal power can reach higher peak levels before the fuel salt temperature increases and compensates for external reactivity through negative fuel temperature feedback. The fuel heat capacity has a correlation of 0.73 between the maximum core input temperature, while the correlation between fuel heat capacity and the maximum core outlet temperature is -0.53. When the heat capacity of the fuel salt is high, the core outlet temperature is reduced, as it requires more heat to increase the fuel temperature. Meanwhile, the low temperature difference between fuel salt and tube bundle in PHX reduces the efficiency of heat removal through convection. These effects are reflected in the correlation coefficients between fuel salt heat capacity and maximum core inlet and outlet temperatures. When the correlations of the reactor parameters and the heat transfer coefficients are considered, it is evident that the heat transfer coefficient between fuel and the tube bundle of the PHX have no strong correlations. On the contrary, some correlations can be observed between the core temperatures and the heat transfer coefficient between the fuel and graphite. Increasing the heat transfer coefficient between fuel and graphite allows for higher cooling of graphite while heating up fuel salt residing in the core. This is reflected

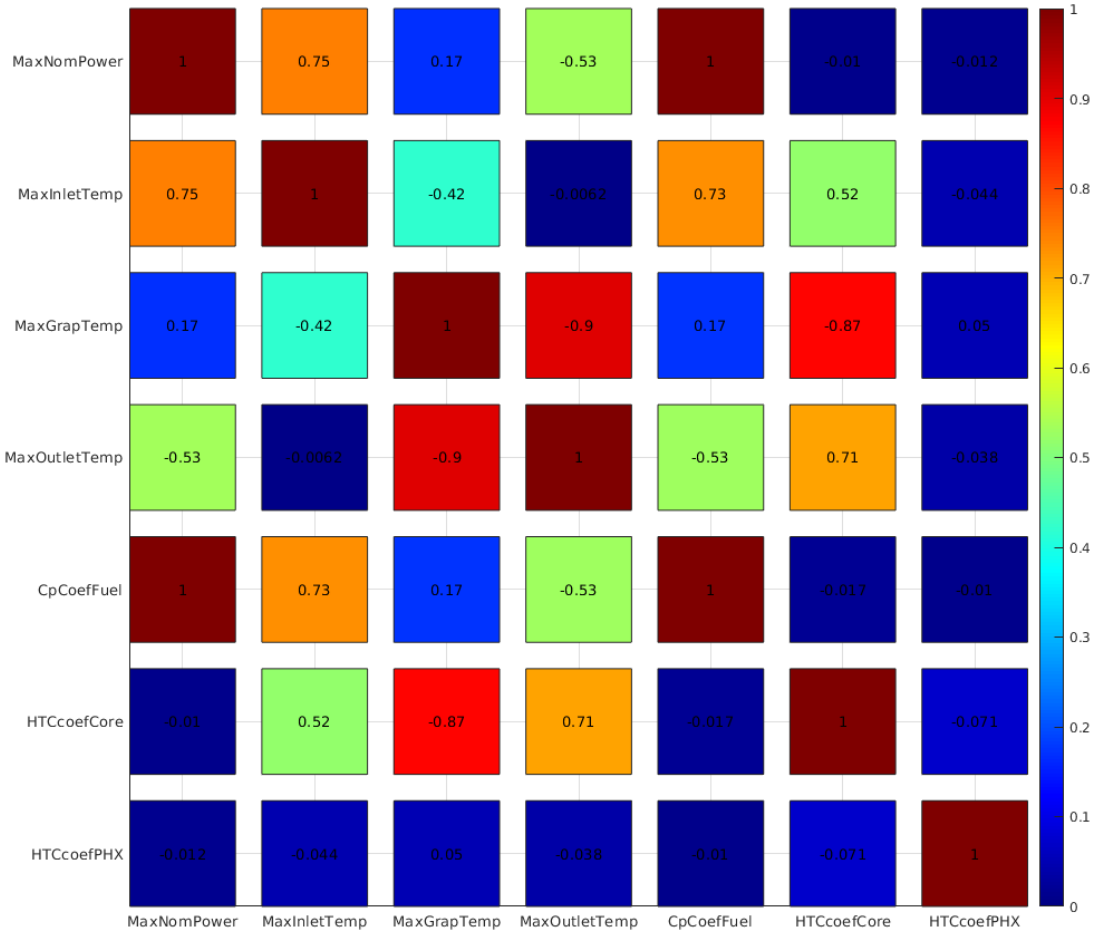

Figure 5.8: Correlations of reactor parameters important for safety against heat capacity, heat transfer coefficients in core and PHX for a 100 pcm step insertion [15]

in correlation coefficients of core heat transfer coefficient between maximum graphite temperature, maximum core inlet and outlet temperature which are -0.87, 0.52 and 0.71 respectively.

5.2 MSDR Transients

Disclosure - This section and the included subsections were originally published as part of a journal article [14]. The text here is slightly modified to fit this publication.

In this section, three transients and two sensitivity analysis are presented to evaluate the effects of depletion on the dynamic behavior of MSDR as well as to demonstrate some of the model functions. These are 1. Step reactivity insertion, 2. trip of the UHX with simultaneous opening of the DHRS, 3. Pump and UHX trip with simultaneous DHRS opening and drop of control rods.

5.2.1 Step Insertion of Positive Reactivity

An external step reactivity insertion was simulated to evaluate the system response for a hundred simulations during the depletion time. In these simulations, the SG was used as the UHX. The DHRS remained closed and all pumps remained fully operational throughout the simulation.

The simulation was carried out as follows. First, the simulation was run for 2000 s, $t \in \langle -2000, 0)$ seconds, to allow the model to stabilize at a full operational power of 750 MW_t. Then an external positive reactivity of 100 pcm was added at t = 0 s of the transient simulation time. The transient progression at the Beginning of the Cycle (BOC), Middle of the Cycle (MOC), and End of the Cycle (EOC) are shown in Figure 5.9. Values of interest for each transient include the maximum nominal power, the FWHM of the power peak, the maximum core temperature, and the maximum

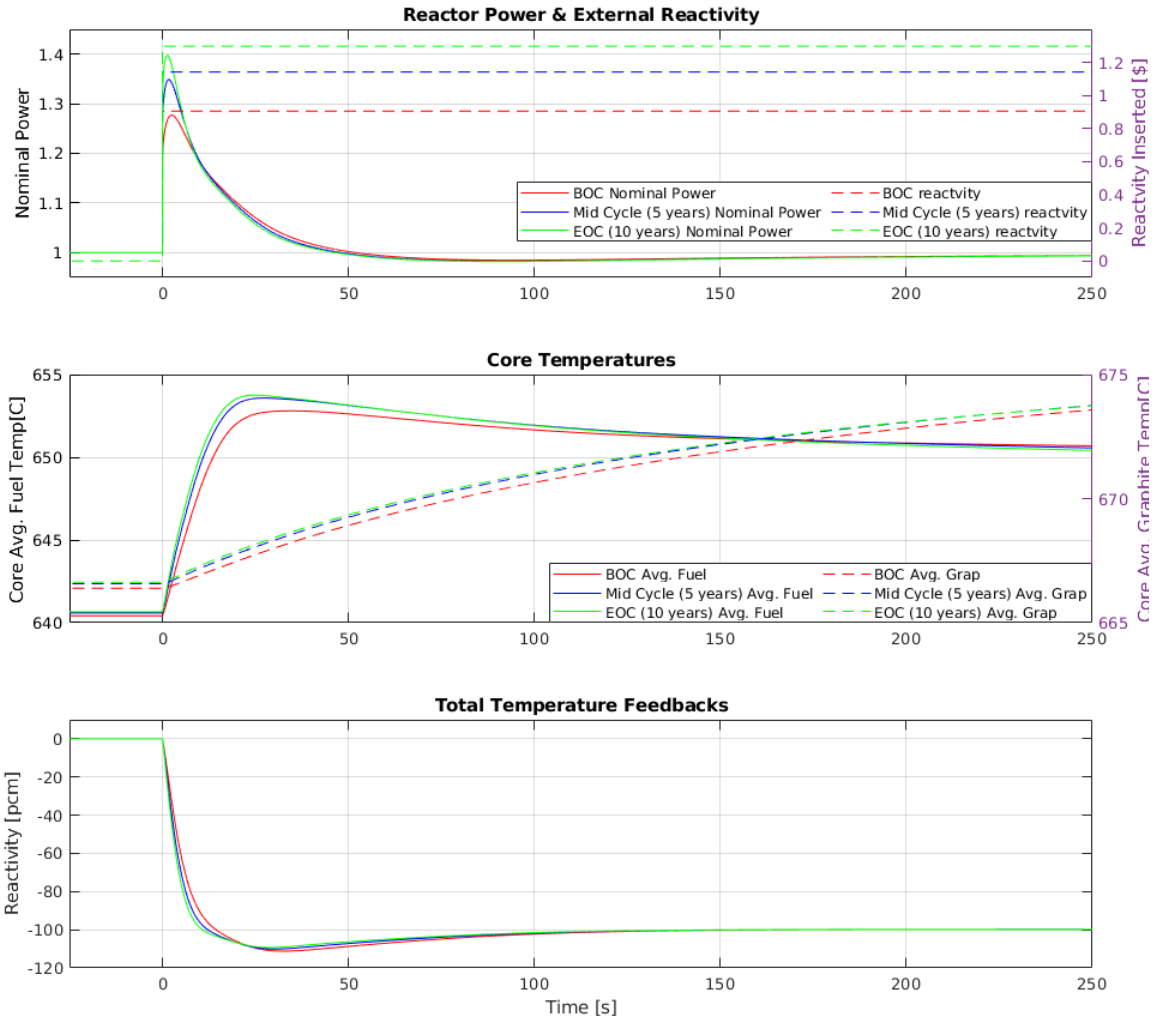

Figure 5.9: Reactor behavior at BOC, MOC, and EOC following a 100 pcm step reactivity insertion transient, including (top) reactor absolute power and relative dollar worth of reactivity insertion, (middle) core-average fuel and graphite temperature, and (bottom) temperature-induced reactivity feedback [14]

value of the temperature feedbacks. These data are plotted along the depletion time in Figure 5.10.

Several interesting effects in the transient behavior arising from depletion are captured in Figure 5.9. For example, in Figure 5.9 (top panel), the absolute nominal power increases toward the EOC, but overall the shape of the transient remains the same. The increase in maximum power can be explained in relation to the reactivity worth 100 pcm in terms of dollar denomination; that is, with the decrease in β_{eff} over the cycle (see Figure 2.3), the excess reactivity of delayed neutrons in MSDR at EOC is 110 pcm.

As shown in Figure 2.3, the total delayed neutron fraction decreases with depletion and subsequent plutonium buildup. As a result, the dollar value of 100 pcm increases from BOCto EOC (shown in Figure 5.9, top). Hence, identical absolute reactivity insertions lead to an increase in the value of the reactivity dollar as the fission contribution of ^{239} Pu increases with depletion. This phenomenon is well known in conventional reactors; however, these results confirm that it should also be accounted for in MSR designs and operational procedures.

The middle and bottom panels of Figure 5.9 show the core average fuel and graphite temperature and temperature feedback during the BOC, MOC and EOC transients. The maximum core fuel average temperature reached increases towards EOC. The general shape of the temperature transients at all three operational points is similar. Similarly, the buildup of temperature-induced reactivity feedbacks in the core follows a similar pattern. The feedback builds somewhat faster at the EOC, corresponding to the faster rise in core temperature.

The depletion dependencies of the maximum power reached during the transient and the FWHM of the power peak are shown in the top panel of Figure 5.10. The maximum nominal power reached during the transient increases steadily with depletion, while the FWHM decreases. Meanwhile, the maximum average core fuel temperature during the transient period (Figure 5.10, middle) only increases by

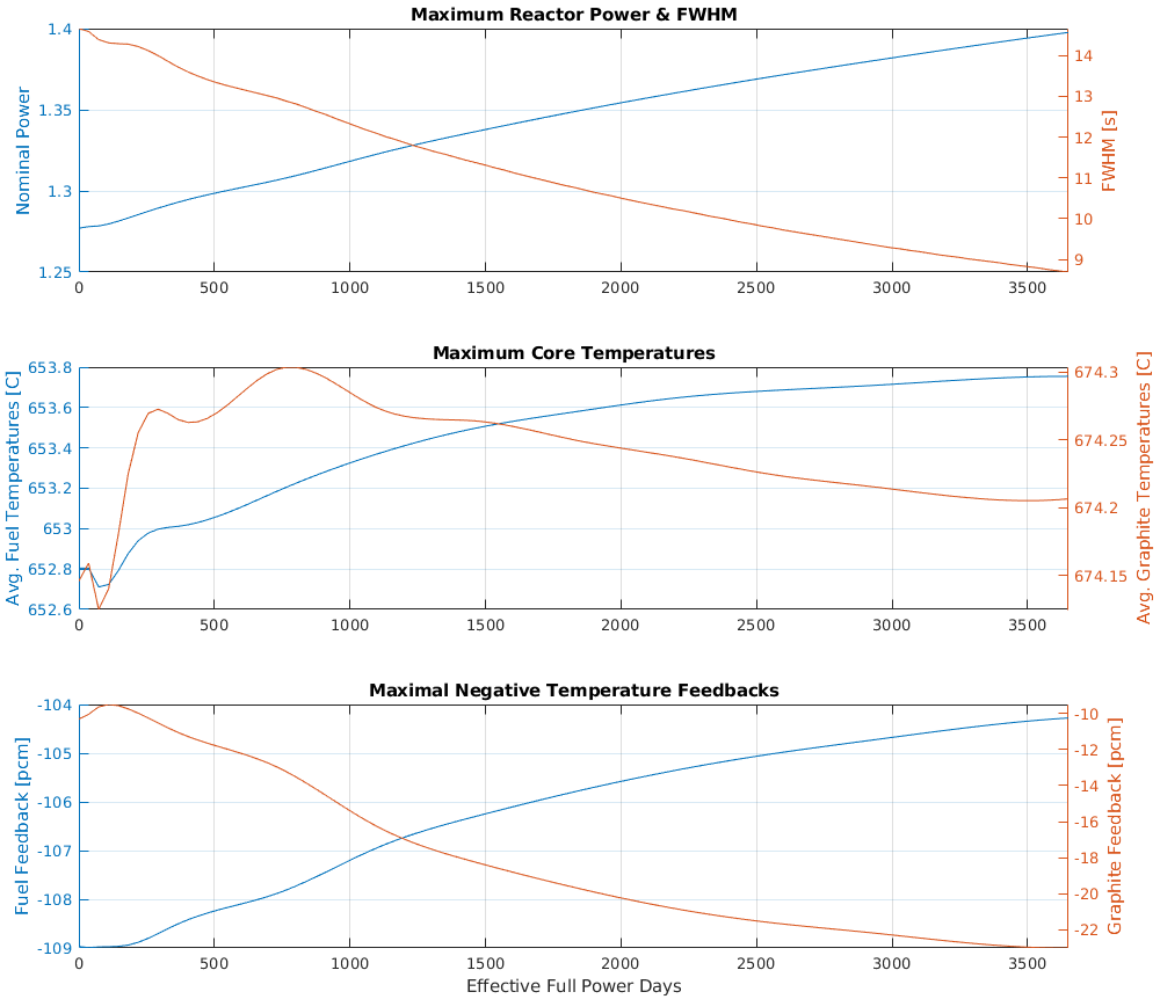

Figure 5.10: Depletion-dependent deviation of important reactor parameters for a 100 pcm step reactivity perturbation; (top) maximum reactor power and FWHM, (middle) maximum temperatures of the fuel and graphite, and (bottom) maximum (negative) temperature-induced feedback from the fuel salt and graphite moderator [14]

approximately 1 K over 10 years of depletion. The maximum temperature reached by graphite appears to reach its peak at around 800 days; however, its absolute change with depletion is minuscule (less than 0.2 K). Finally, the maximum temperature feedback observed from the fuel and graphite temperature feedback is illustrated as the bottom panel of Figure 5.10. Because the feedbacks are negative in this transient, this corresponds to the largest (absolute) reactivity feedback from the fuel and graphite. Consistent with the temperature feedback coefficients dependent on the depletion calculated for fuel and graphite (Figure 2.3, bottom), it is observed that the reactivity feedback slowly decreases with the depletion of fuel (and increases for graphite).

5.2.2 Simultaneous Trip of UHX and Open DHRS

The simultaneous trip of the UHX and DHRS opening transient is evaluated to observe the effects of depletion on system re-criticality behavior described in [13]. In this transient, the SG represents the UHX and DHRS is used to remove 3% of nominal power when activated with a characteristic time τ of 10 seconds.

After the solver stabilization period, at t=0 s the SG is tripped and the DHRS is opened simultaneously. The transient is then run repeatedly along the depletion timeline in 101 individual simulations.

The following data are saved in these simulations, the maximum and minimum temperatures of the hot and cold legs and the graphite, the maximum power reached during the recriticality event, and the time from the initiating event to recriticality.

The time to re-criticality in this context is defined as the time from the transient initiation to reaching the lowest decay power of the reactor. When the reactor reaches the subcritical state, decay heat is the only heat source in the system. As decay heat diminishes with time, the power production rate likewise decreases over time; however, heat is removed at a constant rate by the DHRS, thereby allowing thefuel salt to

cool down. As the fuel salt and graphite cool down, the total temperature feedback increases, causing the system to achieve criticality again at a lower temperature.

The system behavior during this transient at BOC, MOC, and EOC is depicted in Figure 5.11 (nominal power behavior, average core fuel temperature, and total temperature reactivity feedback in the top, middle and bottom panels, respectively), and the evolution of depletion of the values of the above-mentioned data is shown in Figure 5.12.

The nominal power response of the system (Figure 5.11, top) shows that towards the EOC, the recriticality is reached sooner than at the BOC. All three nominal power transients show similar trends. After the reactor reaches recriticality, a damping power oscillation follows and reaches a new nominal power of 3% which is the power removed by the DHRS. Figure 5.12 (top panel) illustrates the maximum power during recriticality and the time to reach re-criticality; the provided insert shows the details of the recriticality event. The same general shape is observed at all three depletion points for the average fuel temperature (see Figure 5.12, middle), with the recriticality occurring sooner the more the core is burned. However, the maximum average core fuel temperature reached by the transient in the BOC is higher than that in the EOC, and the minimum temperature is lower in the BOC than in the EOC. Finally, the total temperature feedback transient (see Figure 5.11, bottom) shows similar trends across the conditions of BOC, MOC, and EOC.

The maximum re-criticality power with depletion (see Figure 5.12, top, left y-axis) exhibits little change with burnup as it stays at almost 9% of full power. The time to re-criticality is shown on the right y-axis, which steadily decreases from about 55 minutes at BOC to about 47 minutes at EOC. The second, third and fourth panels in Figure 5.12 show the evolution of depletion of the temperature data of the primary loop. Maximum and minimum temperatures in the cold leg reached during the transient (shown in the second panel) trend oppositely as a function of depletion. The maximum temperature of the cold leg decreases by 3 K, while the

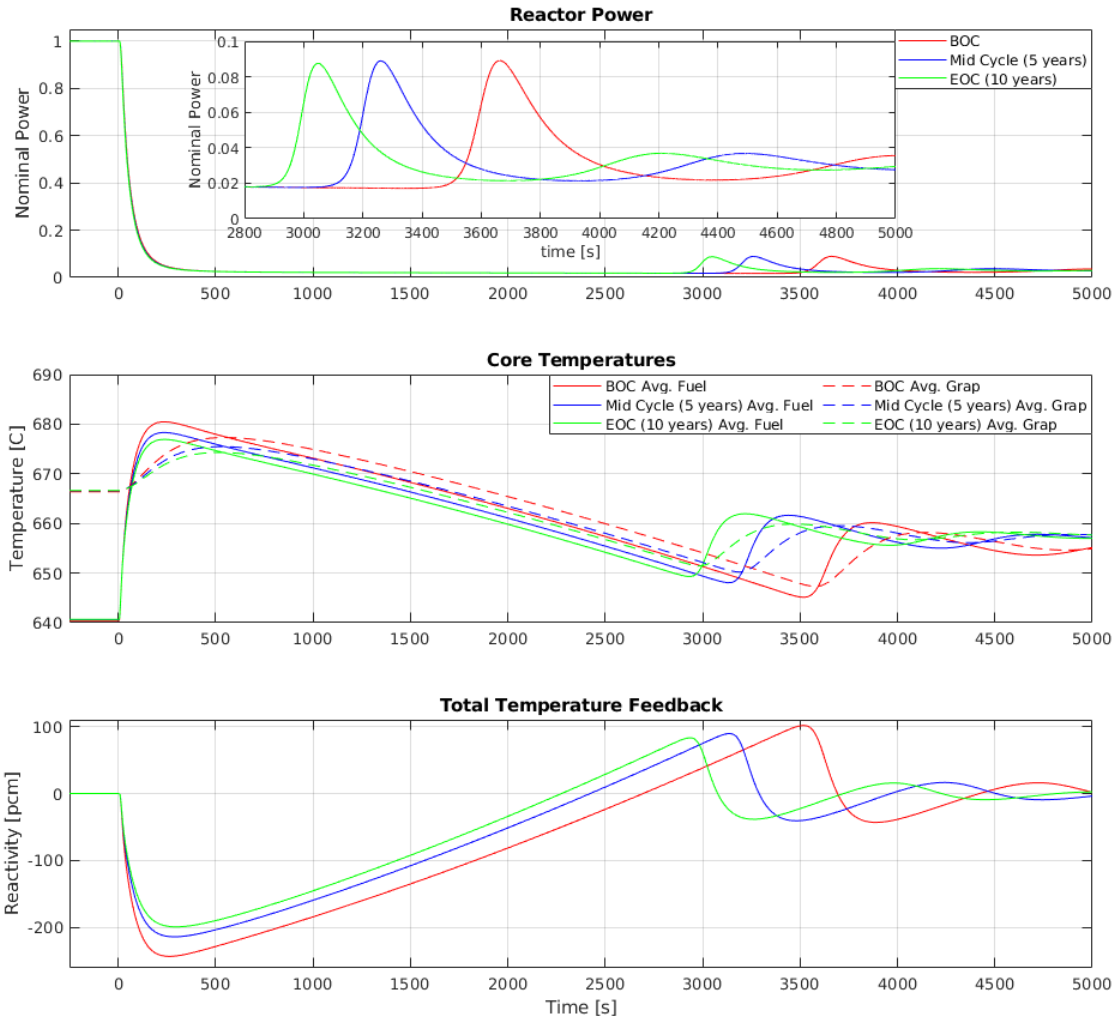

Figure 5.11: Reactor behavior during simultaneous loss of UHX and DHRS (3% nominal power) opening transient: (top) absolute reactor power, (middle) core-average fuel and graphite temperature, and (bottom) total temperature-induced reactivity feedback [14]

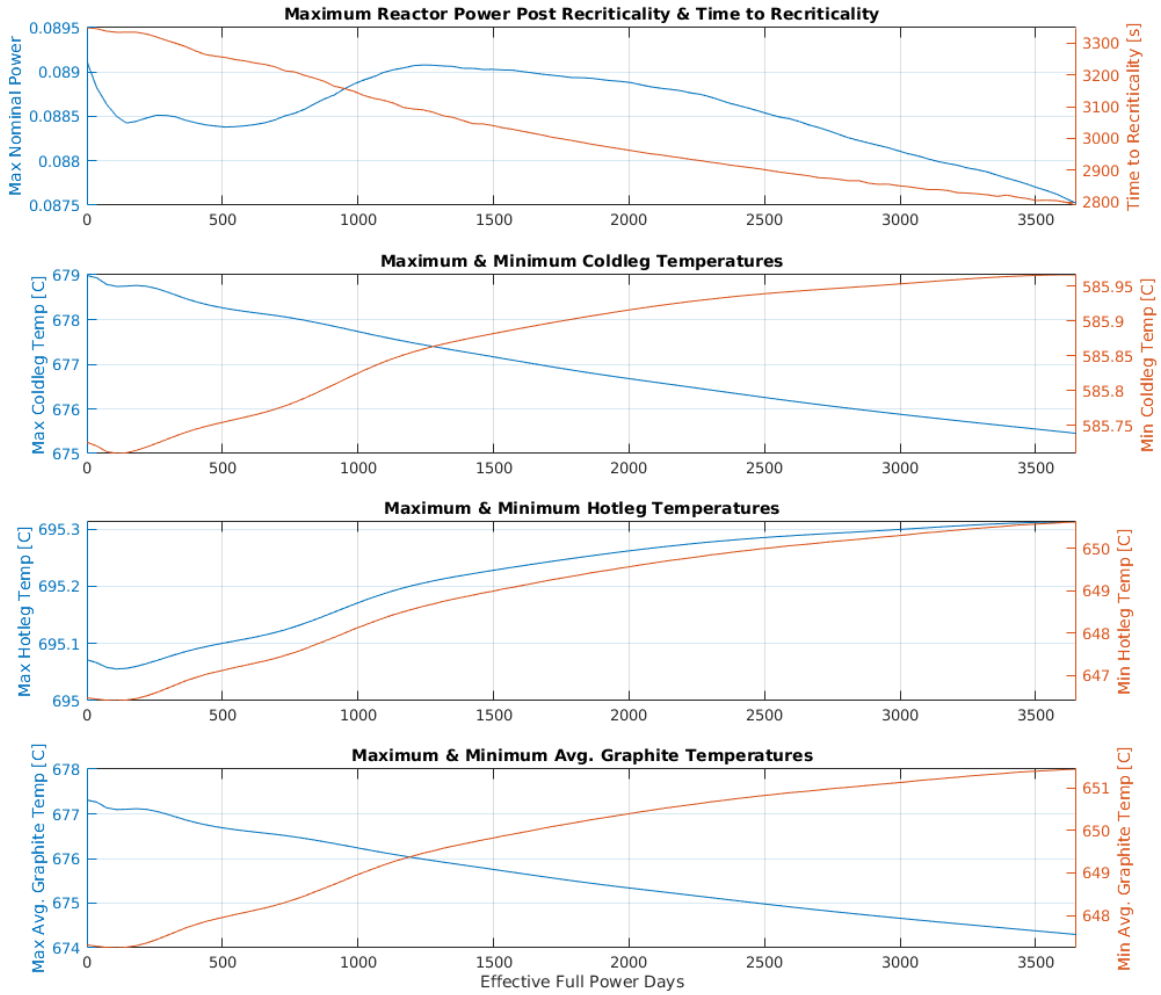

Figure 5.12: Depletion dependent evolution of several reactor parameters for simultaneous loss of UHX and DHRS (3% nominal power) opening transient; from the top: maximum nominal power and time to recriticality, maximum and minimum temperatures in the cold leg, maximum and minimum temperatures in the hot leg, and maximum and minimum temperatures in the graphite [14]

minimum temperature of the cold leg increases by 0.8 K during 10 years of depletion. The maximum and minimum hot leg temperatures reached in the transient (see Figure 5.12, third panel) increase over the 10 years of depletion. The maximum temperature of the hot leg increases by 0.9 K, while the minimum temperature of the hot leg increases by 4.9 K. Maximum and minimum graphite temperatures (see Figure 5.12, bottom panel) have opposing trends over almost equal ranges of about 4 K.

5.2.3 Simultaneous Pump Trip, UHX loss, Negative Reactivity Insertion, and Open DHRS

In this transient, the previously presented simultaneous SG trip and the DHRS open transient are combined with two additional perturbations of the system. These include the trip of two out of three primary, secondary, and tertiary circulation pumps along with a simultaneous insertion of - 1400 pcm reactivity. During pump trips, the flow rate transient is modeled as an exponential decay to a nonzero free convection flow rate, the implementation of which is discussed in [13]. For the purposes of this transient, the pump trip constant K_{pump} is set to $0.2\,\mathrm{s}^{-1}$, and it is assumed that the free convection is 5% of nominal flow rate. The model can accommodate transient scenarios where all pumps are tripped.

The transient evolution of BOC, MOC, and EOC is shown in Figure 5.13. The evolution of the select parameters with the depletion timeline is shown in Figure 5.14.

As seen in the top panel of Figure 5.13, the reactor power drop is faster than during the previous transient discussed in Section 5.2.2. The sharper drop is a result of the insertion of the external step reactivity -1400 pcm. Unlike the previous transient shown in Figure 5.11, the fuel temperature is rapidly decreasing. When the UHX is blocked off, the only path for the heat of the system to dissipate is through the opened DHRS. The heat flow of the system reverses, allowing the flow into the primary loop from its secondary and tertiary loops.

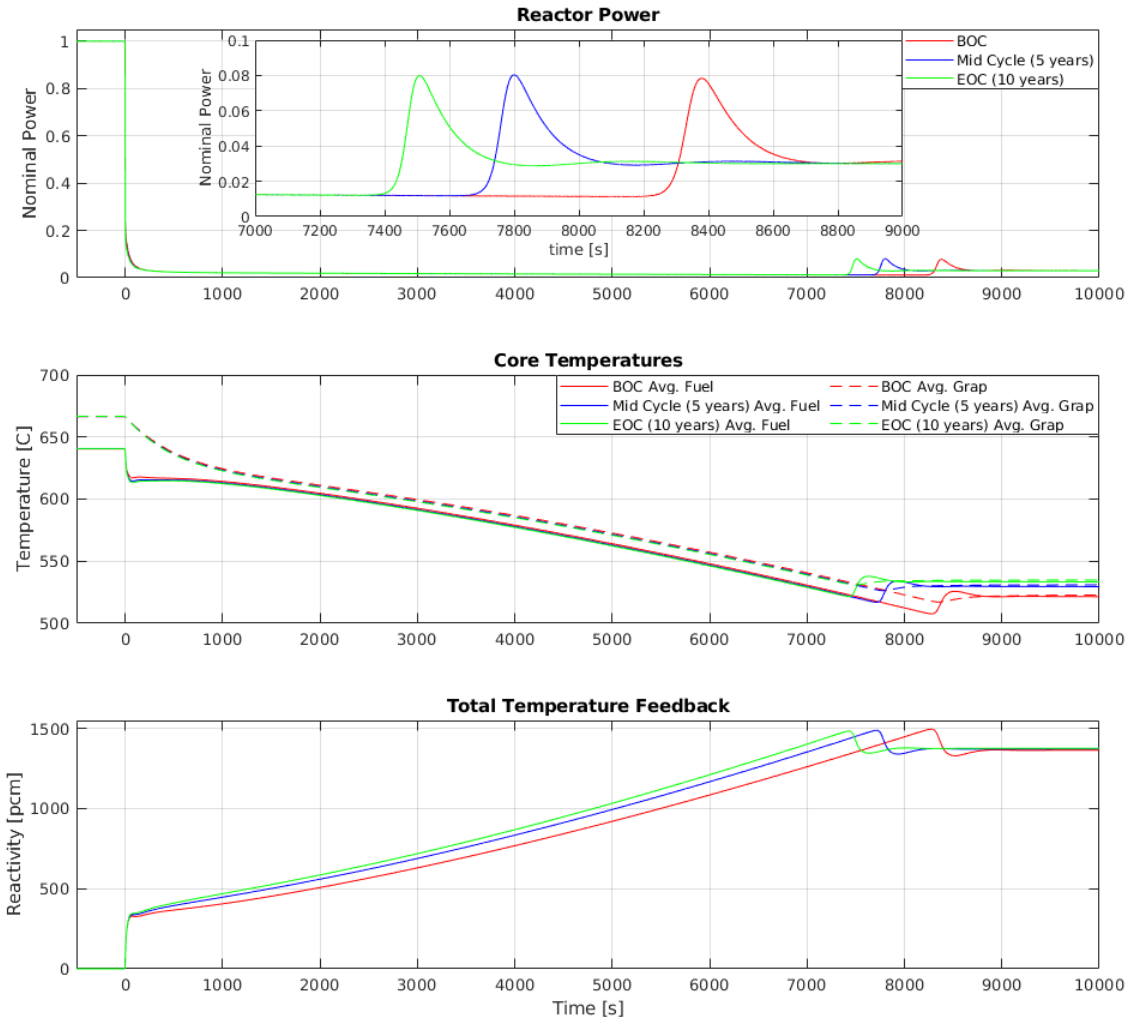

Figure 5.13: Reactor behavior during simultaneous loss of SG, 2 of 3 loops lost, DHRS (3% nominal power) open, and reactor SCRAM with -1400 pcm of reactivity [14]

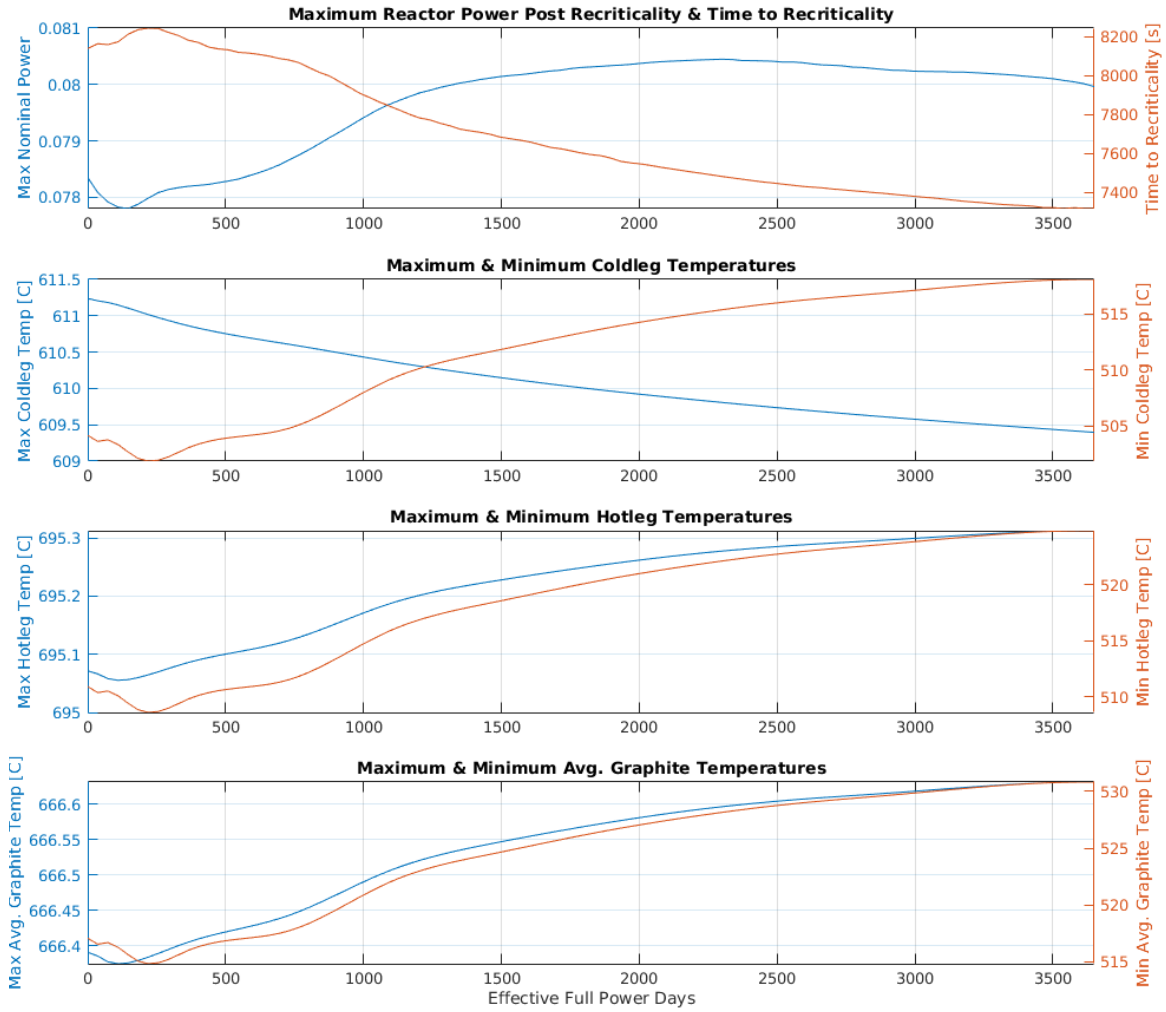

Figure 5.14: Depletion dependent deviation of important reactor parameters for simultaneous, SG, 2 of 3 pumps lost in all loops, DHRS (3% nominal power) open, and reactor SCRAM with -1400 pcm of reactivity; from the top: maximum nominal power and time to re-criticality, maximum and minimum temperatures in the cold leg, maximum and minimum temperatures in the hot leg, and maximum and minimum temperatures in the graphite [14]

The rapid reduction in core temperature is reflected in the temperature reactivity feedbacks shown in the bottom panel of Figure 5.13. After the core becomes subcritical, the decay heat dominates the power production. The decay power decreases over time, while the DHRS keeps removing the constant 3% of the nominal reactor power. Therefore, the fuel salt is cooling at an increasing rate.

As the fuel salt and the graphite are cooled, the temperature reactivity feedbacks increase, until the feedback-induced reactivity compensates the inserted external reactivity. Then the system becomes critical again, now at a lower temperature. The system behavior after recriticality shows strongly damped oscillation and finally stabilization at a new power level, which equals the power removal by the DHRS.

The three stages of core burnup, BOC, MOC, and EOC, are shown as different color lines in Figure 5.13. These three lines show identical trends, with recriticality occurring sooner the more the core is depleted, much like in the previous transient shown in Figure 5.11 in Section 5.2.2.

The dependence of depletion of values of interest (maximum reactor power and time to recriticality and then maximum and minimum temperatures for the cold leg, the hot leg, and graphite, respectively) is shown in Figure 5.14. The same trends in the maximum power and time to recriticality as a function of core depletion are observed as in the previous transient; however, duration to recriticality is longer in this transient. The earlier the recriticality is reached, the more the core is depleted. The change in the maximum power reached is small, only about 0.3%. The trends of primary extreme temperatures of the hot and cold legs (the second and third panels in Figure 5.14) exhibit similar trends with respect to depletion compared to the previous transient, Figure 5.12. Interestingly, the maximum temperatures reached change little with respect to depletion in this transient, whereas the minimum temperatures of the hot and cold legs evolve by approximately 20 K over the 10 years of depletion. Both the maximum and minimum cold leg temperatures have opposing slopes, while the

maximum and minimum hot, and also the graphite shown in the bottom panel of Figure 5.14, show increasing trends with depletion timeline.

5.2.4 Uncertainty Quantification of Thermophysical Parameters

A parameter sensitivity study in the context of this dynamic modeling effort determines how the system dynamics is affected by a variation in model parameters. One purpose of the sensitivity analysis is to check whether the lack of accurate knowledge of an input parameter impacts the safety envelope of an MSR operation during expected transients. The variance in the model parameters represents the uncertainty of the corresponding physical value. This methodology can be used to identify parameters whose accuracy needs to be improved to allow a reactor system to operate safely. Previous work [55] and [25, Chapter 6] explored the impact of system parameters' uncertainties on transient progression in BOC. Herein, this methodology is extended to uncertainty of depletion-dependent parameters and quantification of its impact on transients over the fuel cycle duration.

A sensitivity analysis was performed for a transient in which an external reactivity 100 pcm is added to the system as a step insertion to investigate the effects of depletion-dependent uncertainty in thermophysical parameters, specifically the fuel salt heat capacity and PHX heat transfer coefficient. A step reactivity insertion transient was chosen to demonstrate the effects because a step insertion is a familiar transient that is easy to characterize, interpret, and understand.

The uncertainties of the thermophysical parameters are assumed to be linearly increasing with respect to the depletion time. A range of 0 to $\pm 50\%$ from BOC to EOC was simulated for the two parameters mentioned above. The model is capable of assigning separate depletion-dependent modifying coefficients to heat capacities of all materials as well as heat transfer coefficients on relevant surfaces of the system's components.

In an effort to keep the demonstration transients simple, we performed the impacts of variance of the heat capacity of the fuel salt and the heat transfer coefficients of the PHX surfaces as two separate and independently simulated sets of transients.

The sensitivity of the heat capacity of the fuel salt is shown in Figures 5.15 and 5.16. The sensitivity of the PHX heat transfer coefficients is depicted in Figures 5.17 and 5.18. It should be noted that some results are omitted from Figures 5.16 and 5.18 to make the graphs legible while capturing the underlying phenomena.

5.2.5 Fuel Salt Heat Capacity

Changes in heat capacity and conductivity of the materials of reactor components are important to investigate and estimate, as they can affect operational safety. Fuel depletion will change the heat capacity of fuel salt over the operational time as a result of the build-up of plutonium and fission products. Fuel salt heat capacity variations can have significant impacts on dynamic behavior.

The transient step with changes in the heat capacity of the fuel salt in the range of ±50% from BOC to EOC is simulated in a total of nine values within this range. It should be noted that this is a demonstration of the methodology and that it is unrealistic for the fuel salt heat capacity to deviate by 50% in the EOC.

The effects of the change in heat capacity on the transient progression are shown in Figure 5.15. The top panel shows that increasing the heat capacity results in an increase in the maximum nominal power and its FWHM. The reactivity insertions of 100 pcm at BOC and EOC correspond to 0.91 and 1.30 dollars, respectively, which is shown on the right y-axis in the top panel. The reverse is observed for heat capacity reduction. The middle panel shows that increasing of heat capacity results in a higher steady-state core average fuel temperatures of the system while its reduction results in lower core average temperatures. However, the deviation of a post-transient equilibrium core average fuel temperature with increasing and decreasing fuel salt heat capacity is not symmetrical.

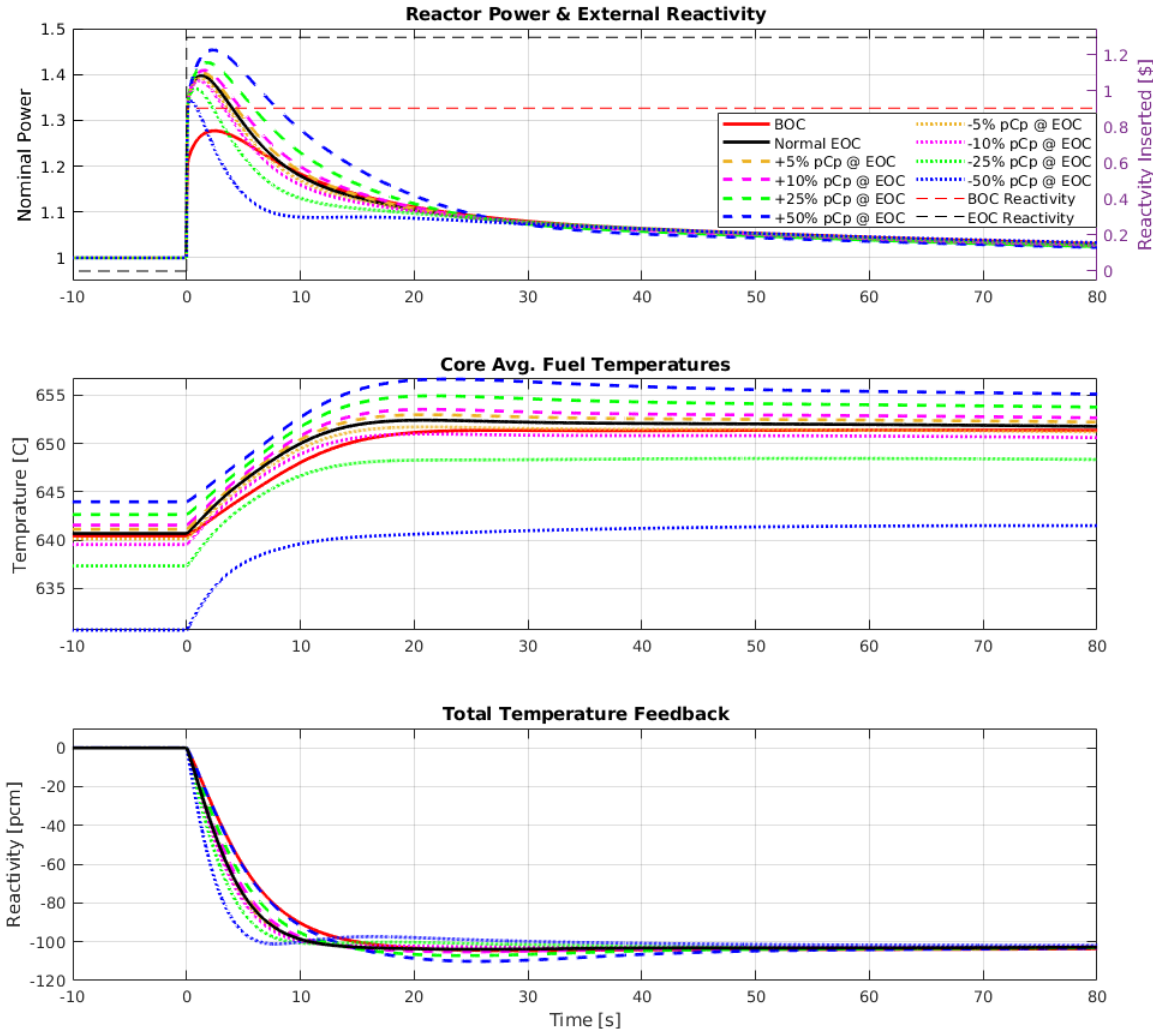

Figure 5.15: Transient progression of a 100 pcm step insertion at BOC and EOC with varying fuel salt heat capacities for (top) reactor power and relative dollar-worth reactivity, (middle) core-average fuel temperature, and (bottom) total temperature-induced reactivity feedback [14]

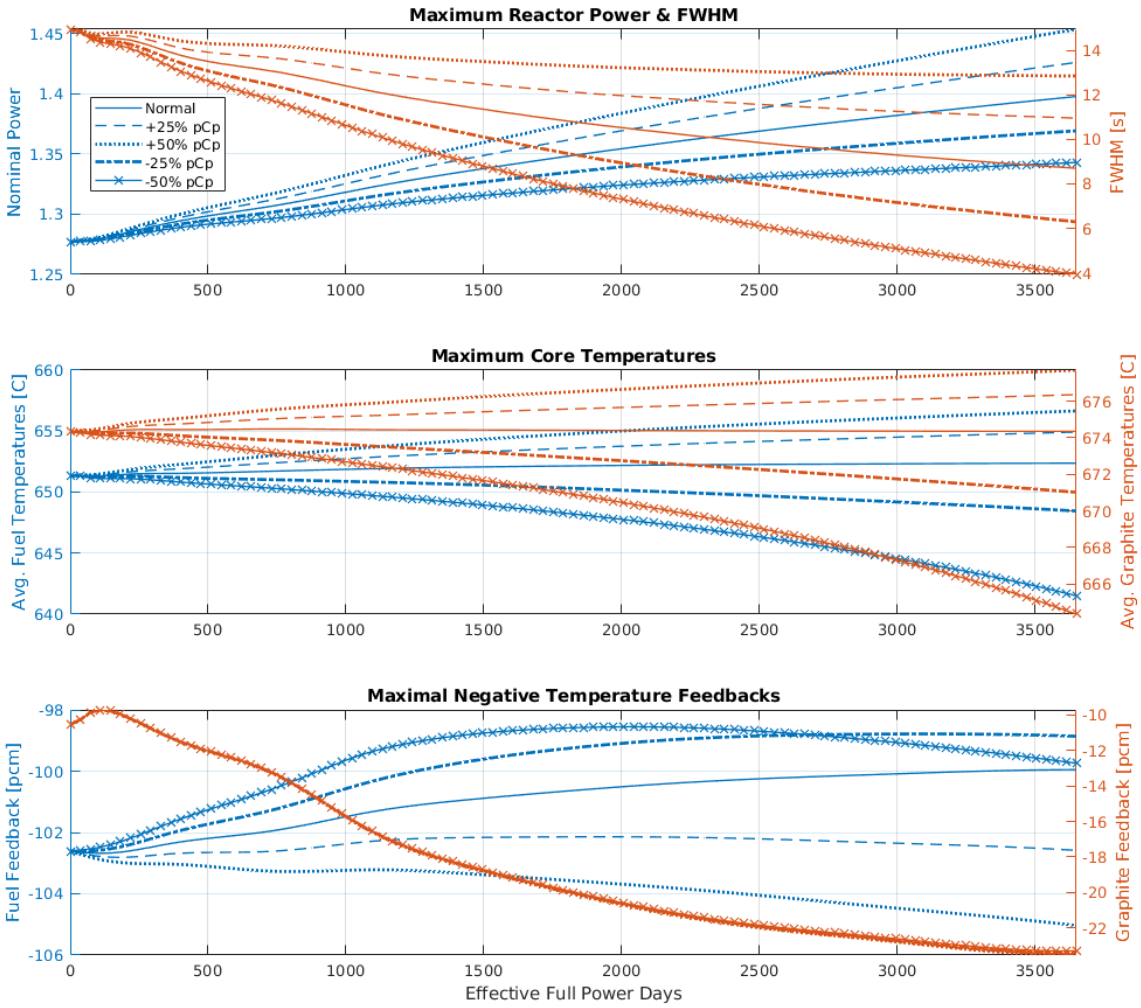

Figure 5.16: Depletion-dependent parameter deviations during a 100 pcm step insertion with varying fuel salt heat capacities: (top) maximum reactor power and FWHM, (middle) maximum core temperature, and (bottom) maximum (negative) temperature-induced reactivity feedback [14]

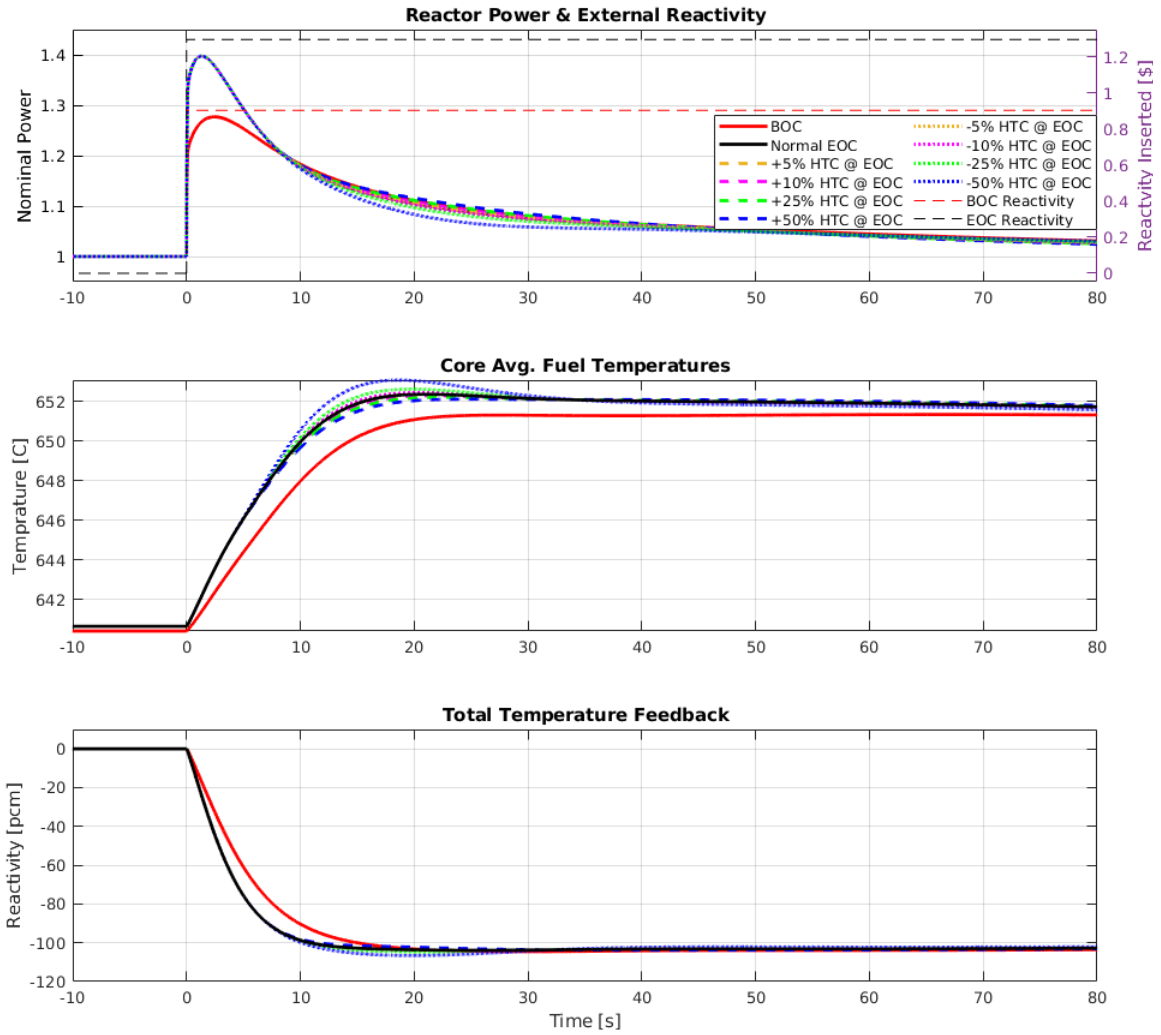

Figure 5.17: Transient behavior of a 100 pcm step insertion at BOC and EOC with varying heat transfer coefficient of PHX [14]

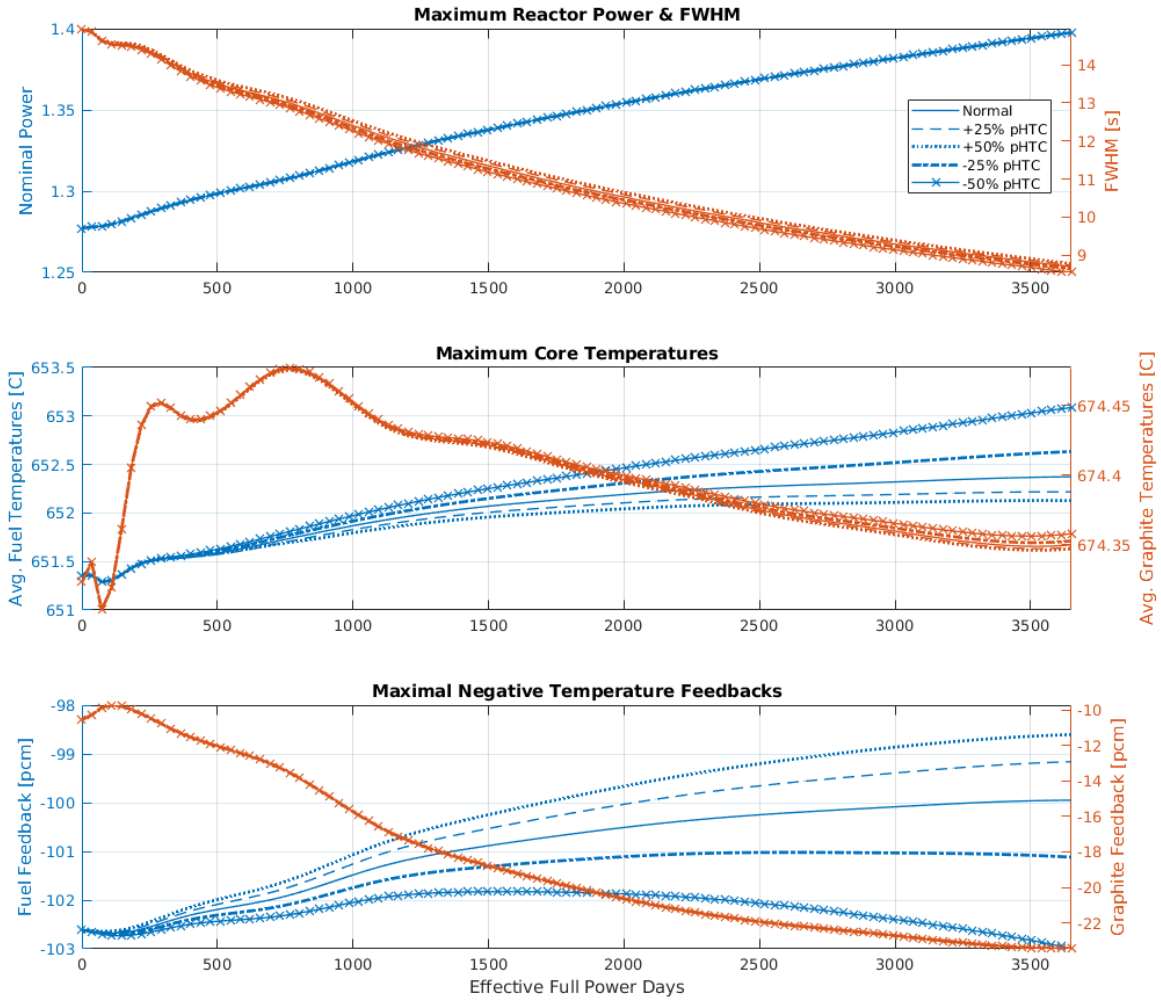

Figure 5.18: Depletion-dependent parameter deviations during a 100 pcm step insertion with varying primary heat transfer coefficient: (top) maximum reactor power and FWHM, (middle) maximum core temperature, and (bottom) maximum (negative) temperature-induced reactivity feedback [14]

The sensitivities to uncertainty in the heat capacity of the fuel salt to various dependent variables of interest are analyzed as a function of the history of depletion in Figure 5.16. For clarity, only five of the nine cases are shown: the nominal ±25% and ±50% in the EOC. The four cases where the heat capacity is modified from BOC to EOC show similar trends to the nominal case where the heat capacity remains constant. Increasing fuel heat capacity allows the fuel to carry more energy per degree of temperature change. From a reactor system, the dynamic prospective allows the fuel to bear more energy without inducing as much temperature feedback as the change in its temperature is less.

The maximum reactor power reached during the transient step (see Figure 5.16, top panel, left axis) and the FWHM of the power peak (top, right y-axis) for the insertion of the transient step along the depletion timeline. If the heat capacity increases with depletion, a higher reactor power is reached, and the power peak lasts longer after a transient step reactivity insertion.

The evolution of the maximum core average fuel and graphite temperatures (Figure 5.16, middle) shows a significant decrease in the maximum temperatures reached during the transient progression along the depletion, when the fuel heat capacity decreases toward the end of EOC. It should be emphasized that the changes dependent on the depletion of the maximum temperatures are minor when the heat capacity of the fuel salt remains constant, as previously shown in Section 5.2.1. The lower the fuel salt's heat capacity, the faster the feedbacks act, thereby reducing the temperature maxima.

The maximum temperature reactivity feedbacks during the transient step along the depletion timeline (see Figure 5.16, bottom) indicate that lowering the heat capacity of the fuel makes the reactor respond faster, thus lowering the magnitude of the feedbacks during the transient. Interestingly, the deviation of the heat capacity of the fuel does not affect the maximum temperature feedback of the graphite.

5.2.6 Heat Transfer in Primary Heat Exchanger

A heat transfer coefficient potentially depends on many variables and is susceptible to rapid changes due to various phenomena. Because of the high boiling points of alkali-halide salts, MSRs do not suffer from a departure from nucleate boiling that changes local heat transfer coefficients in LWRs. However, MSRs have several unique problems that can create undesirable scenarios with respect to heat transfer coefficients. Since the fuel itself is the coolant, the FPs are circulated around the primary loop. Some of the less soluble FPs, noble and seminoble metals, will be plated on relatively cold surfaces, namely heat exchangers and pipes [56, 57]. Plating out of FPs can change the material's heat conductivity, its surface texture, and even cause blockages in tubing in extreme cases. All these phenomena change the heat transfer coefficient and typically reduce the efficiency of heat transfer. The sensitivity study presented in this section investigates depletion-dependent changes of heat conductivity in the primary heat exchanger.

Figure 5.17 shows the transient progression of the insertion of 100 pcm steps in the EOC for the nominal PHX heat transfer coefficient and 8 steps in the range up to ±50%. The red line shows a nominal progression at BOC for comparison. The top panel shows that the change in heat transfer coefficient did not affect the initial power excursion after step insertion. However, a difference in progression can be observed after the initial power peak and before the asymptote, approximately 10 to 30 seconds after the transient initiation. This observation also applies to the fuel salt average core temperature shown in the middle panel and the total temperature feedbacks shown in the bottom panel. Increases in the PHX heat transfer coefficient will increase the heat transfer from the core, thus reducing the fuel salt temperature and vice versa. The core fuel salt temperature change is not instantaneous: the fuel salt has to flow around the primary loop to experience the change in the PHX heat transfer coefficient. This circulation delay explains why all trends in the EOC in Figure 5.17 are identical until approximately 10 s after the step insertion.

The sensitivities of changes in the PHX heat transfer coefficient to select dependent variables of interest are shown as a function of the history of depletion in Figure 5.18. The top panel clarifies that changes in the heat transfer coefficient do not change the maximum reactor power reached during the step insertion transient progression, and the FWHM of the power peak is affected only slightly. All lines in the top panel trend with the nominal EOC case, and do not diverge by a considerable amount. In the middle panel, the maximum core temperature shows that the decrease in the PHX heat transfer coefficient results in an increase in the maximum fuel temperatures and a negligible increase in the graphite temperatures.

The maximums of negative temperature reactivity feedbacks reached during the transient from separate fuel and graphite contributions are shown in the bottom panel. The lower the PHX heat transfer coefficient, the lower the minimum fuel temperature feedback. Note that the minimum temperature feedback corresponds to the maximum of absolute value of the feedback since the feedbacks is negative. The graphite temperature feedback appears to be unaffected.

5.3 MSRR Transients

Several transients were perfomed with developed MSRR model as described in Section 3.3. Transients include step insertion transients to evaluate normalized power behaviour with respect to effective delayed neutron fraction and a demonstration of a possible MSRR start-up.

5.3.1 Step Insertions at Full Circulation

Three reactivity insertion transients were performed at nominal circulation speed to understand reactor behavior under super-prompt critical, prompt critical, and sub-prompt critical step insertions at nominal flow speed. The effective DNP fraction, β_{eff} at nominal flow rate is 589.1 pcm. Transients are performed by inserting step

reactivities of 2 $, 1 $ and 0.5 $ after 2000 s of steady state. The inserted reactivities are equal to 1178 pcm, 589.1 pcm and 294.5 pcm, respectively. The transient behavior of the reactor power, the core temperatures and the total temperature feedback is captured in Figure 5.19. The leading 2000 s of the steady state is offset to make the reactivity insertion time 0 s. The results are plotted in three colors for clarity. Transient results of 2 $, 1 $ and 0.5 $ are captured in green, blue and red in order.

In Figure 5.19 the first panel is normalized power, the second panel is the average fuel temperature of the core, the third panel is the graphite core temperature and the fourth panel is the total temperature feedback. When the normalized power is examined, it is clear that 2 $ reactivity insertion caused the highest peak power followed by 1 $ and 0.5 $. The maximum powers reached are 1.71E3, 53.2 and 6.73 of nominal power for 2 $, 1 $ and 0.5 $ step reactivity insertions of 2 $, 1 $ and 0.5 $, respectively. Both super-prompt critical and prompt critical reactivity insertions resulted in immediate power excursions. The time elapsed between the insertion of the reactivity and the maximum powers for 2 $ and 1 $ insertions are 0.3 s and 1.1 s respectively. The maximum power of the 0.5 $ step reactivity insertion was reached after 12.2 s of the insertion. All three power transients show that power transients following step reactivity insertions return to previous steady state of nominal power. There is a slight oscillation after 200 s, however, this oscillation is dampening. The second panel core average fuel temperatures reflect that 0.5 $ insertion resulted in the lowest fuel temperature increase while the 2 $ insertion resulted in the highest increase in fuel temperature. Maximum temperatures reached are 799.3 °C, 672.7 °C, and 622.1 °C for step insertions of 2 $, 1 $ and 0.5 $ step reactivities respectively. The 0.5 $ step insertion shows a gradual increase in the average fuel temperature, while the other two transients show sharp increases. It is clear that all three core average fuel temperatures are reaching a new steady state. The new average core fuel temperatures are 673.3 °C 621.7 °C 595.9 °C for insertions of 2 $, 1 $ and 0.5 $ respectively. The core graphite temperatures shown in panel three reflect the insertion

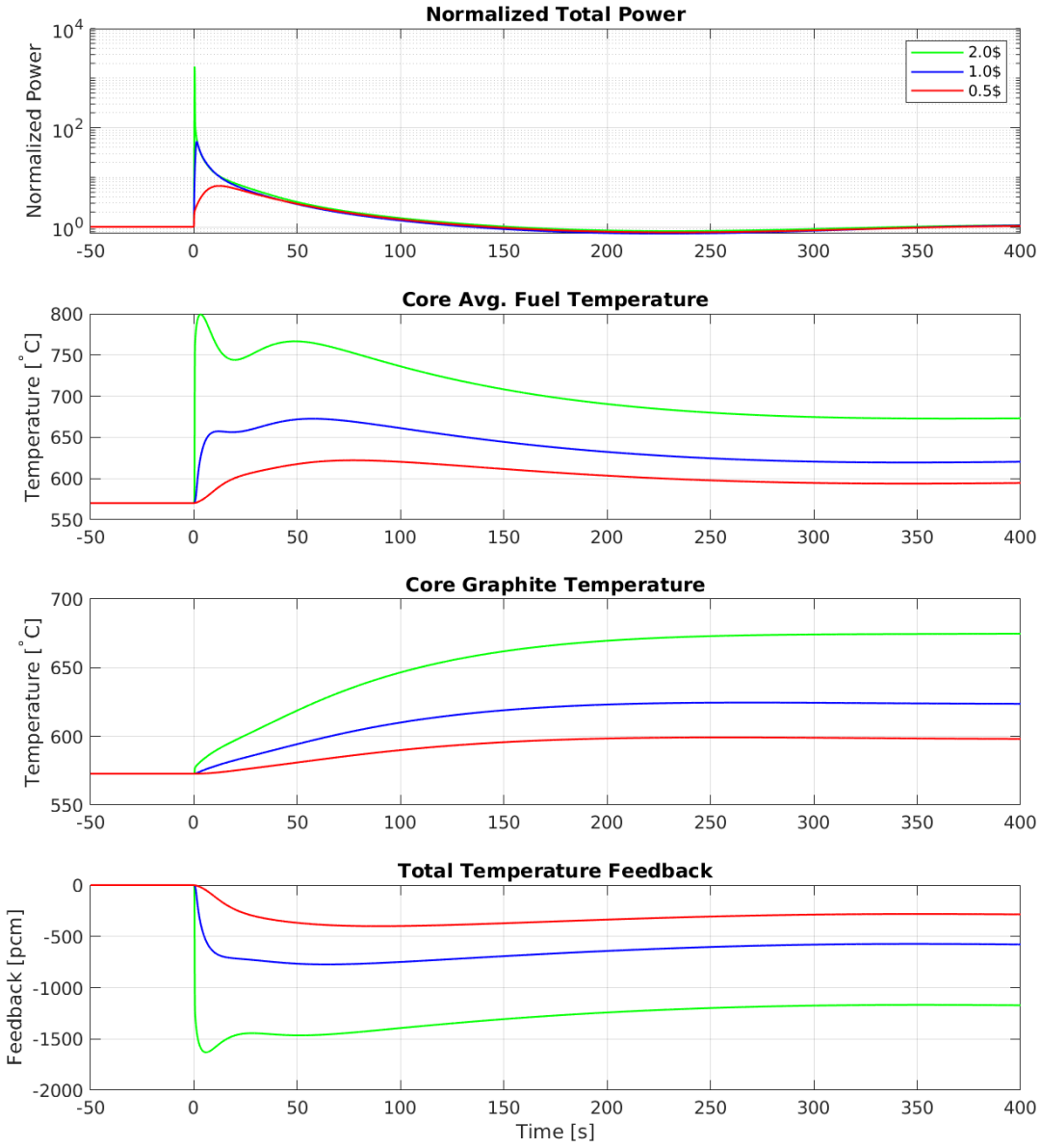

Figure 5.19: Reactivity insertions at nominal circulation

of 2 $ resulted in the highest graphite temperature of 675.9 °C. The 1 $ step insertion resulted in the core graphite temperature reaching a maximum of 624.6 °C while the 0.5 $ insertion reached a maximum of 599.2 °C of graphite temperature. All graphite temperature transients are gradual, unlike average core fuel temperatures. The total temperature feedback resulting from each transient is captured in the last panel of the Figure 5.20. The total negative temperature feedback from the step insertion of 2 $ is immediate and reaches a maximum of -1630.5 pcm. The insertion of step 1 $ also produces a rapid total negative temperature feedback, but does not reach the maximum of -773.1 pcm until 64.8 s passes from the reactivity insertion. The transient of 0.5 $ reaches the lowest maximum total negative temperature feedback among the three transients and the recorded maximum value of -400.2 pcm. All three temperature feedback transients reach a new steady state to counteract the amount of reactivity inserted making the net reactivity of the system at asymptotic reactor state.

5.3.2 Step Insertions at Variable Circulation Speeds

Three-step insertions were made at varying circulation speeds to demonstrate the change in dollar worth of inserted reactivity. The effective DNP fraction, β_{eff} at a nominal flow rate of MSRR is 589.1 pcm. The transients were performed at flow rates of 1, 2/3 and 1/3 of the nominal flow fractions. For three transients, 589.1 pcm is added as a external reactivity step. To perform transients first, all simulations were brought to steady state at full power with full circulation for 2000 s. At the simulation time 2000 s, the fuel salt flow rates were changed by tripping the primary pump. The desired flow fractions 1, 2/3 and 1/3 were set to be the free-convection flow fraction after pump trip. The simulations were allowed to reach a new steady state at their respective flow fractions for another 2000 s. Reactivities of steps of 589.1 pcm were inserted into each simulation. The results of each simulation are collected, and the parameters that can characterize the transient are captured in

Figure 5.20. Figure 5.20 shows the normalized power in the first panel, the average temperature of the core fuel in the second panel, the temperature of the core graphite in the third panel, and the total temperature feedback in the last panel. Three transients are captured in green, blue, and red, which correspond to flow fractions 1, 2/3, and 1/3, respectively. The first 4000 s of all transients was compensated for to make the insertion time of the reactivity step 0 s. The effective DNP fractions, β_{eff} at 2/3 and 1/3 of the flow fractions are 599.9 pcm and 617.1 pcm, respectively. Inserted reactivity 589.1 pcm worth 0.98 \$ and 0.95 \$ at 2/3 and 1/3 flow fractions, in order.

The normalized power shown in the first panel of Figure 5.20. Upon close inspection of normalized power transients, it is clear that the maximum power reached decreases as the flow fraction reduces. The normalized peak power achieved by the simulation with nominal flow fraction is 53.22 while the simulation with 2/3 flow fraction achieved 47.9. The simulation with a 1/3 flow fraction recorded a maximum normalized power of 40.81. All three power transients have the same general trend; however, transients with nominal flow fraction and 2/3 flow fraction behave similarly. The average core fuel temperature shows that the transient with 1/3 flow fraction reached the highest temperature at 673.5 °C while the lowest average core fuel temperature is recorded on the transient with nominal flow fraction at 672.6 °C. The average core fuel temperatures do not follow a general trend. The third panel, core graphite temperatures show that the transient with the nominal flow fraction achieves the highest graphite temperature, and the transient with 1/3 flow fraction shows the lowest. The temperature trends can be attributed to the change in the heat transfer coefficients as a result of the change in flow fraction. The heat transfer coefficient between graphite and fuel salt is higher when the flow fraction is high. When considering the total temperature feedback in panel four, it is clear that the change in flow fraction did not affect how fast the feedback is acting. All panels show that respective quantities reach a new steady state post step insertion. It is clear that

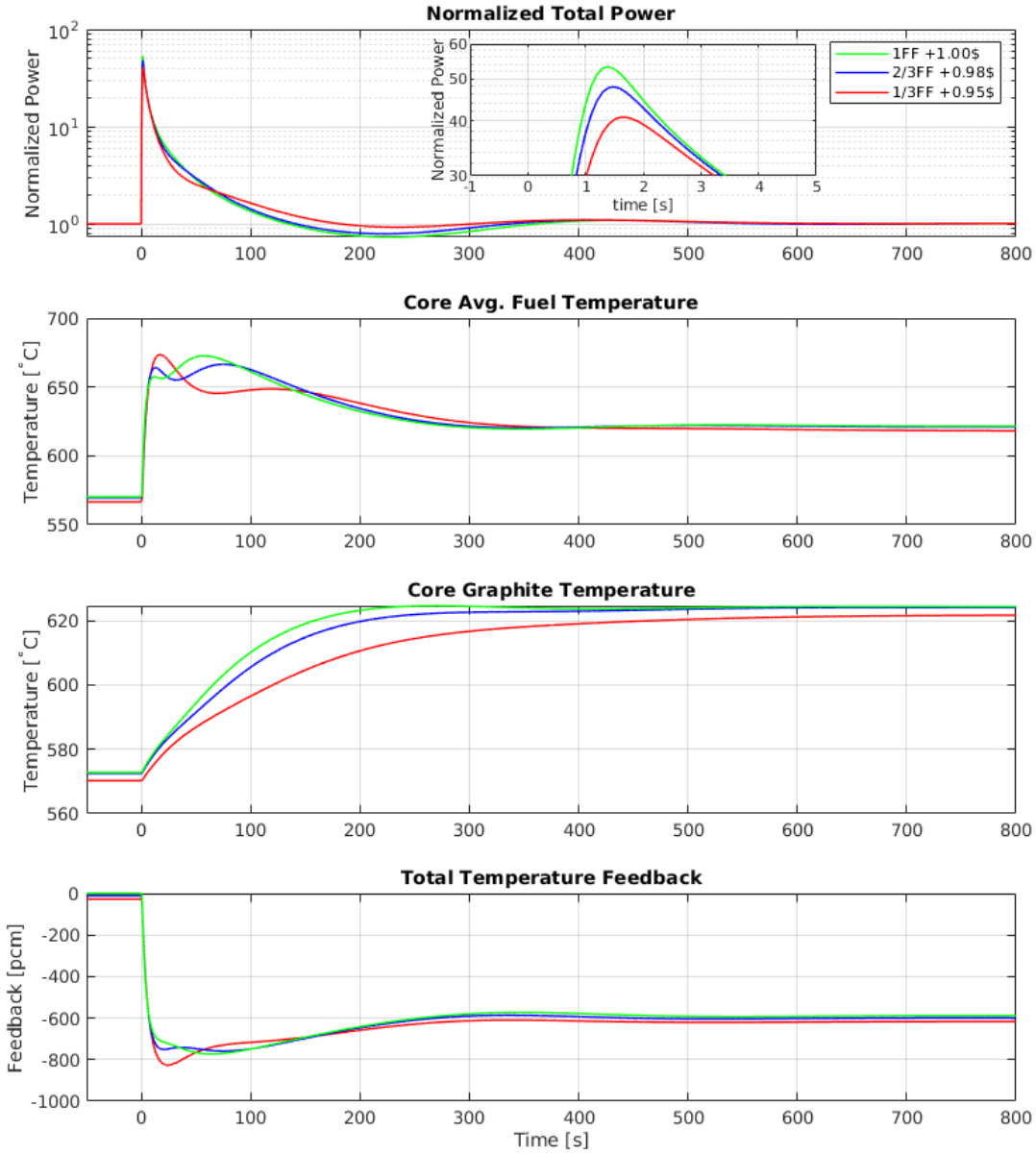

Figure 5.20: Reactivity insertions at various circulation speeds

the change in flow rate affects the MSRR behavior. However, the behavior change for the insertion of the 589.1 pcm step is not drastic. This quality stems from MSRR primary loop design. The core resident time is much larger than that of the loop resident time.

5.3.3 Hypothetical Maximum Accident Transient

The postulated maximum accident transient for MSRR was simulated using the developed MSRR model. The event sequence of the postulated transient presented here is discussed in the Section. The simulation was initialized at full power and the solvers were allowed to come to steady state for 2000 s of simulation time. The radiator, the primary pump, and the secondary pump were tripped simultaneously at the simulation time stamp of 2000 s. The radiator trip transient is a step down of heat removal from 100 % to 0. Parameters important for reactor safety are extracted and captured in Figure 5.21. The transient is in the order of hours; therefore, the time axis is represented in hours. The steady state before the perturbation is also included in the plot to provide a reference. The steady state is offset to create the transient initiation time stamp 0 hr. In Figure 5.21, the first panel shows the normalized total reactor power and its components, the normalized fission power, and the normalized decay power. The core fuel inlet and outlet temperatures and graphite temperatures are captured in the second panel. The third panel shows the total feedback due to temperature.

Upon close inspection of the normalized power panel in Figure 5.21, it is clear that the initial total power is slightly higher than 1. This is due to radiative heat loss to the reactor trench. The ambient temperature of the reactor trench was assumed to be 550 °C. The net heat loss from radiation is $\approx 2\,\%$ of the normalized reactor power during steady state. At the 0 hr mark the normalized fission power slightly increases. The increase in fission power is reflected in the normalized total power. This slight increase in fission power is caused by the reduction of DNP advection

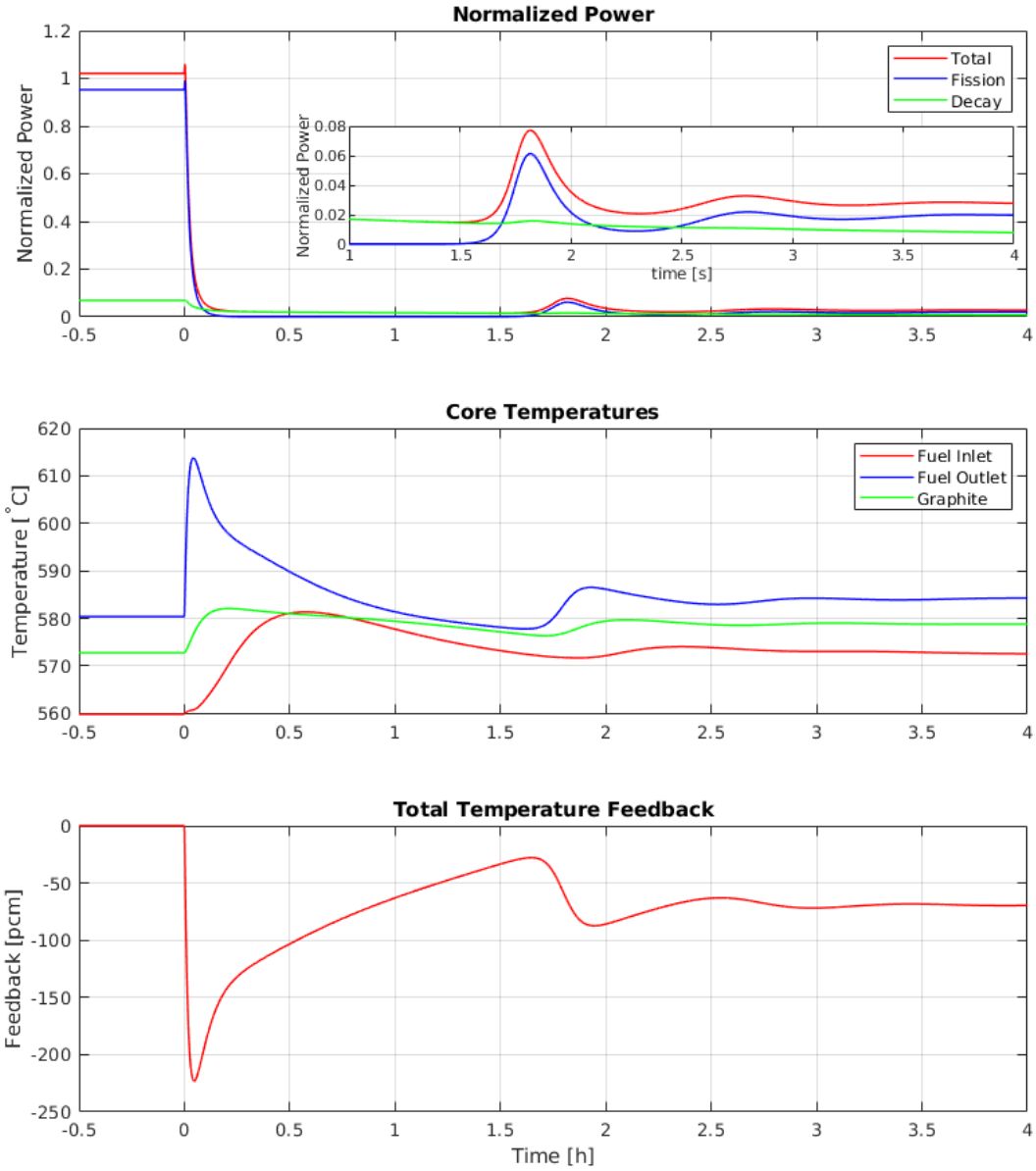

Figure 5.21: Hypothetical Maximum Accident Transient

following the primary pump trip. However, this slight increase in power is short-lived, as reduction of fuel flow combined with loss of heat removal through the radiator increases core temperatures which can be seen from the temperature panel. The normalized fission power rapidly decreases as the risen core temperatures increase the negative temperature feedback. The fission power becomes ≈ 0. The FP inventory driven decay heat produces power in the entire primary loop. Highly radioactive FPs rapidly decay producing decay power. The highly radioactive FPs are short-lived; therefore, the normalized decay heat reduces from its steady state value of 6.8 % of total power to 2 % by the 1.5 hr mark. When attention is paid to the core temperatures captured in the second panel, it is evident that the core fuel inlet and outlet temperatures and the graphite temperature increase following the transient initiating event. The core fuel outlet temperature increases rapidly, even though the fission power is decreasing. The rapid increase in the temperature of the core fuel outlet is due to the deposition of decay heat. The MSRR has a total fuel salt capacity of 500 L. The reactor vessel accounts for 400 L of the total fuel salt volume of the system. Therefore, 80% of decay heat is produced within the reactor vessel. The core temperatures reach their maximum values and gradually reduce to the simulation time 1.5 hr due to radiative heat loss. The total temperature feedback captured in panel three correlates power and temperature results, as seen so far. Negative temperature feedback gradually decreases as fuel salt and graphite temperatures reduce. The decrease in negative temperature feedback causes the reactor to become recritical at 1.5 hr. The recriticality event can be seen from the normalized fission power in the power panel. During the recriticality power excursion, the normalized power reaches a maximum of 0.08 while the normalized fission power reaches a maximum of 0.06 at 1.75 hr of simulation time. It is clear that the recriticality event is followed by dampening power oscillation, which subsides as the system reaches a new steady state. The normalized power in the new steady state is 0.027. The reactor temperature of the new steady state is higher than that of the nominal steady state and is reflected

in the total negative temperature feedback. It is clear that radiative heat loss has increased by 0.7 % from the nominal steady state. This increase is caused by an increase in the average temperature of the system.

5.3.4 Approach to Criticality

A simulation is performed to understand the reactor behavior during a MSRR start up. The start up transient presented here is described in detail in Section 3.4.5. Each transient step is performed incrementally with gaps of 1 hr where applicable to increase the clarity of the results. It is possible to perform the transient in a shorter period of time. The MSRR model is slightly modified by changing initial conditions. The normalized neutron population is set to 0 and the option for the DNP drift correction was turned off. A negative reactivity of -3600 pcm was inserted. The initial temperature of the primary loop components and the ambient temperature of the trench are set to the mean core temperature of 570°C. The radiator and secondary pump remained closed throughout the transient. The primary pump was closed during the initial stage but turned on as the transient progressed. The simulation was brought to steady state and held for an hour of simulation time to converge all the solvers prior to initiating the transient sequence. The entire transient of the neutron population is captured in Figure 5.22. The total transient is made up of four phases and is indicated in Figure 5.22.

Phase 1 of the transient is shown in Figure 5.23. Phase 1 starts with the initial steady state that lasts from 0 hr to 1 hr. The primary pump remains turned off during the first phase. The neutron population is zero at that period of time. At the 1 hr mark, an external neutron source is inserted into the core with a neutron emission rate of 1E6 n/s. The multiplication approach of the source is applied from the 2 hr mark in increments of 0.1 of the multiplication factor k_{eff} to find the static criticality. Reactivity steps are added to the system until static criticality is achieved at 13 hr. The source was removed 100 s after achieving criticality. The sudden increase in

neutron population at 13 hr is the result of leaving the source for 100 s. This spike was used as a visual confirmation of static criticality.

Phase 2 of the transient begins with static criticality from 13 hr and the neutron population is depicted in Figure 5.24. Static criticality is maintained until the 14 hr mark. The primary pump was turned on and ramped up to 25 % of the nominal flow rate at 14 hr. The neutron population suddenly decreases as a result of DNP drift. The primary pump flow rate increases and comes to a steady state of 25 % of the nominal flow rate by 15 hr. The external neutron source is inserted into the core again at 15 hr and allowed to come to steady state until 16 hr. From 16 hr source multiplication method is performed to find the criticality at the nominal flow rate of 25 %. The criticality at 25 % nominal flow rate is achieved at 19 hr. The spike in neutron population at the 19 hr mark confirms the criticality and the source is withdrawn.

Phase 3 of the transient begins with criticality at 25 % fuel flow rate and the transient neutron population is shown in Figure 5.25. The primary pump speed increased from 25 % of the nominal flow rate to 50 % nominal flow rate at 20 hr. The DNP drift increases as the fuel flow increases, and as a result, the neutron population decreases. The neutron population stabilizes at 21 hr and the source is inserted. After inserting the source, an hour is given to the neutron population to come back to a new steady state. The source multiplication method is applied from 22 hr and the criticality at 50 % fuel flow rate is established at 24 hr and the source is withdrawn.

Phase 4 starts with criticality at 50 % fuel flow rate, and the neutron population is captured in Figure 5.26. The primary pump is ramped to increase the nominal flow rate from 50 % to 100 % at 25 hr. As previously seen, the neutron population gradually decreases as the fuel flow rate increases. The neutron population stabilizes at 100 % of the nominal fuel flow rate at 26 hr and the external neutron source is introduced to the core. Once the neutron population has reached a steady state with

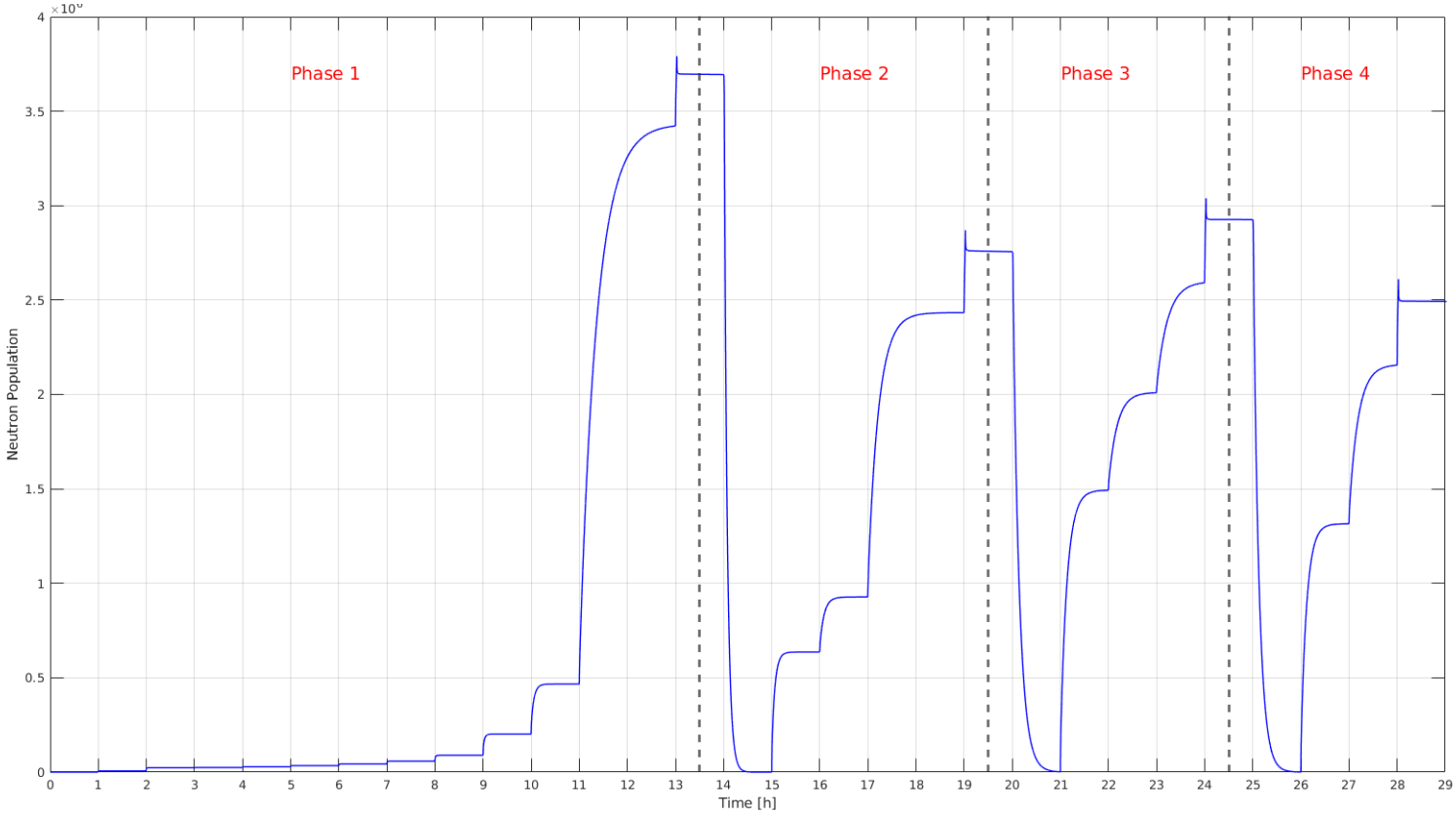

Figure 5.22: Approach to Criticality Full Transient

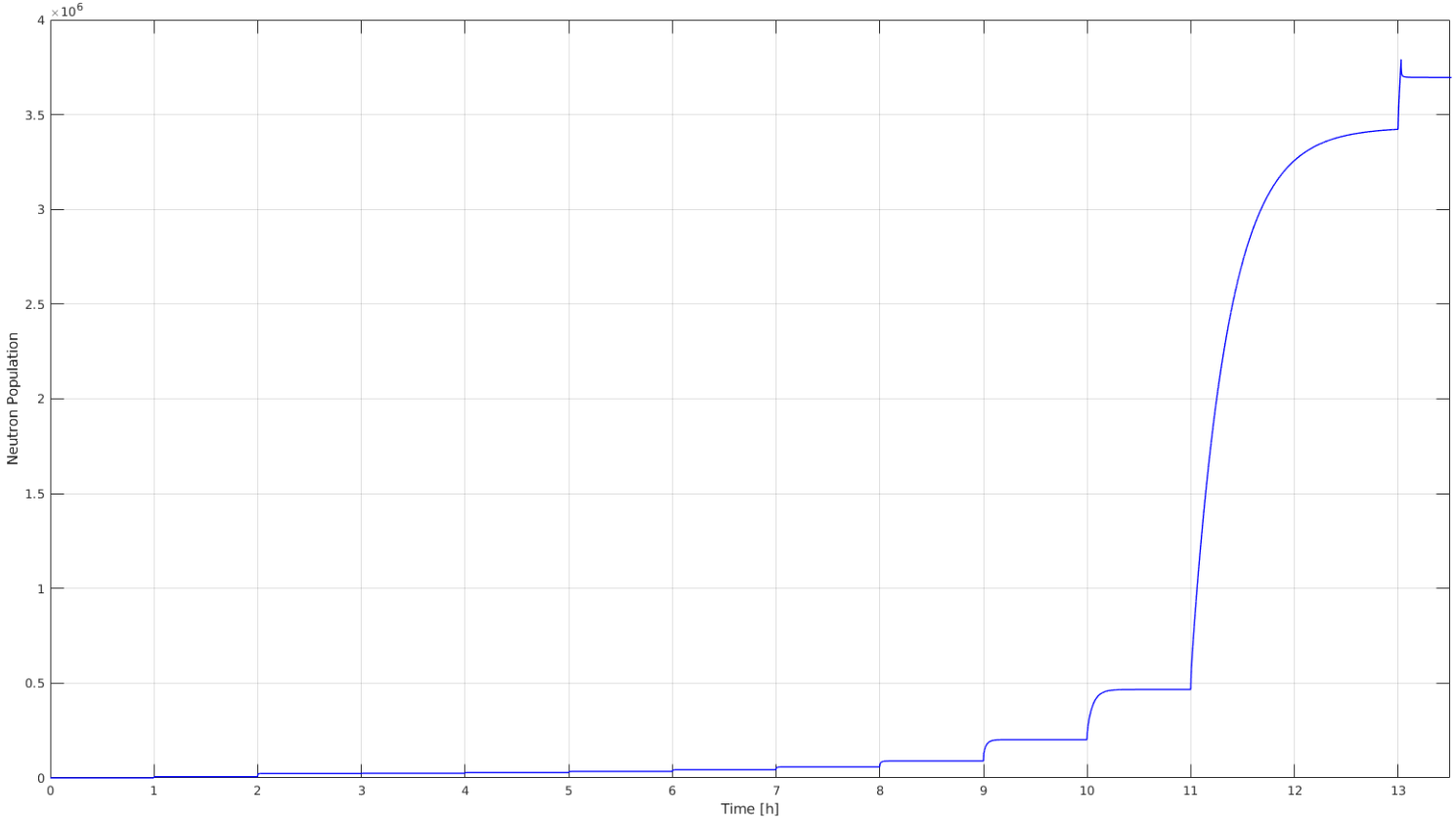

Figure 5.23: Approach to Criticality Phase 1

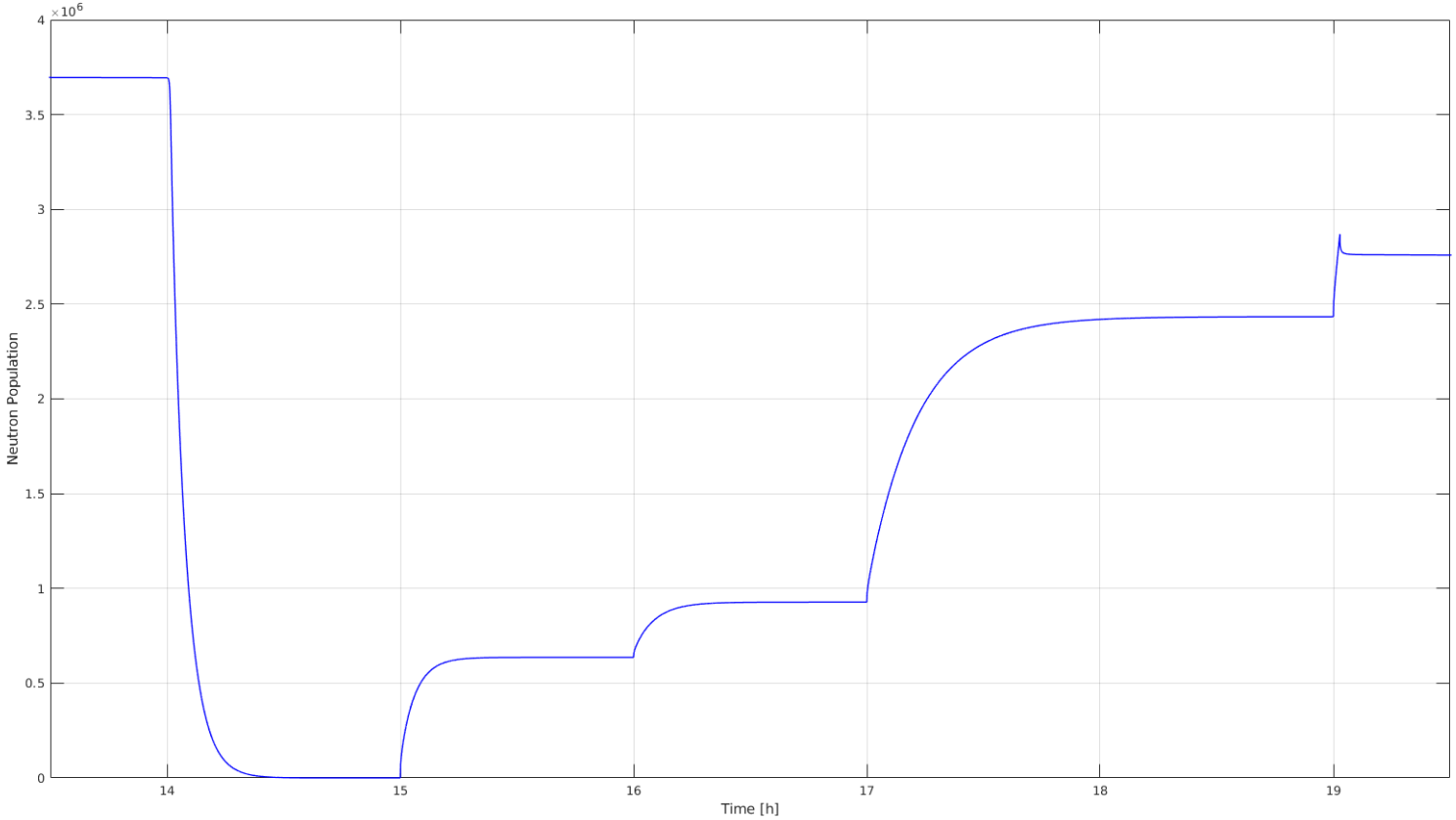

Figure 5.24: Approach to Criticality Phase 2

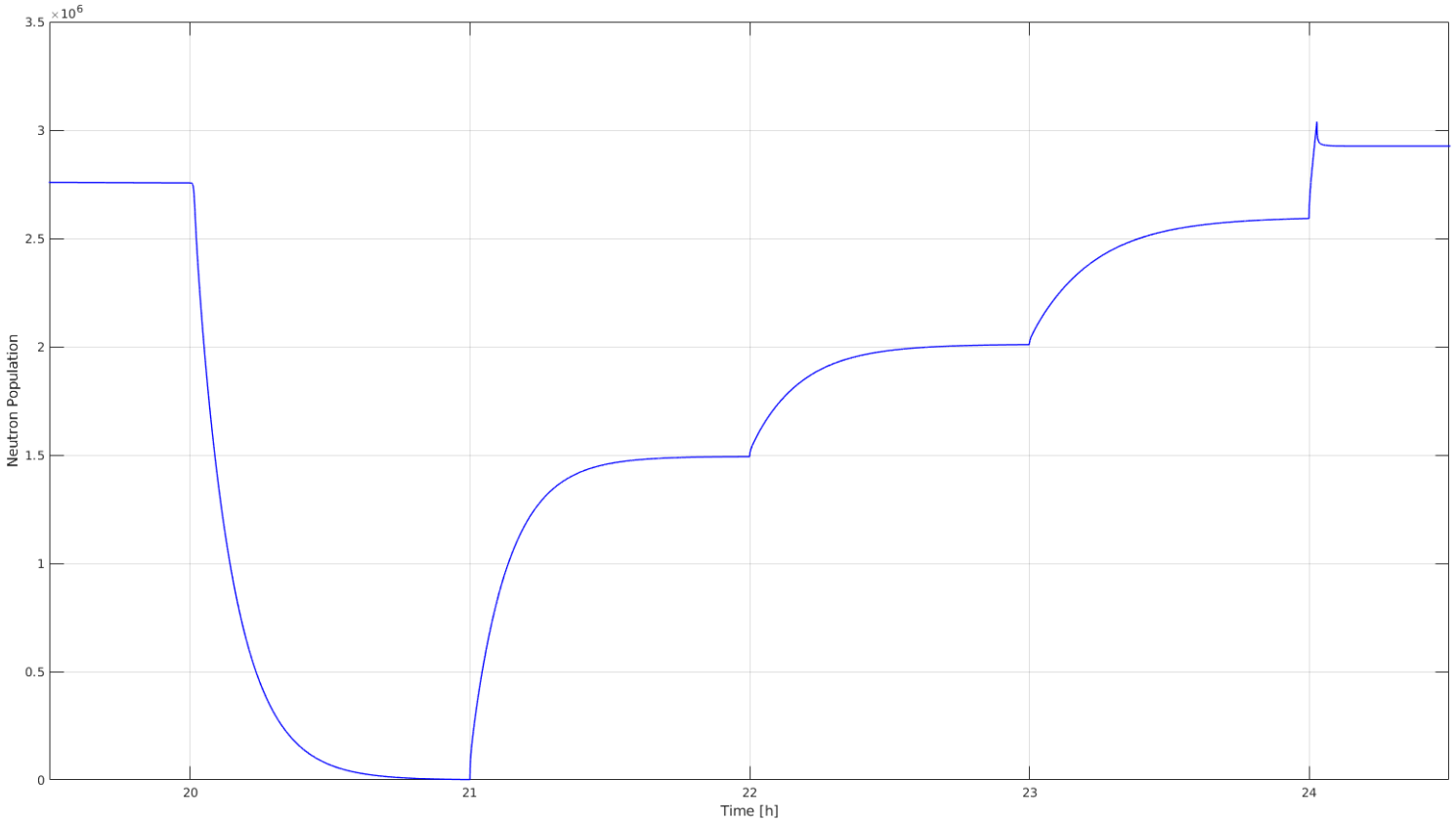

Figure 5.25: Approach to Criticality Phase 3

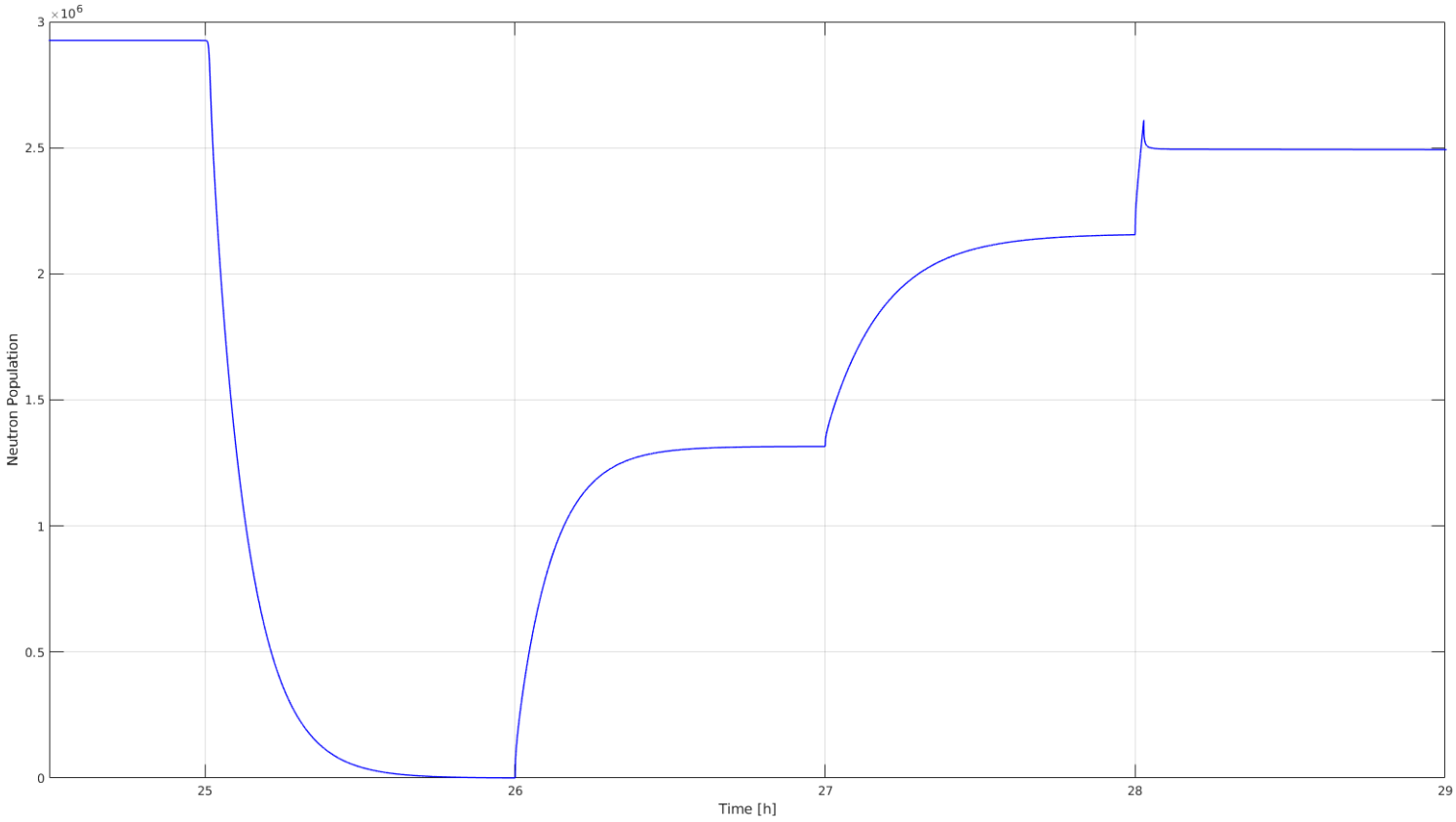

Figure 5.26: Approach to Criticality Phase 4

the neutron source, the source multiplication method is used to find the criticality from 27 hr. The criticality at full fuel circulation speed is established at 28 hr.

From the demonstrated start up transient, it is clear that MSR startup procedures are unique due to DNP drift caused when the primary pump becomes operational. The neutron population decreases when the DNP drit rate increases. If the primary pump fails after it has been brought online, it can add positive reactivity to the system. This presents a safety concern; therefore, the pump speed should be increased incrementally to ensure that the neutron population does not increase without control rod withdrawal. The initial heating of the fuel salt and components of the system requires further investigation to improve the understanding of the duration and dynamics of a start-up procedure for MSRR.

Chapter 6

Conclusions and Future Work

MSRs dyanmic behavior is unique due to the fluidity of the fuel. The developed MSR dynamic modeling toolkit is capable of modeling normal and off-normal transients of MSR with low fidelity. The validation transients performed on the available MSRE results show that the model performance is adequate for first-order engineering calculations. Low fidelity simulations can be performed with limited design information to establish an initial understanding of the system behavior. This was demonstrated with the models presented. Initial investigations of system dynamics allow the development of a design criteria envelope that can be used to optimize SSC functionalities and address safety-related requirements. The SMD-MSR is a simple toolkit that can be used to perform depletion and sensitivity studies, which is useful since limited data is available on MSR depletion and material behavious. The modeling method can be greatly improved by including momentum balances and closure models. The following improvements are suggested to greatly enhance the modeling capabilities of SMD-MSR,

- Include momentum balance to calculate pressure drop
- Include closure models to calculate heat transfer coefficents internally
- Expand use of temperature based physical-properties

- Allow user to define a required number of nodes for a components to increase fidelity
- Develope an interface to perform depletion and sensitivity studies
- Improve the QA program

Bibliography

[1] V. Smil, *Energy in nature and society : general energetics of complex systems*. Cambridge, Mass: The MIT Press, 2008. 2

[2] OECD, "Total energy supply by source." https://www.iea.org/reports/key-world-energy-statistics-2021/supply. Accessed: 2022-08-14. 2

[3] IAEA, "Power reactor information system." https://pris.iaea.org/PRIS. Accessed: 2022-08-14. 4

[4] U.S. Energy Information Administration, "Electricity data browser." https://www.eia.gov/electricity/data/browser/. Accessed: 2022-08-14. 5

[5] Lawrence Livermore National Laboratory, "Energy flow charts." https://flowcharts.llnl.gov. Accessed: 2022-08-14. xii, 5, 6

[6] Department of Energy and Mineral Engineering Pennsylvania State University, "Basic economics of power generation, transmission and distribution." https://www.e-education.psu.edu/eme801/node/530. Accessed: 2022-08-14. 7

[7] J. Lane and U.S. Atomic Energy Commission, *Fluid Fuel Reactors*. Addison-Wesley books in nuclear science and metallurgy, Addison-Wesley Publishing Company, 1958. 8

[8] M. W. Rosenthal, P. R. Kasten, and R. B. Briggs, "Molten-salt reactors-history, status, and potential," *Nuclear Applications and Technology*, vol. 8, pp. 107–117, February 1970. 13

[9] General Electric Co., "Giving wings to the atom: Chronological history of nepa and ge-anp aircraft nuclear propulsion program 1946-1961." http://leehite.org/anp/documents/Giving_Wings_To_The_Atom.pdf, 1996. 13

[10] E. S. Bettis, R. W. Schroeder, G. A. Cristy, H. W. Savage, R. G. Affel, and L. F. Hemphill, "The aircraft reactor experiment—design and construction," *Nuclear Science and Engineering*, vol. 2, no. 6, pp. 804–825, 1957. 13

[11] R. C. Robertson, "Msre design & operations report Part I description of reactor design," Tech. Rep. ORNL-TM-0728, Oak Ridge National Laboratory, Oak Ridge, TN, USA, January 1965. 14, 152

[12] P. N. Haubenreich and J. R. Engel, "Experience with the molten-salt reactor experiment," *Nuclear Applications and Technology*, vol. 8, no. 2, pp. 118–136, 1970. 14

[13] V. Pathirana, A. M. Wheeler, and O. Chvála, "Scalable modular dynamic molten salt reactor system model with decay heat," *Annals of Nuclear Energy*, vol. 154, p. 108060, 2021. xiii, xiv, 18, 21, 33, 90, 92, 93, 94, 98, 101, 150, 152, 153, 154, 155, 156, 157, 158, 172, 176

[14] V. Pathirana, O. Chvala, and S. Skutnik, "Depletion dependency of molten salt reactor dynamics," *Annals of Nuclear Energy*, vol. 168, p. 108852, 2022. xii, xiii, xv, xvi, 18, 21, 43, 46, 90, 98, 100, 165, 168, 169, 171, 174, 175, 177, 178, 182, 183, 184, 185

[15] V. Pathirana, S. E. Creasman, O. Chvála, and S. Skutnik, "Molten salt reactor system dynamics in simulink and modelica, a code to code comparison," *Nuclear*

Engineering and Design, vol. 413, p. 112484, 2023. x, xi, xii, xiii, xiv, 18, 21, 65, 67, 70, 91, 95, 129, 130, 131, 133, 135, 137, 138, 139, 142, 143, 144, 148, 149, 150, 159, 160, 161, 163, 164, 165, 167

[16] N. Dunkle, J. Richardson, V. Pathirana, A. Wheeler, O. Chvala, and S. E. Skutnik, "Nerthus thermal spectrum molten salt reactor neutronics and dynamic model," *Nuclear Engineering and Design*, vol. 411, p. 112390, 2023. xii, 18, 27, 31, 38, 39, 94

[17] S. E. Creasman, V. Pathirana, and O. Chvala, "Sensitivity study of parameters important to molten salt reactor safety," *Nuclear Engineering and Technology*, vol. 55, no. 5, pp. 1687–1707, 2023. 18, 165

[18] Pathirana, Visura and Fontaine-Hall, Chelsea and Chvala, Ondrej, ""Molten Salt Reactor Kinetics in Zero Power Approximation"," in *ANS Winter 2021 Transactions*, 2021. 18, 27

[19] Dunkle, Nicholas and Pathirana, Visura and Chvala, Ondrej, ""NERTHUS MSR Dynamic Model"," in *ANS Winter 2021 Transactions*, 2021. 18

[20] V. Pathirana and O. Chvala, "Scalable modular dynamic molten salt reactor model with depletion dependency," in *2021 ANS Virtual Annual Meeting 2021 Transactions*, 2021. 18

[21] "Github repository for SMDMSR - Modelica." https://github.com/ondrejch/2021-SMD-MSR_Modelica, 2021. 18, 121, 141

[22] MathWorks Inc., "MATLAB Simulink." https://www.mathworks.com/products/simulink.html. Accessed: 2023-08. 20

[23] Modelica Association, *Modelica-A Unified Object-Oriented Language for Systems Modeling Language Specification Version 3.5*. Modelica Association, February 2021. 20

[24] S. Ball and T. Kerlin, "Stability Analysis of the Molten-Salt Reactor Experiment," Tech. Rep. ORNL-TM-1070, Oak Ridge National Laboratory, Oak Ridge, TN, USA, December 1965. 21, 94, 97, 146

[25] V. Singh, "Study of the dynamic behavior of molten-salt reactors," Master's thesis, University of Tennessee, 2019. 21, 165, 180

[26] K. Ott and R. Neuhold, *Introductory Nuclear Reactor Dynamics*. American Nuclear Society, 1985. 27, 42

[27] I. Pázsit, V. Dykin, and R. Sanchez, "The point kinetic component of neutron noise in an msr," *Annals of Nuclear Energy*, vol. 64, pp. 344–352, 2014. 28

[28] D. Wooten and J. J. Powers, "A review of molten salt reactor kinetics models," *Nuclear Science and Engineering*, vol. 191, 7 2018. 28

[29] J. Macphee, "The kinetics of circulating fuel reactors," *Nuclear Science and Engineering*, vol. 4, no. 4, pp. 588–597, 1958. 28

[30] T. W. Kerlin, S. J. Ball, and R. C. Steffy, "Theoretical dynamics analysis of the molten-salt reactor experiment," *Nuclear Technology*, vol. 10, no. 2, pp. 118–132, 1971. 28, 98, 151

[31] M. S. Greenwood and B. R. Betzler, "Modified point-kinetics model for neutron precursors and fission product behavior for fluid-fueled molten salt reactors," *Nuclear Science and Engineering*, vol. 193, 11 2018. 28, 93

[32] G. R. Keepin, T. F. Wimmett, and R. K. Zeigler, "Delayed Neutrons from Fissionable Isotopes of Uranium, Plutonium, and Thorium," *Phys. Rev.*, vol. 107, p. 1044, 1957. 28

[33] J. R. Engel, P. N. Haubenreich, and B. E. Prince, "Msre neutron source requirements," Tech. Rep. ORNL-TM-935, Oak Ridge National Laboratory, Oak Ridge, TN, USA, September 1964. 29

[34] "Decay Heat Changes to 50.46 and Appendix K." https://www.nrc.gov/docs/ML0217/ML021720702.pdf. 35, 36

[35] U.S. Nuclear Regulatory Commission, "Part 50–domestic licensing of production and utilization facilities." https://www.nrc.gov/reading-rm/doc-collections/cfr/part050/full-text.html. Accessed: 2022-07-12. 38

[36] International Atomic Energy Agency, ""Compilation and evaluation of fission yield nuclear data"," Tech. Rep. IAEA-TECDOC-1168, International Atomic Energy Agency, 12 2000. 41

[37] Lamarsh, J.R. and Baratta, A.J., *"Introduction to Nuclear Engineering"*. Prentice Hall, 1975. 42

[38] E. Nichita and B. Rouben, *"Essential CANDU: Reactor Dynamics"*, ch. 5, p. 32. Canada: UOIT, 2016. 42

[39] B. Betzler. personal communication, August 2019. 45

[40] M. S. Greenwood, B. R. Betzler, A. L. Qualls, J. Yoo, and C. Rabiti, "Demonstration of the advanced dynamic system modeling tool transform in a molten salt reactor application via a model of the molten salt demonstration reactor," *Nuclear Technology*, vol. 206, no. 3, pp. 478–504, 2020. 45

[41] P. N. Haubenreich, J. R. Engel, B. E. Prince, and H. C. Claiborne, "Msre design & operations report PartIII. nuclear analysis," Tech. Rep. ORNL-TM-730, Oak Ridge National Laboratory, Oak Ridge, TN, USA, February 1964. xiii, 96, 109

[42] V. Singh, A. Wheeler, M. Lish, O. Chvála, and B. Upadhyaya, "Nonlinear dynamic model of Molten-Salt Reactor Experiment – Validation and Operational Analysis," *Annals of Nuclear Energy*, vol. 113, pp. 177–193, 2018. 97, 101, 134, 146, 151

[43] V. Singh, A. M. Wheeler, B. R. Upadhyaya, O. Chvála, and M. S. Greenwood, "Plant-level dynamic modeling of a commercial-scale molten salt reactor system," *Nuclear Engineering and Design*, vol. 360, p. 110457, 2020. 98, 99, 101, 151

[44] S. J. Ball, "Approximate models for distributed-parameter heat-transfer systems," *ISA Transactions*, vol. 3, no. 1, pp. 38–47, 1964. 98

[45] Abilene Christian University NEXT Lab, "Abilene christian university molten salt research reactor preliminary safety analysis report." https://www.nrc.gov/docs/ML2222/ML22227A201.html. Accessed: 2023-07-18. x, xi, xiii, 102, 103, 105, 106

[46] S. Cantor, "Physical properties of molten-salt reactor fuel, coolant, and flush salts," Tech. Rep. ORNL-TM-2316, Oak Ridge National Laboratory, Oak Ridge, TN, USA, August 1968. 107, 111, 115

[47] J. W. Cooke and B. Cox, "Forced-convection heat-transfer measurements with a molten fluoride salt mixture flowing in a smooth tube," Tech. Rep. ORNL-TM-4079, Oak Ridge National Laboratory, Oak Ridge, TN, USA, March 1973. 111

[48] R. Serth, *Process Heat Transfer*. Oxford: Academic Press, 2007. 114

[49] K. Thulukkanam, *Heat Exchanger Design Handbook*. CRC Press, Feb. 2000. 114

[50] T. L. Bergman, A. S. Lavine, F. P. Incropera, and D. P. DeWitt, *Fundamentals of heat and mass transfer*. Hoboken, NJ: John Wiley & Sons, 2017. 114, 116, 120

[51] D. Q. Kern, *Process Heat Transfer*. Tokyo, Japan: McGraw-Hill, 1983. 117

[52] "Github repository for SMD-MSRv2." https://github.com/ondrejch/2020-SMD-MSR/tree/master/SMD_MSRv2, 2021. [Online; accessed]2021-02-10]. 126, 151

[53] R. C. Steffy, Jr., "Experimental dynamic analysis of the msre with *sup*233u fuel.," Tech. Rep. ORNL-TM-2997, Oak Ridge National Laboratory, Oak Ridge, TN, USA, January 1970. 130

[54] V. Singh, M. R. Lish, A. M. Wheeler, O. Chvála, and B. R. Upadhyaya, "Dynamic modeling and performance analysis of a two-fluid molten-salt breeder reactor system," *Nuclear Technology*, vol. 202, no. 1, pp. 15–38, 2018. 151

[55] V. Singh, A. M. Wheeler, O. Chvála, and B. R. Upadhyaya, "Exploring molten-salt reactor dynamic behavior and control strategies," in *61st Annual ISA POWID Symposium Proceedings, Knoxville, TN, USA*, 2018. 180

[56] R. Kedl, "ORNL-TM-3884: The Migration of a Class of Fission Products (Noble Metals) in the Molten-Salt Reactor Experiment," tech. rep., Oak Ridge National Laboratory, Oak Ridge, TN, USA, December 1972. 187

[57] J. C. Gehin and J. J. Powers, "Liquid Fuel Molten Salt Reactors for Thorium Utilization," *Nuclear Technology*, vol. 194, no. 2, pp. 152–161, 2016. 187

Vita

Visura Pathirana was born in Colombo, Sri Lanka. He obtained his Bachelor's degree in Nuclear Engineering from Pennsylvania State University, University Park in 2018 and his Master's degree in Nuclear Engineering from the University of Tennessee, Knoxville in 2021. Upon completion of his doctorate, he is looking to continue work on MSRs.